

Microgels at Liquid Interfaces

Von der Fakultät für Mathematik, Informatik und Naturwissenschaften der RWTH
Aachen University zur Erlangung des akademischen Grades eines Doktors der
Naturwissenschaften genehmigte Dissertation

vorgelegt von

Steffen Bochenek, Master of Science Chemie

aus

Viersen, Deutschland

Berichter: Univ.-Prof. Dr. Walter Richtering
Prof. Dr. Lucio Isa

Tag der mündlichen Prüfung: 19.10.2020

Diese Dissertation ist auf den Internetseiten der Universitätsbibliothek verfügbar.

the little things... it's the little things...

Die vorliegende Arbeit wurde im Zeitraum April 2016 bis Mai 2020 am Insitut für Physikalische Chemie der Rheinisch-Westfälischen Technischen Hochschule (RWTH Aachen University) angefertigt.

The following parts of this thesis have been published previously:

Chapter 4. Effect of the 3D Swelling of Microgels on Their 2D Phase Behavior at the Liquid-Liquid Interface, S. Bochenek, A. Scotti, W. Ogieglo, M. A. Fernández-Rodríguez, M. F. Schulte, R. A. Gumerov, N. V. Bushuev, I. I. Potemkin, M. Wessling, L. Isa, W. Richtering, *Langmuir*, **2019**, *35*, 16780-16792.

W. R., L. I. and I designed the study. I performed the microgel synthesis, characterization, interfacial experiments, and data analysis. I revised and improved the used Matlab script. I recorded most of the atomic force microscopy images. W. O. and I carried out the ellipsometry measurements and data analysis. I wrote and revised the manuscript, which was corrected by all authors.

Chapter 5. Temperature-sensitive Soft Microgels at Interfaces: Air-Water versus Oil-Water, S. Bochenek, A. Scotti, W. Richtering, *Soft Matter*, **2020**, DOI: <https://doi.org/10.1039/D0SM01774D>.

W. R. and I designed the study. I performed the microgel synthesis, characterization, interfacial experiments, and data analysis. I wrote and revised the manuscript, which was corrected by all authors.

Chapter 8. Exploring the Colloid-to-Polymer Transition for Ultra-Low Crosslinked Microgels from Three to Two Dimensions, S. Bochenek, A. Scotti, M. Burgnoni, M. A. Fernández-Rodríguez, M. F. Schulte, J. E. Houston, A. P. H. Gelissen, I. I. Potemkin, L. Isa, W. Richtering, *Nature Communications*, **2019**, *10*, 1418.

A. S. and W.R. designed the study. M. B., A. P. H. G. and I performed the microgel synthesis and characterization. I performed the interfacial experiments, and data analysis. I revise and improve the used Matlab script. I recorded most of the atomic force microscopy images. A. S. and I carried out the rheological measurements. I wrote and revised the manuscript together with A. S., which was corrected by all authors.

The author has contributed to the following publications:

Stimulated Transitions of Directed Nonequilibrium Self-Assemblies, A. A. Steinschulte, A. Scotti, K. Rahimi, O. Nevskiy, A. Oppermann, S. Schneider, S. Bochenek, M. F. Schulte, K. Geisel, F. Jansen, A. Jung, S. Mallmann, R. Winter, W. Richtering, D. Wöll, R. Schweins, N. J. Warren, F. A. Plamper, *Advanced Matter*, **2017**, *29*, 1703495.

Tuning the Structure and Properties of Ultra-Low Cross-Linked Temperature-Sensitive Microgels at Interfaces via the Adsorption Pathway, M. F. Schulte, A. Scotti,

M. Burgnoni, S. Bochenek, A. Mourran, W. Richtering, *Langmuir*, **2019**, *35*, 14769-14781.

Flow Properties Reveal the Particle-to-Polymer Transition of Ultra-low Crosslinked Microgels, A. Scotti, M. Burgnoni, C. G. Lopez, S. Bochenek, J. J. Crassous, W. Richtering, *Soft Matter*, **2020**, *16*, 668-678.

Influence of Charges on the Behavior of Polyelectrolyte Microgels Confined to Oil–Water Interfaces, M. M. Schmidt, S. Bochenek, A. A. Gavrilow, I. I. Potemkin, W. Richtering, *Langmuir*, **2020**, *37*, 11079-11093.

Stiffness Tomography of Ultra-Soft Nanogels by Atomic Force Microscopy, M. F. Schulte, S. Bochenek, M. Burgnoni, A. Scotti, A. Mourran, W. Richtering, *Angewandte Chemie International Edition*, **2020**, DOI: <https://doi.org/10.1002/anie.202011615>.

Phase Behavior of Ultrasoft Spheres Show Stable BCC Lattices, A. Scotti, J. E. Houston, M. Burgnoni, M. M. Schmidt, M. F. Schulte, S. Bochenek, R. Schweins, A. Feoktystov, A. Radulescu, W. Richtering, *Physical Review E*, **2020**, *105*, 052602.

Kurzzusammenfassung

Mikrogele sind dreidimensionale, vernetzte Polymernetzwerke mit kolloidaler Größe, die in einem guten Lösungsmittel dispergiert und gequollen sind. Sie kombinieren Eigenschaften sowohl von Polymeren als auch von kolloidalen Partikeln, wie z. B. das Quellen oder Entquellen als Reaktion auf Umgebungsveränderungen oder ihre Kristallisation bei hohen Volumenanteilen. Weiterhin wurde gezeigt, dass Mikrogele leicht an Grenzflächen adsorbieren und responsive Emulsionen, Schäume oder Beschichtungen formen. Obwohl Mikrogele in Lösung eine isotrope, sphärische Form haben, werden sie bei der Adsorption anisotrop. Die typische Struktur regulär vernetzter Mikrogele an Grenzflächen wird von einer Kern-Korona-Morphologie beschrieben. Hier werden die Temperaturempfindlichkeit und der Polymer-Partikel-Übergang von Mikrogele an flüssigen Grenzflächen untersucht.

Das zweidimensionale Phasendiagramm von poly(*N*-isopropylacrylamid) (pNIPAM) Mikrogele unterhalb und oberhalb ihrer Volumenphasenübergangstemperatur wird mithilfe von Kompressionsisothermen, Rasterkraftmikroskopie, Bildanalyse und Reflektometrie untersucht. Bei geringer Kompression dominieren die stark gespreiteten Koronen der Mikrogele ihre Wechselwirkungen untereinander und das Phasenverhalten der Mikrogelmonolagen ist bei beiden Temperaturen gleich. Polymersegmente in direktem Kontakt mit der Grenzfläche verlieren aufgrund der Oberflächenenergie ihre Temperaturempfindlichkeit. Bei höherer Kompression werden die Teile der Mikrogele, welche sich in der wässrigen Phase befinden, relevant und überwiegen bei ihren Wechselwirkungen. Diese Teile können entquellen, was zu einer Veränderung des isostrukturellen Phasenübergangs führt. Diese Veränderung tritt sowohl an der *n*-Dekan-Wasser- als auch an der Luft-Wasser-Grenzfläche auf. Daraus folgt, dass die temperaturabhängige Quellung senkrecht zur Grenzfläche die Kompressibilität innerhalb der Grenzfläche beeinflusst.

Verschiedene pNIPAM-basierte Systeme, angefangen bei linearen Polymeren, über regulär vernetzte, bis hin zu hohlen Mikrogele werden untersucht. Ähnlich wie bei Mikrogele in Lösung zeigt sich, dass die Verformbarkeit oder Weichheit von Mikrogele aufgrund von Einschränkungen des Polymernetzwerks, eine dominierende Eigenschaft für ihr Grenzflächenverhalten ist. Ihr weiches Wechselwirkungspotential kann nicht nur durch eine Variation des Vernetzergrades, sondern auch durch die Architektur des polymeren Netzwerks, z. B. durch den Einbau eines Hohlraums, eingestellt werden.

Um den Übergang von Polymeren zu Teilchen, d. h. der Übergang von linearen Polymeren zu regulär vernetzten Mikrogele, genauer zu bestimmen, werden ultraniedrig vernetzte Mikrogele untersucht. Bei diesen handelt es sich um die pNIPAM Mikrogele mit der geringsten Anzahl von Vernetzungspunkten, welche durch Fällungspolymerisation synthetisiert werden können. Ihr Phasenverhalten und ihre rheologischen Eigenschaften in Lösung entsprechen denen von anderen weichen Kolloiden. Werden diese Mikrogele jedoch an eine Öl-Wasser-Grenzfläche gebracht, ähneln ihre Kompressionsisothermen denen flexibler Polymere, und es wird eine konzentrationsabhängige Topographie beobachtet. Abhängig von der Kompression können sich diese Mikrogele wie flexible Polymere verhalten, die ein Substrat mit einem gleichmäßigen Film bedecken, oder wie Mikrogele, die eine Monolage von unterscheidbaren Partikeln bilden.

Abstract

Microgels are three-dimensional, cross-linked polymer networks of colloidal size which are dispersed in and swollen by a good solvent. They combine properties of polymers and colloidal particles, such as their swelling or deswelling in response to external stimuli or their crystallization at higher volume fractions. Furthermore, microgels have been shown to readily adsorb to interfaces and form responsive or “smart” emulsions, foams and coatings. Though having an isotropic, spherical shape in bulk solution, the microgels become anisotropic upon adsorption. The structure of regular cross-linked microgels at interfaces is described by a core-corona morphology. In this thesis, the temperature-sensitivity and polymer-to-particle transition of microgels at fluid interfaces are investigated.

The two-dimensional phase diagram of poly(*N*-isopropylacrylamide) (pNIPAM) microgels below and above their volume phase transition temperature is investigated with a combination of compression isotherms, atomic force microscopy, image analysis, and reflectometry methods. At low compression, the interaction between adsorbed microgels is dominated by their highly stretched corona and the phase behavior of the microgel monolayers is the same. The polymer segments within the interface lose their temperature-sensitivity due to the influence of surface free energy. At high compression, however, the portions of the microgels that are located in the aqueous side of the interface become relevant and prevail in the microgel interactions. These portions are able to deswell and, consequently, the isostructural phase transition is altered. It is shown that this effect is presented at both decane- and air-water interface. Thus, the temperature-dependent swelling perpendicular to the interface (“3D”) affects the compressibility parallel to the interface (“2D”).

Different pNIPAM-based systems, starting from linear polymers, through regular cross-linked, to hollow microgels were investigated. Similar to microgels in bulk solution, it is shown that the deformability and softness of microgels, due to the constraints of the polymer network, is a dominant property for the interfacial behavior. Their soft interaction potential cannot only be tuned by the variation of cross-linker but also by the architecture of the polymeric network, *e.g.*, the incorporation of a solvent filled cavity.

A closer look was taken at the polymer-to-particle transition. Therefore, ultra-low cross-linked (ULC) microgels were investigated, which are the pNIPAM microgels with the lowest number of cross-linking points within their network that can be synthesized by precipitation polymerization. Their phase behavior and rheological properties in bulk are those of soft colloids. However, when these microgels are confined at an oil-water interface, their compression isotherms resemble that of flexible polymers and a concentration-dependent topography is observed. Depending on the compression, these microgels can behave as flexible polymers, covering the substrate with a uniform film, or as colloidal microgels leading to a monolayer of particles.

Contents

1	Introduction	13
2	Scientific Background	17
2.1	Thermo-Responsive Microgels	17
2.2	Microgels at Liquid Interfaces	18
3	Methods	23
3.1	Langmuir and Langmuir-Blodgett Trough	23
3.2	Atomic Force Microscopy	26
3.3	Image Analysis	28
3.4	Reflectometry	32
3.4.1	Neutron Reflectometry	33
3.4.2	Ellipsometry	35
4	Effect of the 3D Swelling of Microgels on Their 2D Phase Behavior at the Liquid-Liquid Interface	37
4.1	Introduction	37
4.2	Experimental	38
4.2.1	Materials	38
4.2.2	Synthesis	38
4.2.3	Compression Isotherms and Depositions	39
4.2.4	Atomic Force Microscopy	40
4.2.5	Image Analysis	40
4.2.6	Ellipsometry	41
4.2.7	Dynamic Light Scattering	42
4.2.8	Small-Angle Neutron Scattering	42
4.2.9	Electrophoretic Mobility and Zeta-Potential	42
4.3	Results and Discussion	43
4.3.1	Characterization of Microgels in Solution	43
4.3.2	Two-dimensional Phase behavior of Microgels at Liquid Interfaces	44
4.3.3	Three-dimensional Swelling of Microgels at the Interface	52
4.3.4	Combining Two- and Three-dimensional Results	54
4.4	Conclusion	57
4.5	Data Availability	58
5	Comparison of Microgel Monolayers at Oil-Water and Air-Water Interfaces and their Temperature-Dependent 2D Phase Behavior	59
5.1	Introduction	59
5.2	Experimental	59
5.2.1	Materials	59
5.2.2	Compression Isotherms and Depositions	60
5.2.3	Image Analysis	60
5.3	Results and Discussion	61
5.4	Conclusion	72

5.5	Data Availability	73
6	Out-of-Plane Structure of Microgels at the Air-Water Interface	75
6.1	Introduction	75
6.2	Experimental	75
6.2.1	Materials	75
6.2.2	Specular Neutron Reflectometry	76
6.2.3	Compression Isotherms and Depositions	76
6.2.4	Image Analysis	76
6.2.5	Data Correction and Reduction	78
6.2.6	Data Analysis	78
6.3	Results and Discussion	79
6.3.1	Neutron Reflectivity as a Function of Temperature	79
6.3.2	Neutron Reflectivity as a Function of Compression	82
6.3.3	Neutron Reflectivity of Ultra-Low Cross-Linked Microgels	86
6.4	Conclusion	88
7	Influence of the Architecture on the Interfacial Properties of Microgels: Transition from Linear Chains to Hollow Microgels	89
7.1	Introduction	89
7.2	Experimental	89
7.2.1	Materials	89
7.2.2	Synthesis	89
7.2.3	Compression Isotherms	90
7.3	Results and Discussion	91
7.4	Conclusion	97
8	Exploring the Colloid-to-Polymer Transition for Ultra-Low Cross-linked Microgels from Three and Two Dimensions	99
8.1	Introduction	99
8.2	Experimental	100
8.2.1	Materials	100
8.2.2	Synthesis	100
8.2.3	Capillary Viscosimetry	101
8.2.4	Rheology	101
8.2.5	Langmuir-Blodgett Trough	101
8.2.6	Atomic Force Microscopy	101
8.2.7	Image Analysis	102
8.3	Results	102
8.3.1	Characterization of Microgels in Solution	102
8.3.2	Bulk Phase Behavior	104
8.3.3	Mechanical Response of Monolayers	106
8.3.4	Two Dimensional Phase Behavior	108
8.4	Conclusion	111
8.5	Data Availability	113
9	Conclusion and Outlook	115
9.1	Summary and Conclusion	115
9.2	Outlook	117

List of Figures	120
List of Tables	121
Bibliography	123
Appendix	143
A.1 Microgel Synthesis and Characterization	143
A.2 Interfacial Rheology	148

1. Introduction

Microgels are three-dimensional, cross-linked polymer networks of colloidal sizes which are dispersed in and swollen by a good solvent. Their most well-known characteristic is their swelling or deswelling in response to external stimuli. [1, 2] This sensitivity is an intrinsic property connected to the used polymers: the size of the microgels is determined by the balance of the free energy between the components of the binary polymer-solvent system and the elasticity of the network. When the free energy is altered, for example by changing of temperature, the microgel size changes until the energies across the polymer network are balanced again. [2] Consequently, the softness (deformability) of single microgels and the interaction between microgel cannot only be influenced *ex-situ* by the number of cross-linking points within the network during the synthesis but also *in situ* by changing the environmental conditions. This versatility earned microgels the classification as stimuli-responsive or “smart” materials.

The stimuli-responsiveness but also the excellent colloidal stability, the ease of preparation, the fine control of size, the low polydispersity, and the convenient functionalization make microgels and microgels suspensions of high interest for fundamental studies and applications, likewise. Microgels are employed as model systems to investigate questions related to strong and fragile glass formers [3, 4], to the glass and jamming transition [5, 6], to solid-to-solid phase [7, 8] and melting-freezing transitions [9–11]. For applications, microgels are considered to be used in controlled drug delivery [12, 13], (bio-) sensors [14–16], (bio-) catalysis and micro-reactors [17, 18], membranes [19], and fabrications of artificial muscles [20, 21].

In addition, microgels are highly interfacial active and lower the interfacial tension. When they adsorb to interfaces their deformable and swollen network is stretched to increase the contact area and maximize the gain in interfacial energy. This stretching is restricted by the cross-linking, *i.e.*, the elasticity, of the polymer network. The resulting conformation, combined with the adjustability of their interaction and functionality, leads to a rich 2D-phase behavior. For example, the tuneability of the microgel-to-microgel distance within the monolayer gives opportunities for soft- (nanoparticle) templating [22, 23], production of photonic crystals [24], or cell culture substrates [25, 26]. Most importantly, microgels retain their stimuli-responsiveness from bulk at interfaces and formed emulsions or foams that are responsive or “smart”, which display on one hand high stability and on the other hand, can be broken at will.

Emulsions and foams are omnipresent in nature and industrial applications, ranging from biology, meteorology, food, and geology to the petroleum industry, material science, medicine, health, and personal care products. [27] This broad variety underscores that progress and problems are usually interdisciplinary and of great interest not only for the scientific community but also for the public. There are two major class of stabilizers for liquid-liquid or liquid-gas interfaces: (i) surfactants and polymers, and (ii) particles. Without this third component, the thermodynamically unstable small droplets or bubbles are driven towards free energy minimization and undergo coagulation, Ostwald ripening, or coalescence leading to demixing and phase separation. While surfactant stabilized systems suffer in long term stability problems and sometimes show skin irritations, particle-stabilized systems show bet-

ter stability but need rigorous mixing due to a high energy barrier upon adsorption. For both systems, the demulsification and defoaming are complicated and might include strong changes in environmental conditions, the addition of further chemicals, destruction of the emulsifier, or filtration. [28] Therefore, it has been the focus of research in the past decades to find or modify systems to be stimuli-responsive, where moderate changes in the local environment induce phase separation.

Therefore, microgels gained a lot of popularity in recent years, although their interfacial behavior, the correlation between their bulk structure and interfacial conformation, and their stimuli-responsiveness at interfaces is not fully understood. This thesis aims to broaden the understanding of microgels confined in two-dimensions, elucidating before mentioned issues. In detail, we investigated the following aspects:

- The influence of temperature on microgel monolayers. It was studied how the properties of single microgels, *e.g.*, their in-plane and out-of-plane conformation, and the corresponding two-dimensional phase behavior of microgel monolayers are affected by changing the temperature from below to above the volume phase transition temperature of poly(*N*-isopropylacrylamide). Single microgels and monolayers were examined below and above their phase transition temperature at both air- and oil-water interfaces.
- The polymer-to-particle transition. Poly(*N*-isopropylacrylamide) with different numbers of grafting and cross-link points were experimentally studied to elucidate the relationship between their conformation, their two-dimensional phase behavior, and their architectural complexity. Particular focus was placed on the transition from monolayers of flexible linear polymers to cross-linked polymer networks.

To address these aspects, microgel model systems were synthesized and characterized. The poly(*N*-isopropylacrylamide)-based microgels were studied in solution with scattering methods (dynamic light scattering, small-angle neutron scattering), electrophoresis, viscosimetry, and rheology (Chapters 4 and 9.2). A careful and comprehensive analysis of the microgels is crucial to draw conclusions and correlate the results of interfacial experiments to their internal conformation and make predictions for other systems.

The interfacial behavior of the poly(*N*-isopropylacrylamide) microgels was investigated at flat liquid interfaces that are easily accessible and provide insights into the properties of microgels in emulsion droplets (or foam bubbles). The compressibility and microstructure of microgel monolayers at air- and decane-water interfaces were investigated with Langmuir compression isotherms and gradient Langmuir-Blodgett type depositions. The influence of temperature on the two-dimensional phase behavior is emphasized in Chapters 4 and 5. Image procedures and analysis are employed to determine the in-plane dimensions of the microgel monolayers below and above their volume phase transition temperature. The out-of-plane extension of the monolayers as a function of temperature at the air-water interface are studied with reflectometry techniques (Chapters 4 and 6). The combination of in-plane and out-of-plane experimental techniques in Chapter 4 reveals that the temperature-dependent swelling perpendicular to the interface (“3D”) affects the compressibility parallel to the interface (“2D”). The perpendicular, out-of-plane conformation of microgels at interfaces is the crucial factor that should always be considered. [29]

Finally, the polymer-to-particle transition is addressed by the comparison of compression isotherms and deposited monolayers for different poly(*N*-isopropylacrylamide) systems in Chapters 7 and 8. Chapter 8 focuses especially on the case of ultra-low cross-linked microgels, which are the microgels with the lowest cross-linker content possible to synthesize with precipitation polymerization. These microgels can show polymer- and microgel-like behavior depending on the dimensionality (two- or three-dimensions) or the compression of the monolayer. [30, 31]

2. Scientific Background

2.1. Thermo-Responsive Microgels

The archetype of responsive or “smart” microgels, first reported by Pelton and Chibante in 1986, [32] is based on *N*-isopropylacrylamide (NIPAM), cross-linked with *N,N'*-methylenebisacrylamide (BIS) and synthesized by precipitation polymerization. Poly-*N*-isopropylacrylamide (pNIPAM) shows a lower critical solution temperature, LCST, of $\approx 32\text{ }^{\circ}\text{C}$ [33, 34] in water, consequently the resulting microgels displayed a thermo-responsive behavior. Since then, different co-monomers were successfully incorporated giving rise to numerous other responsivenesses, such as solvent composition [35, 36], pH [37–39], salt concentration [39–41], electromagnetic fields [42, 43], electrochemical potential [44, 45], and light [46–48].

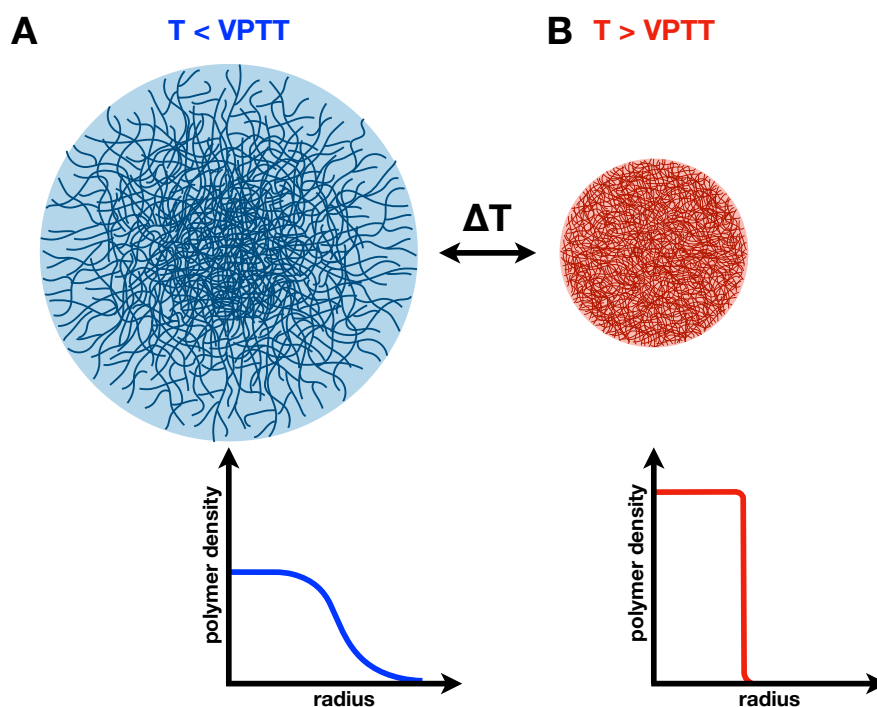


Figure 2.1: Structure of a pNIPAM microgel synthesized *via* precipitation polymerization with inhomogeneous cross-linker distribution below and above the VPTT. Polymer density profiles emphasize the structural differences between the swollen and deswollen state.

In this work, we focus on the thermo-responsiveness of pNIPAM microgels. Below the LCST of NIPAM, the polymeric network of the microgels is strongly swollen by water. Their structure was investigated by small-angle neutron scattering and is described by a fuzzy-sphere (model). [49] As depicted in Figure 2.1A, microgels display a strongly cross-linked core (hard sphere) with a decreasing polymer density towards their periphery and their outermost part is composed of dangling polymer chains (Gaussian for the decrease). The reason for this is the different reactivity of the NIPAM and the usually used cross-linker BIS. [50, 51] In this state, microgels are deformable and interact *via* a soft potential. [52] When the temperature is

raised above the LCST of NIPAM, microgels deswell and undergo an endothermic entropy-driven first order volume phase transition. Hydrophobic interactions and weakening of hydrogen bonds between water and amide groups lead to expulsion of solvent molecules from the polymer network and their density increases. Consequently, the structure of the microgels changes and they recall hard spheres, in both their polymer density profile (Fig. 2.1B) [49] and their microgel-to-microgel interaction [53]. The temperature, where the strongest change in volume is observed, is called volume phase transition temperature, VPTT. This transition is fully reversible. [32] The thermo-responsiveness of the microgels allows tuning their softness, dimensions, density, and interaction potential after the synthesis *in situ* by changing the temperature of the surrounding medium. [1, 54]

The temperature of the volume phase transition can be finely tailored by employing different *N*-substitute poly(acrylamides), such as *N*-isopropylmethacrylamide (NIPMAM), *N*-ethylacrylamide (NEAA), or *N,N'*-diethylacrylamide (DEAAM). For example, microgels synthesized from NIPMAM display a VPTT of ≈ 44 °C [55, 56], and those from DEAAM a VPTT of 26 °C [57]. It also has been reported that mixing different *N*-substitute poly(acrylamides) shifts the VPTT of the microgels. [58, 59]

2.2. Microgels at Liquid Interfaces

Microgels are highly interfacial active and stabilize emulsions [60–64] and foams [65–67]. When adsorbed to the interface, microgels lower the interfacial tension, like surfactants (amphiphiles or surface-active polymers) and rigid nano- or microparticles. In fact, microgels show a polymer-to-particle duality in solution [68] and at interfaces [69]. On one hand, they demonstrate spontaneous, barrier-free adsorption [69] and a change of conformation (or structure), [70–72] typical for polymer systems. [73] On the other hand, they display superior stability [60, 74] like Pickering emulsions, due to their strong anchoring to the interface that exceeds thermal energy by a factor of 10^6 . [69] Furthermore, the responsiveness of the microgels in bulk is preserved at interfaces and leads to the formation of smart emulsions (and foams) which can be broken at will. [60, 64, 67] Their duality, the microgels' intrinsic responsiveness, and their permeability [75] make them appealing for fundamental studies and applications likewise.

When a single microgel adsorbs to an interface, its soft, polymeric network deforms and spreads [70, 76, 77] to increase interfacial contact area and maximize the gain in surface free energy (Fig. 2.2A and B). This effect is related to the thermodynamics determining the swelling equilibrium of microgels. [29, 69, 78, 79] The size of a neutral microgel in solution is given by the balance between the elastic free energy of the polymeric network, F_{el} , and mixing between the solvent and polymer, F_{mix} . [80] For the adsorbed microgel another term has to be taken into account: the surface free energy of the boundary between oil (or air) and water, γ . The new swelling equilibrium is given by:

$$F_{el} + F_{mix} + \gamma = 0 . \quad (2.1)$$

Their structure can be visualized by fluorescence microscopy [81], cryo-scanning electron microscopy (cryo-SEM) [70, 71, 77], and transmission x-ray microscopy (TXM) [82]. These techniques disclose a core-corona or fried-egg like morphology as depicted in Figure 2.2A and B.

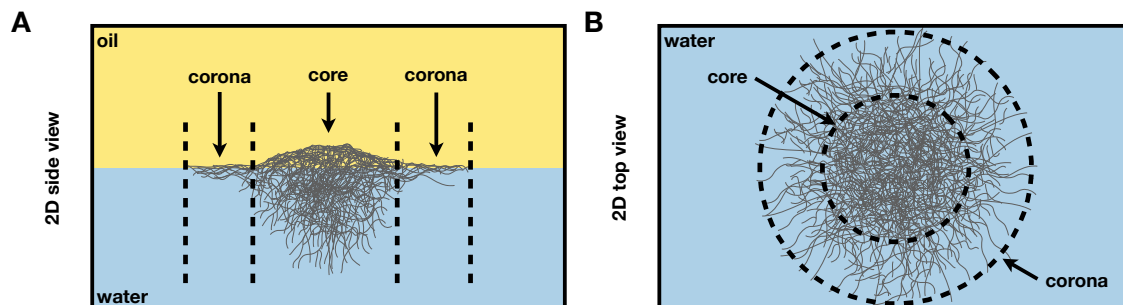


Figure 2.2: Sketch of the conformation of a pNIPAM microgel with inhomogeneous cross-linker distribution at the oil-water interface. (A) side view and (B) top view.

This morphology is a consequence of their architecture in bulk: microgels have a decreasing cross-linker and polymer content from the center to their periphery (Section 2.1). [49] Less cross-linked regions (the corona) are stretched more as they have a lower stiffness and regions of higher cross-linking, *i.e.*, the core, is stretched less. Indeed, in contrast, microgels with a nearly homogeneous bulk polymer density profile have a pancake structure (Chapter 8). [11] Another important fact is that microgels are three-dimensional objects confined in a two-dimensional space (the interface). Not all parts of the microgels can adsorb, because bending rigidity, cyclic interconnections (or cross-links), intermolecular steric and electrostatic repulsion restricts conformational freedom of the polymeric network. Thus, parts of the microgel are situated in the bulk phases, according to the affinities of the polymers the microgel is composed of. [29, 79, 83]

Increasing the interfacial concentration of microgels leads to self-assembly and their peculiar anisotropic shape produces a rich two-dimensional phase behavior. The mechanical properties of microgel monolayers can be investigated with a Langmuir or Langmuir-Blodgett trough. Geisel *et al.* showed that microgels have interesting mechanical properties and their compression isotherms show two increases. [84] Qualitatively equivalent courses of the compression isotherms were observed for many different microgel systems. [23, 76–78, 84–90] The microstructure of microgel monolayers was in particular studied by Rey *et al.* with gradient Langmuir-Blodgett trough experiments. [76] A tilted solid substrate is lifted during the compression through the interface and the monolayer is transferred with increasing packing density. The monolayer is imaged *ex situ* and the positions of the images are connected to the barrier position of the trough, that is, the surface pressure (for details the Chapter 3). They concluded that the in-plane core-corona heterogeneity of the individual microgels leads to the special course of compression isotherms. At low compression, the microgels form hexagonal crystalline lattices and only their coronae are in contact (Fig. 2.3B). Increasing the compression leads to a reduction of the center-to-center distances (Fig. 2.3C). When the coronae of the microgels are fully compressed (compressed corona-corona contact), their cores start to interact and monolayers undergo an isostructural solid-to-solid phase transition. As em-

phasized in Fig. 2.3D a second hexagonal phase with core-core contacts emerges inside the compressed corona-corona contact phase. This coexistence extends until all microgels are in the second hexagonal phase with core-core contact. The second hexagonal phase can be compressed further (compressed core-core contact), and the surface pressure increases once again before the monolayer fails (Fig. 2.3E). The isostructural phase transition has also been observed by *in situ* techniques. [61, 83]

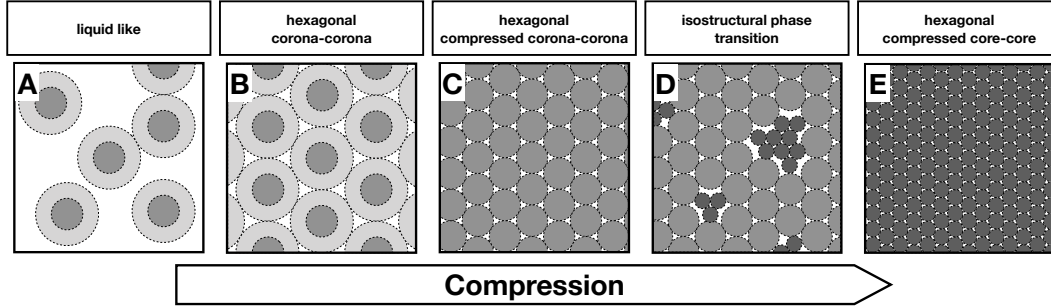


Figure 2.3: Schematic of the microstructures of microgel monolayers as a function of compression. (A) Microgels in a liquid-like state. (B) Hexagonal crystalline lattices with microgels in corona-corona contact. (C) Hexagonal crystalline lattices with microgels in compressed corona-corona contact. (D) Isostructural phase transition between microgels in compressed corona-corona and core-core contact. (E) Hexagonal crystalline lattices with microgels in compressed core-core contact. Light to dark gray gradient indicates the increasing density.

The influence of the microgels' softness, size, architecture, as well as the effects of external stimuli on their mechanical properties and microstructure have been subject of many studies in the last decade. Rey *et al.* realized a series of microgels with different amounts of cross-linker with comparable sizes. Besides a stronger spreading, softer microgels do not show an isostructural phase transition, but a continuous decrease of center-to-center distance. If the softness of the microgels is pushed to its limits, *i.e.*, the smallest amount of cross-linker is used, a strong polymer-to-particle duality for the microgels is observed. As shown in the scope of this thesis (Chapter 8), these ultra-low cross-linked microgels display homogeneous polymer films or layers of distinguishable microgels as a function of compression. [30] Similar to rigid colloids, capillary forces become important for microgels depending on their size: small microgels behave liquid like with random ordering before they get into contact (Fig. 2.3A). In contrast, larger microgels deform the interface leading to the formation of 2D aggregates. [23] The same effect can be seen when an inorganic core, *e.g.*, a silica particle, is surrounded by a microgel shell. These core-shell microgels are much heavier than normal microgels and also deform the interface. [77] The silica core of the microgels can also be dissolved, with etching by sodium hydroxide, leading to hollow microgels. In bulk and at the interface this cavity makes the microgels easier to be compressed, while still showing a compression isotherm with two increases. [88]

Destabilization of microgel stabilized emulsions (or foams) can be initiated by applying an external trigger, such as a change in pH, salt concentration, or temperature. [60, 62, 64, 65, 67] In contrast to the responsiveness of the microgels to stimuli in bulk, their response at the interface is poorly understood. In particular, changing

the pH affects the dimensions of the microgels in bulk aqueous solution, but although the adsorption kinetic of microgels is influenced [89], the lateral dimension of the adsorbed microgels is not. [70, 84, 89] Even more surprisingly, Geisel *et al.* showed that the pH-responsive microgels made of NIPAM co-polymerized with methacrylic acid (MAA) can be compressed easier at high pH when the microgels are charged and one would expect strong electrostatic repulsion. [84]

As described in Chapter 2.1, changing the solvent quality, *i.e.*, increasing the temperature above the VPTT of the microgels, leads to a change in size, internal network density, and structure in bulk. Two recent publications, one of these in the scope of this thesis, show that the parts of the microgel network directly adsorbed to the interface lose their thermo-responsiveness. [29, 79] Only the fractions of a microgel that are still situated inside the aqueous phase react to temperature changes. Furthermore, the increase of the density of these parts at elevated temperatures influences the two-dimensional phase behavior of microgel monolayers. Even though qualitatively the same microstructures are observed, the second hexagonal phase in core-core contact (Fig. 2.3E) becomes virtually incompressible. Consequently, the compression isotherms of microgels at temperatures larger than their VPTT only show a single increase. [29]

Lastly, the destabilization of microgel stabilized emulsions has been attributed to the desorption of microgels or microgel segments due to an increase in the particle hydrophobicity and the reduction of surface activity. [62, 63, 91–93] The reduced coverage of the interface results in phase separation. However, different studies have shown that the surface activity, that is, the surface tension, is not strongly affected by pH [60] and temperature [94]. Instead, the change of the viscoelastic properties of the microgel monolayer is crucial for the destabilization process. It has been shown that softer microgels form more stable emulsions [71] whereas the softness can be tuned by cross-links [95] or charges [61, 96]. Likewise, the repulsion between emulsion droplets plays an important role. In uncharged state and at high temperatures, electrostatic and steric repulsions are minimized, promoting the demulsification. [70, 79, 97]

3. Methods

3.1. Langmuir and Langmuir-Blodgett Trough

In this section a short paragraph about the definition of surface tension is provided. Elementary introduction to the thermodynamic of surfaces is provided by Israelachvili [98] or Butt [99]. A more detailed description is given, for example, by Lyklema [100].

The interface between two immiscible materials always display an excess of free energy; this is due to the differences in environment between the atoms, or molecules, at the interfaces and those in the bulk. This difference in free energy is denoted as surface free energy. [98–100] Depending on the interface referred to, the surface free energy is called surface (gas-liquid) or interfacial tension (liquid-liquid, liquid-solid or solid-air). In the following, no distinction will be made between surface and interfacial tension.

The interfacial tension, γ , is a measure of force per unit length (N/m). γ is the infinitesimal variation of the work, dW , related to the infinitesimal change of the interfacial area, ds . If the process is reversible one can write [98, 99]:

$$\gamma = -\frac{dW}{ds} = -\frac{F}{2b}, \quad (3.1)$$

where F is the force needed to increase the area of the interface and b is a unit length.

The interfacial tension of a flat interface is thermodynamically defined by the following partial differential [98, 99]:

$$\gamma \equiv (\partial G / \partial s)_{T,P,n}, \quad (3.2)$$

where G is the Gibbs free energy of the system, and the temperature, T , the pressure, P , and composition, n , are held constant.

A Langmuir trough is an apparatus to investigate monolayers of molecules, macro-molecules, and particles at liquid interfaces and measure interfacial phenomena due to compression, *e.g.* their packing density. The measured quantity is the surface or interfacial pressure, Π , which is the difference between the interfacial tension of the clean interface, γ_0 , and the interfacial tension of the substance laden interface, γ_c .

$$\Delta\gamma = \Pi = \gamma_0 - \gamma_c, \quad (3.3)$$

consequently, Π has the same unit as the surface tension.

Most commonly the Wilhelmy plate method is used to measure the interface pressure during the measurement. For this, a probe connected to an electronic force balance is brought into contact with the interface. The probe is typically a plate made from paper, glass, or platinum and is roughened to ensure optimal wetting. Surface pressure and gravity pull the plate downwards, and buoyancy, due to displaced water, acts upwards on the Wilhelmy plate. In case of a rectangular plate with the density, ρ_p , the dimensions, l_p , w_p , and d_p , the immersion depth of the plate, h_p , and the liquid density, ρ_l , the net downward force is given by [101]:

$$F = \rho_p l_p w_p d_p g + 2\gamma(d_p l_p) \cos \theta - \rho_l d_p l_p h_p g, \quad (3.4)$$

where g is the gravitational acceleration, and θ is the contact angle of the liquid with the plate.

For a completely wetted plate the contact angle between the liquid and the plate is $\theta = 0^\circ$ and the surface pressure can be described as:

$$\Pi = \Delta\gamma = \frac{\Delta F}{2(l_p + d_p)}. \quad (3.5)$$

Where ΔF is the difference between the force acting on the stationary plate when the interface is clean and when a surface-active material is present. Thus, the surface pressure is directly determined from the forces acting on the plate with a known perimeter ($2(l_p + d_p)$). [101, 102] Typically, interfacial active materials are measured as a function of the trough area and at constant temperatures. The result is an interfacial pressure-area (Π - A) isotherm or simply isotherm.

A Langmuir Trough can also be used to transfer the monolayer to a solid support and there are a number of different ways to achieve this. The most prominent way was proposed by Langmuir and Blodgett in the 1930s. In the Langmuir-Blodgett technique the monolayer is transferred to a vertically standing substrate as it is moved through the interface. It has been shown that this method can be used to deposit more than one layer to the substrate. [103, 104] Other examples are the toughing method proposed by Schulmann *et al.* [105] or the lifting method of Langmuir and Schaefer [106]. These examples have in common that they are conducted at a fixed surface pressure of the monolayer. A more detailed explanation, different designs, potential applications, and a historical background for the Langmuir and Langmuir-Blodgett trough technique can be found in the work of Roberts [101] or Gaines [107].

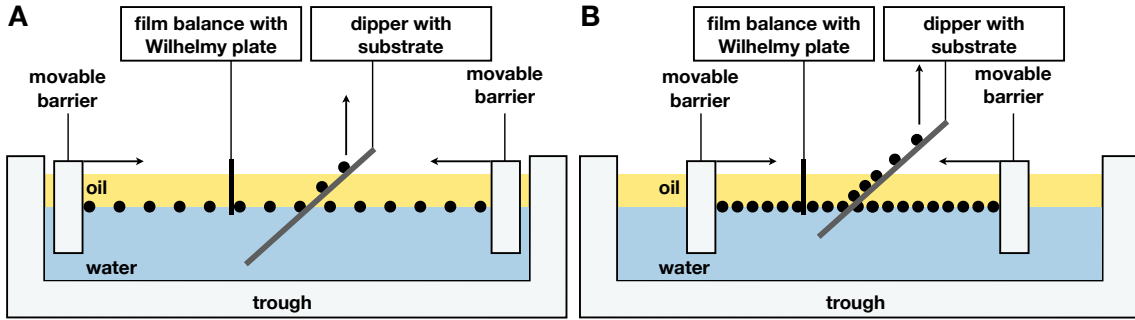


Figure 3.1: Schematic figure of a Langmuir trough used for gradient Langmuir-Blodgett type depositions. The surface pressure is measured by a Wilhelmy plate connected to a film balance between two movable barriers. A surface-active material is represented by black circles. A solid substrate is lifted by a dipper through the monolayer with an angle of $\approx 45^\circ$ to transfer the surface-active material for subsequent imaging. (A) and (B) show different compression of the monolayer and position of the substrate.

A way to obtain Π - A isotherms and information about the microstructure of the monolayers are gradient Langmuir-Blodgett type depositions [22, 29, 76, 108] shown in Fig. 3.1. Here, the substrate is immersed into the sub-phase before the monolayer is spread and has an angle between 0 and 90° relative to the interface. While the monolayer is compressed the substrate is lifted in between the barriers

through the interface. The process produces a gradient of packing density of the deposited monolayer, schematically shown in Fig. 3.1B. Subsequently, the deposition is investigated *ex situ* with imaging techniques, such as atomic force or scanning electron microscopy, and the structure can be connected to the mechanical properties of the monolayer. [29, 76]

3.2. Atomic Force Microscopy

An atomic force microscope is a mechanical imaging instrument that measures the three-dimensional topography as well as the physical properties of a surface using a probe. Atomic force microscopy (AFM) gives images with extremely high (nanometer range) resolution in xyz direction, while the image size limit is several tens of micrometers. [109] In addition, samples imaged with AFM do neither require any special treatments, such as metal coating or labeling with fluorescent stains, nor special measurement environments for proper operation are needed. A drawback is slow scanning speed compared to optical or electron microscopy; scanning of a single image takes usually minutes to tens of minutes. [110]

The schematic structure of an atomic force microscope is sketched in Figure 3.2A. The outermost part of this probe that interacts with the sample is called a tip. Different geometry of tips are available and there are two general categories [111–116]: (i) blunt tips with small aspect ratios and large radii, for example, colloidal probes which are spheres, and (ii) sharp tips with large aspect ratios and small radii, typically pyramidal or needle-like. Whereas the latter is preferentially employed for imaging of samples, [110, 111] blunt tips are especially used to investigate the forces between colloidal particles and/or surfaces. [115, 116]

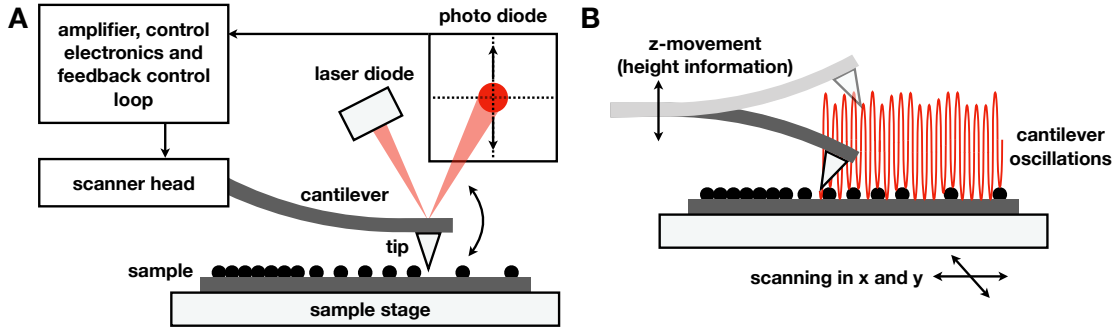


Figure 3.2: (A) Schematic structure and functionality of an atomic force microscope with block diagram (B) Schematic figure of the tapping or intermediate contact mode for imaging.

The tip is attached to a spring-like cantilever. The cantilever is an essential part of the force transducer of the atomic force microscope that converts the forces into a measurable voltage signal. When the tip interacts with the sample the cantilever is deflected. The deflection, δ_{afm} , of the cantilever can be measured and most frequently the laser beam bounce method is used. [117, 118] For this method, a laser is directed onto the backside of the cantilever and the beam is reflected onto a position-sensitive photo diode. Often the backside of the cantilever is coated or polished to increase the reflection. The deflection can then be related to a force, F_{afm} , by the spring constant, k_{afm} , of the cantilever using Hooke's law. k_{afm} can be measured or calculated from the dimensions of the cantilever. [110]

The cantilever is connected to the cantilever holder, also called chip, which allows the whole probe to be mounted into the scanning head of the atomic force microscope. The scanning head contains piezoelectric motors for fine movement in xyz-direction.

One of the strong points of atomic force microscopy is the versatility, *i.e.*, the microscope can be operated in many different modes. The most common modes to

measure the topography of a sample are contact, tapping, and non-contact mode. In this work the tapping mode of the atomic force microscope was exclusively used; therefore, this mode will be briefly discussed.

In tapping mode, the surface of the sample is tapped by the probe, which means the tip has short, intermediate contacts to the sample. [119] Therefore, the piezoelectric motors of the scanner head drive the cantilever to vertical oscillate near its resonance frequency and with an amplitude that usually varies from a few to hundreds of nm. As the cantilever oscillates, the reflected laser beam is deflected in a regular pattern over the photo diode. Thus, a sinusoidal electronic signal is detected. When the tip approaches and encounters the sample, interaction forces, such as van-der-Waals, dipole-dipole, and electrostatic forces, act on the cantilever. These forces lead to a change of the oscillation amplitude of the cantilever and the detected signal. A closed feedback loop regulates the sample-probe distance and the adjustments are used to create a three-dimensional image of the sample surface. [109, 119]

Furthermore, the phase shift between the driving signal and the recorded frequency of the cantilever can be used for phase imaging. For a free oscillating probe, the phase shift equals the dissipated energy into the environment. If the tip contacts the surface, the energy dissipation changes depending on the mechanical properties of the sample and a different phase shift is monitored. Therefore, phase images show regions of varying stiffness, adhesion, viscoelasticity, and contact area and are useful to characterize heterogeneous samples with low topographic differences. [120, 121] Topographic and phase images can be recorded at the same time in tapping mode.

3.3. Image Analysis

Image analysis is a fundamental, interdisciplinary tool for finding and recognizing objects present in an image. Thereby, meaningful information of two- (2D) or three-dimensional (3D) digital images are extracted using digital image processing techniques. [122, 123] Image analysis tasks range from simple recognition of bar codes [124], through the determination of clinically relevant areas in magnetic resonance images (MRI) [125], identifying persons [126], to environment perception for self-driving cars [127]. While identifying objects is done easily and a million times a day by persons, for computers it is extremely hard to do. On the other hand, further steps, such as determination and extraction of numeric values, information about image characteristics, detection and prediction of trends, or calculation of statistics of investigated objects, are much faster executed and done with higher accuracy by computers.

Throughout this thesis gradient Langmuir-Blodgett type depositions (for details see Chapter 3.1) were conducted to correlate the mechanical behavior (compression isotherms) of microgels confined in two-dimensions with their interfacial dimensions and microstructure. For the (atomic force microscopy) images of deposited microgel monolayers image analysis was employed to extract meaningful parameters, such as the number of microgels per area, N_{area} , the mean nearest neighbor distances, NND , or the hexagonal order parameter, Ψ_6 . The whole process of evaluating the depositions can be divided into two parts: (i) the connection of the image positions with the surface pressure, and (ii) the extraction of the parameters from the images (image analysis).

Although the first part does not contain any image analysis *per se* it is an important component worth explaining here. The positions of the images and the surface pressure of the monolayer are encoded by geometric calculations. A reference point, p_r , on the substrate is obtained by stopping the dipper and barrier movement at the smallest available area or highest surface pressure, respectively (Figure 3.3A). Subsequently, the barriers are fully opened and the substrate is rapidly moved through the interface. Because the inter-particle distance of the microgel monolayer depends on the compression (the surface pressure), this creates a visible discontinuity on the substrate (As sketched in Figure 3.3A or shown in images K-L and W-X in Figure 4.4).

The image positions relative to the discontinuity, *i.e.*, p_r , are calculated after the depositions are imaged. Therefore, the position of the reference point and the real image positions are recorded; using the distance between the reference point and real image positions, d_i , the image positions relative to the reference, i_p , are obtained (Figure 3.3A). Then, the length of the deposition on the substrate is calculated from: $c = a / \sin(\Theta_{sub})$, where a is the distance the dipper arm was moved during the experiment, and Θ_{sub} the angle of the substrate with respect to the air- or decane-water interface (Figure 3.3A). Although Θ_{sub} is given by the dipper head geometry, it is verified prior to each deposition experiment: when the substrate is immersed into the sub-phase, the distance the dipper arm moves for a defined length between two marks on the substrate is measured. The deposition and compression are started at and conducted for the same time. Therefore, i_p can be converted into a barrier position, bp , using the ratio between the distance the barriers moved during the experiment Δbp and c with the equation: $bp = bp_{end} - (\Delta bp / c) \cdot i_p$, with bp_{pr} the

barrier position of the reference point. As shown in Figure 3.3A, the barrier position is directly connected to Π and the surface pressure of each image is obtained.

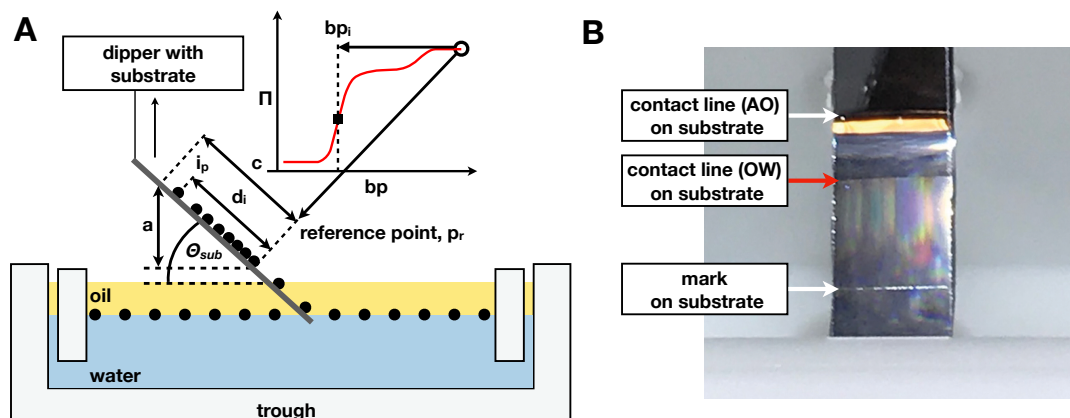


Figure 3.3: Connection of image positions and surface pressure. (A) Sketch of the geometric relationship between image positions and barrier position (see text for details). (B) Proof of concept for the image analysis supported direct correlation of image position and Π . The image shows a substrate (silicon-wafer) during deposition from the decane-water (OW) interface. This image was taken with an iPhone 7 camera.

These calculations assume that the contact angle of the substrate and the three-phase contact line (between the substrate, water, and air or oil) does not change due to the presence of the microgel monolayer at different compressions. Thus, utmost care must be taken during the experiment and encoding. However, the encoding of Π and the image position can be improved by employing image analysis. As shown in Figure 3.3B (red arrow), the position of the decane-water (OW) interface on the substrate is visible during the deposition experiment. The substrate, typically a silicon-wafer, could be imprinted with a scale on one side. Figure 3.3B (mark on the substrate) shows that such a scale would be visible in a digital image as well. The position of the interface during the experiment could be tracked with a camera and image analysis methods employed to determine the interface's position relative to the scale in a time series of images. Consequently, the position of the interface at different times and the position of the images can be directly correlated to the surface pressure. The second part is the image analysis step within the evaluation of gradient Langmuir-Blodgett type depositions where (AFM) images of dried microgel monolayers are analyzed. For this, an optimized version of the custom-written Matlab script of Ref. [76] is employed. This Matlab script is based on the particle tracking algorithm from Crocker and Grier [128] and its public available Matlab version by Blair and Dufresne [129]. In general, this procedure is based on thresholding, *i.e.*, the creating of binary images, to determine the (central) position of spherical objects in an image. The routine uses a three-stepped procedure: firstly, a band-pass filter (Gaussian for lowpass and Boxcar for highpass) is applied that smooths the image and subtracts the background. Secondly, the centers of the remaining bright spots (blobs) in the image are identified by comparing pixel-wise the brightness within a blob and picking the brightest. Thirdly, the locations of the objects' centers are re-evaluated by creating a small area (working array) around each located center. The total brightness of this working array is weight averaged

and the position of the center is determined (with sub-pixel accuracy). The eminent drawbacks of this procedure are the dependence on input parameters, such as a (good) estimate of distance and brightness, and that it is restricted to circular objects. Other possible methods that do not have these problems or have it to a lesser extent. Options would be to visualize discontinuities present in the images (edge detection) with, for example, the methods proposed by Canny [130] and Prewitt [131], or the Matlab functions *imfindcircles* (for circular objects) and *regionprops* (for any shape). However, the procedure based on Crocker and Grier gives good results with little computational effort, thus the particle tracking routine was neither changed nor exchanged.

Optimizations and changes to the Matlab script of Ref. [76] were mostly done to achieve automatic detection of different phases within an image. Microgel monolayers display an isostructural solid-to-solid phase transition where microgels coexist in two hexagonal lattices with different lattice constants (for detail see Chapter 2.2). The detection of this phase transition can be done by hand, for example, the introduction of a threshold value for the center-to-center distance; however, for the analysis of large sets of data it is advantageous that the routine can achieve this task automatically, based on the information of the image.

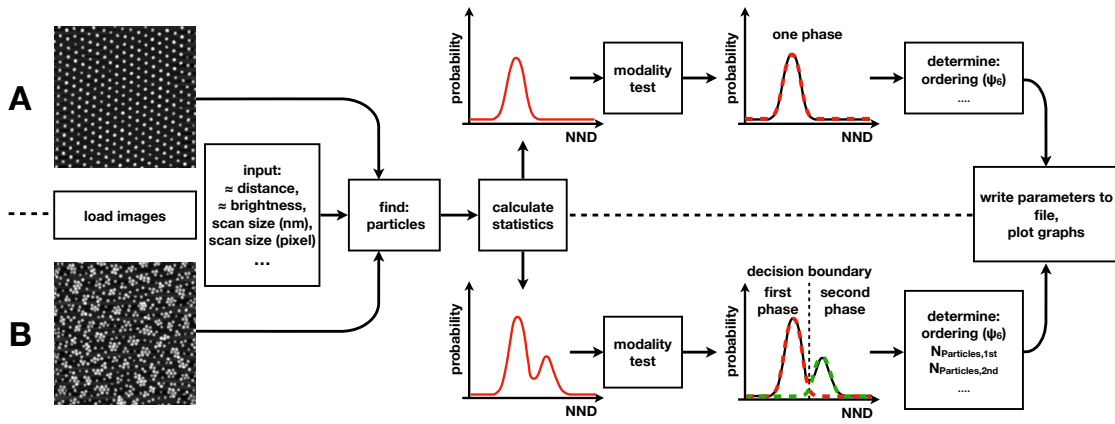


Figure 3.4: Flow chart of the image analysis routine. Path (A) for a microgel monolayer with a single hexagonal lattice. Path (B) for a microgel monolayer in the isostructural solid-to-solid phase transition. For more details see text.

Statistical modality tests [132] were implemented into the Matlab routine to automatize the detection of the isostructural phase transition. After the localization of the centers, a Delaunay triangulation (Matlab function *delaunayTriangulation*) and the corresponding dual graph, the Voronoi tessellation (Matlab function *voronoi*), are performed. The resulting center-to-center distances, areas, and circumference of the triangles formed by adjacent microgels are summarized in histograms (Figure 3.4 path A and B). In the case of the isostructural phase transition, distributions are not mono- but bimodal (Figure 3.4 path B). Therefore, primitive modality tests are conducted, which search for local minima, inflection, and/or saddle points. After the modality test, statistic values are determined, *e.g.*, by fitting normal distributions to the curves. In the case of a bimodal function, the modality test yields a decision boundary, for example, the local minimum in Figure 3.4 path B. Consequently, the convolution of two single Gaussians are fitted to the probability distribution. The obtained parameters (peak height, peak position, and variance) are filtered for un-

physical values, and, in-case, the image is re-evaluated. The decision boundary is used to determine which microgels are and the number of microgels in the first and second phase. Subsequently, all relevant parameters and diagrams are saved.

Obviously, this routine has some drawbacks, for example, for a low number of occurrences, *i.e.*, a small number of microgels on the image, the statistic is superimposed with noise. Further for small separations or similar center-to-center distances of the first and second phase, mono- and bi-modality are hardly distinguishable. Nevertheless, a comparison of the results with the manual determination shows good agreement. This optimized routine has been used to compute the results presented in Chapters 4, 5 and 8.

Lastly, further possible optimizations to the Matlab script should be discussed. A key point to understand the behavior of microgels confined in two-dimensions is their core-corona structure (Chapter 2.2). In Chapters 4 and 5, it is discussed that the occurrence of the isostructural phase transition is directly connected to this structure or the size of the microgel fractions situated in the aqueous phase, respectively. Therefore, extraction not only of center-to-center distances but also of the size of these fractions within the Matlab script is a desirable goal. As shown in Chapter 5, this could be done by extraction of height profiles through the apices of the microgels at different angles with respect to the fast scan direction of the AFM. The averaged height profiles can be used to approximate the size of the microgel fractions situated in the sub-phase.

Furthermore, the implementation of different particle tracking algorithms as discussed above are needed to analyze monolayers of microgels with more complex architecture, such as hollow (Chapter 7) or anisotropic microgels.

3.4. Reflectometry

Reflectometry is a generic concept for various methods that are based on the reflection of radiation at an interface. They are non-invasive, non-destructive, and non-contact methods to obtain the structure of a sample normal to its surface with high (Ångstrom range) resolution. One of their main disadvantages is that they are indirect and a model is needed to obtain physical parameters. Reflectometry methods are categorized by the radiations used, such as light, x-rays, or neutrons. In sections 3.4.1 and 3.4.2 brief introductions to neutron reflectometry and ellipsometry are given, respectively. Full introductions and in-depth explanations for ellipsometry can be found in the work of Tompkins [133] and Fujiwara [134] and for neutron reflectometry in the work of Cubitt [135], Daillant [136], and other reviews [137–139].

All reflectivity methods are based on the same optical principles. In the following paragraphs, a basic introduction to these principles [140, 141] is given using the example of a specular (mirror-like) reflection of a beam, the wave vector, k , and the normal to the propagation direction, the normal wave vector k_{\perp} , from a flat air-water interface.

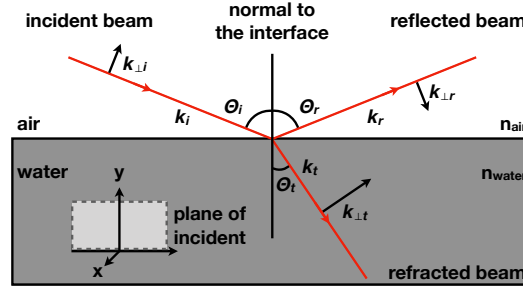


Figure 3.5: Schematic figure of an incident beam with the angle of incidence, Θ_i , being reflected (Θ_r) and refracted (Θ_t) at an air-water interface with the index of refraction $n_{air} < n_{water}$. The beam propagates in z -direction. The plane of incidence is the yz -plane, and the interface is the xz -plane. k is the wave vector of the beam and k_{\perp} its normal wave vector with the indices i , r and t for incident, reflected and transmitted, respectively.

As shown in Fig. 3.5, when a beam interacts with a boundary it is reflected (into the air) and refracted (transmitted into water). For the reflected part of the beam, the angle of reflection is defined by the law of reflection; the angle of reflection is equal to the angle of incidence, or $\Theta_i = \Theta_r$. For the refracted part the indices of refraction of the two media have to be considered. The angle of the transmitted beam is given by Snell's law [142]:

$$n_1 \sin \Theta_1 = n_2 \sin \Theta_2, \quad (3.6)$$

where n_i are the indices of refraction of the two media, and Θ_j are the angles relative to the normal of the interface. Snell's law is valid for any wave passing from one medium to another. The total reflection of a beam is achieved when the angle of incidence is larger than a critical angle, Θ_c . Under this condition, the entire incident beam is reflected. The critical angle can be calculated by Equation 3.6 using $\Theta_1 =$

Θ_c and $\Theta_2 = 90^\circ$:

$$\Theta_c = \arcsin \frac{n_2}{n_1}, \quad (3.7)$$

and total reflection is only defined when $n_2 \leq n_1$, that is, the incident beam goes from a medium with a larger refractive index to a medium with a smaller refractive index.

In reflectometry, the amounts of reflected and transmitted radiation compared to the incident beam are of interest, which are described by the Fresnel coefficients. [141] For the reflected and transmitted part, these coefficients are also called reflectance and transmittance, respectively. In case of the considered beam (Fig. 3.5), its normal wave vector (k_\perp) is parallel to the plane of incidence and the Fresnel coefficients are denoted with an index p for parallel [143]:

$$r_p \equiv \frac{k_{\perp,r}}{k_{\perp,i}} = \frac{n_t \cos \Theta_t - n_i \cos \Theta_i}{n_i \cos \Theta_t + n_t \cos \Theta_i}, \quad (3.8)$$

and for the transmitted beam:

$$t_p \equiv \frac{k_{\perp,t}}{k_{\perp,i}} = \frac{2n_i \cos \Theta_i}{n_i \cos \Theta_i + n_t \cos \Theta_t}. \quad (3.9)$$

These two coefficients are ratios of the amplitude of the normal wave vector. The Fresnel coefficients for an orthogonal wave, perpendicular to the plane of incidence can be found elsewhere. [140, 141] Conventional reflectometry measures the reflectivity of the system. The reflectivity is the ratio of the intensities, and one can relate the Fresnel coefficients to the measured quantity [141]:

$$R = \frac{I_r}{I_i} = \left| \frac{k_{\perp,r}}{k_{\perp,i}} \right|^2 = |r_p|^2, \quad (3.10)$$

with I_r the intensity of the reflected beam and I_i the intensity of the incident beam.

3.4.1. Neutron Reflectometry

Neutrons are subatomic particles without any electric charge, a negative magnetic moment, and a mass slightly more than one atomic mass unit. As they have no electric charge, neutrons do not interact with the electron cloud of an atom, but with the nuclei by strong interactions. Therefore, they have exceptional high penetration depth into materials. Neutrons show also characteristics of a wave, with a distinct wavelength, λ , given by the de Broglie relation. As the quantum mechanic description of a wave, the Schrödinger equation, in analogous to Maxwell's wave equations, neutrons follow the same optical principles, such as reflection, total reflection, and refraction, mentioned before. [144] The refractive index of neutrons, n_N , depends on the scattering length of the nuclei, b_i , instead of the atomic number, Z , as for X-rays. The scattering length varies by element and isotope in a non-monotonic way, for example, hydrogen ($H = -0.374 \cdot 10^{-12} \text{cm}$) and deuterium ($D = 0.6671 \cdot 10^{-12} \text{cm}$). [145] n_N for any material can be calculated by $n_N^2 = 1 - \frac{\lambda^2}{\pi} N_b$, where N_b is the scattering length density. The scattering length density is given by the sum of the number of nuclei per unit volume, n_i , and b_i of the i -th species, or simple $N_b = \sum_i b_i n_i$. The refractive index of neutrons is for most materials slightly less than one (air or vacuum $n_N = 1$). Consequently, total reflection is more frequently observed (Equation 3.7).

A specular (mirror-like) neutron reflectometry experiment is performed to measure the reflectivity (Equation 3.10) as a function of the transfer momentum perpendicular to the interface, q , given by $q = 4\pi \sin \Theta / \lambda$. Please note that in neutron reflectometry the grazing angle, Θ_G , is usually used, that is, 90° minus the angle of incidence. The range of q can be probed either by variation of the angle of incidence while λ is fixed (monochromatic mode), or by varying the wavelength while Θ_i is fixed (time-of-flight mode, TOF). A schematic reflectivity curve of a flat air-deuterated water interface is given in Figure 3.6.

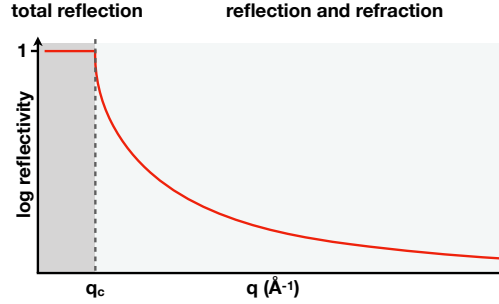


Figure 3.6: Schematic reflectivity curve in a semi-log representation of a flat air-heavy water interface. q_c represents the critical wave vector which is proportional to the critical angle, Θ_c . At $q \leq q_c$ total reflection and at $q > q_c$ reflection and refraction is observed.

In Fig. 3.6 the critical transfer momentum, q_c is marked, that separates total reflection ($q \leq q_c$) and partial reflection where a part of the beam is refracted ($q > q_c$). This ideal case can indeed be described by Equation 3.10, substituting the angles in the Fresnel coefficients (Equations 3.8 and 3.9) by the transfer momentum, q .

However, real systems, *e.g.*, thin layers on top of a water film, have modulations from the ideal reflectivity. These modulations can be caused by (i) constructive and destructive interference of reflected and refracted parts of the beam. This leads to the formation of interference fringes or oscillations in the reflectivity curve. (ii) Surface roughness which leads to diffuse or off-specular reflection.

Thus, analyzing the data of specular neutron reflectometry involves the construction of a model of the interface. The model is a scattering length density profile normal to the interface with n parallel layers of homogeneous material. [143] Each layer is characterized by a scattering length density, $N_{b,n}$, a roughness, σ_n , and a thickness, d_n . The reflectivity of the model is then calculated using the transfer-matrix method. [146] For each layer a characteristic matrix is created, containing the Fresnel coefficients modified by an error function [147] for the roughness between two layers, $\sigma_{n,n+1}$, and a phase factor for the thickness. The model is then fitted to the experimental data optimizing the three parameters and minimizing χ^2 in an iterative process.

To increase the accuracy and overcome the phase problem [148], additional physical and chemical information are needed. For thin film at the air-water interface, the most common choice is to use different solvents (Contrast variation). Therefore, measurements of the same film are conducted at the heavy (D_2O) and the air-contrast matched water (ACMW) interface. For ACMW heavy and regular water are mixed until their scattering length density matches the one of air. The specu-

lar reflectivity profile arises just from the thin film as the contrast between air and ACMW is zero. The specular neutron reflectometry data from at both contrast can then be fitted simultaneously

3.4.2. Ellipsometry

Light is a transverse electromagnetic wave with a wavelength, λ , in the range of 400-700 nm. An electromagnetic wave always consists of a coupled oscillating, orthogonal electric (E) and magnetic (B) field perpendicular to the propagation direction. In a medium, light waves are linked to the induced motion of electric charges of electrons and atomic nuclei, forming macroscopic electric currents. Therefore, the action light has on matter depends preferential on the direction of the E-field. In unpolarized light, the electric field fluctuates randomly in time. If the direction of the electric field of light is well defined, it is called polarized. In Fig. 3.7A, linear polarize light is shown, its electric field (red line) oscillates in the xy-plane, perpendicular to the propagation direction z. This oscillation can be viewed as the addition of two linearly polarized waves, one in the xz-plane (grey) and one in the yz-plane (light grey). The state of polarization is expressed by a phase difference, Δ_{ell} , between these two perpendicular waves. Light can be linearly (no phase difference), circularly ($\frac{\pi}{2}$ phase difference), or elliptically ($0 < \delta < \frac{\pi}{2}$) polarized. For ellipsometry, linearly and elliptically polarized light is important and depicted in Fig. 3.7A and B.

As introduced in Chapter 3.4, when light moves into a medium its propagation direction changes following the law of reflection and Snell's law (Equation 3.6). In this context, the aforementioned two linear polarized waves (in xz- and yz-plane) can also be viewed as parallel and perpendicular to the plane of incidence which is normal to the interface. The parallel wave is called p-polarized and the perpendicular wave s-polarized (for "senkrecht"). These two components behave distinctly different when reflected or refracted at an oblique angle of incidence and the light is depolarized.

Ellipsometry is a specular optical reflectometry method that measures the state of polarization of the reflected wave compared to the state of polarization of the incident wave. This means that in contrast to other reflectometry methods, not the reflectivity is measured, but the complex reflectance ratio, p_{ell} , according to Equation 3.11.

$$p_{ell} = \frac{r_p}{r_s} = \tan(\Psi_{ell})e^{i\Delta_{ell}}, \quad (3.11)$$

where r_p and r_s are the Fresnel coefficients of the p- and s-polarized light, Ψ_{ell} is the angle of the amplitude ratio (Fig. 3.7B), Δ_{ell} is the phase difference (Fig. 3.7B), and i is the imaginary unit. Please note that Δ_{ell} and Ψ_{ell} can indeed be negative, that is when the rotation of the E-field in time is reversed (counter-clockwise), which is not considered in Fig. 3.7B. Equation 3.11 can be equally defined for the refracted beam using the Fresnel transmittance (Equation 3.9).

¹In A and B the orthogonal components are denoted x and y. Only when a reference, such as the plane of incidence is provided, the orthogonal components are called s-plane and p-plane.

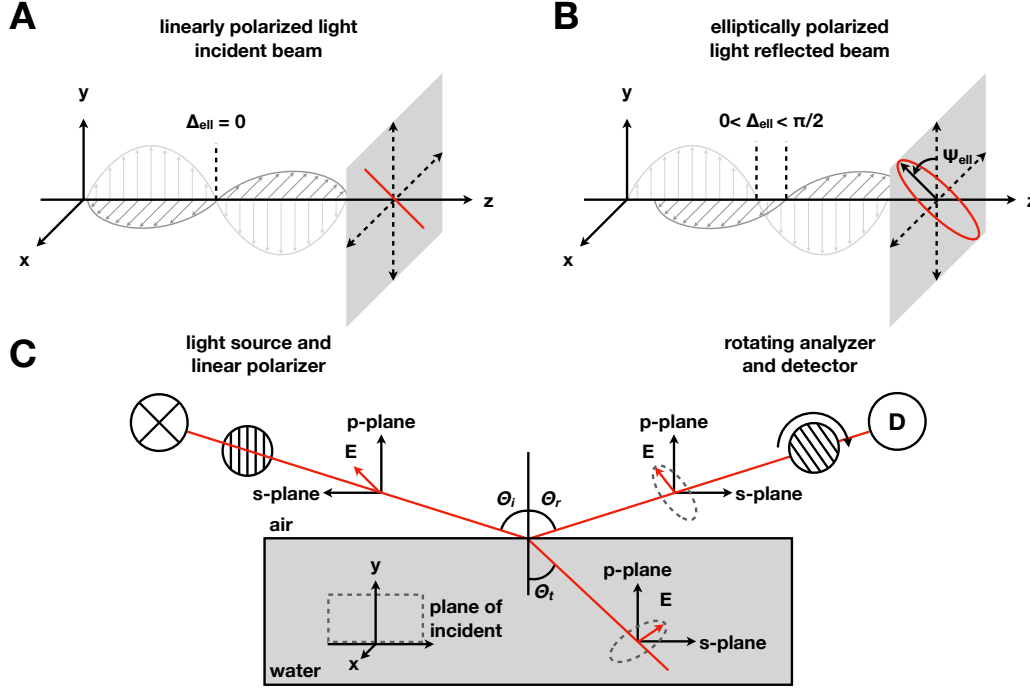


Figure 3.7: (A) Linearly polarized light of the incident beam. (B) Elliptically polarized light of the reflected beam.¹(C) Schematic structure of a rotating analyzer ellipsometer (see text for details).

The general setup of an ellipsometer is shown in Fig. 3.7C by the example of a rotating analyzer ellipsometer. The light from a source is linearly polarized and directed at the interface at an angle θ_i . When the light reflects off the interface, the amplitude and mutual phase of the p- and s-polarized waves change and the light becomes elliptically polarized. The light travels through the continuously rotating polarizer (rotating analyzer) and the amount of light that passes depends on the orientation of the analyzer, relative to the oscillatory direction of the E-field. In other words, the detector measures the form of the ellipse as a function of time. Common ellipsometer setups employ broadband light sources, which can also cover non-visible spectral regions. [134] Consequently, the ellipsometric parameters, Δ_{ell} and Ψ_{ell} are measured as a function of λ .

For simple systems, such as polished substrates or thin films with known refractive index, direct calculation of the optical and physical parameters (film thickness, refractive index or dielectric properties) is possible using Equation 3.11. [133, 149, 150] However, similarly to neutron reflectometry, real systems show surface roughness, interference of reflected and refracted beams, and multiple reflection and refraction, making direct interpretation of the measurements results nearly impossible. Therefore, the data analysis to obtain the optical and physical parameters is conducted indirectly, using a model-based approach. [133, 134] An example, how these models are constructed can be found in Chapter 4.

4. Effect of the 3D Swelling of Microgels on Their 2D Phase Behavior at the Liquid-Liquid Interface¹

4.1. Introduction

Responsive nano- and microgels, *i.e.*, polymer networks of colloidal sizes that are swollen by a good solvent, are highly interfacial active and adsorb spontaneously to interfaces. Similar to rigid particles, they can form monolayers at oil (or air)-water interfaces and stabilize emulsions. [54, 60, 83, 151, 152] However, in contrast to rigid colloidal particles, microgels strongly deform during adsorption until the elasticity of the polymer network balances the energy gain due to adsorption. [72, 153, 154] Thus, the effective lateral diameter of microgels at interfaces is significantly larger than in solution leading to an anisotropic shape which makes them distinctly different as compared to rigid nanoparticles [78, 84, 86, 155].

pNIPAM microgels typically reveal an inhomogeneous distribution of cross-links with a higher cross-linking density in the center as compared to the periphery. Consequently, the polymer density profile of the microgels decays from the center outside of the network. As a result of this internal structure, microgels adopt a structure which is described as fried-egg, core-corona, or core-shell morphology. [72, 76, 84, 153, 156–158]

This peculiar structure of microgels at interfaces leads to a rich 2D-phase behavior. Gradient Langmuir-Blodgett type experiments demonstrated that monodisperse microgels form hexagonal lattices with increasing concentration at the interface. [76, 84, 86, 89] In particular, Rey *et al.* concluded that the in-plane core-corona heterogeneity of the individual microgel leads to the increase of the compression isotherm in two steps. The compression isotherm of the monolayer is related to an isostructural phase transition between two hexagonal-packed monolayers with different lattice constants. [76]

In contrast to the responsiveness of microgels to external stimuli in bulk, their response at the interface is poorly understood. Stimuli that affect the dimensions of the microgels in bulk aqueous solution have been shown to affect the adsorption kinetic [69, 94, 159] but not the deformation of the adsorbed microgels. [84, 89] Even less is known about how the stimuli-responsiveness of the microgels affects their packing in the monolayer and the corresponding 2D-phase behavior. On one hand, Maldonado-Valderrama *et al.* observed that the average nearest neighbor distances, NND, or in-plane dimensions, decreased with increasing temperature for poly(N-vinylcaprolactam) microgels. [85] Similarly, interfacial rheology measurements suggested a strong collapse in the lateral diameter for pNIPAM-based microgels. [93, 94] On the other hand, Harrer *et al.* demonstrated that the reduction of interfacial coverage is only marginal at low and intermediate surface pressures. They found that the microgels display the core-corona morphology both below and above the volume phase transition temperature (VPTT). [79]

In order to get deeper into these observations, one needs to consider that microgels at interfaces are three-dimensional objects. While parts of the microgel are

¹This chapter has been adapted and reprinted in part with permission from Bochenek, S., *et al.*, *Langmuir*, **2019**, 35, 16780-16792. Copyright 2019 American Chemical Society.

confined at the interface, some of its volume is still situated in the aqueous phase, where it maintains its capability to respond to external stimuli. Ellipsometry [93] and computer simulations [72, 79, 88] showed that the out-of-plane extension of the microgels into the water phase is reduced with increasing temperature. However, it is not understood how the properties of the microgel monolayer depend on the interaction between (i) the parts of the microgels that are confined at the interface and thus in direct contact with the oil, and (ii) the parts that are located in the aqueous phase.

In this chapter, the interfacial behavior of pNIPAM microgels at temperatures below and above their VPTT is explored. The focus is on their two-dimensional phase behavior. Compression experiments at decane-water interfaces are carried out above and below the bulk VPTT of the microgels. The microgel monolayers are deposited onto a solid substrate in gradient Langmuir-Blodgett type depositions to investigate their in-plane structure *ex-situ* utilizing atomic force microscopy (AFM) and quantitative image analysis. Finally, we employ variable-angle spectroscopic ellipsometry at the air-water interface to investigate the out-of-plane extension of the microgels as a function of temperature. These results of microgel monolayers below and above the VPTT shows how the two dimensional phase behavior of microgels is affected by the three-dimensional swelling within the aqueous phase.

4.2. Experimental

4.2.1. Materials

N-isopropylacrylamide (NIPAM) (Acros Organics, Belgium), *N,N'*-methylenebisacrylamide (BIS) (Alfa Aesar, USA), *N*-(3-aminopropyl) methacrylamide hydrochloride (APMH) (Polysciences Inc., USA), 2,2'-azobis(2-methylpropionamidine) dihydrochloride (V50) (Sigma-Aldrich, USA), and cetyltrimethylammonium bromide (CTAB) (Fluka Biochemica, Switzerland) were used as received. For all interface experiments, ultrapure water (Astacus², membraPure GmbH, Germany) with a resistivity of 18,2 MOhm·cm was used as a sub-phase. Decane (Merck KGaA, Germany) was used as an oil-phase. Decane was filtered three times over basic aluminium oxide (90 standardized, Merck KGaA, Germany). The last filtration step was done just before the experiment. To facilitate spreading, propan-2-ol (Merck KGaA, Germany) was used.

4.2.2. Synthesis

pNIPAM-based microgels were synthesized by precipitation polymerization. The monomers, NIPAM (5.4546 g), BIS (0.3398 g), and APMH (0.1474 g), were dissolved in 370 mL double-distilled water. A small amount of the comonomer APMH (≈ 2 mol%) was incorporated to allow for post modification of the microgels, such as covalent labeling with fluorescent dyes. [160, 161] The primary amine is positively charged at neutral pH. Therefore, a cationic initiator (V50) and a cationic surfactant (CTAB) were used to prevent aggregation. There are no indications that the small amount of APMH influences the interfacial behavior of the microgels. The monomer solution was heated to 65 °C and purged with nitrogen under constant stirring (270 rpm). Simultaneously, 0.2253 g of the initiator (V50) and 0.0334 g of CTAB were each dissolved in 20 mL water in two separate vessels and degassed for

1 h. The surfactant was injected into the reaction vessel and stirred for 30 more minutes to equilibrate. The polymerization was initiated by adding the initiator solution. The reaction was carried out for 4 h at 65 °C under constant nitrogen flow and stirring. The obtained microgels were purified by threefold ultra-centrifugation at 30 000 rpm (70 000 RCF) and subsequent redispersion in fresh, double-distilled water. Lyophilization was applied for storage.

4.2.3. Compression Isotherms and Depositions

Compression isotherms and depositions (gradient Langmuir-Blodgett type) were conducted at the decane-water interface in a customized liquid-liquid Langmuir-Blodgett trough (KSV NIMA, Biolin Scientific Oy, Finland) made of poly(oxy-methylene) glycol and an area of $\approx 402 \text{ cm}^2$. Decane was chosen as oil-phase as pNIPAM microgels are not soluble in alkane oils. [82, 83] It has been shown that microgels display qualitatively the same compression isotherms and microstructures at alkane-water, *e.g.*, hexane and decane, and air-water interfaces. [76, 78, 84–86, 89]

For each measurement, the trough was carefully cleaned and a fresh decane-water interface was created. For temperature control, the trough was connected to an external water bath. Before each experiment, the trough was tempered to the respective temperature. The microgel solution with a concentration of 10 mg mL^{-1} was mixed with 20 vol-% of propan-2-ol to facilitate spreading. However, the propan-2-ol concentration is negligible after applying the microgel suspension to the interface and the alcohol has no effect on the measurements. After temperature equilibration, the microgel solution was added to the interface. Compression isotherms and depositions were conducted at $(20.0 \pm 0.5) \text{ }^\circ\text{C}$ and $(40.0 \pm 0.5) \text{ }^\circ\text{C}$.

The compression of the microgel monolayer was synchronized with the deposition onto a solid substrate as described in Ref. [76]. Comparison with scanning electron cryomicroscopy strongly indicates that the interfacial dimensions, ordering, and microgel-to-microgel distances are not influenced by the deposition. [61, 77, 78, 84, 108, 156] Briefly, for the experiments, two parallel-moving barriers were closed at a velocity of $v = 6.48 \text{ cm}^2 \text{ min}^{-1}$ to increase the interfacial concentration of the microgels by decreasing the available area. The minimum area was fixed to $\approx 44 \text{ cm}^2$. Simultaneously, a cleaned rectangular piece of ultra-flat silicon wafer ($\approx 1.1 \times 6.0 \text{ cm}$, P{100}, NanoAndMore GmbH, Germany) was lifted up ($v = 0.15 \pm 0.004 \text{ mm min}^{-1}$) between the barriers. The substrate was mounted to the dipping arm with an angle of $\approx 25^\circ$ with respect to the interface. This leads to a deposition length of $\approx 20 \text{ mm}$. The dipping arm was constructed to be always above the decane-water interfaces to reduce disturbance of the interface.

The surface pressure, Π , was probed with a highly porous platinum Wilhelmy plate (perimeter = 39.24 mm, KSV NIMA, Biolin Scientific Oy, Finland) to ensure optimal wetting with the aqueous sub-phase and thus a contact angle of 0° . The probe was attached to an electronic film balance (KSV NIMA, Biolin Scientific Oy, Finland) and placed parallel to the barriers.

After full compression, the barrier- and dipper movement was stopped. Subsequently, the barriers were opened to $\approx 402 \text{ cm}^2$ and the substrate was moved rapidly through the interface and fully out of the oil-phase. Thus, a defined reference point on the substrate, the point of highest compression, was obtained. The immobilized microgel monolayers were dried and investigated *ex situ* by AFM.

We connect the mechanical properties of the microgel monolayers to the results of the deposition experiments by geometrical calculations. First the length of the deposition is calculated: $c = a/\sin(\Theta_{sub})$, where a is the distance the dipper arm moved during the experiment, and Θ_{sub} the angle of the substrate relative to the decane-water interface. Both deposition and compression were started and conducted for the same time. Thus, the positions of the AFM images relative to the reference point, i_p , can be converted into a barrier position, bp , using: $bp = bp_{end} - (\Delta bp/c) \cdot i_p$, where bp_{end} is the barrier position of the reference point, and Δbp is the distance the barriers moved during the experiment. The barrier position is directly connected to Π and the surface pressure of each image is obtained.

4.2.4. Atomic Force Microscopy

AFM measurements of the microgels in the dry state, at the solid-air interface, were performed using a Dimension Icon with closed-loop (Veeco Instruments Inc., USA, Software: Nanoscope 9.4, Bruker Co., USA). The images were recorded in tapping mode using TESPA tips with a resonance frequency of 320 kHz, a nominal spring constant of 42 N m⁻¹ of the cantilever and a nominal tip radius of ≈ 8 nm (Bruker Co., USA) and OTESPA tips with a resonance frequency of 300 kHz, a nominal spring constant of 26 N m⁻¹ of the cantilever and a nominal tip radius of < 7 nm (NanoAndMore GmbH, Germany). The programmed move function was used to capture images of $7.5 \times 7.5 \mu\text{m}$ (512×512 pixels) in a straight line along the gradient direction on the substrate every 250 or 500 μm . For each line, an image at the position of highest compression was taken to obtain the position of the fixed point.

4.2.5. Image Analysis

The open-source analysis software *Gwyddion* 2.50 was used to process the AFM images. All images were leveled to remove the tilt and the minimum value was fixed to zero height.

The processed AFM micrographs were analyzed with a modified version of the custom-written Matlab script in Ref. [76]. The centers of the microgels were determined with the public available Matlab version of the IDL particle tracking code by Crocker and Grier [128]. A Delaunay triangulation and Voronoi tessellation were used to compute their nearest neighbor connections.

To obtain information on the long-range order we computed the radial distribution function, $g(r)$, defined as

$$g(r) = \frac{1}{N_p} \left\langle \sum_{i \neq k}^{N_p} \delta(r_i - r_k) \right\rangle, \quad (4.1)$$

where r_i and r_k are the positions of the i th and k th microgel, respectively, and $\langle \dots \rangle$ is the radial average over all possible orientations.

The mean nearest neighbor distances, NND , corresponds to the distance of the maximum of the first peak of $g(r)$.

$$NND = (r | \max [g(r)]), \quad (4.2)$$

Here, we determined the *NND* with fitting a Gaussian to the distance probability functions after a Delaunay triangulation. As these functions can be mono- or bimodal, either a single Gaussian (monomodal) or the convolution of two Gaussians (bimodal) were fitted. The *NND* are the expectation values of the probability density function of the Gaussian following the equation:

$$f(x | \mu, \sigma^2) = \frac{1}{\sqrt{2\pi\sigma^2}} e^{-\frac{(x-\mu)^2}{2\sigma^2}}, \quad (4.3)$$

The variance is considered as the error of *NND*.

The hexagonal order parameter, Ψ_6 , was calculated to obtain information about the short-range order. The following formula was used:

$$\Psi_6 = \left\langle \frac{1}{N_b} \left| \sum_{j=1}^{N_b} \exp(i6\theta_j) \right| \right\rangle, \quad (4.4)$$

where N_b is the number of nearest neighbors, θ_j is the angle between a chosen reference axis and the vector from the center microgel to its j th nearest neighbor. Ψ_6 is the ensemble averaged or mean value of all microgels of one image. The error of Ψ_6 is given by its standard deviation s :

$$s = \sqrt{\frac{1}{N-1} \sum_{i=1}^N (x_i - \bar{x})^2}, \quad (4.5)$$

The number of microgels per area, N_{area} , can be calculated by the number of localized microgel centers, N_p , divided by the area of an image, A_{image} : $N_{area} = N_p/A_{image}$. Both N_p and A_{image} are corrected to exclude microgels at the edges. N_{area} represents the interfacial number concentration of the microgels.

Furthermore, we compute the generalized area fraction, defined as

$$\zeta_{2D} = \frac{N_p \cdot A_{p,sep}}{A_{image}}, \quad (4.6)$$

where $A_{p,sep}$ is the mean area of well separated, isolated, and uncompressed microgels measured from AFM phase images (Fig. 4.3, blue and red circles). From the measured areas we also calculate the diameter of the individual microgels, $D_{2D} = \sqrt{(4 \cdot A_{p,sep})/\pi}$, and the diameter of the cores, $D_{core} = \sqrt{(4 \cdot A_{core})/\pi}$.

4.2.6. Ellipsometry

Spectroscopic ellipsometry of microgel monolayers at the air-water interface was conducted with an RC2 ellipsometer (J. A. Woollam Co., USA) operating in a wavelength range between 192 and 1690 nm. The microgel solution was spread in a plastic Petri dish to obtain a fixed interfacial concentration of $area/mass = 1500 \text{ cm}^2$. The Petri dish was placed on top of a 3 mm thick Peltier element used to increase or reduce the temperature. A thermocouple was immersed in water a few cm away from the measurement spot for temperature readout. Ellipsometry measurements were taken using focusing optics (300 μm short axis) which produced an elliptical measurement spot of about 300 μm by 900 μm . Temperature-dependent measurements of the microgel layer were performed at 3 angles of incidence (65, 70,

and 75°) with a light collection time of 1 min at each angle. Optical modeling was done by dividing the microgel layer into two distinct layers. The top layer (dense polymer layer) was modeled by a simplified Cauchy type optical dispersion that parametrized the refractive index as $n_{ell}(\lambda) = A + B/\lambda^2$. The top layer optical dispersion included an Urbach-tail extinction coefficient, k , to account for a slight light absorption towards the UV spectral region. The second layer (intermix layer) was positioned below the top layer and its optical constants were approximated as an arithmetical average between the top layer and bulk water. Temperature-dependent optical constants of water were taken from an inbuilt library of the modeling software CompleteEASE 6.43. An extensive, wide-ranged global fit was applied to simultaneously fit all parameters: thicknesses of the top and intermix layers, and the optical dispersion of the top layer. Fit parameters intercorrelations were always carefully evaluated to assure the numerical uniqueness of the obtained parameters.

4.2.7. Dynamic Light Scattering

Dynamic light scattering (DLS) was measured using a laser with a vacuum wavelength of $\lambda_0 = 633$ nm. Diluted suspensions of the microgels in water have a refractive index of $n(\lambda_0) = 1.33$. The temperature was changed from $T = (15.0 \pm 0.1)^\circ\text{C}$ to $T = (49.0 \pm 0.1)^\circ\text{C}$ in 2°C steps using a thermal bath filled with toluene to match the refractive index of the glass cuvettes. The scattering vector $q = 4\pi n/\lambda_0 \sin(\theta/2)$ was changed by varying the scattering angle, θ , between 30° and 130° , in steps of 20° . The hydrodynamic radius of the microgels, R_h , is computed from the diffusion coefficient *via* the Einstein-Stokes equation. The VPTT is obtained from the inflection point of a logistic “S” shape function fitted to the data.

4.2.8. Small-Angle Neutron Scattering

Small-angle neutron scattering (SANS) experiments were performed at the KWS-2 instrument operated by JCNS at the Heinz Maier-Leibnitz Zentrum (MLZ), Garching, Germany. The q -range of interest was covered by using a wavelength for the neutron beam of $\lambda = 0.5$ and 1 nm and three sample-detector distances: 20 , 8 , and 2 m. The scattering vector is $q = 4\pi/\lambda \sin(\theta/2)$, with θ the scattering angle. The detector is a 2D- ^3He tubes array with a pixel size of 0.75 cm and a $\Delta\lambda/\lambda = 10\%$. The data were corrected accounting for sample transmission and dark count (B_4C used). The background, heavy water, was subtracted from all data. The data were acquired at $T = 20^\circ\text{C}$ and $T = 40^\circ\text{C}$ and fitted with a fuzzy sphere model.

4.2.9. Electrophoretic Mobility and Zeta-Potential

The electrophoretic mobility, μ_{el} , was measured in a NanoZS Zetasizer (Malvern Instruments Ltd., England) in the range of $T = 10$ to 50°C in 2°C steps. For the electrophoretic measurements, a laser with a vacuum wavelength of $\lambda_0 = 633$ nm was used. The electrokinetic transition temperature (ETT) [162] is obtained from the inflection point of a logistic “S” shape function fitted to the data.

4.3. Results and Discussion

4.3.1. Characterization of Microgels in Solution

A comprehensive characterization of the microgels in solution is needed to give the results general validity. Therefore, the structure and responsiveness of the microgels in aqueous solution was investigated by means of dynamic light scattering, electrophoretic mobility as well as by small-angle neutron scattering.

The microgels have a hydrodynamic radius of $R_h = (153 \pm 3)$ nm at $T = 20$ °C and of $R_h = (84 \pm 2)$ nm at $T = 40$ °C. The swelling ratio, defined as $R_{h, 20^\circ\text{C}}/R_{h, 40^\circ\text{C}}$, is close to 1.8, a value comparable to microgels with similar size and cross-linker content. [163] The full temperature dependence of R_h is presented in Figure 4.1A.

The microgels were synthesized with the addition of a small amount of APMH. The primary amine moieties of the APMH allow post-modification of the microgels, *e.g.*, covalent labeling with fluorescent dyes. [160, 161] To prevent aggregation of oppositely charged groups, a cationic initiator and surfactant. The electrophoretic mobility, μ_{el} , and zeta potential, ζ_{pot} , as a function of the temperature are given in Figure 4.1B. The latter is computed with the Smoluchowski approximation. Despite this is a standard routine, it should be highlighted that this approximation is not valid for microgels as they do not have a well-defined interface and are porous. Therefore, the values of ζ_{pot} are meant to show simply a qualitative trend of the data and are given for comparison with the literature. The microgel is slightly positively charged in pure water (Fi. 4.1B, black squares), due to the primary amine groups (APMH) and initiator fragments. The electrophoretic mobility increases with temperature, which is attributed to the decrease of the particle size and the reorganization of the charged groups to the surface of the microgels. [162]

The internal structure of the pNIPAM microgels in solution can be investigated by SANS, SAXS, or SLS measurements. [49] SANS data of the pNIPAM microgels were measured at $T = 20$ and 40 °C, the scattering curves ($P(q)$ versus q) are shown in Figure 4.1C. Both temperatures were fitted with the fuzzy sphere model (Fig. 4.1C, solid black lines). The results of the fits show the typical decay of the polymer volume fraction from the center to the periphery at 20 °C and a box-like profile in the collapsed state (Fig. 4.1D, solid blue line and solid red line, respectively). [49, 95, 164–166] During the fitting, the value of the volume fraction of the core is fixed to one. The data are then normalized to the area underlying the radial distribution of the collapsed state since: (i) above the VPTT the microgels have a more defined profile with higher contrast due to the collapsed polymer; (ii) the mass of the polymer is conserved. The blue line in Fig. 4.1D shows that in the swollen state the polymer occupies ≈ 18 % of the volume occupied in the collapsed state. As reported by Stieger *et al.* [49], as well as more recently by Cors *et al.* [166], SANS shows that the polymer volume fraction within a microgel well above the VPTT is $\approx 40 - 50\%$. This can be considered valid for our microgels too. This means that at $T = 20$ °C the volume fraction of polymer in the core is ≈ 10 %. Again, this value agrees with the values reported in the literature [49, 166]. The size polydispersity of the microgels is calculated from the SANS data. We obtain a polydispersity of (7 ± 1) % for both temperatures.

Thus, the microgels can be considered monodisperse, are swollen at $T = 20$ °C and fully deswollen (and still colloidally stable) at $T = 40$ °C.

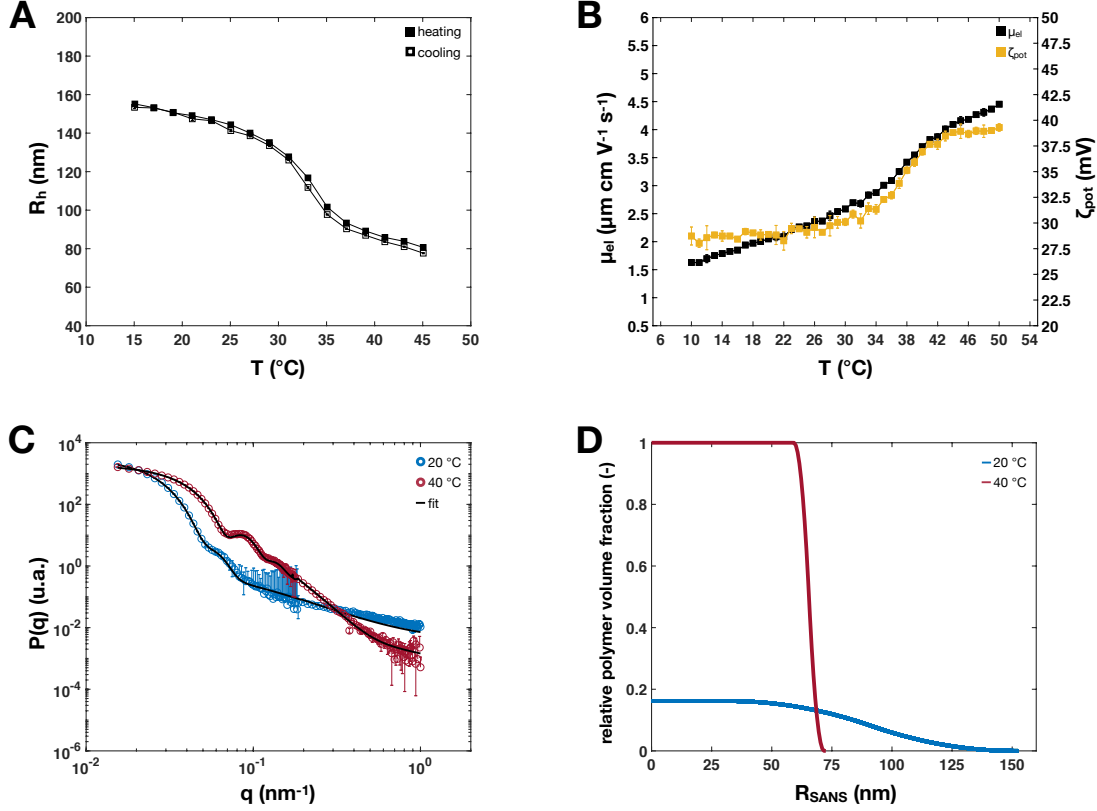


Figure 4.1: Characterization of pNIPAM microgels in solution. (A) Dynamic light scattering, hydrodynamic radius, R_h , versus temperature, T . Full and open black squares are the heating and cooling cycle, respectively (B) Electrophoretic mobility, μ_{el} , (black squares) and zeta potential, ζ_{pot} , (golden squares) as a function of temperature. (C) SANS form factor, $P(q)$, versus scattering vector, q , for pNIPAM microgels in dilute suspensions of D₂O at $T = 20$, blue circles, and 40 °C, red circles. The solid black lines are fits with the fuzzy sphere model [49]. (D) Relative polymer volume fraction versus radius obtained from the data fit for pNIPAM microgels at $T = 20$, blue solid line, and 40 °C, red solid line.

4.3.2. Two-dimensional Phase behavior of Microgels at Liquid Interfaces

In Fig. 4.2A, we present the compression isotherms for 20.0 and 40.0 °C, where the surface pressure is plotted as a function of N_{area} , *i.e.*, the interfacial number concentration.

The blue data points show the compression isotherm of the pNIPAM microgels at $T = 20$ °C. One can see that the surface pressure increases in two steps. Following the literature, [76, 78] five distinct regimes are identified: (I) diluted state, (II) corona-to-corona contact, (III) isostructural phase transition region, (IV) core-to-core contact, and (V) the failure of the monolayer. The different states are also visible in the AFM images in Fig. 4.4A-J. Similar compression isotherms have been observed for nearly all kinds of microgels below their respective VPTT, *e.g.*, microgels synthesized with different monomers [85], different cross-linking densities [86], different sizes [23, 78], oppositely charged comonomers [84, 89], different initiators [23, 76, 78, 84, 86], more complex architectures (hollow, core-shell) [87, 88],

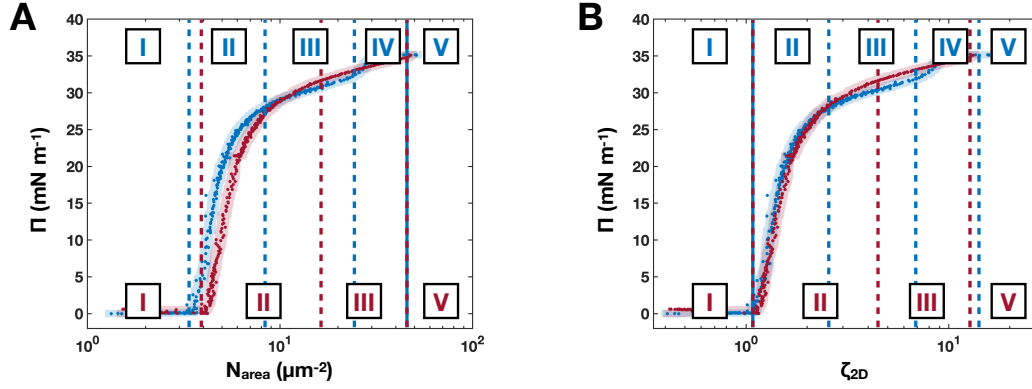


Figure 4.2: (A) Compression isotherms, Π versus number of microgels per unit area, N_{area} . (B) Compression isotherms, Π versus area fraction, ζ_{2D} , of the microgels. Blue for $T = 20\text{ }^{\circ}\text{C}$ and red for $T = 40\text{ }^{\circ}\text{C}$. The dashed lines represent values where transitions are observed in the AFM images. The different regimes are labeled by roman numerals in the corresponding colors. Errors from the repetition of the measurements are presented as error areas.

and hybrid inorganic/organic microgels [77, 88]. Therefore, our microgels display the general 2D phase behavior. The incorporated APMH does not change the microgels' interfacial behavior. However, there are a few examples where a different course is observed. These examples have in common that the microgels have very few cross-links, *i.e.*, they are extremely soft. [11, 23, 86]

Before we start to discuss the compression isotherms of the pNIPAM microgel monolayers at $T = 40\text{ }^{\circ}\text{C}$, we take a closer look at individual microgels in the diluted state. In the first regime (I) the surface pressure is independent of N_{area} . Microgel monolayers either have a gas-like phase or form 2D clusters due to attractive capillary forces that depend on the size of the microgels. [11, 23, 76, 86] We observe the first scenario at both $T = 20\text{ }^{\circ}\text{C}$ and $T = 40\text{ }^{\circ}\text{C}$, as Fig. 4.4A-B and Fig. 4.4M-N show. The average distance between the microgels is larger than their diameter at the interface and the microgels are mostly well separated.

We can probe the structure of individual microgels in the diluted state using the phase mode of the AFM. The phase mode allows imaging of the thin outer layer of adsorbed microgels. [167, 168] Fig. 4.4A and M clearly show that the microgels have a core-corona (fried-egg) structure at both temperatures. The persistence of the core-corona structure at both temperatures can be explained when considering the thermodynamics determining the swelling equilibrium of microgels. In solution, the size of a neutral microgel is determined by the balance between its elastic free energy and the mixing free energy between the solvent and polymer. [80] The latter being strongly dependent on temperature. Upon adsorption of the microgels to the interface another term has to be considered, the gain in surface free energy. This contribution is much larger than the mixing free energy [69, 72, 79, 153, 154] and, for the temperature range studied here, nearly constant with temperature. [169] Consequently, the part of the microgel's polymer network, which is in contact with the interface, is stretched until the gain in surface free energy is balanced by its elasticity. Whereas, the portions of the microgels that are still situated in the aqueous phase remain thermo-responsive.

The phase images were also used to determine the dimensions of the individual microgels. We analyzed more than 250 microgels for each temperature and calculated the overall in-plane diameter (core + corona), D_{2D} , and the diameter of the core, D_{core} . The difference between core and corona is clearly visible by the contrast of the AFM phase images. The results are plotted in a size histogram and fitted with a Gaussian distribution (Fig. 4.3).

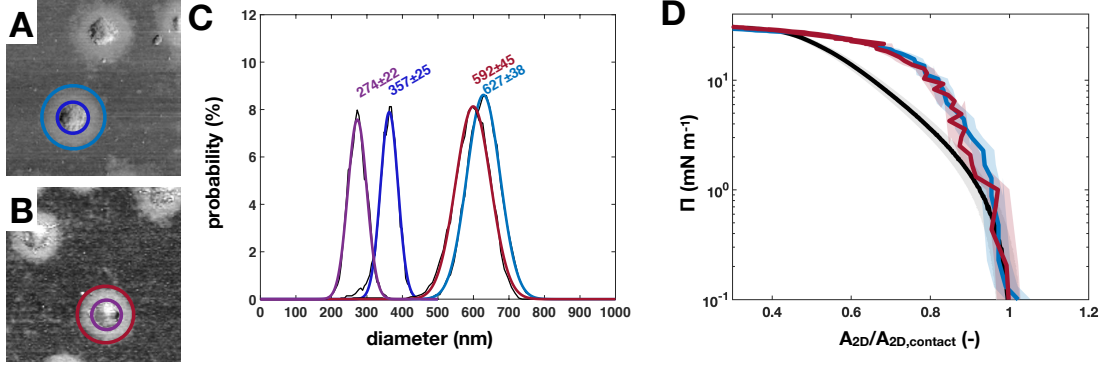


Figure 4.3: In-plane diameter of microgels at different temperatures ($T = 20$ and 40 °C). (A and B) AFM phase images of microgels in the dried state. The circles indicate the core and the whole microgel visible in the AFM images. (A) $T = 20$ °C, decane-water interface. Blue circle: core+corona, dark blue circle: core. (B) $T = 40$ °C, decane-water interface. Red circle: core+corona, purple circle: core. (C) Black lines are the diameter probability functions of pNIPAM microgels. For each temperature at least 250 microgels were analyzed. The functions were fitted with normal distributions and the colors correspond to the circles in A and B, the labels give the mode and the variance of the Gaussian. (D) Compression isotherms Π versus the area normalized by the area at the contact, $A_{2D}/A_{2D,contact}$. Blue and red lines represent the microgels at $T = 20$ and 40 °C, respectively. The black line represents linear pNIPAM at $T = 20$ °C.

We can compare the dimensions of the microgels at the interface (D_{2D} and D_{core} in Tab. 4.1) with their diameter in solution (D_h , Fig. 4.7C) below and above the VPTT. In bulk, the microgels deswell from roughly 300 to 170 nm in D_h between $T = 20$ and 40 °C ($\approx 45\%$). In contrast, the difference for D_{2D} in the same temperature range is less than 6%, which is in good agreement with the decrease in surface free energy ($\approx 5\%$). [169] The polymer network at the interface is mostly influenced by the decrease of the gain in surface free energy and nearly temperature independent. The microgels portions situated in the aqueous phase still undergo a volume phase transition. Their lateral diameter, D_{core} , is reduced by $\approx 30\%$ (Tab. 4.1) from $T = 20$ to 40 °C. The smaller lateral collapse of the microgel fractions in water compared to the deswelling in solution shows that the core deswelling in the aqueous phase is constrained by the stretching of the polymer at the interface that is not thermo-responsive. Nevertheless, these portions significantly collapse onto the center of the microgel, decreasing the size of the core. The combination of non-thermo-responsive polymer in direct contact with the interface with thermo-responsive microgel portions in the water phase leads to a larger width of the corona at the oil-water interface at 40 °C.

In Fig. 4.2A, we present the compression isotherms of pNIPAM microgels at

the liquid interface at $T = (40 \pm 0.5)^\circ\text{C}$, *i.e.*, well above their VPTT in solution. Remarkably, the red data points show a single increase of the compression isotherm with only four regimes.

The transition from the diluted state (regime red I) to a packed layer (regime red II) occurs when the extended microgel coronae start to interact. [78, 84, 86] A sharp increase in surface pressure is monitored as a result. AFM images, such as Fig. 4.4P, show that in regime II the microgels are in contact and form hexagonal lattices. For the microgel monolayers, the transition takes place at $N_{area} \approx 3.9 \mu\text{m}^{-2}$ for $T = 40^\circ\text{C}$ (red dashed line) and at $N_{area} \approx 3.5 \mu\text{m}^{-2}$ for $T = 20^\circ\text{C}$ (blue dashed line). The differences are larger than the experimental errors associated to the repetition of the measurements (Fig. 4.2A). The compression isotherms give the same result as the analysis of the microgels in the diluted state: the microgels show only minor differences in the overall in-plane size below and above their VPTT, which is in agreement with a recent report by Harrer *et al.* [79].

The dashed red line at $N_{area} \approx 17 \mu\text{m}^{-2}$ marks the transition from regime II to III at 40°C where the surface pressure becomes nearly independent of the interfacial concentration. Regime III is typically characterized by the melting of the initial lattice and the formation of a second hexagonal phase with a significantly smaller lattice constant. The AFM images in Fig. 4.4R-U clearly show that an isostructural phase transition takes place at 40°C . The coexistence of the two crystalline phases (regime III) extends until $N_{area} \approx 47 \mu\text{m}^{-2}$.

At $N_{area} \geq 47 \mu\text{m}^{-2}$, we observe a prominent difference with respect to the monolayers at $T = 20^\circ\text{C}$. As soon as all microgels are in the second hexagonal phase (Fig. 4.4V) the monolayer at $T = 40^\circ\text{C}$ cannot be compressed further, contrary to the microgels at 20°C , Fig. 4.4I-J. In other words, microgel monolayers at $T = 40^\circ\text{C}$ do not display the regime IV, *i.e.*, a second increase of the surface pressure. The monolayer fails (regime V) directly after the isostructural phase transition is complete. Reducing the area by further closing the barriers does not lead to an increase of surface pressure Π . All AFM images of the deposited monolayers in regime V show the same number of microgels and one can see multiple data points at nearly the same N_{area} in Fig. 4.2A. In literature, the failure of a monolayer is generally explained by buckling, the formation of multilayers, or desorption. [76, 108].

As reported for microgel monolayers below the VPTT [76], the lateral compression of the monolayer is also reversible at 40°C . The AFM images of the reference point and beyond (Fig. 4.4K-L and Fig. 4.4W-X) show that the monolayers relax. The microgels return to larger center-to-center distances after opening the barriers. We do not observe clustering or microgels in significantly short center-to-center distances.

We compute the generalized area fraction, ζ_{2D} , for our microgels at 20 and 40°C (for details see Experimental section) to provide a convenient way to compare the microgels at different temperatures. Furthermore, using ζ_{2D} , we can see how the temperature affects the transitions. For rigid spherical colloids the maximum density of a hexagonal close packing, *i.e.*, circle close packing, is $\pi\sqrt{3}/6$; however, for soft microgels the density, ζ_{2D} , can reach greater values, reflecting deformation, compression or interpenetration.

Figure 4.2B shows the surface pressure as a function of ζ_{2D} for 20 and 40°C . For both temperatures the transition from regime I to II takes place at $\zeta_{2D} \approx 1.06$. To calculate the area fraction we used the area of the microgels obtained in the

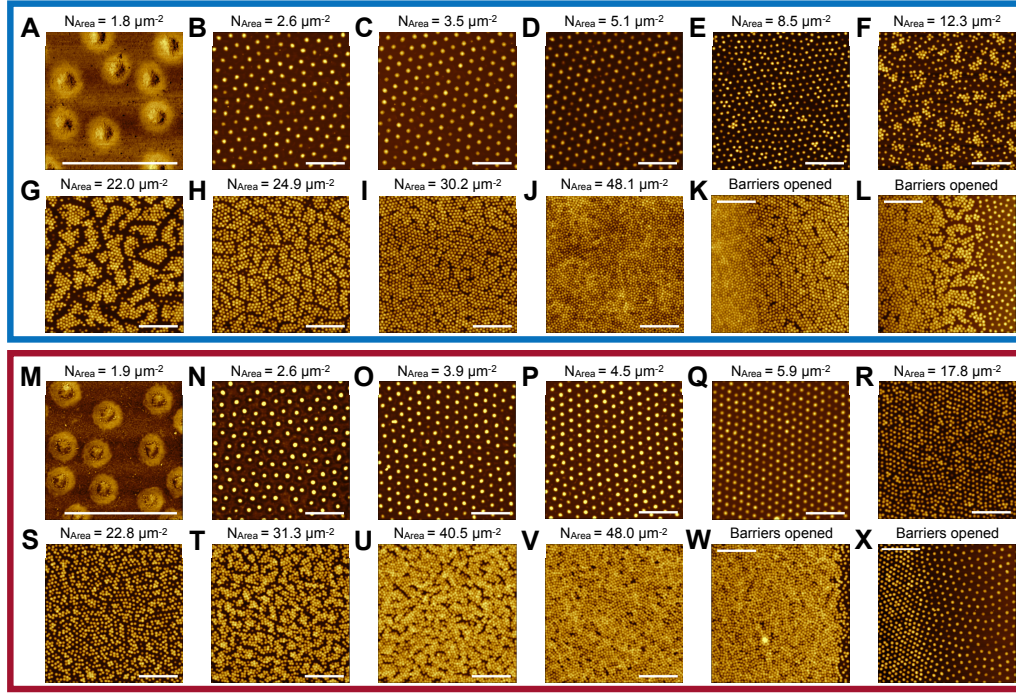


Figure 4.4: Atomic force micrographs of the microgel monolayers at $T = 20$ °C (A-L, blue box) and 40 °C (M-X, red box). Micrographs in A and M are phase images. Micrographs in K-L and W-X are captured after the barriers were opened and were rotated by 180°. The scale bars are $2 \mu\text{m}$.

diluted state. The value of $\zeta_{2D} > \pi\sqrt{3}/6$ demonstrates that the microgels are compressed, interpenetrate or deform compared to their stretched core-corona morphology (Fig. 4.3A-C) before an increase of the surface pressure is observed. Both compression isotherms fully agree and fall onto the same master curve up to a surface pressure of $\approx 25 \text{ mN m}^{-1}$, *i.e.*, when the isostructural phase transition of the monolayer at $T = 20$ °C starts. Apparently, at low Π there is no difference of the compressibility of the microgels below and above their VPTT. This means that the corona-corona interaction is not influenced by the temperature.

Furthermore, the compression isotherms of the microgels at $T = 20$ and 40 °C can be compared with linear pNIPAM polymer at 20 °C. Figure 4.3D gives a closer look at the low surface pressure regime. For the pNIPAM microgels, the surface pressure is plotted as a function of their interfacial area normalized to the interfacial area at the contact, *i.e.*, the area when the surface pressure first increases. For the linear pNIPAM polymer the trough area, A_{2D} , was normalized by the trough area at the contact, $A_{2D, \text{contact}}$. At very low compression ($\Pi < 1 \text{ mN m}^{-1}$) the microgel monolayers display the same compressibility as linear pNIPAM polymer (Fig. 4.3D); implying that the first interaction between the microgels is mediated by the interaction of dangling chains, which is independent of temperature. The deviation of the curves at $\Pi > 1 \text{ mN m}^{-1}$ is a strong indication that the coronae of the microgels not only consist of loosely dangling chains but also of loosely cross-linked polymer.

The compression isotherms of the microgels in Fig. 4.2 deviate from each other at surface pressures above $\Pi \approx 25 \text{ mN m}^{-1}$ and the microgels at $T = 40$ °C display higher surface pressures at the same ζ_{2D} values. In Fig. 4.2 the transition from

regime II to III for $T = 20^\circ\text{C}$ and $T = 40^\circ\text{C}$ is marked by blue and red dashed lines at $\zeta_{2D} \approx 2$ and 3.4 , respectively. The onset point of the isostructural phase transition is at higher ζ_{2D} for microgels above their VPTT. In other words, to undergo the transition from the first to the second hexagonal lattices the microgels at $T = 40^\circ\text{C}$ are significantly more compressed as compared to the microgels at 20°C . Corresponding AFM images are shown in Fig. 4.4E and Fig. 4.4R where microgels with significantly smaller distances first appear.

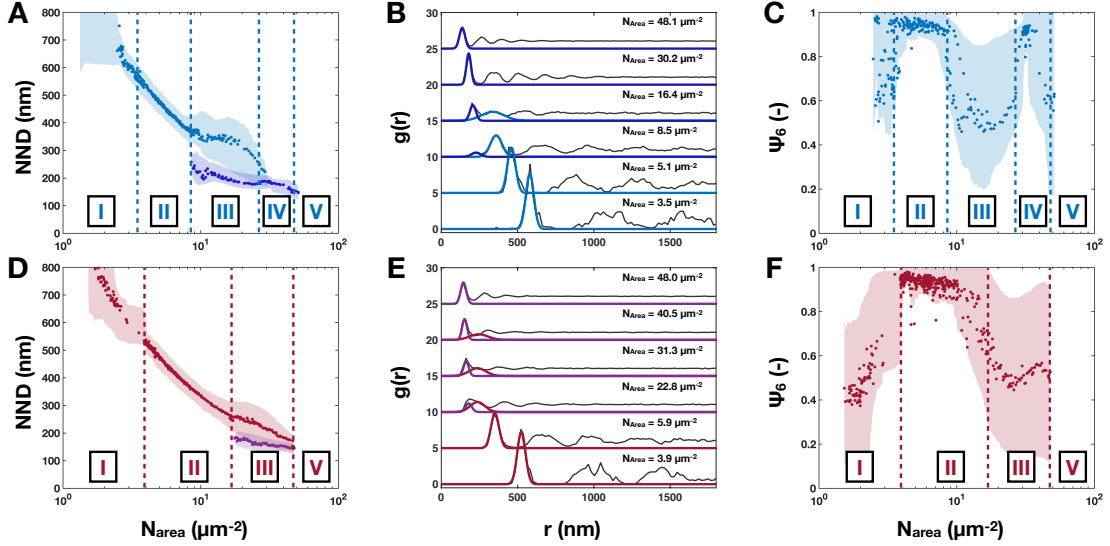


Figure 4.5: Results of the quantitative image analysis of all AFM images. (top) $T = 20^\circ\text{C}$, and (bottom) $T = 40^\circ\text{C}$. (A + D) nearest neighbor distances, NND , (B + E) pair correlation functions, $g(r)$, and (C + F) hexagonal order parameter, Ψ_6 . Errors discussed in the experimental part are plotted as shaded areas in the corresponding colors.

We describe the microstructure of the monolayer more quantitatively by the center-to-center distance (NND), the short-range (Ψ_6), and long-range ($g(r)$) order. The results are presented in Fig. 4.5 for 20°C (top row) and 40°C (bottom row).

The first column of Fig. 4.5 shows the mean nearest neighbor distances as a function of N_{area} at $T = 20$ and 40°C . Significant values of NND are presented in Tab. 4.1. For both temperatures, the graphs look very similar. In regime I and II the NND decreases with increasing compression. In regime III, the isostructural phase transition takes place and the NND splits, while microgels coexist in two phases. The position of the first peak decreases significantly until no microgels are in the first hexagonal lattice. The NND in the second phase is nearly constant with compression. In contrast to literature [76, 89] we name these two phases core-core (lattice with larger NND) and compressed core-core (lattice with smaller NND). After the peaks re-merge, we observe that at 20°C the microgels can be compressed further (regime IV) before the monolayer fails (regime V). In contrast, the monolayer at 40°C fails directly after regime III (Fig. 4.5D).

Two more differences can be seen for the NND when comparing Fig. 4.5A and 4.5D. Both the core-core and the compressed core-core distances in the third regime are smaller at 40 than at 20°C (Tab. 4.1, regime III). At $T = 40^\circ\text{C}$ the compressed core-core distance in regime III is equal to the NND of the microgels when

the monolayer fails. In contrast, the second phase at 20 °C displays larger NND , which is further reduced in regime IV upon compression. At both temperatures the monolayers fail at the same NND (Tab. 4.1, regime V).

Table 4.1: Physical dimensions of microgels monolayers at different compressions deposited from decane-water interfaces at $T = 20$ and 40 °C. Center-to-center distance for the first phase, NND_{1st} , the second phase, NND_{2nd} , the in-plane diameter, D_{2D} , and the core diameter, D_{core} , of the microgels at different compressions.

Temperature (°C)	Regime -	Π (mN m ⁻¹)	N_{area} (μm^{-2})	NND_{1st} (nm)	NND_{2nd} (nm)	D_{2D} (nm)	D_{core} (nm)
20	I	0	< 3.5	-	-	(627 ± 38)	(357 ± 25)
	II	0.2	3.5	(570 ± 20)	-	-	-
	III	27.5	8.3	(370 ± 40)	(210 ± 20)	-	-
	IV	31.1	26	-	(180 ± 10)	-	-
	V	34.7	48	-	(146 ± 12)	-	-
40	I	0	< 3.9	-	-	(592 ± 45)	(274 ± 22)
	II	0.2	3.9	(540 ± 25)	-	-	-
	III	32	17	(270 ± 35)	(170 ± 20)	-	-
	III	34.2	47	(170 ± 15)	(145 ± 15)	-	-
	V	34.8	48	-	(148 ± 15)	-	-

The second and third column of Fig. 4.5 provide information on the long-range and short-range order of the monolayers. Pair correlation functions $g(r)$ are shown for different representative N_{area} values.

The pair correlation functions of hexagonal lattices show characteristic peaks at NND , $\sqrt{3}NND^2$ and $2NND$. At low N_{area} , immediately after the contact, the curves for $T = 20$ and 40 °C have peak positions at 580 nm, 1040 nm, 1160 nm, and 530 nm, 950 nm, 1050 nm, respectively. These positions are in good agreement with the values expected from theory (Fig. 4.6A-F), showing that the monolayers have high hexagonal translational order at both temperatures. The long-range order of the monolayers is maintained for the entire regime II, as shown by the curves at $N_{area} = 5.1 \mu\text{m}^{-2}$ for $T = 20$ °C and $5.9 \mu\text{m}^{-2}$ for $T = 40$ °C. In the third curve for both temperatures, a peak at lower distances emerges and the intensity of the initial peak is reduced. The translational order fails, as expected during the isostructural phase transition in regime III. Differences are visible for the curves with a concentration $> 30 \mu\text{m}^{-2}$: below the VPTT, the pair correlation function at $N_{area} = 30.2 \mu\text{m}^{-2}$ shows again peaks at the theoretical positions of hexagonal lattices (Fig. 4.6C). The monolayer becomes disordered at the highest concentration. On the contrary, the pair correlation functions at $T = 40$ °C show no long-range order.

The short-range order is analyzed by the hexagonal order parameter, Ψ_6 , as a function of N_{area} in the last column of Fig. 4.5 below (C) and above (F) the VPTT. In regime I and II, the same behavior is observed. With increasing N_{area} , the short-range order increases until it reaches a plateau in regime II and shows a fully hexagonal phase ($\Psi_6 \approx 1$). In regime III, Ψ_6 has values around 0.5 with high errors due to the concurrent presence of the two distinct lattices, even though the individual phases show a hexatic ordering (Fig. 4.4G-I, Fig. 4.4S-U and the 2D-FFT of Fig. 4.6D). Upon further compression, the hexagonal order parameter shows the

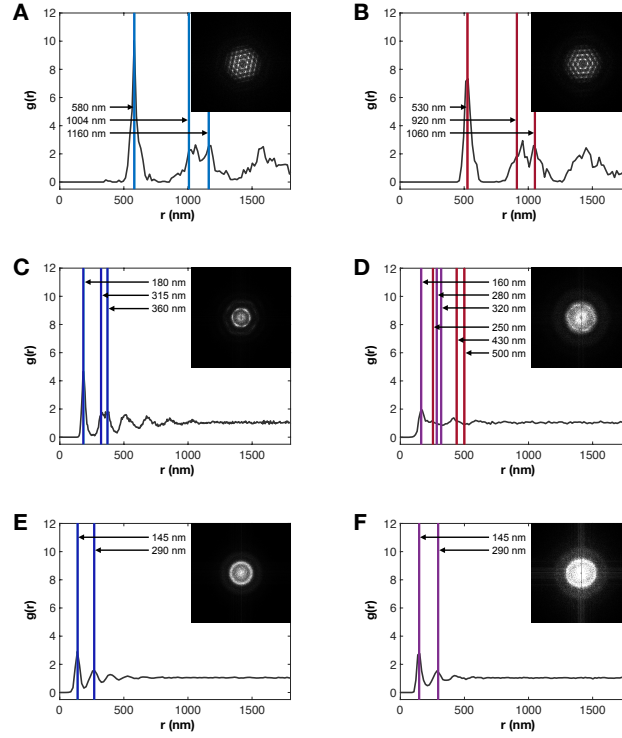


Figure 4.6: Pair correlation functions and 2D-*fast Fourier transform*, FFT, patterns of microgel monolayers at (left) $T = 20^\circ \text{C}$ and (right) $T = 40^\circ \text{C}$. (A) $N_{area} = 3.5 \mu\text{m}^{-2}$, (C) $N_{area} = 30.2 \mu\text{m}^{-2}$, (E) $N_{area} = 48.1 \mu\text{m}^{-2}$, (B) $N_{area} = 3.9 \mu\text{m}^{-2}$, (D) $N_{area} = 31.3 \mu\text{m}^{-2}$, (F) $N_{area} = 48 \mu\text{m}^{-2}$. Solid lines represent the theoretical values at NND , $\sqrt{3}NND$, and $2NND$. (blue) first phase for $T = 20^\circ \text{C}$, (dark blue) second phase for $T = 20^\circ \text{C}$, (red) first phase for $T = 40^\circ \text{C}$, (purple) second phase for $T = 40^\circ \text{C}$. In D the overlap of the two phases results in a nearly disordered pair correlation function, but the single phases are still crystalline as one can see Bragg reflections in the FFT.

same behavior as the long-range order: (i) the microgel monolayers at $T = 20^\circ \text{C}$ become ordered again in regime IV, and (ii) the final state at both temperatures is the same.

The detailed analysis of the 2D phase behavior of the microgel monolayers below and above their VPTT leads to the following observations: (i) at low surface pressure ($\leq 25 \text{ mN m}^{-1}$), the 2D phase behavior is independent of temperature; (ii) the NND of the isostructural phase transition is affected by temperature; (iii) at 40°C , regime IV is absent; (iv) at both temperatures, the monolayers fail at the same Π and center-to-center distances (NND).

These facts cannot be explained by the in-plane structure of the microgels alone, and it has to be considered that adsorbed microgels remain three-dimensional objects with a significant fraction of a microgel being in the aqueous phase. [82] To gain more insight into this aspect, we studied the microgel structure perpendicular to the interface by ellipsometry.

4.3.3. Three-dimensional Swelling of Microgels at the Interface

Ellipsometry measures the changes in the polarization of light reflected from a material. These changes are represented as the ellipsometric amplitude ratio, Ψ , and phase shift, Δ . A suitable model must be fitted to the data to convert these parameters into experimentally meaningful quantities describing our monolayers, such as the refractive index and thickness. We use a simple model consisting of only two layers, which we sketch in Fig. 4.7A and B.

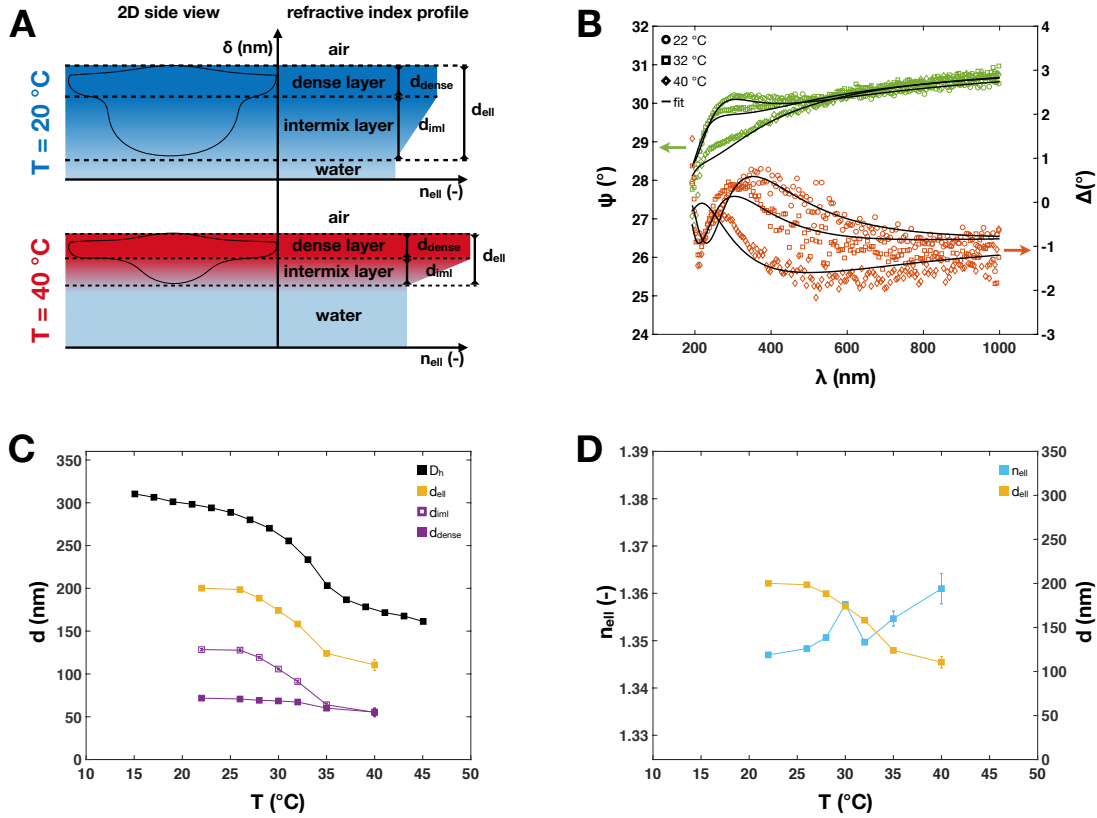


Figure 4.7: Spectroscopic ellipsometry of microgel monolayers at the air-water interface as a function of temperature. (A) Schematic sketch of the ellipsometry model for $T = 20$ and 40 °C. The solid lines represent a 2D side view of the microgels. The schematic refractive index profiles are shown on the right side. (B) Ellipsometric amplitude ratio, Ψ , (green symbols) and Ellipsometric phase shift, Δ , (orange symbols) versus the wavelength, λ . Different symbols, open circles, squares and diamonds, display different temperatures, 22 , 32 , and 40 °C. (C) Influence of temperature on the swelling of microgels in solution, hydrodynamic diameter, D_h , (full black squares) and on the total monolayer thickness, d_{ell} , (full golden squares), the thickness of the intermix layer, d_{iml} , (open purple squares) the dense layer, d_{dense} , (full purple squares) at the air-water interface. (D) Ellipsometric refractive index, n_{ell} , (full cyan squares) and total monolayer thickness, d_{ell} , (full golden squares) versus temperature.

The first layer has a homogeneous refractive index, n_{ell} , as a function of the distance from the interface (Fig. 4.7A dense layer). This dense layer describes the

polymer layer at and in close proximity of the interfaces. Previous studies have shown that microgels protrude into the hydrophobic phase while still being hydrated, creating a roughness or waviness of the monolayer. [72, 82, 84, 88, 170] This is indicated in Fig. 4.7A by the solid lines which illustrate the shape of single microgels. For simplicity, we neglect this roughness in our model.

The second layer, termed “intermix layer” describes a gradual decrease of the refractive index, starting with the n_{ell} of the dense layer to the refractive index of water ($n_{ell, 632.8nm} = 1.325$). This is indicated in Fig. 4.7A by the slope of n_{ell} and the color gradient. This diffuse layer accounts for two important characteristics of the portions of the microgels that are situated in the aqueous phase, *i.e.*, below the interface. Since the microgels display a fried-egg shape [29, 72, 79], contacts between the coronae lead to free spaces between neighboring microgels, which are not occupied by polymer, as represented by the solid contours in Fig. 4.7A. Additionally, in the direction perpendicular to the interface, analogously to the previously discussed structure of microgels in solution at temperatures below the VPTT [49], the microgels present a decreasing gradient of polymer density. [29, 72, 79] Both these characteristics lead to a gradual decline of the averaged polymer density in infinitesimal thin layers parallel to the interface.

To simplify the experimental setup, ellipsometry measurements were conducted at the air-water interface at constant compression ($\approx 15 \text{ mN m}^{-1}$ or $5.5 \mu\text{m}^{-2}$) with microgels in corona-corona contact between 22 and 40 °C. From the literature it is known that microgels show similar compression isotherms and microstructures at alkane-water and air-water interfaces, respectively. [76, 78, 84, 86, 89] At both interfaces, the microgels protrude into the hydrophobic phase while still being hydrated, whereby the extent of protrusion might be different. [82, 83, 93, 170] Therefore, the results at the air-water interface may be quantitatively slightly different compared to the decane-water interface, but they help to qualitatively understand the behavior of our microgel systems at different temperatures.

The model is applied to determine the thickness, d_{dense} , and refractive index of the dense layer, the thickness of the intermix, d_{iml} , and the total thickness of the microgel monolayer, $d_{ell} = d_{dense} + d_{iml}$, as a function of temperature (Fig. 4.7C). The ellipsometric spectra including the fits are shown in Figure 4.7B.

We compare the hydrodynamic diameter (black squares) and d_{ell} (golden squares) in Fig. 4.7C. The total thickness of the monolayer follows the same trend as D_h and is in agreement with recent literature [93]. A strong decrease in d_{ell} is observed at the VPTT ($T \approx 33^\circ \text{C}$) of the microgels in solution. Both D_h and d_{ell} are reduced by a factor of ≈ 1.8 from 22 to 40 °C. D_h decreases from roughly 300 to 170 nm and d_{ell} from ≈ 200 to 110 nm.

The ratio D_h/d_{ell} is ≈ 1.5 , showing that the microgels are deformed and flattened at the interface independently of the temperature. The effect of compression on the monolayer thickness becomes evident in comparison with literature data. At higher compression ($\Pi = (27 \pm 1) \text{ mN m}^{-1}$) the ratio D_h/d_{ell} decreases to 1.1. [93]

The dense polymer layer (Fig. 4.7C, full purple squares) shows a slight decrease in thickness from $d_{dense} = (72 \pm 1)$ to (56 ± 4) nm, while its refractive index, n_{ell} , increases from (1.347 ± 0.001) to (1.361 ± 0.003) as shown in Fig. 4.7D. The increase in n_{ell} occurs concurrently with the reduction of the total thickness (d_{ell}) and reflects an increase in the density of the monolayer above the VPTT.

The open purple squares in Fig. 4.7C show the temperature-dependent swelling

of the intermix layer. The thickness, d_{iml} , decreases more significantly from (128 ± 2) nm at 22°C to (55 ± 5) nm at 40°C . At temperatures below the VPTT, the fractions of the microgels that are located inside the aqueous phase are strongly swollen. The intermix layer extends into the water phase due to both the swelling of polymer segments perpendicular to the interface and the interstitial volume. Upon temperature increase the polymer-polymer interactions become more favorable and the portions of the microgels situated in water deswell. At the present compression, the intermix layer still remains as the interstitial volume leads to a gradual decrease of the averaged polymer density with increasing distance from the interface. Our model and experimental results are supported by computer simulations of microgels at the oil-water interface. [29, 72, 79] Exactly as observed in the ellipsometry experiments, the microgel fractions situated in the aqueous phase remain thermo-responsive and at both temperatures a dense polymer and intermix layer are observed.

The ellipsometry measurements prove that our microgels at liquid interfaces are still thermo-responsive in the direction perpendicular to the interface. At the compression, at which we performed the ellipsometry experiments ($\approx 15 \text{ mN m}^{-1}$), our microgels display a core-corona structure (Fig. 4.4D and 4.4P). The microgels are deformed and flattened at the interface compared to their bulk diameter independent of temperature.

4.3.4. Combining Two- and Three-dimensional Results

We now combine the information of the Langmuir-Blodgett trough (2D in-plane), ellipsometry (3D out-of-plane) and scattering (in solution) experiments to explain the differences between the monolayer properties below and above the VPTT. The sketch in Fig. 4.8 is used to illustrate our explanation.

Figure 4.8 shows schematic illustrations of the microgels in different shades of blue and red for 20 and 40°C , respectively. The three differently tinted circles of the same color represent different material properties or polymer densities. The colors are consistent through all regimes. In the 2D top view, the microgels' schemes overlay the AFM images. The dimensions are taken directly from the quantitative analysis (Tab. 4.1) and drawn to the scale bar of the images. In the 2D side view, the microgel structures are drawn according to computer simulations [29, 72, 79] and the thickness is derived from ellipsometry measurements (Fig. 4.7C).

Dilute State

First we briefly recapitulate the features of the microgels in the dilute state (regime I). In the 2D top view of Fig. 4.8 individual and well separated microgels can be seen in the phase images. At both temperatures the same core-corona structure commonly observed for microgels can be seen. The diameters D_{2D} and D_{core} are extracted from the images. In contrast to the strong collapse in solution, we observe that the overall in-plane diameter (D_{2D}) changes by 6% and D_{core} by 30% (Tab. 4.1, regime I at 20 and 40°C).

Even though these images are obtained *ex situ* after deposition and in a dried state, it is known from the literature that the core-corona structure persists at oil-water or air-water interfaces. [61, 72, 79, 84, 156] Thus, we sketch the microgels in

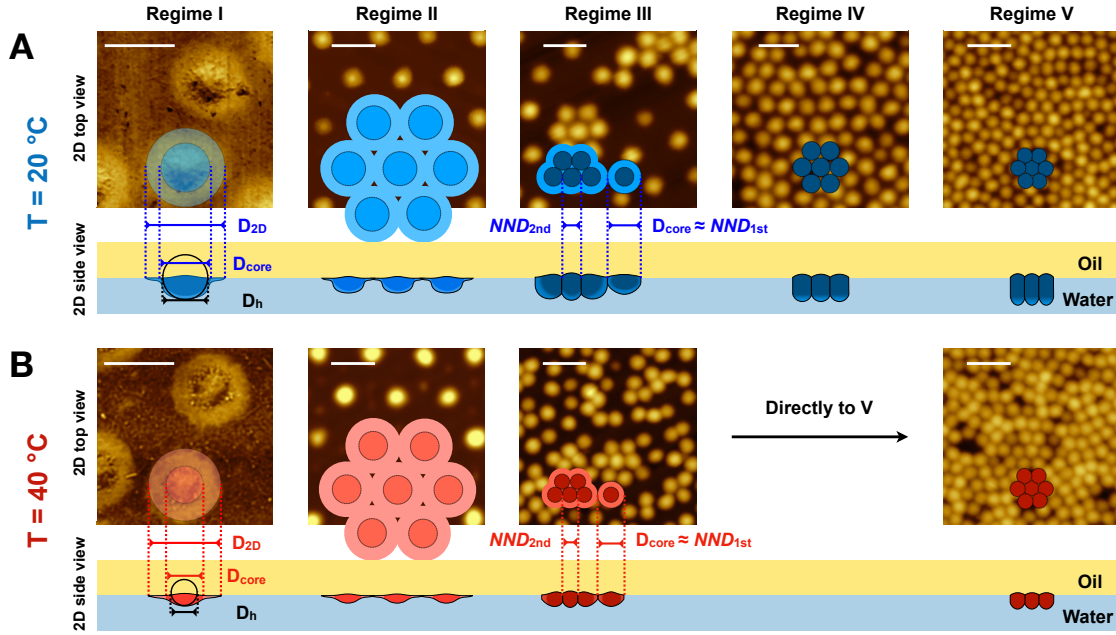


Figure 4.8: Sketch of the microgel monolayers under compression for $T = 20\text{ }^{\circ}\text{C}$ (A) and $T = 40\text{ }^{\circ}\text{C}$ (B). The microgels are schematically illustrated with different shades of blue and red for 20 and 40 $^{\circ}\text{C}$, respectively. (2D top view) Single microgels and microgel microstructure view from above. The differently tinted circles represent: light for the corona, medium for the core and darker color to state that the core is significantly compressed. (2D side view) Illustration of a 2D cross-section of the microgels perpendicular to the interface. D_h at 20 and 40 $^{\circ}\text{C}$ are given by black solid circles. Scale bars are 500 nm.

a 2D side view with the same diameter at the oil-water interface. From the ellipsometry measurements (and neutron reflectometry measurements, Chapter 6), we know that the microgel fractions inside the water phase are still thermo-responsive. These fractions display a similar thermo-responsiveness as the microgels in solution. Increasing the temperature from 22 to 40 $^{\circ}\text{C}$ leads to a reduction of the thickness d_{ell} by a factor of ≈ 1.8 (Fig. 4.7C).

Isostructural Phase Transition

In the second regime (II) the microgels form monolayers with hexagonal ordering and similar lattice constants. The course of the isotherms is the very same for $\Pi < 25\text{ mN m}^{-1}$ (Fig. 4.2B), demonstrating that the coronae of the microgels have the same stiffness independently of temperature.

Differences can be seen above 25 mN m^{-1} , where the monolayer starts to undergo an isostructural phase transition at $T = 20\text{ }^{\circ}\text{C}$. In regime III the NND splits into two distinct lattice constants (Tab. 4.5, regime III). We can compare the NND of the first phase at the transition from regime II to III to D_{core} in regime I (Tab. 4.1). At $T = 20\text{ }^{\circ}\text{C}$ the first hexagonal lattice melts at a NND equal to $(370 \pm 40)\text{ nm}$ where D_{core} is $(357 \pm 25)\text{ nm}$. Similarly, for 40 $^{\circ}\text{C}$, the melting is observed at a NND equal to $(270 \pm 35)\text{ nm}$ and D_{core} is $(274 \pm 22)\text{ nm}$. This means that the isostructural phase transition starts when microgels are compressed to $NND \approx D_{core}$ at $T = 20$ and 40 $^{\circ}\text{C}$ (Fig. 4.8, regime III). We further emphasize this in the 2D

side view of regime III, where the corona is fully compressed and the core regions of the microgels are in contact.

Having a core-core contact implies that at distances larger than D_{core} , the compression behavior is dominated by the compressibility of the corona. The isotherms diverge when the center-to-center distances become comparable to D_{core} - and the coronae are overcome. Upon further compression the contribution of the microgel volumes situated in the aqueous phase must be taken into account. Thus, the swelling state of the microgel volume in the aqueous phase (3D) directly influences the phase behavior of the microgels at the liquid-liquid interface (2D).

Furthermore, as also observed in the literature [171, 172], the AFM images (Fig. 4.8, regime III) clearly show an isostructural phase transition for both temperatures. Some of the microgels are at a NND equal to D_{core} (core-core contact) while other are at a center-to-center distance (Tab. 4.1, regime III) significantly smaller than D_{core} (compressed core-core contact). Below and above the VPTT the second phase displays grains with hexagonally-packed microgels (Fig. 4.4E-H and 4.4R-4.4U). The inter-particle distance in these grains is slightly smaller at $T = 40$ than at 20 °C (Tab. 4.1, regime III).

Considering the different core-core and compressed core-core distances, one can anticipate that the microgel monolayers also undergo an isostructural phase transition as a function of temperature (Fig. 4.2A). By changing the temperature at constant N_{area} in regime III, the microgel portions situated in the aqueous phase swell or deswell. Therefore, the density and the interaction between the microgels within the monolayer are altered. This drastically influences the ordering of the microgel lattices (Fig. 4.4, and Tab. 4.1) and the mechanical properties of the monolayer, *e.g.*, the surface pressure of the system (Fig. 4.2A).

Monolayer Failure

Lastly, we discuss the absence of regime IV of the microgel monolayers above the VPTT. To explain this, we have to consider two facts: (i) the microgel monolayers display smaller NND in core-core and compressed core-core contacts at 40 than at 20 °C (Tab. 4.1); (ii) the monolayer is thinner at 40 than at 20 °C (Fig. 4.7). This leads to an increased averaged polymer density at and in proximity of the interface. A higher averaged polymer density within the volume of the microgel makes it more difficult to further compress or interpenetrate the microgel, *i.e.*, increases its stiffness. [11, 173]

At 40 °C the averaged polymer density within the microgels in compressed core-core contact is making them virtually incompressible, during and directly after the isostructural phase transition. The coronae are nearly unaffected by the changes in temperature and the polymer mostly deswells onto the core region of the microgels as shown by computer simulations [29, 72, 79]. Therefore, once the microgels are in compressed core-core contact further compression in lateral direction of the monolayer is impossible. This leads to a direct transition from regime III to V, without passing through regime IV.

In contrast, at $T = 20$ °C the volume situated in the aqueous phase is still swollen and the NND is larger leading to a lower averaged polymer density within the microgels and at the interface. This is confirmed by the different values of Π for regime blue III and red III in Fig. 4.2. Indeed the value of Π is related to how many oil-water contacts are substituted by oil-polymer-water contacts. [174] This means

that after the isostructural phase transition is completed the microgels in core-core contact can be compressed further before reaching regime V and, therefore, regime IV is observed.

The microgel monolayers fail at the very same Π (Fig. 4.2) and NND (Fig. 4.5A and 4.5D). This implies that there is a maximum density of polymer that can be reached within a microgel before the monolayer fails. This limit can be reached either by triggering the monolayer density using temperature (Fig. 4.8B regime V) or compression (Fig. 4.8A regime V) but cannot be overcome.

4.4. Conclusion

In this chapter, the phase behavior of microgel monolayers adsorbed at fluid interfaces was investigated by compression isotherms, atomic force microscopy and ellipsometry below and above the volume phase transition temperature. It is known that in bulk, microgels present the same phases independently of the swelling state, but shifted to lower volume fraction with increasing temperature due to the harder inter-particle potential between collapsed microgels. [9, 175] Here, we show that in 2D the microgel monolayers show a more complex change in phase behavior as a function of temperature.

The microgels have the same typical core-corona structure below and above the VPTT. Furthermore, their total diameter at the interface (D_{2D}) is virtually the same at both temperatures. However, the diameter of the core (D_{core}) shrinks by $\approx 30\%$ above the VPTT. While the strong stretching of the entire microgel is caused by the adsorption to the oil-water interface, the shrinking of the core is a consequence of the deswelling of the fraction of the microgel that is located in the aqueous phase. Because the stretched, fuzzy, and easily compressible corona of the microgels at the interface is independent of temperature, the first stages of the compression of the microgel monolayers (regime I and II) are identical below and above the VPTT. The compression isotherms overlap for $\zeta_{2D} < 2$ (Fig. 4.2B) and the microstructure, as imaged by AFM, is the same (Fig. 4.4).

At higher compressions an isostructural phase transition is observed and the effect of temperature on the monolayers becomes clearly visible. Once microgel cores get into contact, $NND \approx D_{core}$, their 2D phase behavior differs. At $T = 20^\circ\text{C}$ the part of the microgels that is located in the aqueous side of the interface, remains swollen during and after the isostructural transition. Thus, the microgel monolayers can be compressed further (regime IV). In contrast, at 40°C the portion of the microgel in aqueous sub-phase is collapsed and the core region at the interface is thinner and denser. The averaged polymer density at the interface is increased and the microgels become incompressible once the isostructural transition is completed. An intermediate phase, where the microgels can be further laterally compressed, is absent (regime IV) and monolayer failure occurs immediately upon further compression (regime V).

Noteworthy, the microgel monolayers fail at the very same surface pressures and nearest neighbor distances independent of temperature. These two facts indicate that there is a limited, maximum amount of polymer segments that can be confined at and in close proximity of the interface. Trying to overcome this limit leads to a failure of the monolayer. This limit can be reached in two ways: either by compressing swollen microgels laterally ("2D") or by increasing temperature and

thus collapsing the microgel perpendicular to the interface (“3D”).

Our results demonstrate how softness and deformability of temperature-sensitive nano-, and microgels make them fundamentally different from rigid nanoparticles. While being isotropic and temperature-sensitive in aqueous bulk solution, they are highly stretched and anisotropic at interfaces independent of temperature. The temperature-sensitivity is lost at the interface, however the portions of the microgels that are located in the aqueous side of the interface are still temperature-sensitive. At low compression, the interaction between microgels is dominated by their strongly stretched corona and thus independent of temperature. At high compression, however, the microgels’ portions within the aqueous side of the interface become relevant. The temperature-dependent swelling perpendicular to the interface (“3D”) affects the compressibility parallel to the interface (“2D”). This perpendicular, out-of-plane structure of microgels at interfaces is the crucial factor that always has to be considered.

4.5. Data Availability

Research data for this chapter may be accessed at <https://hdl.handle.net/21.11102/17d74812-1b59-11ea-9a63-e41f1366df48>.

5. Comparison of Microgel Monolayers at Oil-Water and Air-Water Interfaces and their Temperature-Dependent 2D Phase Behavior ¹

5.1. Introduction

Although emulsions and foams are fundamentally different [27], it has been shown that microgels can be used as both smart emulsifiers [60–64] and foamers. [65–67] In recent years many studies have been conducted to elucidate the properties and destabilisation mechanism of microgels stabilized emulsion and foams. A clear understanding of these features allows tailoring of microgels for specific applications and fundamental studies.

A key point to clarify is the influence of the single microgels swelling properties on the two-dimensional macroscopic phase behavior of microgel monolayers. Langmuir and Langmuir-Blodgett trough experiments were conducted in which the environmental condition of the sub-phase, *i.e.*, the aqueous phase, and the conformation of the microgels were varied. Stimuli, such as pH, salt concentration and temperature, or different cross-linker contents, architectures and hybrid microgels have been investigated in the literature. [29, 30, 70, 76, 79, 86, 89]

Up to date, no studies have been conducted on the influences of the top-phase, *i.e.*, air or decane, with a direct comparison of the same microgel. Definitely, the choice of top-phase has a profound impact on the microscopic conformation of the microgels at interfaces [83] and factors, such as the solubility of the microgel in the two immiscible phases or surface tension, play an important role. Similar to bulk, the swelling equilibrium of a neutral microgel at the interface is determined by the free energy of mixing and elasticity but also the free energy of the surface, *i.e.*, surface tension. [69, 78]

In this chapter, we quantitatively compare compression isotherms and Langmuir-Blodgett type depositions of the same microgels at air-water and oil-water interface to study the effect of the top-phase on the microgel monolayers' two dimensional phase behavior. Characteristic quantities, such as the center-to-center distance, the ordering and height in dried state are determined to obtain a full description of the deposited monolayers. Furthermore, we explore the effect of the 3D swelling of the microgels due to temperature on their 2D phase behavior at the air-water interface and compare the outcome to the results presented in Chapter 4.

5.2. Experimental

5.2.1. Materials

For all interface experiments, ultrapure water (Astacus², membraPure GmbH, Germany) with a resistivity of 18,2 MOhm-cm was used as a sub-phase. Decane (Merck KGaA, Germany) was used as oil-phase. The decane was filtered three times over

¹This chapter has been adapted and reprinted in part with permission from Bochenek, S., *et al.*, *Soft Matter*, **2020**, DOI: <https://doi.org/10.1039/D0SM01774D>. Copyright 2020 The Royal Society of Chemistry.

basic aluminum oxide (90 standardized, Merck KGaA, Germany). The last filtration step was done just before the experiment. Pieces of an ultra-flat silicon wafer ($\approx 1.1 \times 6.0$ cm, P{100}, NanoAndMore GmbH, Germany) were used for depositions. The microgels were spread from aqueous solutions (concentration of 10 mg mL^{-1}) mixed with 20 vol% of propan-2-ol (Merck KGaA, Germany) at the decane-water interface. For measurements at the air-water interfaces, either aqueous solutions (concentration of 10 mg mL^{-1}) mixed with 50 vol% of propan-2-ol, or solution with a concentration of 1 mg mL^{-1} in chloroform (Merck KGaA, Germany) were used. Both approaches lead to the same results.

5.2.2. Compression Isotherms and Depositions

The procedure for compression isotherms and depositions at the decane-water interfaces is explained in detail in Chapter 4. The measurements at the air-water interfaces were conducted in the same way, but instead of 80/20 vol% mixtures of water-propan-2-ol, 50/50 vol% mixtures of water-propan-2-ol or microgels suspended in chloroform were used. This was done to maximize the adsorption of the microgels to air-water interfaces and minimize partial loss of microgels into the sub-phase. This loss is unavoidable if the surface-active component and the spreading agent are soluble in one of the two immiscible phases.

5.2.3. Image Analysis

The open-source analysis software *Gwyddion* 2.54 was used to process the AFM images. All images were leveled to remove the tilt and zero height was fixed as the minimum z-value of the image. AFM images of the deposited dried microgel monolayers were analyzed with a custom-written Matlab script based on the image analysis routine of Ref. [76]. The script was already used in Chapter 4 and details can be found there. The number of microgels per area, the mean nearest neighbor distances, and the hexagonal ordering parameter were calculated for all images.

The analysis of microgel monolayers was extended by height profiles of the microgels in the dried state. Profiles were extracted through the apex of the microgels and at different angles with respect to the fast scan direction. Multiple height profiles of one image were summarized and aligned to the apex (zero coordinate of the x-axis) to obtain averaged microgel profiles and not to bias the results. The averaged profiles are presented with the standard deviations as the error. The apex height of the averaged microgels was computed using the Matlab function *findpeaks* and the averaged diameter of the microgels was determined by the *knnsearch* [176] with a threshold of 1.5 nm.

5.3. Results and Discussion

Studies at air- (AW) and alkane-water (OW) interfaces have shown that microgel monolayers possess qualitatively the same compression isotherms and microstructures at these interfaces. [76, 84, 86, 89] In this chapter a more quantitative description of the effect of the top-phase (air or decane) on the compressibility, microstructure and in-plane dimensions of microgel monolayers is given. Therefore, combined compression and depositions experiments were conducted at the air-water interface (for details see Chapter 4) using the same very pNIPAM microgels. These results are compared to the outcome of measurements at the decane-water interface already discussed in Chapter 4. Furthermore, the experiments were conducted below and above the VPTT to elucidate and compare the influence of temperature at both air- and decane-water interfaces.

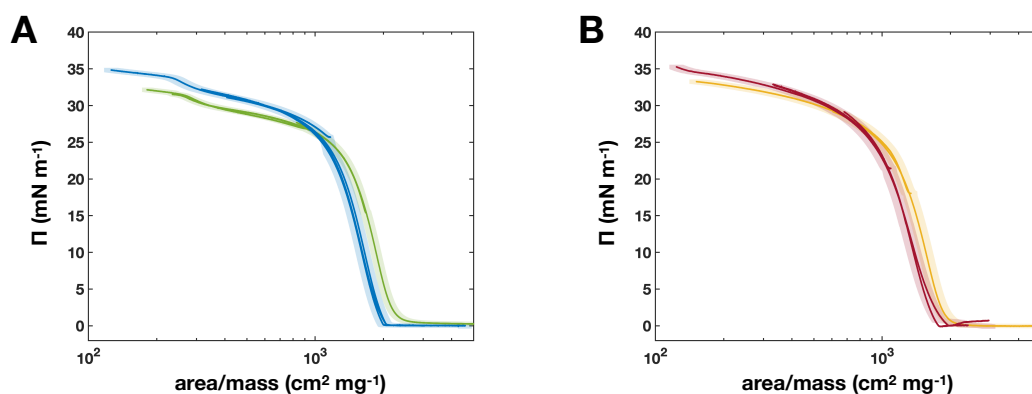


Figure 5.1: Compression isotherms, Π versus area per mass of microgel added to the interfaces, area/mass , of pNIPAM microgels at the air-water and decane-water interface. (A) Comparison of air-water (green) and decane-water (blue) interfaces at $T = 20$ °C. (B) Comparison of air-water (gold) and decane-water (red) interfaces at $T = 40$ °C. The errors are presented as shaded areas in the respective color.

The Π -area compression isotherms normalized to the initial amount of microgel added to the interface, area/mass , are presented in Figure 5.1A and B. Microgel monolayers at the air-water interface are plotted in green ($T = 20$ °C) and gold ($T = 40$ °C), the decane-water measurements are plotted in the same colors as in Chapter 4, blue for $T = 20$ °C and red for $T = 40$ °C. As expected, the general trend of the compression isotherms is the same at AW and OW interfaces. Likewise, the transition from two increases to a single increase is also observed for isotherms at $T = 40$ °C at the air-water interface. Nevertheless, there is a small qualitative difference between the isotherms at the AW and OW interface. In case of decane-water interfaces a sharp transition takes place at the contact point, where the isotherms increase for the first time. For isotherms at the air-water interface this passage is much smoother and further extended. This change is observed at both temperatures (Fig. 5.1A and B).

The isotherms show quantitative differences in the surface pressure for the microgel monolayers at the air- and decane-water interface at both temperatures. The surface free energy, *i.e.*, the surface tension, is a measure of excess energy that a material has at the surface or interface compared to the bulk. For Langmuir or

Langmuir-Blodgett experiments $\Pi = \gamma_0 - \gamma_c$ is measured, where γ_0 and γ_c are the surface tensions of the bare and of the microgel laden interface, respectively (Chapter 3.1). This means that microgel monolayers display higher excess of energy at the air-water interface compared to the decane-water interface. In other words, although microgels are insoluble in both air and decane, pNIPAM-decane contacts are energetically more favorable than pNIPAM-air contacts.

Another difference is the *area/mass* value at the contact point. The surface pressure of the pNIPAM monolayers at the air-water interface at $T = 20^\circ\text{C}$ starts to increase at $\approx 3000\text{ cm}^2\text{ mg}^{-1}$, in contrast to the OW interface where *area/mass* $\approx 2000\text{ cm}^2\text{ mg}^{-1}$. A similar increase in *area/mass* from the decane-water to the air-water interface is observed for the isotherms at $T = 40^\circ\text{C}$. Even though larger *area/mass* values appear logical, because air-water interfaces display larger surface free energy values and the spreading equilibrium of microgels depends on the surface free energy, this could also be result of the normalization. For the normalization it is assumed that all microgels contained in the spreading solution adsorb to the interface, but the real amount which adsorbs might be drastically different for the air- and decane-water interface.

The pNIPAM microgel monolayers at the air-water interface were deposited to a solid substrate and analyzed with the same method as described in Chapter 4 to bypass this assumption. The depositions were imaged with an atomic force microscope, the images analyzed with a custom-written Matlab script and the image positions correlated to the surface pressure. Isotherms with Π as a function of the number of microgels per area, N_{area} , are presented in Figure 5.2A and B.

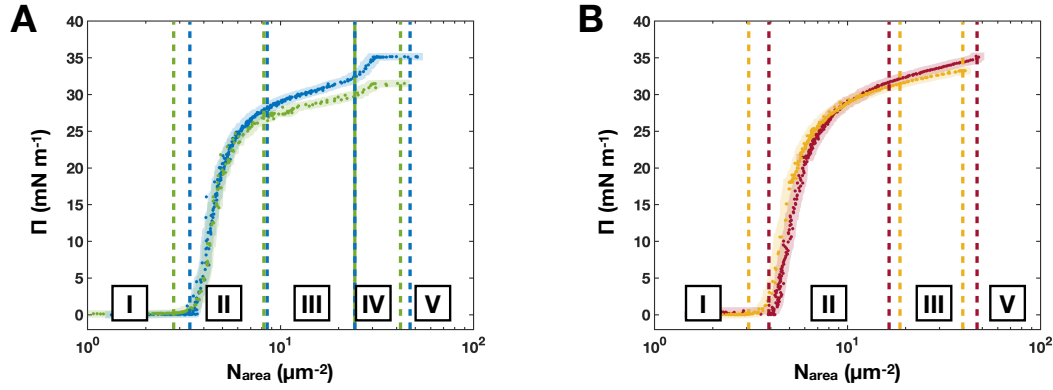


Figure 5.2: Compression isotherms, Π versus number of microgels per area, N_{area} , of pNIPAM microgels at the air-water and decane-water interface. (A) Comparison of air-water (green) and decane-water (blue) interfaces at $T = 20^\circ\text{C}$. (B) Comparison of air-water (gold) and decane-water (red) interfaces at $T = 40^\circ\text{C}$. The errors are presented as shaded areas. The different regimes visible in the isotherms are labeled in roman numbers. Dashed lines in the respective colors indicate the transitions.

At both temperatures, the monolayers at the AW interface display the same two-dimensional phase behavior as their temperature equivalents at the decane-water interface. The distinct regimes visible in the compression isotherms are indicated by dashed lines in the corresponding colors. Below the VPTT microgels display five regimes labeled in roman numbers from I to V, namely a diluted state (I), the corona-to-corona contact (II), the isostructural phase transition region (III), the core-to-core

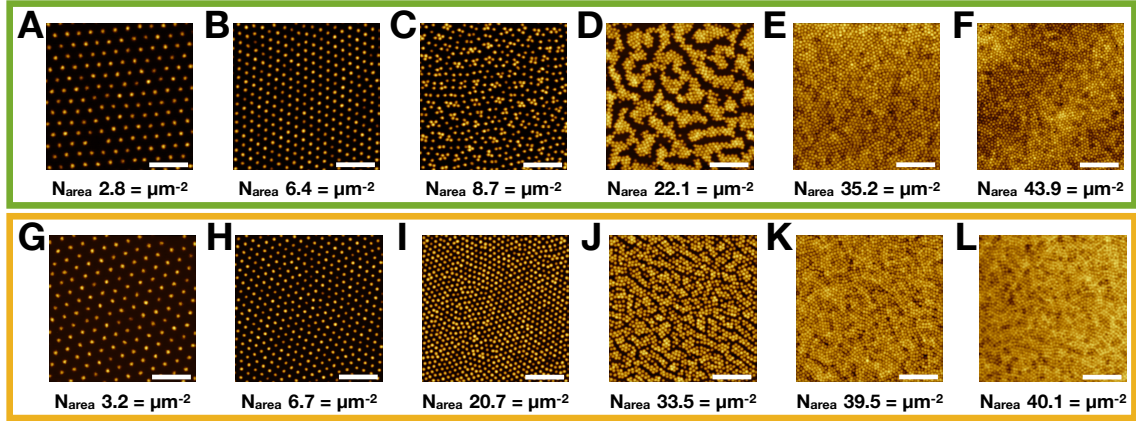


Figure 5.3: Atomic force micrographs of pNIPAM microgel monolayers at $T = 20\text{ °C}$ (A-F, green box) and 40 °C (G-J, golden box) deposited from the air-water interface at different compressions. The scale bars are $2\text{ }\mu\text{m}$.

contact (IV), and the failure of the monolayer (V). Again, the microgel monolayers at temperature above the VPTT (Fig. 5.2B, golden data points) display only a single increase and regime IV, where microgels in core-to-core contact are compressed, is missing. The different regimes are also visible in atomic force microscopy images below (Fig. 5.3A-F) and above (Fig. 5.3G-L) the VPTT.

The difference in size, *e.g.*, larger $area/mass$ values discussed before, is also observed in the Π - N_{area} -isotherms. Thus, the phase images of single and well-separated microgels were investigated to determine their in-plane dimensions. For each interface and temperature the contact areas of roughly 250 microgels were measured and the overall (core+corona) and core diameter calculated. A difference between the core and the corona is clearly visible in the contrast of the AFM phase images in Figure 5.4A-D. Circles representing the core and the overall microgel are added for clarity.

The resulting diameter probability distributions (Figure 5.4E and F, black lines) were fitted with normal distributions to obtain the mean overall, D_{2D} , and core diameter, D_{core} . The Gaussians are plotted with the respective colors of Figure 5.4A-D. At equivalent temperatures D_{2D} increases from the decane-water to the air-water interface by $\approx 60\text{ nm}$, whereas D_{core} is constant below the VPTT and increases marginally by 15 nm (274 ± 22 to $289 \pm 15\text{ nm}$) above the VPTT (Tab. 5.1).

The increase of D_{2D} is not surprising since upon adsorption the microgels are laterally stretched to increase their contact area with the interface and maximize the gain in surface free energy, *i.e.*, surface tension. [69, 70, 72, 78, 177] Air-water interfaces have a surface tension of 72.3 mN m^{-1} [178] at 20 °C compared to the decane-water interface with 52.3 mN m^{-1} [169] at 20 °C . Likewise, the decrease of surface tension with temperature is similar for both interfaces ($\approx 3\text{ mN m}^{-1}$). As for both experiments the very same pNIPAM microgels, Langmuir-Blodgett setup, sub-phase, and substrates were used, the different stretching of the microgels must only depend on the surface free energy of the interface. Consequently, the microgel fractions at the interface are more stretched and have a larger diameter at AW interfaces.

Interestingly, the fractions of the microgel situated in the aqueous sub-phase, that is D_{core} , do not display a considerable increase. In Chapter 4, we discussed

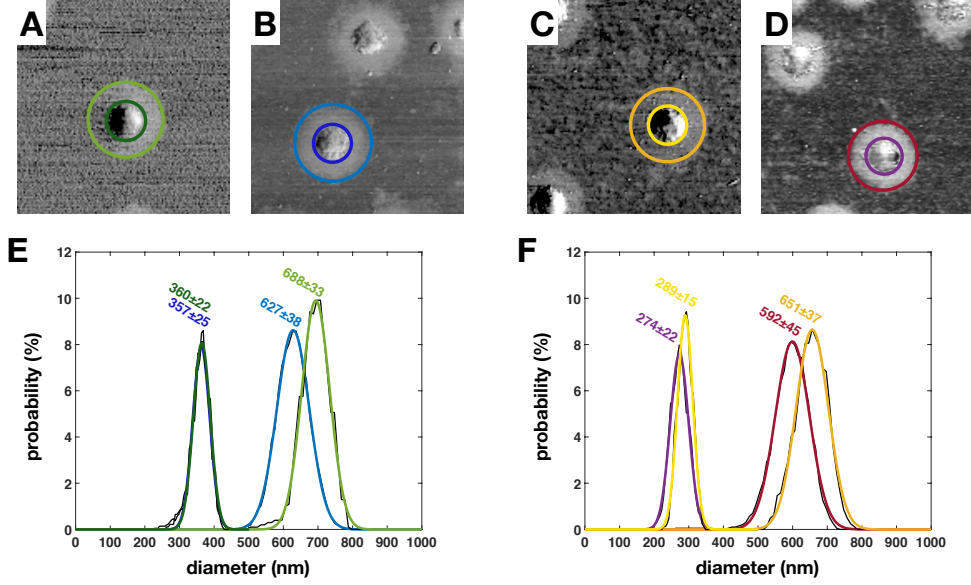


Figure 5.4: In-plane diameter of microgels at different temperatures ($T = 20$ and 40 °C) and interfaces (air-water and decane-water). (A-D) AFM phase images of microgels in dried state. The circles indicate the core and the whole microgel visible in the AFM images. (A) $T = 20$ °C, air-water interface. Green circle: core+corona, dark green circle: core. (B) $T = 20$ °C, decane-water interface. Blue circle: core+corona, dark blue circle: core. (C) $T = 40$ °C, air-water interface. Golden circle: core+corona, yellow circle: core. (D) $T = 40$ °C, decane-water interface. Red circle: core+corona, purple circle: core. (E and F) Black lines are the diameter probability functions of pNIPAM microgels. For each curve ≈ 250 microgels were analyzed. The functions were fitted with normal distributions and the colors correspond to the circles in A-D, the labels give the mode and the variance of the Gaussian.

that the reduced collapsed of D_{core} , from 360 to 270 nm, in comparison to D_h , from 300 to 170 nm, is due to the constrain of the stretched polymer layer, *i.e.*, the corona, at the interface. Following the above explanation one would expected that at the AW interface D_{core} would increase likewise.

Furthermore, the measured D_{2D} as a function of Π can be used to estimate the surface elasticity and its counterpart in bulk, the elastic modulus. As in this experiment the spreading of individual microgels after adsorption is compared, we start with the equation of the hydrostatic compression in two dimensions, defined as [179]:

$$K \equiv -\frac{\Delta p}{\Delta s/s}, \quad (5.1)$$

where K is the two-dimensional modulus of compression, p is the two-dimensional analog of pressure (in force per unit length), and s is the interfacial area. Hydrostatic compression defines that the film is compressed uniformly in all directions. [179] For our case, we can rewrite this equation into:

$$K \equiv \frac{\Delta \gamma}{\Delta D_{2D}/D_{2D}}, \quad (5.2)$$

where γ is the surface tension and ΔD_{2D} is the difference of the total diameter

between the air- and decane-water interface. We omit the negative sign as the force is in the opposite direction, *i.e.*, an expansion is performed. With Equation 5.2, a two-dimensional modulus of compression of $K = (210 \pm 12) \text{ mN m}^{-1}$ is calculated for the microgels at the air- and decane-water interface.

The compression modulus in two dimensions and the surface elasticity are connected by the following relation: $E^{(2D)} = 2K(1 - \nu^{(2D)})$ [180]. Here, $\nu^{(2D)}$ is the two-dimensional Poisson's ratio and $E^{(2D)}$ is the surface elasticity or two-dimensional elastic modulus. The two-dimensional Poisson's ratio can be obtained from the three-dimensional one using the relations $\nu^{(2D)} = \nu^{(3D)}$ for plane stress and $\nu^{(2D)} = \nu^{(3D)} / (1 - \nu^{(3D)})$ for plane strain. [180] As aforementioned, it is observed that (i) D_{2D} changes with γ , but D_{core} does not, and (ii) the compressibility at larger microgel-to-microgel distances is independent of the polymer network fractions in the aqueous phase. Thus, we assume that for the stretching of the individual microgels plane stress conditions are valid, where the polymer in-plane and in close proximity to the interface dominates the elasticity. This assumption is in agreement with recent literature [181], and therefore, $\nu^{(2D)} = \nu^{(3D)}$ is used. This relation leads to the equation:

$$\frac{E^{(2D)}}{2 - 2\nu^{2D}} = K \equiv \frac{\Delta\gamma}{\Delta D_{2D}/D_{2D}}. \quad (5.3)$$

In the literature, $\nu^{(3D)}$ values are reported in the range between ≈ 0.25 to 0.5 for pNIPAM gels. [25, 182–185] For a perfectly incompressible isotropic material ($\nu^{(3D)} = 0.5$), Equation 5.3 becomes the same as Hooke's law. However, we calculate the surface elasticity using $\nu^{(3D)} = 0.4$ [184] and obtain a value of $E \approx 250 \text{ mN m}^{-1}$.

For the comparison of the results with the literature, the surface elasticity in 2D is converted into the Young's Modulus, $E^{(3D)}$. As we assumed that the stress normal to the interfacial plane is zero (plane stress), the relation between $E^{(2D)}$ and $E^{(3D)}$ is given by [181]: $E^{(2D)} = E^{(3D)}/d$, where d is the thickness perpendicular to the interface. Although the maximal extension of the polymer network into the aqueous phase can be measured with ellipsometry (Chapter 4), we follow the suggestion of Camerin *et al.* [181] and consider d to be significantly smaller, in the order of a few nm. This is in agreement with the above-mentioned assumption that the polymer in-plane and close proximity to the interface dominates the elasticity. Consequently, we calculate the elastic modulus using $d = 5 \cdot 10^{-9} \text{ m}$ according to the film thickness of linear pNIPAM polymer measured with ellipsometry and neutron reflectometry at the air-water interface. [170, 186–188] A Young's modulus of $E^{(3D)} \approx 50 \text{ MPa}$ is obtained, which is significantly larger than the E-moduli measured by AFM in the literature (3 kPa to 13 MPa) [25, 189, 190]. Nevertheless, and despite the vast amount of simplifications in our calculation, qualitatively the same trend was observed by computer simulation [181], which is associated with the stiffening of the polymer network in the interfacial plane compared to the polymer network normal to the liquid interface.

Next, the evolution of the in-plane diameter of the pNIPAM microgel monolayers at the air-water interface is followed by plotting the mean nearest neighbor distance, NND , as a function of N_{area} (Figure 5.5A and B). In regime I the microgels are separated and a decrease of available area brings the microgel centers closer to each other. Starting from regime II a confluent monolayer is observed. The lateral compression with the barriers leads to a compression of the microgel coronae until in regime III the isostructural phase transition takes place (Figure 5.5A and B).

Here, microgels in two phases coexist and the number of microgels in the second phase constantly increases. At the beginning of regime III, the microgel monolayers below and above the VPTT have different NND ; at $T = 20^\circ\text{C}$ the transition starts at 380 nm, and at $T = 40^\circ\text{C}$ at 260 nm (Tab. 5.1). Below the VPTT, all microgels have passed to the second phase (regime IV). This layer can be compressed further and the NND is reduced from 190 to 160 nm. The monolayers above the VPTT do not display the regime IV and a direct transition from the third to the fifth regime is observed where the monolayers fail. At both temperatures the failure of the monolayer takes place at the same NND of approximately 160 nm.

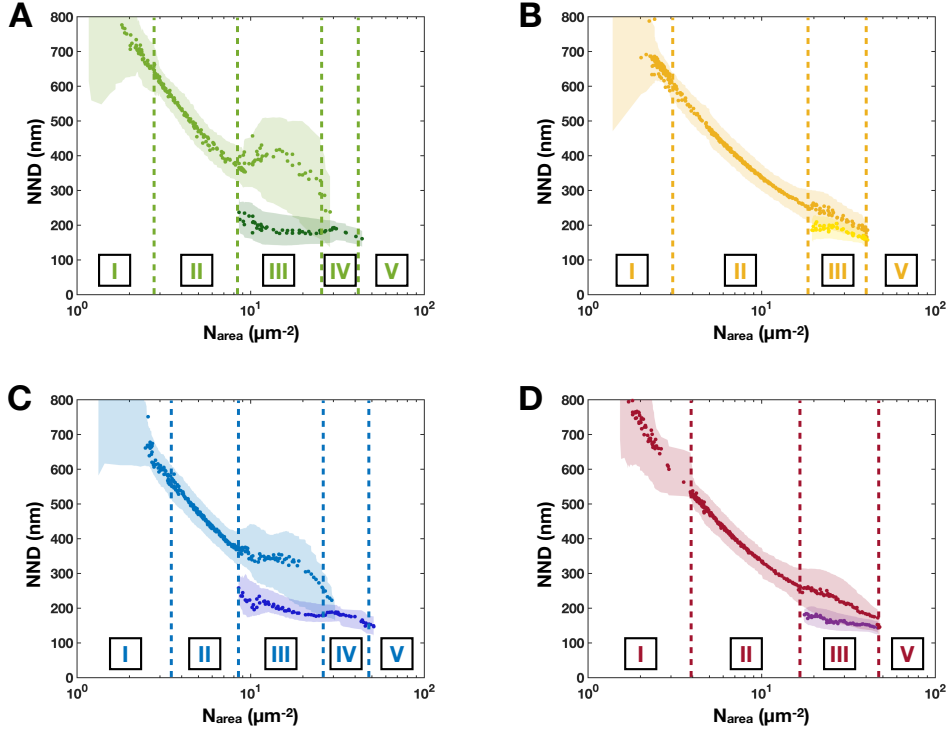


Figure 5.5: Mean nearest neighbor distances, NND , versus number of microgels per area, N_{area} , of pNIPAM microgels at the air-water and decane-water interface. (A) $T = 20^\circ\text{C}$, air-water interface. First phase: green, second phase: dark green. (B) $T = 40^\circ\text{C}$, air-water interface. First phase: gold, second phase: yellow. (C) $T = 20^\circ\text{C}$, decane-water interface. First phase: blue, second phase: dark blue. (D) $T = 40^\circ\text{C}$, decane-water interface. First phase: red, second phase: purple. The errors are presented as shaded areas in the respective color. Dashed lines indicate the transitions between different regimes. The regimes are labeled in roman numbers.

The NND versus N_{area} graphs for the decane-water interfaces are presented in Figure 5.5C and D. The values at characteristic points for all interfaces are summarized in Tab. 5.1. Comparing the values of both interfaces, it stands out that the isostructural phase transition takes place at nearly the same NND , for monolayers below the VPTT at 370-380 nm and above the VPTT at 260-270 nm, although D_{2D} is significantly larger at the AW interface. Furthermore, a different NND for air- and decane-water interfaces is observed in regime V, when the monolayer is fully compressed and fails. Independently of temperature, the failure at the air-water interface is observed at 160 nm, in contrast to the decane-water interface (145 nm).

This indicates, that although the in-plane extension of the core seems not to be affected, the amount of confined polymer increases with increasing surface free energy of the interface.

Table 5.1: Physical dimensions of microgels monolayers at different compressions deposited from air- and decane-water interfaces at $T = 20$ and 40 °C. Center-to-center distance for the first phase, NND_{1st} , the second phase, NND_{2nd} , the in-plane diameter, D_{2D} , and the core diameter, D_{core} , of the microgels at different compressions.

Temperature (°C)	Regime -	Π (mN m ⁻¹)	N_{Area} (μm^{-2})	NND_{1st} (nm)	NND_{2nd} (nm)	D_{2D} (nm)	D_{core} (nm)
air-water interface							
20	I	0	< 2.8	-	-	(688 ± 33)	(360 ± 22)
	II	0.2	2.8	(630 ± 25)	-	-	-
	III	26.5	8.1	(380 ± 40)	(220 ± 20)	-	-
	IV	30	25.2	-	(190 ± 15)	-	-
	V	31.5	43.9	-	(160 ± 12)	-	-
40	I	0	< 3.2	-	-	(651 ± 37)	(289 ± 15)
	II	0.2	3.2	(600 ± 20)	-	-	-
	III	31.3	18	(260 ± 30)	(190 ± 20)	-	-
	III	33.2	39.5	(185 ± 15)	(160 ± 15)	-	-
	V	33.2	40.7	-	(160 ± 14)	-	-
decane-water interface							
20	I	0	< 3.5	-	-	(627 ± 38)	(357 ± 25)
	II	0.2	3.5	(570 ± 20)	-	-	-
	III	27.5	8.3	(370 ± 40)	(210 ± 20)	-	-
	IV	32.1	25.8	-	(180 ± 10)	-	-
	V	34.7	48	-	(146 ± 12)	-	-
40	I	0	< 3.9	-	-	(592 ± 45)	(274 ± 22)
	II	0.2	3.9	(540 ± 25)	-	-	-
	III	32	17	(270 ± 35)	(170 ± 20)	-	-
	III	34.2	47	(170 ± 15)	(145 ± 15)	-	-
	V	34.8	48	-	(148 ± 15)	-	-

Furthermore, we can use the AFM images to extract height profiles of the microgels within the monolayer to compare the evolution of D_{core} but also the height of the dried microgels, as a function of compression and the interface. Definitely, these height profiles do not give information about the *in situ* thickness of the microgel monolayers in hydrated state, but they give another dimension to explore the spreading of the microgels at different interfaces.

Representative height profiles averaged over at least 40 individual profiles are given in Figure 5.6A-D, the standard deviation is plotted as shaded area in the corresponding color. The height of the microgels at the apex, H_{core} , is determined from the maximum value on the y-axis, D_{core} is compute using the Matlab function *knnsearch* [176] and a threshold value of 1.5 nm. At the highest surface pressures, microgel cores start to overlap, therefore, multiple microgels are shown. Here, D_{core} was calculated from the distance between the apices (Fig. 5.6A and C, red curves and Fig. 5.6B and D, purple curves). H_{core} and D_{core} are summarized in Table 5.2 for all profiles. In addition the NND are included for microgels at $\Pi > 0$ mN m⁻¹.

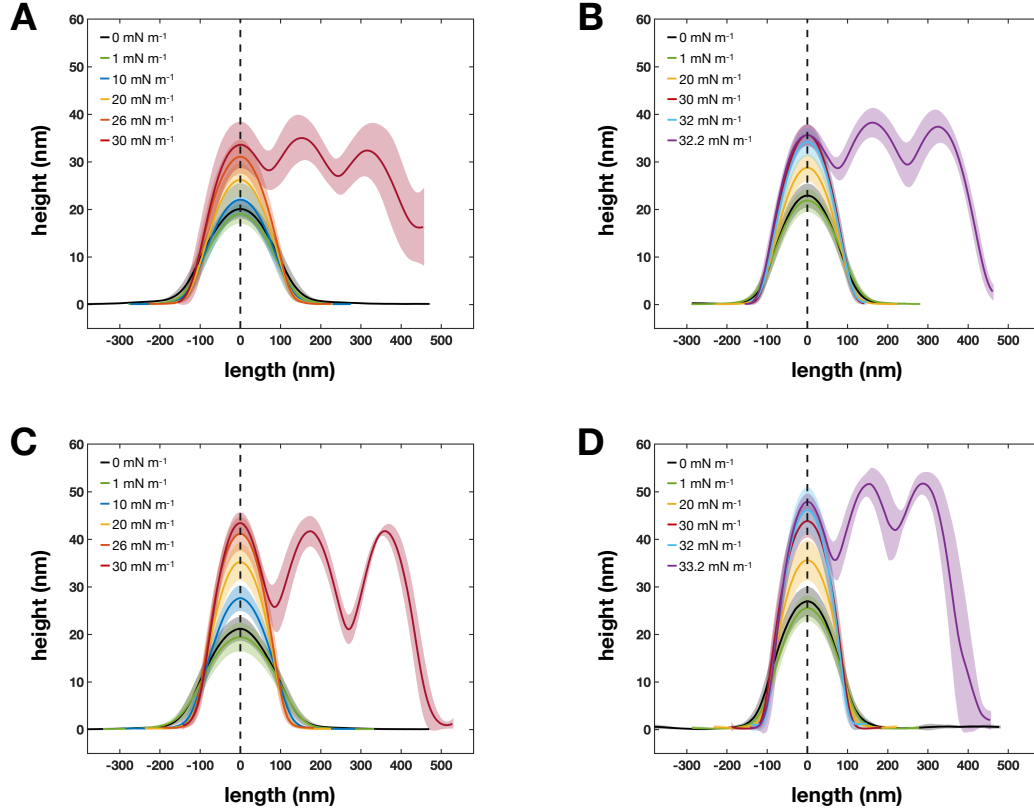


Figure 5.6: Averaged height profiles of microgels in dried state after deposition to a solid substrate at different temperatures ($T = 20$ and 40 °C), interfaces and compressions. For each profile ≈ 40 microgels were analyzed. (A) $T = 20$ °C, air-water interface. (B) $T = 40$ °C, air-water interface. (C) $T = 20$ °C, decane-water interface. (D) $T = 40$ °C, decane-water interface. Different colors represent different compressions. The standard deviation in height and length is given as shaded areas in the corresponding color.

Height profiles at 0 mN m^{-1} are depicted by black lines in Figure 5.6A-D. A decrease of H_{core} is observed for microgels below (from 21 to 20 nm) and above (from 27 to 23 nm) the VPTT from the decane- to the air-water interface. In contrast, the values of D_{core} do not change between the OW and AW interface, as already determined by the phase images and compression isotherms (Tab. 5.1 and Tab. 5.2).

To explain this observation, one has to first recall the characteristics of microgels. In solution, microgels display a polymer volume fraction decay from the center to the periphery. [49] Reaction kinetic data prove that this is a consequence of the faster consumption of the cross-linker (BIS) during the polymerization. [50, 51] Thus, microgels also display a cross-linker gradient from the core to the outside. Indeed, this characteristic dominates their conformation at the interface and microgels depict a core-corona or fried-egg like structure, as shown in Chapter 4 and sketched in Figure 5.7.

This structure also suggest that the polymer layer actually adsorbed or in very close proximity to the interface is not exclusively composed of the lowly cross-linked polymer network or dangling chains, but apparently also of the more cross-linked

sections of the microgel. In other words, if one would only look at a cross-section a few nm thick (Figure 5.7A), with its center at the interfacial plane, it would be very likely that this quasi 2D polymer network displays an inhomogeneous cross-linking and polymer distribution from the center to the periphery (Fig. 5.7B). Clearly, this is a strong simplification that does not consider two important factors: (i) the bending of the interface due to the microgels, and (ii) the parts of the microgel not adsorbed to the interface. Nevertheless, the assumption can be justified to some extent taking results for silica-core-polymer-shell microgels into account. [191] The silica cores in these hybrid-microgels have an exceptional higher density than the core of regular pNIPAM microgels, but still the cores touch the oil-water interface.

Let's now imagine that this quasi 2D construct is adsorbed to the liquid interface and its structure is influenced by the additional surface free energy (Fig. 5.7B). The polymer network is stretched and flattened to increase the number of contacts with the liquid interface. The polymer chains, typically displaying random coil conformation in solution, are straiten and extended in length due to the tensile stress of the interface, giving a penalty in entropy, *i.e.*, free energy of elasticity. [2] It can be expected that the center of the network, on one hand, gives more resistance to deformation due to the higher cross-linker content [2, 192], and on the other, experience less stress due to the higher polymer content [174]. If now the surface free energy is increased, *e.g.*, from the decane- to the air-water interface, the microgel as a whole displays larger in-plane dimensions (D_{2D}), mostly because of the outer parts of the network. Although the core experience the same change, the effect would be mitigated due to aforementioned reasons and the increase could be so small that it is not registered by our analysis. Especially, because although assumed to be monodisperse, microgels actually display a size polydispersity of $\approx 8\%$ in solution (Chapter 4).

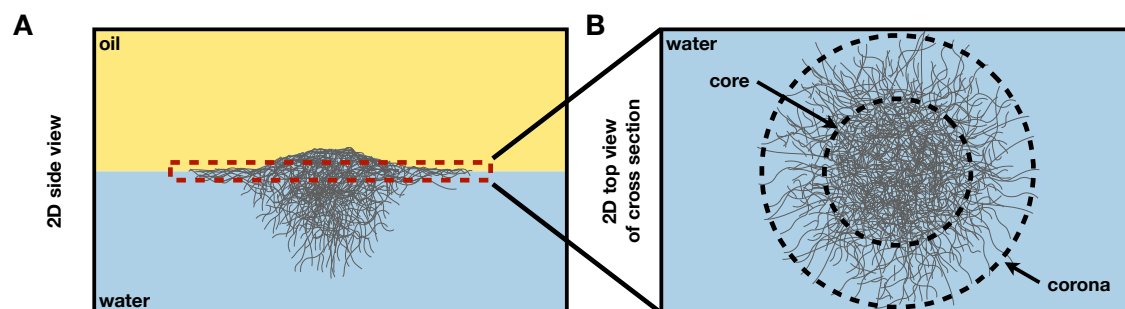


Figure 5.7: Sketch of the conformation of a pNIPAM microgel with inhomogeneous cross-linker distribution at the oil-water interface. (A) side view with a cross-section (red dashed box) and (B) 2D top view of the cross-section.

Furthermore, for the center of the microgels it has to be considered that there is more polymer in the third dimension (Figure 5.7 A), *e.g.*, out-of the interfacial plane, whose adsorption could be energetically more favorable in contrast to stretching the network further. Because the differences in H_{core} between the decane- and air-water interface are small compared their standard deviation (Tab. 5.2), a clear statement cannot be made. Nevertheless, the decrease of the averaged height at least indicates that the increased surface free energy leads to a stronger adsorption of fractions of the polymer network situated in the aqueous phase.

Consequently, changing the surface tension of the interface has the same effect on the different parts of the microgels, *i.e.*, the core and the corona, but their response is different. While the corona of the microgels is stretched significantly more ($D_{2D} - D_{core} \approx 60$ nm), the core seems to be nearly unaffected. This difference might be explained by the stronger resistance to deformation of the microgel center, due to a higher polymer and cross-linker density, and stronger adsorption of polymer from out-of the interfacial plane. Clearly, this hypothesis has to be verified, using for example softer microgels [86], or by further variation of the γ difference [193].

We can now focus our attention on the case of microgels under compression. Around $0.2\text{--}1$ mN m⁻¹, the microgels get into contact and a nominal decrease of the height is observed by about 1 nm independently of the interface and temperature (Tab. 5.1). This reduction of the height is related to the topographic measurement in the AFM. For a dried sample, only the height difference of the protruding structures is sensed. Therefore, all heights within one AFM image are relative to the lowest point of the image. At $\Pi = 0$ mN m⁻¹, the microgels are not in contact and the lowest point is the bare substrate. In contrast, after the contact ($\Pi > 0$ mN m⁻¹), the whole substrate is covered by polymer and H_{core} is relative to the surface of the microgels' coroneae. Since the height of adsorbed polymer chains on a solid substrate is roughly 1 nm [194], the decrease in height from 0 mN m⁻¹ to $0.2\text{--}1$ mN m⁻¹ is due to the thickness of the polymer layer surrounding the cores which is not resolved. Especially at higher compression the disparity of the measured height and absolute height of the monolayer increases, because the microgels are laterally compressed and the unresolved polymer layer becomes thicker.

Between $0\text{--}26$ mN m⁻¹ for 20°C and $\Pi \approx 0\text{--}30$ mN m⁻¹ for 40°C H_{core} increases and D_{core} decreases with compression. In this Π -range the nearest neighbor distance is larger than D_{core} , the cores are not in contact (Tab. 5.2) and compression is believed only to act on the corona (Chapter 4). The height profiles underline that this assumption is not entirely correct. Although the corona is preferentially compressed (the expansion of the corona is proportional to $NND - D_{core}$), the core is also influenced. Following the above explanation, it seems logical that the more cross-linked and denser part of the quasi 2D object is much harder to compress. Accompanied by the decrease of D_{core} the height of the core must increase due to volume conservation of the microgels. It is questionable if the hydrated cores show the same dependence. Microgels are interconnected networks and the tensile stress on the adsorbed polymer layer is passed on through the cross-linker to fractions of the network further away from the interface. But pNIPAM is a highly flexible polymer [2] and the stress can be dissipated through the swollen network with increasing distance from the interface. During the deposition and drying in the Langmuir-Blodgett trough experiment, the network is affected by the displacement of the interconnection points and the stretching (or compression) of the adsorbed polymer layer. As a result, the lateral size (D_{core}) becomes smaller and the height (H_{core}) of the dried microgels increases.

At surface pressures in the range of the phase transition, $\Pi \approx 26\text{--}30$ mN m⁻¹ for 20°C and $\Pi \approx 30\text{--}33$ mN m⁻¹ for 40°C , only a slight increase of H_{core} is observed. In this state (regime III) the hydrated cores of the microgels touch. Upon drying the polymer has to collapse onto itself forming a thick underlying layer which can not be resolved by AFM. For these surface pressures, D_{core} is calculated from the distance of the apices, and thus, the values are in agreement with NND_{2nd} .

Table 5.2: Physical dimensions of microgels monolayers at different compressions deposited from air- and decane-water interfaces at $T = 20$ and 40 °C. Averaged height of microgel profiles at the apex, H_{core} , the core diameter, D_{core} , the nearest neighbor distance of the first phase, NND_{1st} , and the nearest neighbor distance of the second phase, NND_{2nd} , at different compressions.

Π (mN m ⁻¹)	H_{core} (nm)	D_{core} (nm)	NND_{1st} (nm)	NND_{2nd} (nm)	Π (mN m ⁻¹)	H_{core} (nm)	D_{core} (nm)	NND_{1st} (nm)	NND_{2nd} (nm)
air-water interface									
20 °C					40 °C				
0	(20 ± 2)	(369 ± 35)	-	-	0	(23 ± 2)	(277 ± 23)	-	-
0.2-1	(19 ± 2)	(328 ± 34)	(610 ± 40)	-	0.2-1	(22 ± 2)	(289 ± 31)	(590 ± 36)	-
10	(22 ± 2)	(304 ± 30)	(520 ± 41)	-	20	(29 ± 3)	(253 ± 25)	(470 ± 39)	-
20	(26 ± 3)	(292 ± 30)	(460 ± 48)	-	30	(34 ± 3)	(245 ± 26)	(320 ± 31)	-
26	(31 ± 3)	(286 ± 27)	(380 ± 40)	-	32	(35 ± 3)	(249 ± 23)	(260 ± 53)	(185 ± 29)
30	(33 ± 5)	(158 ± 43)	(285 ± 100)	(181 ± 40)	32.2	(35 ± 3)	(162 ± 23)	(190 ± 35)	(162 ± 20)
decane-water interface									
20 °C					40 °C				
0	(21 ± 2)	(358 ± 35)	-	-	0	(27 ± 3)	(280 ± 30)	-	-
0.2-1	(20 ± 2)	(363 ± 36)	(575 ± 40)	-	0.2-1	(26 ± 3)	(265 ± 25)	(515 ± 42)	-
10	(28 ± 2)	(294 ± 30)	(510 ± 48)	-	20	(36 ± 4)	(245 ± 24)	(430 ± 47)	-
20	(35 ± 3)	(272 ± 25)	(460 ± 42)	-	30	(44 ± 3)	(239 ± 20)	(315 ± 33)	-
26	(41 ± 3)	(266 ± 26)	(390 ± 40)	-	32	(46 ± 5)	(230 ± 30)	(275 ± 39)	-
30	(43 ± 2)	(181 ± 19)	(340 ± 90)	(200 ± 40)	33.2	(49 ± 3)	(156 ± 30)	(250 ± 77)	(158 ± 30)

Lastly, the ordering of the interfaces is presented by the hexagonal order parameter, Ψ_6 , as a function of N_{area} in Figure 5.8A-D. Besides the already discussed differences of the onset points of the transitions from one regime to the other, the trend of Ψ_6 at the air-water interface (Figure 5.8A-B) and the decane-water interface (Figure 5.8C-D) shows no substantial differences and there is no evidence that changing the interface influences the short- and long-range order of the pNIPAM microgels. The evolution of both, Ψ_6 and the pair correlation function, $G(r)$, are discussed in more detail in Chapter 4.

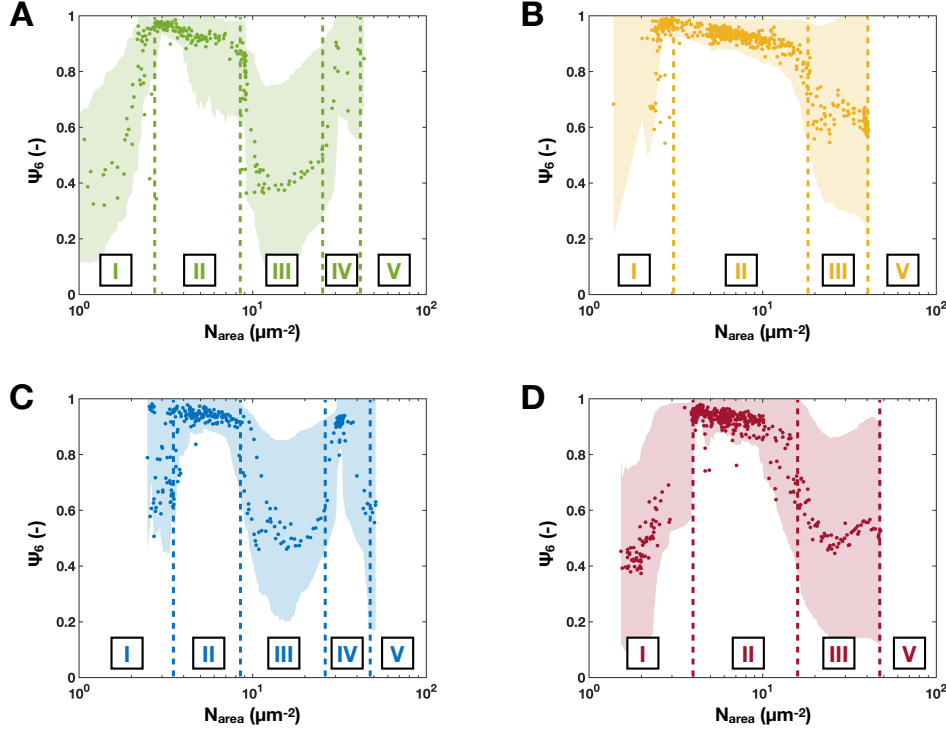


Figure 5.8: Hexagonal order parameter, Ψ_6 , as a function of number of microgels per area, N_{area} , of pNIPAM microgels at the air-water and decane-water interface. (A) green full circles: $T = 20$ °C, air-water interface. (B) golden full circles: $T = 40$ °C, air-water interface. (C) blue full circles: $T = 20$ °C, decane-water interface. (D) red full circles: $T = 40$ °C, decane-water interface. The errors are presented as shaded areas in the respective color. Dashed lines indicate the transitions between different regimes. The regimes are labeled in roman numbers.

5.4. Conclusion

In summary, the two-dimensional phase behavior of adsorbed microgel monolayers at the air-water interfaces below and above the volume phase transition temperature was investigated. Langmuir-Blodgett type depositions were conducted and imaged by atomic force microscopy to get information on the in-plane dimensions and to obtain the microstructures. It is shown that microgel monolayers at the air-water interface have the same temperature dependence as expected from the oil-water interface.

The aim of this chapter was not only a qualitative but also quantitative comparison to elucidate the influence of the surface free energy on the single microgel conformation. Therefore, the results were directly compared to equivalent measurements of the same pNIPAM microgels at the decane-water interface. [29] Differences between the air- and decane-water interfaces are observed for the total diameter of the microgels at the interface (D_{2D}). The increased surface tension (air-water 72.3 mN m^{-1} [178] at 20 °C and decane-water 52.3 mN m^{-1} [169] at 20 °C) leads to a stronger stretching of the microgel coroneae, but not for the size of the microgel cores (D_{core}). This effect is associated with the core-corona structure of microgels in bulk and at the interface. The cross-linking and polymer volume fraction gradient

of the microgels in aqueous solutions [49–51] forces also a gradient in the adsorbed polymer layer. The denser and more cross-linked area (\approx the core) of the microgels gives a stronger resistance to deformation.

Stronger adsorption of the polymer network to the air-water interface becomes obvious when the inter-particle distance (NND) of the monolayer failure is examined. Similar to the decane-water interface the failure of the monolayer is independent of the temperature, indicating that there is a maximum number of polymer segments that can be confined at or in close proximity of the interface. In contrast to the decane-water interface, this limit is reached at larger NND proving that with an increase of surface free energy more segments of a single microgel adsorbed to the interface.

Finally, the results demonstrate that microgels at the air-water and decane-water have the same temperature-dependent two-dimensional phase behavior. At both interfaces the temperature-dependent swelling perpendicular to the interface (“3D”) affects the compressibility parallel to the interface (“2D”).

5.5. Data Availability

Research data for this chapter may be accessed at <https://hdl.handle.net/21.11102/7d2ae8aa-e857-11ea-afb2-e41f1366df48>.

6. Out-of-Plane Structure of Microgels at the Air-Water Interface

6.1. Introduction

The combination of responsiveness and flexibility of microgels leads to interesting opportunities for fundamental studies [30, 195, 196] and applications [16, 75, 197] in bulk and at interfaces. The structure of microgels and their response to external stimuli is well understood in solution [49, 54] and more complex systems have been investigated in recent years. [198–201] In contrast, a full description of the microscopic structure of adsorbed microgels at liquid interfaces is still missing. On one hand, the in-plane structure and ordering of adsorbed microgels has extensively investigated by experiments and simulations; [70, 76, 89, 202] on the other hand, only few experimental studies deal with their out-of-plane structure. In most cases, computer simulations are used to elucidate the microscopic conformation of microgels normal to the interface and access information which are not experimentally measurable. [72, 79, 88] However, a sophisticated model is needed to not bias the results, and experimental data and evidence are needed to improve the quality of simulations to obtain a comprehensive understanding of the out-of-plane conformation of microgels at interfaces.

Neutron reflectometry (NR) is a powerful technique to obtain information on the structure and physical properties of interfaces and thin films, such as chemical aggregation, polymer and surfactant adsorption, magnetic systems, and biological membranes. [135–138, 203] The unique strong point of NR, compared to other reflectometry techniques, is the possibility of isotropic contrast variation. As opposed to electromagnetic radiation, neutrons interact with the nuclei and not with the electron cloud of atoms. The contrast of nuclei varies in a non-monotonic way between isotopes and elements. [145] Thus, it is possible to change the contrast of a system dramatically, for example, by exchanging hydrogen with deuterium, without considerably changing the chemistry of a system. Recently, Zielińska *et al.* used NR to investigate the adsorption and structure of nanogels ($D_h < 40$ nm) at interfaces highlighting the feasibility also for microgels. [170, 204]

In this chapter, we present *in situ* neutron reflectometry data of conventionally cross-linked and ultra-low cross-linked microgels at fluid interfaces. The evolution of the reflectivity curves is studied at different temperatures and/or compressions. The data were fitted with a slab model to generate out-of-plane scattering length density profiles of these microgels. These experimental results can be of great help to elucidate the microscopic conformation of microgels normal to interfaces and validate existing computer simulations.

6.2. Experimental

6.2.1. Materials

For the interface experiments, deuterium oxide (D_2O) was purchased from Merck KGaA, Germany. Air-contrast matched water (ACMW) was produced by mixing

8 vol% D₂O with 92 vol% H₂O. For ACMW and cleaning Milli-Q water (Merck KGaA, Germany) with a resistivity of 18,2 MOhm·cm was used. Deuterated Chloroform (CDCl₃) was purchased from Alfa Aesar, USA. CDCl₃ was used as solvent and spreading agent of the microgels. All chemicals were used as received.

6.2.2. Specular Neutron Reflectometry

Specular neutron reflectometry measurements were conducted on the Fluid Interfaces Grazing Angles Reflectometer (Figaro) in the Institute Laue-Langevin, Grenoble, France and the Apparatus for Multi-Optional Reflectometry (Amor) in the Paul Scherrer Institute, Villigen, Switzerland.

6.2.3. Compression Isotherms and Depositions

The procedure for compression isotherms and depositions at the decane-water interfaces is explained in detail in Chapter 4. The measurements at the air-water interfaces were conducted in the same way, but instead of 80/20 vol% mixtures of water-propan-2-ol, 50/50 vol% mixtures of water-propan-2-ol or microgels suspended in chloroform were used. This was done to maximize the adsorption of the microgels to air-water interfaces and minimize partial loss of microgels into the sub-phase. This loss is unavoidable if the surface-active component and the spreading agent are soluble in one of the two immiscible phases.

6.2.4. Image Analysis

The open-source analysis software *Gwyddion* 2.54 was used to process the AFM images. All images were leveled to remove the tilt and zero height was fixed as the minimum z-value of the image. AFM images of the deposited dried microgel monolayers were analyzed with a custom-written Matlab script based on the image analysis routine of Ref. [76]. The script was already used in Chapter 4 and details can be found there. The number of microgels per area, the mean nearest neighbor distances, and the hexagonal ordering parameter were calculated for all images.

The analysis of microgel monolayers was extended by height profiles of the microgels in the dried state. Profiles were extracted through the apex of the microgels and at different angles with respect to the fast scan direction. Multiple height profiles of one image were summarized and aligned to the apex (zero coordinate of the x-axis) to obtain averaged microgel profiles and not to bias the results. The averaged profiles are presented with the standard deviations as the error. The apex height of the averaged microgels was computed using the Matlab function *findpeaks* and the averaged diameter of the microgels was determined by the *knnsearch* [176] with a threshold of 1.5 nm.

Figaro

Figaro is a high flux, flexible resolution time-of-flight (TOF) reflectometer with a horizontal sample stage. It is used for studies of thin films at air-liquid, liquid-liquid, and solid-liquid interfaces. The instrument is capable of upward and downward reflection at a wide q -range between 0.0045 to 0.45 Å⁻¹. The q -range is controlled by the incoming beam wavelengths (2 to 30 Å) and the grazing angle of incidence,

Θ_G , (0.615 to 3.766°). Here, two configurations were used to cover a q -range of 0.0089 to 0.35 Å⁻¹ with the incoming beam wavelengths between 2 to 20 Å and 2 to 30 Å at Θ_G 0.615 and 3.766°, respectively. The resolution, $\Delta q/q$, of Figaro can be varied between 1.2 and 9.8% to maximize the flux at very low grazing angles. In all Figaro experiments the resolution was set to 7%. Typically, an area of $\approx 10 \times 40$ mm² is illuminated with the neutron beam. Reflected neutrons are detected by a two-dimensional multitube detector positioned at a distances of 3 m from the sample. The detector consist of an aluminum plate with 64 squared channels cut into it, giving a horizontal resolution of 8 mm and a vertical resolution of 2 mm. Each of these tubes is filled with ³He and CF₄ and contains Stablohm wire, which detects neutrons by charge division.

For the experiments a teflon Langmuir trough with an area of 100 cm² and a volume of ≈ 60 mL equipped with two parallel moving teflon barriers was used. The trough was placed inside an gas-tight box with heated sapphire or quartz glass windows to prevent condensation. The box is placed on an active anti-vibration stage which can be moved vertically and horizontally. Prior to a measurement series (measurements between 10 and 40 °C in 10 °C steps) the trough was carefully cleaned and a fresh air-water (D₂O or ACMW) interface was created. For temperature control, the trough was connected to an external water bath. The trough was cooled down to 10 °C and left to equilibrate for 30 mins. The microgels were added to the interface from solution with a concentration of 1 mg mL⁻¹ in deuterated chloroform. Subsequently, the interface was compressed to 13 mN m⁻¹ and the first measurement was conducted. Afterwards the trough was tempered to the next temperature and left to equilibrate for 30 mins. For each contrast measurements at 10, 20, 30, and 40 °C were conducted. A feedback loop controlled and adjusted the surface pressure during the experiments. Surface pressures were measured with paper Wilhelmy plates.

Amor

Amor is a neutron reflectometer capable of measuring in both TOF and monochromatic mode, with polarized and unpolarized neutrons at PSI. Amor has a horizontal sample-plane geometry to study air-liquid, liquid-liquid, and solid-liquid interfaces. In TOF mode a q -range up to 0.2 Å⁻¹ is attained by varying the wavelength of the incoming beam between 1.5 and 13 Å and the grazing angle of incidence between 0.5 and 3.0°. Here, three configurations to cover the q -range from 0.009 to 0.2 Å⁻¹ were used with the neutron wavelengths between 3.5 and 12 Å and grazing angles of $\Theta_G = 0.5, 1.4, 3.0^\circ$. The area the neutron beam illuminates is approximately 100 mm². Amor is equipped with a multi detector system consisting of two ³He-detector tubes and a multi-wire ³He-chamber with 2 mm spacial resolution.

In the experiments NR measurements were performed at the air-liquid interface. A temperature-controlled teflon Langmuir trough with a single teflon barrier was used to reach and control different the surface pressures. The initial trough area is 160 cm² and compression is possible down to 70 cm², to leave enough space for the surface pressure sensor and the neutron path. Surface pressures were measured with paper Wilhelmy plates. Previous to the measurements the trough was carefully cleaned and a fresh air-D₂O interface was created. Microgels were spread from a 1 mg mL⁻¹ solution in deuterated chloroform directly to the air-water interface with a Hamilton syringe. Subsequently, the monolayer was compressed to the

desired surface pressures and the reflectometry measurement was conducted. The surface pressures were between 1 and 30 mN m⁻¹ and could not be reached with one compression. Thus, different initial amounts of microgel solutions were spread to fresh air-D₂O interfaces to reach all measurement points. The temperature was set to $T = (20 \pm 0.5)^\circ\text{C}$.

6.2.5. Data Correction and Reduction

The reflectivity of a sample is the ratio of the number of reflected and incident neutrons. The number of incident neutrons is recorded by a direct beam measurement, that is, without the sample environment in the neutron path. As the collimation and wavelength of the neutron beam changes for different grazing angles, direct beam measurements are conducted for each setup. The reflection of the clean interface, *i.e.*, without a thin film present, is measured to obtain the background. The background measurements are conducted for each sub-phases, D₂O and ACMW, and each grazing angle of incidence. The results of the specular NR measurements of the sample are then corrected and reduced to one-dimensional reflectivity curves as a function of the normal scattering vector q . A full reflectivity curve, over the whole q -range, is obtained by merging together the results from the different angle of incidence. It is important to have significant q overlap of the different measurements to reduce errors. The reduction is performed using computer programs such as COSMOS [205] in the LAMPS [206] framework.

6.2.6. Data Analysis

The resulting 1D-reflectivity curves have to be analyzed to obtain physical meaningful parameters. Generally, a direct inversion of the experimental data is not possible due to the loss of phase information. Therefore, a model-based approach is used to fit the data. The model consists of n parallel layers placed between the fronting or top-phase and the backing or sub-phase. Each distinct layer of the film consists of a homogeneous material with a scattering length density, $N_{b,n}$, a roughness, σ_n , and a thickness, d_n . From these values the reflectivity curve of the model system is calculated using the recursive Parratt- [207], Born and Wolf matrix-formulism [143], or Abeles matrix method [146]. The calculated reflectivity curve is compared to the experimental data and the goodness of the fit is determined, for example by the least-squares method or χ^2 -test. The parameters, $N_{b,n}$, σ_n , and d_n , are optimized by a recursive algorithm reducing χ^2 until the best fit of the given model is achieved. Here, the program Motofit [208] was used to create and optimize a model for the thin films. Motofit employs Abeles matrix method: starting from the Fresnel coefficients (Equation 3.8 and 3.9 in Chapter 3.4) the roughness or diffuseness between the layers n and $n + 1$ is accounted for by an error function, following Névot and Croce [209] (Equation 6.1).

$$r_{n,n+1} = \frac{k_n - k_{n+1}}{k_n + k_{n+1}} \exp(-2k_n k_{n+1} \sigma_{n,n+1}^2), \quad (6.1)$$

where k_n is the wave vector of each layer given by $k_n = \sqrt{k_0^2 - 4\pi(N_{b,n} - N_{b,0})}$. $k_0 = q/2$ and $N_{b,0}$ is the scattering length density of the top-phase or fronting. The thickness of each layer is introduced by a phase factor $\beta_n = k_n d_n$. The method of Abeles defines a characteristic matrix, C_n , for each layer in terms of the modified

Fresnel coefficients and the phase factor:

$$C_n = \begin{bmatrix} \exp(\beta_n) & r_{n,n+1} \exp(\beta_n) \\ r_{n,n+1} \exp(-\beta_n) & \exp(-\beta_n) \end{bmatrix}. \quad (6.2)$$

The product of the characteristic matrices for each layer, $M = [C_1][C_2]...[C_n]$, gives the reflectivity of the sample:

$$R = \left| \frac{M_{11}}{M_{12}} \right|^2. \quad (6.3)$$

With the parameters, $N_{b,n}$, σ_n , and d_n , of the best fit the scattering length density profiles normal to the interface, $N_{b,z}$, are calculated using Equation 6.4.

$$N_{b,z} = \sum_0^n \frac{N_{b,n} - N_{b,n+1}}{2} \left(1 + \operatorname{erf} \left(\frac{z - z_n}{\sigma_n \sqrt{2}} \right) \right), \quad (6.4)$$

where z is the distance from the top-phase, and erf is the error function [210].

Similar to microgels in bulk [49], the total thickness of the microgel monolayer can be approximated taking into account the thickness, d_n , of the layers and the smearing into the top- and sub-phase, *i.e.* the roughness. The total layer thickness is defined by:

$$d_{total} = d_{one}...d_n + 2\sigma_{one} + 2\sigma_{bkg}. \quad (6.5)$$

It has to be clarified that due to the naming in Motofit [208] σ_{one} is the roughness between the zero and first layer (top-phase and first layer of the film) and σ_{bkg} is the roughness between the n th layer and the background (last layer of the film and the sub-phase).

In the fitting process of the data, the resolution, $\Delta q/q$, given by Equation 6.6 for TOF measurements is account for by a constant factor ($\Delta q/q = 7\%$).

$$\left(\frac{\Delta q}{q} \right)^2 = \left(\frac{\Delta t}{t} \right)^2 + \left(\frac{\Delta \Theta_G}{\Theta_G} \right)^2, \quad (6.6)$$

where Δt is the pulse time length, and t is the time-of-flight of the pulse.

6.3. Results and Discussion

6.3.1. Neutron Reflectivity as a Function of Temperature

Figures 6.1A and B present the reflectivity of pNIPAM microgels at $T = 10, 20, 30$, and 40°C and at two contrasts, D_2O or ACMW, with $N_b = 6.36$ and $0 \cdot 10^{-6} \text{ \AA}^{-2}$ [211], respectively. The microgels are the very same as already characterized in Chapters 4 and 5. The measurements were conducted at constant surface pressure of $\Pi \approx 13 \text{ mN m}^{-1}$, where the microgels have a center-to-center distance of approximately $NND = 500 \text{ nm}$.

Reflectivity curves of thin films typically have oscillations, called Kiessig fringes [146, 212], or Bragg-peaks [213]. These features appear due to destructive or constructive interference of reflected beams from the different interfaces, *e.g.*, the top-phase-thin-film, or thin-film-substrate interface. Their amplitude and frequency are greatly affected by roughness, diffusiveness, film thickness, and scattering length

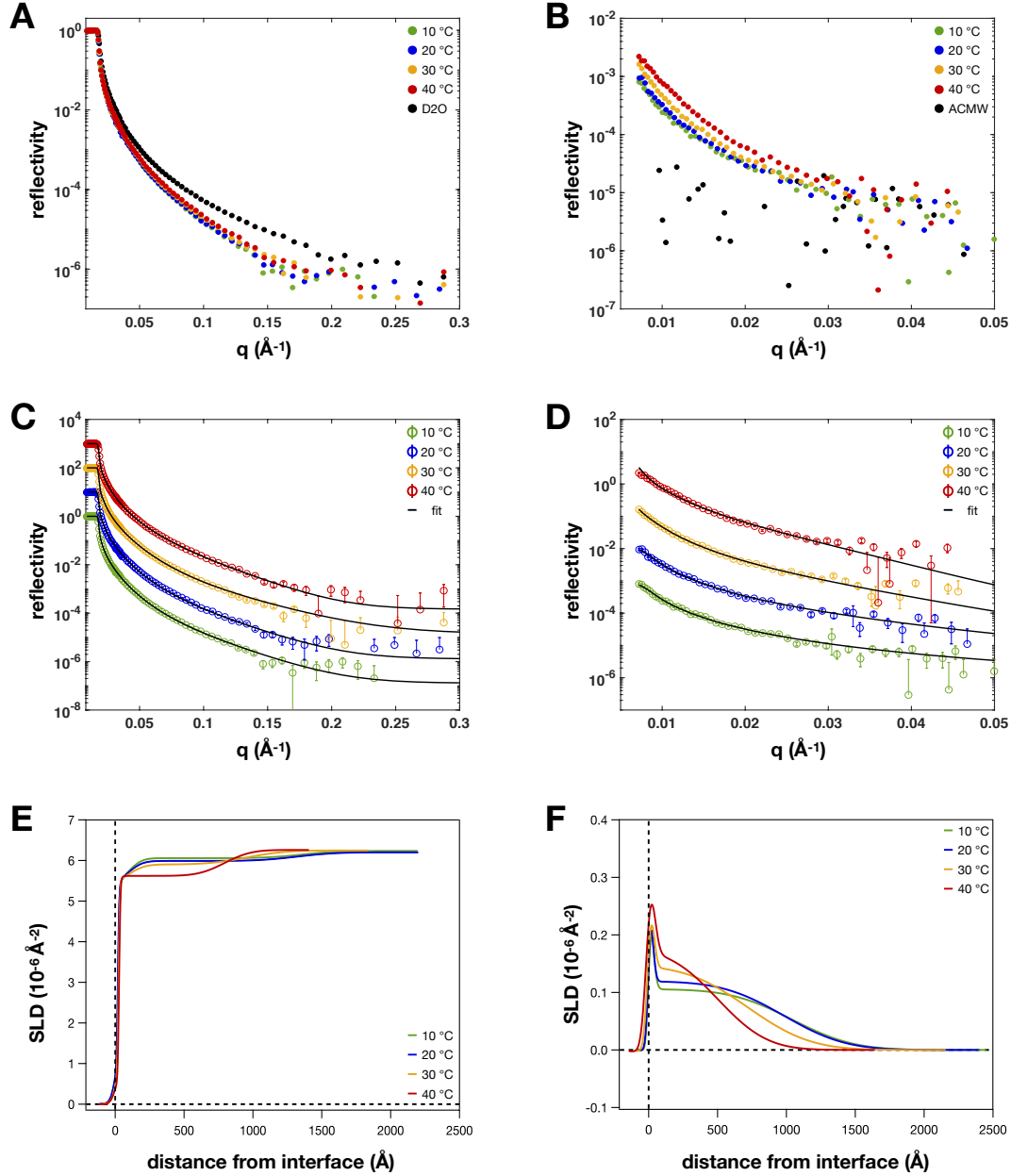


Figure 6.1: Reflectivity curves of pNIPAM microgels at $T = 10, 20, 30,$ and 40 °C at the air-D₂O (A,C) and air-ACMW (B,D) interface. Black circles in A and B correspond to the reflectivity of the bar interface. For reasons of clarity, error bars are not plotted. Reflectivity curves with fits (black solid lines) at the air-D₂O (C) and air-ACMW (D) interface. The curves are shifted in y-direction to make them more recognizable. (E) Scattering length density profiles at the air-D₂O interface from the fits in C. (F) Scattering length density profiles at the air-ACMW interface from the fits in D. Dashed black lines indicate zero SLD and zero distance from the interface.

density (SLD) contrast, which is the difference in SLD between two neighboring layers. [214]. For example, the spacing of the fringes can be used to calculate the thickness of the film by $d = 2\pi/\Delta q$.

For the pNIPAM microgel films (Fig. 6.1A and B) no features are observed and

all reflectivity curves decay smoothly until they reach the values of the background (between 10^{-7} - 10^{-6}). This can be related to the structure and conformation of microgels; their solvent swollen polymer network, without a clearly defined surface, composed of pNIPAM ($N_b = 0.939 \cdot 10^{-6} \text{ \AA}^{-2}$) [211] damps the oscillations until no features are visible.

Nevertheless, a clear difference in reflectivity is observed for the pNIPAM microgel films (colored circles) compared to the bare interface (black circles) at both contrasts. Furthermore, with increasing temperature also the reflectivity curves of the pNIPAM microgel monolayers change. This effect is rather small at the air-D₂O, but well pronounced at the air-ACMW interface. In Fig. 6.1A and B it is shown that increasing the temperature above the VPTT of the microgels (around 32 °C) leads to an increase of reflectivity (yellow and red circles) while at $T = 10$ and 20 °C the curves coincident (green and blue circles). In bulk the polymer network of a microgels expels solvent and deswells, increasing its density and refractive index with temperature. Consequently, we interpret the change of reflectivity as a decrease in the thickness of the film. These measurements once more confirm that microgels are still thermo-responsive normal to the interface.

A more quantitative description of the influence of temperature on the reflectivity of the microgel films is obtained fitting the curves with an appropriated model. In the absence of a well-described neutron reflectivity model for microgels, we used the model proposed by Zielińska *et al.* for nanogels. [170]. This model consists of three layers; the first is in direct contact with the top-phase, and therefore, is composed of air, polymer (pNIPAM), and solvent (D₂O or ACMW). The air is also taken into consideration, as it has been shown that the microgels partially protrude into the top-phase. [70, 72] However, this protrusion is dependent on the solubility of the microgels in the top-phase and the surface tension between top- and sub-phase. [83] For air-water interfaces, the lowest protrusion is expected because pNIPAM is insoluble in air and the air-water interface has the highest surface tension. [169, 178, 215] The second and third layers are composed of polymer and solvent only and are characterized by a decreasing amount of polymer with increasing distance from the interface.

In Fig. 6.1C and D the reflectivity curves of the pNIPAM microgel are shown again, this time, shifted in the y-direction to make them more recognizable and with the fit of the three-layer model (solid black lines). In Table 6.1 the parameters of the best fits and the total thickness of the film approximated with Equation 6.5 are presented. From these parameters, SLD profiles normal to the interface are calculated using Equation 6.4. The profiles are shown for D₂O and ACMW in Figure 6.1E and F, respectively. Most informative are the SLD profiles at the air-ACMW interface. Here, the profile of the microgels is directly visible, because there is no contrast between the top- and sub-phase. Independent of temperature, close to the interface a thin layer is observed that has a high SLD and protrudes slightly into the air. Then the scattering length density of the film rapidly decays, stays nearly constant for a certain distance until it gradually smears out. The SLD of the fit, $N_{b,fit}$, are directly connected to the polymer volume fraction by $N_{b,fit} = \phi_{pNIPAM} N_{b,pNIPAM} + (1 - \phi_{pNIPAM}) N_{b,solvent}$, and consequently, the SLD profiles are proportional to the volume fraction of the polymer network.

The influence of temperature on the microgel monolayers can be followed from the values in Tab. 6.1 and the SLD profiles at the air-ACMW interface (Fig. 6.1F).

Increasing the temperature above the VPTT of the microgels leads to changes in the SLD profiles. The first layer of condensed polymer increases in thickness (≈ 17 to 29 \AA), roughness (25 to 30 \AA), and SLD (0.22 to $0.60 \cdot 10^{-6} \text{ \AA}^{-2}$). For linear pNIPAM polymers and nanogels at ambient temperature d -values in the range of 7 - 20 \AA were observed. [170] Furthermore, Fig. 6.1F shows that the protrusion into air increases by a few nanometers. For the remaining part of the polymer network, a scenario similar to the behavior of microgels in bulk is observed [49]: increasing the temperature above the VPTT leads to a strong decrease of the size (thickness) and solvent content. For the first three measured temperatures, the second layer of the model does not significantly change, in contrast to the third layer (Tab. 6.1). At $40 \text{ }^\circ\text{C}$, the second and third layers display almost the same thickness and solvent content with low roughness in between. For comparison with the other temperatures, both layers are merged together. The results display a reduction of the thickness (from ≈ 1200 to 700 \AA), roughness (220 to 170 \AA), and solvent content (97 to $86 \text{ sol}\%$). In the SLD profiles, this transition becomes evident by the decrease of extension into the sub-phase and the increase of $N_{b,z}$.

As expected, the total thickness of the microgel monolayer is constant at $T = 10$ and $20 \text{ }^\circ\text{C}$ and becomes smaller at $T = 30$ and $40 \text{ }^\circ\text{C}$. The thickness decreases from $d_{total} \approx 180$ to 110 nm upon crossing the volume phase transition temperature. This result is consistent with ellipsometry measurements of the same pNIPAM microgels (Chapter 4). Ellipsometry shows a decrease in the thickness of the layer from ≈ 200 to 110 nm , and the same trend has been reported by other groups and methods. [72, 79, 93]

The conformation of the microgels, that is their SLD profile, can be compared to results obtained by computer simulations [72, 177, 216] or for nanogels [170, 204]. During the measurements the surface pressure was constant at $\Pi \approx 13 \text{ mN m}^{-1}$. At this value the center-to-center distance of the microgels is larger than the size of their densely cross-linked core; “free space” is expected between neighboring microgels, which is not occupied by polymer (Chapter 4). In the SLD profiles at the air-ACMW interface this “free space” is filled with the solvent that is invisible for neutrons. In comparison to simulations, the profiles displayed here present an average over a large number of microgels because the illuminated spot size is roughly 10^8 times the size of a microgel. Nevertheless, the experimental profiles of the pNIPAM microgels (Fig. 6.1F) agree with simulated profiles of *in silico* synthesized microgels with a similar cross-linker content ($5.5 \text{ mol}\%$). [72]

6.3.2. Neutron Reflectivity as a Function of Compression

In Figure 6.2A the results of neutron reflectivity measurements of the pNIPAM microgels at $T = 20 \text{ }^\circ\text{C}$ as a function of compression are presented. Π -values were chosen according to their compression isotherms (Chapter 4 and 5). The regular cross-linked microgels display an isostructural phase transition between ≈ 25 and 32 mN m^{-1} , but unfortunately, surface pressures above 30 mN m^{-1} could not be reached with the Langmuir trough setup of Amor. Therefore the surface pressures investigated were $\Pi = 1, 10, 20, 26$, and 30 mN m^{-1} . At these values dried microgel monolayers display averaged center-to-center distances in the range from ≈ 600 to 220 nm (Chapter 5). During the measurements, surface pressures were kept constant by the Langmuir trough setup. To study the influence of compression, NR experiments were only conducted at the air- D_2O interface, because the measurements at

Table 6.1: Results of the three-layer model fit of the reflectivity curves in Figure 6.1 for the pNIPAM microgels at different temperatures. d is the thickness, d_{total} the approximated total film thickness, σ the roughness, and σ_{bkg} the roughness with the background. For the first layer the scattering length density, $N_{b,fit}$, was a free parameter. For layers two and three the concentration of solvent, sol , was fitted. Both contrasts were fitted simultaneously to obtain the data.

Temperature	Layer 1			Layer 2			Layer 3			Background	
(°C)	d (Å)	σ (Å)	$N_{b,fit}$ (10^{-6} Å^{-2})	d (Å)	σ (Å)	sol (%)	d (Å)	σ (Å)	sol (%)	σ_{bkg} (Å)	d_{total} (Å)
10	16	25	0.22	68	12	82	1233	74	97	215	(1797 ± 233)
20	18	26	0.25	66	11	81	1170	90	96	225	(1756 ± 246)
30	22	27	0.36	78	9	83	834	103	93	223	(1434 ± 287)
40	29	30	0.60	345	8	86	357	90	87	176	(1143 ± 263)

the air-ACMW interface would take too much time due to the lower neutron flux of Amor (compared to Figaro) and the low contrast of the microgels.

Again, the reflectivity curves show a distinct difference between the bare air-D₂O and the microgel laden interface. The interface with the lowest surface pressure, *i.e.*, at $\Pi = 1 \text{ mN m}^{-1}$, has the highest reflectivity. With increasing compression, the reflectivity of the monolayer decreases to 30 mN m^{-1} . In comparison with the reflectivity curves at different temperatures (Fig. 6.1A and B), this trend indicates an increase of the microgel monolayer thickness with surface pressure. Furthermore, at higher Π more and more air-D₂O contacts are substituted by polymer. [174] In other words, the increase of polymer density, and simultaneous decrease of D₂O, leads to a reduction of the reflectivity, because D₂O has a much higher scattering length density ($N_b = 6.36 \cdot 10^{-6} \text{ Å}^{-2}$) [211] than pNIPAM ($N_b = 0.939 \cdot 10^{-6} \text{ Å}^{-2}$) [211].

The same model as described above was used to fit the reflectivity data at different compressions to obtain a more quantitative description of the microgel conformations. In Figure 6.2C, the reflectivity curves are shown with the fits, shifted in the y-direction to make them more distinguishable. The results for the best fits are presented in Table 6.2. The model shows that the microgels' film thickness is hardly influenced by compression until 20 mN m^{-1} . Above this value, the thickness strongly increases and is constant again between 26 and 30 mN m^{-1} . We can compare this trend with the height profiles of microgels at different Π after deposition in Chapter 5. At $T = 20 \text{ °C}$, the deposited dried microgels show a monotonic increase of the height between 1 and 26 mN m^{-1} from roughly 20 to 31 nm. Starting from the onset point of the phase transition (around 26 mN m^{-1}) the microgels within the monolayer display a nearly constant height.

We can explain the difference between the *in situ* film thickness and the dry height considering the internal conformation and structure of microgels at interfaces. Upon adsorption microgels laterally stretch to roughly two times their size in solution to maximize their contact area with the interface and display a core-corona structure. [29, 76, 78, 79] In Chapters 4 and 5, it is shown that the onset point of the isostructural phase transition for microgels below and above the VPTT coincides with the lateral size of the microgel fractions situated in the aqueous phase. These fractions are described by the size of the core, D_{core} , in Table 5.1 of Chapter 5. Concluding that until the total in-plane size of the microgels reaches a value close

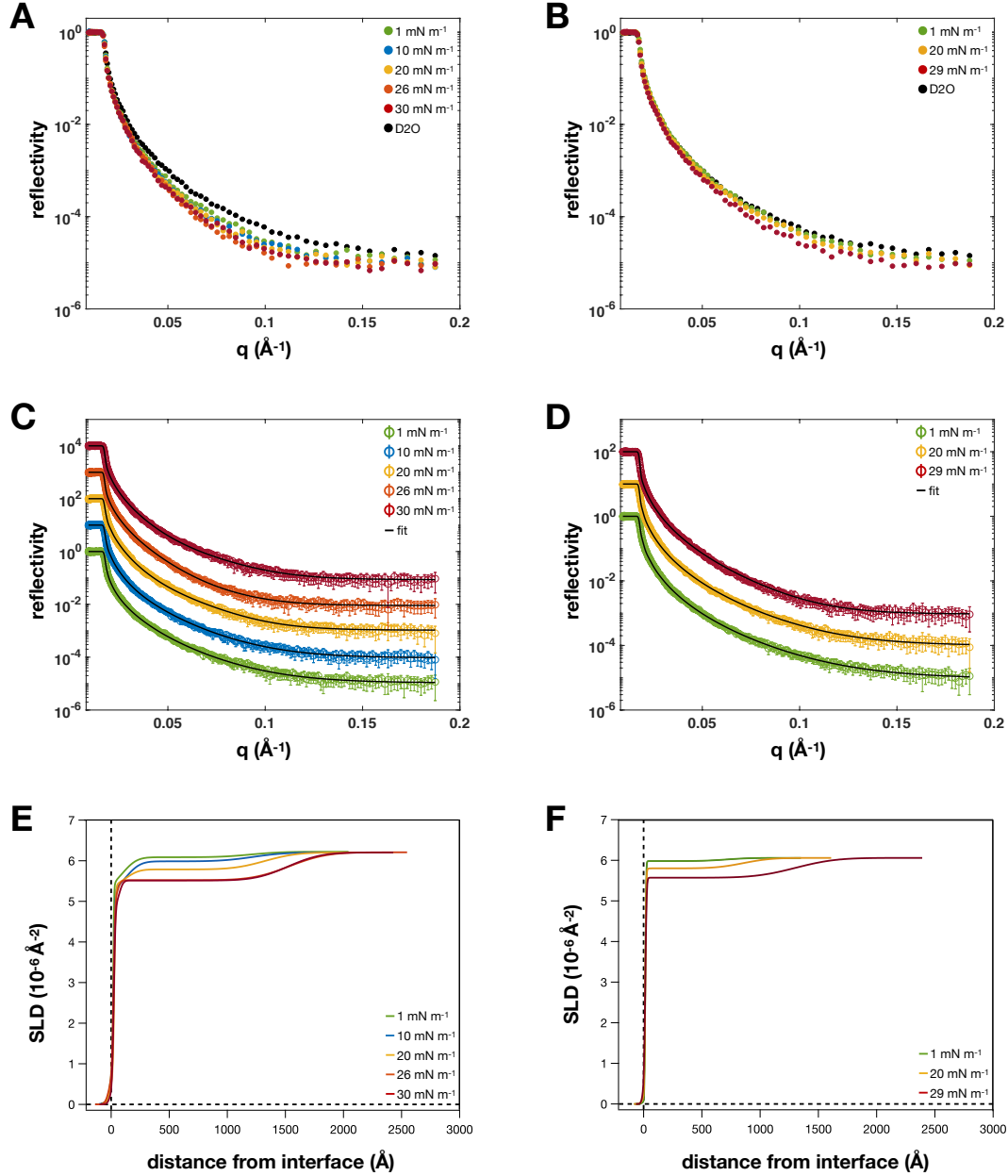


Figure 6.2: Reflectivity curves of pNIPAM and ULC microgels at different surface pressures at the air-D₂O interface. (A) Reflectivity curves of pNIPAM microgels at $\Pi = 1, 10, 20, 26$, and 30 mN m^{-1} . (B) Reflectivity curves of ULC microgels at $\Pi = 1, 20$, and 29 mN m^{-1} . In A and B Only every fourth point was plotted to enhance the visibility. The measurements were conducted at $T = 20^\circ \text{C}$. The Reflectivity curves of pNIPAM (C) and ULC microgels (D) with fits at the air-D₂O interface. Reflectivity curves are shifted to make them more recognizable. (E) Scattering length density profiles at the air-D₂O of pNIPAM microgels interface from the fits in C. (F) Scattering length density profiles of ULC microgels at the air-D₂O interface from the fits in D. Dashed black lines indicate zero SLD and zero distance from the interface.

to D_{core} only the corona, *i.e.*, the part of the polymer network in direct contact with the interface is compressed. This means, that the microgels fractions situated in the

aqueous sub-phase should not be influenced by compression until a surface pressure of about 26 mN m^{-1} . Indeed the *in situ* NR measurements display a significant change in thickness only at $\Pi \geq 26 \text{ mN m}^{-1}$.

Yet, for the microgel height profiles at different compressions, *e.g.*, Fig. 5.6A, an increase of H_{core} is registered at surface pressures even before 26 mN m^{-1} . In Chapter 5, it is discussed that the lateral compression influences both the corona and the core of the microgels, although the response of the core is attenuated due to its higher cross-linker and polymer content. During the deposition and drying of the microgels, this compression becomes visible, consequently the lateral (D_{core}) becomes smaller and the vertical dimension (H_{core}) increases (Chapter 5, Fig. 5.6). Furthermore, it is speculated that in the hydrated state the flexibility of the pNIPAM polymer network can dissipate the applied stress. These NR results strengthen this hypothesis as no significant increase of the monolayer thickness is observed.

When the corona is fully compressed, *i.e.*, $\Pi \approx 26 \text{ mN m}^{-1}$, the fractions of the microgels situated in the aqueous phase start to interact. Similar to bulk, these parts repel each other due to steric and/or electrostatic interactions. As the microgels are fixed at the interface (the desorption energy exceeds $10^6 k_B T$ [69]) compression leads to an increase of polymer density and thickness. Both effects are observed with the NR measurements and captured by the model (Tab. 6.2). Compression from $\Pi = 20$ to 26 mN m^{-1} leads to a decrease of solvent inside the film by only 3 % (93 to 90 sol%), but an increase of the thickness of about 30 nm (1200 to 1500 Å). The work of further compression goes into the nucleation and growth of microgels in the second hexagonal phase [76] and Π increases slowly (Chapter 5). Between $\Pi = 26$ and 30 mN m^{-1} , the NR data do not show a significant increase in the microgel thickness. Unfortunately, measurements at surface pressures higher than 30 mN m^{-1} were not possible, because of the used Langmuir-Blodgett setup.

The results of the NR display an interesting trend which should be investigated by further measurements. The use of a different Langmuir trough setup, to reach higher compressions, and with deuterated pNIPAM microgels to increase the contrast at the air-ACMW interface appears reasonable. In addition, other techniques, such as super-resolved fluorescence microscopy, cryo-TEM, or computer simulations, should be used to investigate and verify the here discussed results.

Table 6.2: Results of the three-layer model fit of the reflectivity curves in Figure 6.2C for the pNIPAM microgels at different compression. d is the thickness, d_{total} the approximated total film thickness, σ the roughness, and σ_{bkg} the roughness with the background. For the first layer the scattering length density, $N_{b,fit}$, was a free parameter. For layers two and three the concentration of solvent, sol , was fitted.

Π	Layer 1			Layer 2			Layer 3			Background	
(mN m^{-1})	d (Å)	σ (Å)	$N_{b,fit}$ (10^{-6} Å^{-2})	d (Å)	σ (Å)	sol (%)	d (Å)	σ (Å)	sol (%)	σ_{bkg} (Å)	d_{total} (Å)
1	20	24	0.50	58	7	84	1087	50	94	241	(1695 ± 356)
10	19	27	0.39	58	10	82	1255	33	93	224	(1834 ± 275)
20	19	24	0.30	56	11	82	1212	26	93	225	(1785 ± 411)
26	20	25	0.80	29	13	79	1542	22	90	232	(2105 ± 505)
30	20	24	1.00	30	10	76	1493	26	90	220	(2031 ± 366)

6.3.3. Neutron Reflectivity of Ultra-Low Cross-Linked Microgels

Lastly, we discuss NR measurements of ultra-low cross-linked (ULC) microgels. These microgels are discussed in more detail in Chapter 8. ULC microgels are the microgels with the lowest number of cross-linking points that can be made by precipitation polymerization. For the synthesis of ULC microgels, no additional cross-linker, such as BIS, is used, and cross-linking of the polymer network takes only place via transfer reactions. [199, 217] This low number of cross-links results in an extreme softness, and they have a distinct polymer-to-particle duality. [30, 31] In contrast to regular cross-linked microgels, such as the pNIPAM microgel discussed before, they do not display a core-corona structure at interfaces. AFM images Fig. 8.6 of Chapter 8 show that they deform into disk-like objects or pancakes, have a height below 2 nm, and a large size polydispersity in the dried state. The same structure was found in the literature. [197, 199, 218] In contrast to regular microgels, which form colloidal crystals confined in 2D, ULC microgels form a uniform polymer film and the single microgels become indistinguishable in the dried state, just around the onset point of the compression isotherm. With increasing surface pressure, the ULC microgels start to become distinguishable again. Their compression isotherms display a single increase with the formation of a (pseudo-) plateau around $\Pi = 28 \text{ mN m}^{-1}$. Based on the isotherms and the AFM images of deposited monolayers surface pressures for the NR measurements were chosen to be $\Pi = 1, 20$, and 29 mN m^{-1} . Again, NR experiments were conducted only at the air- D_2O interface and at $T = 20^\circ\text{C}$.

The reflectivity curves are presented in Figure 6.2B and show the same general trend as the curves of the pNIPAM microgels: increasing the surface pressure decreases the reflectivity of the film. Fitting to the picture of the ULC microgels as a soft object with low density, the reflectivity of the bare air- D_2O interface and at of ULC microgels at $\Pi = 1 \text{ mN m}^{-1}$ are nearly identical. As displayed by gradient Langmuir-Blodgett type depositions, ULC microgels form a closed monolayer at $\Pi = 1 \text{ mN m}^{-1}$. We suggest that the agreement of the curves is not due to the formation of islands and sample inhomogeneity, but due to the nature of the ULC microgels themselves.

The reflectivity curves of the ULC microgels were fitted with a two-layer instead of the three-layer model; one of the solvent-polymer mix layers was removed, due to their pancake structure at the solid-air interface. A two-layer model is typically used to fit linear (pNIPAM) polymer at air-water interfaces. [170, 219] It has been reported that nanogel systems can not be fitted with this model [170], emphasizing the special structure of the ultra-low cross-linked microgels. The fits to the reflectivity curves of the model at different compressions are shown in Figure 6.2D and the parameters are summarized in Table 6.3. The corresponding SLD profiles are shown in Figure 6.2F.

The SLD profiles display a similar behavior as the pNIPAM microgels. A thin polymer layer ($\approx 15 \text{ \AA}$) is in direct contact with the interface, and the second layer composed of polymer and solvent extends into the sub-phase. For example, the second layer at 1 mN m^{-1} is composed of 99 % solvent. In contrast to the regular cross-linked microgels, ULC microgels display a significant increase in thickness in the first increase of the compression isotherm, *i.e.*, between 1 and 20 mN m^{-1} (Tab. 6.3). This difference has to be related to the different structures of the microgels. As discussed above, in the case of regular microgels the coronae have to be

overcome before the cores can be laterally compressed. The absence of the corona for the ULC microgels leads to lateral compression of the whole polymer network starting from the contact point, that is when the surface pressure deviates from 0 mN m^{-1} . Due to the softness of the network, the lateral compression does not fully translate into an increase of the vertical dimensions (700 to 840 \AA) but also into condensing the polymer network (99 to 95 *sol*%). Further compression above the onset point of the pseudo-plateau (Fig. 8.5A in Chapter 8) leads to an even stronger increase in both, the thickness and polymer content of the monolayer (Tab. 6.3, $\Pi = 20$ and 29 mN m^{-1}). The same effect was observed for the deposited ULC microgel monolayers. [30] Since the ULC microgels become indistinguishable at certain compressions, the root means square roughness, σ_{RMS} , of the deposited film was measured (Fig. 8.7B in Chapter 8), instead of analyzing height profiles. The monolayers display a modest increase of σ_{RMS} between 1 and 28 mN m^{-1} , but a strong increase above 28 mN m^{-1} , given complementary results to the data presented here.

To fully elucidate the out-of-plane structure of ULC microgels at liquid-liquid interface further NR measurements, not only at different surface pressures but also as a function of temperature are needed. Recently, deuterated ULC microgels were synthesized by Brugnoli *et al.* [217], allowing contrast variation experiments at air- D_2O and ACMW interfaces. With multiple contrasts a more sophisticated, model-based analysis of the reflectometry data becomes feasible.

Table 6.3: Results of the two-layer model fit of the reflectivity curves in Figure 6.2D for the ULC microgels at different compressions. d is the thickness, d_{total} the approximated total film thickness, σ the roughness, and σ_{bkg} the roughness with the background. For the first layer the scattering length density, $N_{b,fit}$, was a free parameter. For layer two the concentration of solvent, *sol*, was fitted.

Π	Layer 1			Layer 2		Background		
(mN m^{-1})	d (\AA)	σ (\AA)	$N_{b,fit}$ (10^{-6} \AA^{-2})	d (\AA)	σ (\AA)	<i>sol</i> (%)	σ_{bkg} (\AA)	d_{total} (\AA)
1	15	19	0.12	697	6	99	160	(1070 \pm 150)
20	15	19	0.35	841	7	95	190	(1274 \pm 175)
29	15	15	0.84	1290	9	90	270	(1875 \pm 300)

6.4. Conclusion

In this chapter, neutron reflectometry data of regular and ultra-low cross-linked pNIPAM microgel monolayers are presented. The experiments were conducted as a function of the sub-phase temperature and/or compression of the monolayers. A distinct influence on the neutron reflectivity is observed. The resulting reflectivity curves were analyzed by a model-based approach. In absence of a well-defined NR model for the microgel monolayers, a model proposed for nanogels [170] was used, which consists of three distinct regions: a dense polymer layer in direct contact with air and lower water content, followed by two fully hydrated layers with decreasing amount of polymer.

The temperature-dependent measurements at the air-D₂O and air-ACMW interface affirm ellipsometry measurements [29, 93] and computer simulations [29, 72, 79]. Parts of an adsorbed microgel, in direct contact with the interface, do not display any thermo-sensitivity. However, the majority of a microgel is situated in the aqueous phase. Upon an increase of temperature, these fractions still deswell and undergo a volume phase transition. A strong point of neutron reflectometry is that the phase contrast can be changed readily through isotropic substitution (contrast variation). Contrast variation was used to obtain reflectivity curves arising only from the microgel monolayer. The resulting SLD profiles (Fig. 6.1F) display good agreement with simulated out-of-plane density profiles [72].

A series of measurements at different surface pressure was realized to elucidate the influence of lateral compression on the vertical extension of microgel monolayers. These experiments were conducted for two different microgel systems, namely regular and ultra-low cross-linked microgels. Regular cross-linked microgels display a core-corona or fried-egg structure at interfaces, [70, 76, 78, 83, 89] while ULC microgels display a disk-like or pancake conformation [30, 197, 199]. Differences in the evolution of the out-of-plane extensions were observed and connected to the microgels' structural characteristics. For regular cross-linked microgels, the thin corona of adsorbed polymer must first be overcome, in contrast to ULC microgels where the absence of the corona leads to a direct increase in monolayer thickness.

It should be made clear that significant improvements in the experiments and data analysis are needed to fully experimentally elucidate the out-of-plane structure of microgels at liquid-liquid interfaces. Experiments could be conducted with deuterated pNIPAM with a higher contrast to increase the reflectivity of the microgel monolayers or other modeling methods, *e.g.*, the recursive Parratt-formalism [207], could be used to increase the agreement between model and NR data. Nevertheless, the data presented here are the first step and could be used, for example, to build more sophisticated models and stimulate further studies of microgels at air-water interfaces under compression with computer simulations.

7. Influence of the Architecture on the Interfacial Properties of Microgels: Transition from Linear Chains to Hollow Microgels

7.1. Introduction

At interfaces and in bulk, microgels are on the boundary between polymers and particles. Adsorbed to interfaces they have on one hand, strong polymer-like characteristics, showing barrier-free adsorption [69] and conformational (or structural) changes [68]. On the other hand, they have superior stability like Pickering emulsion, due to their strong anchoring to the interface, exceeding thermal energy by a factor of 10^6 . [69] Among others properties, this intriguing duality makes them interesting for both applications and fundamental research.

In solution not only the number of cross-linking points within the polymer network can be used to tune the polymer-to-particle duality of microgels to either side [4, 220] but also the architecture plays an pivotal roll for their softness and deformability. [165] When adsorbed to interfaces the cross-linking density has been shown to effect both the deformation and the phase behavior of the microgels. [30, 86, 89]

In this chapter, we investigate pNIPAM-polymer systems whose topologies or architecture are varied by the increase of cross-linking (or grafting) points and also by incorporation of a solvent filled cavity in the center of microgels. Starting from linear pNIPAM, through star-shaped, ultra-low cross-linked, regular cross-linked, to hollow microgels the interfacial behavior of pNIPAM-based systems is investigated with compression isotherms.

7.2. Experimental

7.2.1. Materials

For all compression isotherms, Milli-Q water (Merck KGaA, Germany) with a resistivity of 18,2 MOhm·cm was used as a sub-phase. Decane (Merck KGaA, Germany) was used as an oil-phase. The decane was filtered three times over basic aluminium oxide (90 standardized, Merck KGaA, Germany). The last filtration step was done immediately before the experiment. To facilitate spreading, propan-2-ol (Merck KGaA, Germany) was used. Pentaerythritol tetrakis(2-bromoisobutyrate) (4f-BiB) and copper(I) bromide were purchased from Sigma-Aldrich, USA. Methoxybenzene (anisole) and *N*-isopropylacrylamide (NIPAM) was purchased from Acros Organics, Belgium, *N,N'*-methylenebisacrylamide (BIS) from Alfa Aesar, USA, and chloroform (CHCl_3) from Merck KGaA, Germany. For the synthesis of linear and star-shaped pNIPAM polymers, NIPAM was recrystallized from n-hexan at 55 °C. If not stated otherwise chemicals were used as received.

7.2.2. Synthesis

Star-shaped pNIPAM polymers (pNIPAM-star) with four arms were synthesized by atom transfer radical polymerization (ATRP). [221, 222] Therefore, anisole was

destabilized over basic aluminum oxide, dried with molecular sieves (3 Å), and degassed under argon atmosphere. 0.001 g of the core (4f-BiB), 0.00156 g of CuBr, and 0.30874 g recrystallized NIPAM were weight-in and placed into a round bottom flask under argon atmosphere for at least 15 minutes. Subsequently, the destabilized anisole was added and the reaction mixture heated to 80 °C. After temperature equilibrium, the reaction was initiated by addition of 0.00251 g of the ATRP ligand Me₆TREN. The reaction was carried out for 24 h and then stopped by quenching with chloroform. The product was purified by column chromatography with basic aluminum oxide to remove the CuBr. The purified star-shaped pNIPAM polymer was analyzed with proton nuclear magnetic resonance spectroscopy, ¹H-NMR, and gel permeation chromatography, GPC. The weight averaged molecular weight of the star-shaped pNIPAM polymer is $M_w = 52650 \text{ g mol}^{-1}$. The polydispersity index is $\text{PDI} = M_w/M_n = 1.67$. The repeating number of monomer units per polymer is $n_M \approx 460$. This means, under the assumption that all arms have equal length, the repeating number per arm is 115 monomer units. The ¹H-NMR shows broad peaks at characteristic chemical shifts, δ_{NMR} , of pNIPAM at ¹H-NMR (400.13 MHz, CDCl₃) δ_{NMR} (ppm): 1.0-1.9 (N-CH-(CH₃)₂); 1.9-2.3 (2H, CH₂); 2.4-2.85 (m, 1H, CH₂-CH-CON); 3.8-4.1 (bs, 1H, NH).

The synthesis and characterization of star-shaped pNIPAM polymer were conducted by T. Kurtschildgen in the scope of his research thesis ‘Synthese von NIPAM-Sternpolymeren und deren Oberflächeneigenschaften’ supervised by Dr. A. A. Steinschulte and myself. Linear pNIPAM polymer (pNIPAM-lin) was synthesized by A. P. H. Gelissen and Dr. A. A. Steinschulte. [30] The same pNIPAM-based 5 mol% cross-linked Microgels, labeled pNIPAM microgels, as in Chapters 4, 5 and 6 were used. The synthesis protocol can be found in Ref. [29]. Ultra-low cross-linked (ULC) microgels and hollow (HS60 and HS105) microgels with different cavity sizes were synthesized and analyzed by M. Brugnoli. Hollow microgels were synthesized by precipitation polymerization of pNIPAM shells with 5 mol% BIS onto sacrificial silica cores with a hydrodynamic radius of ≈ 60 and 105 nm. The instructions and results can be found in Ref. [165]. Synthesis protocol of ULC microgels can be found in Chapter 8.

7.2.3. Compression Isotherms

Compression isotherms were measured at the decane-water interface for all samples. Experiments were conducted in a commercially available liquid-liquid Langmuir trough (KNIC220, KSV NIMA, Biolin Scientific Oy, Finland) and a customized liquid-liquid Langmuir-Blodgett trough (KSV NIMA, Biolin Scientific Oy, Finland) made of poly(oxymethylene) glycol with areas of ≈ 397 and 402 cm², respectively. The minimum area for both troughs was fixed to approximately 40 cm². Decane was chosen as oil-phase as pNIPAM is not soluble in alkane oils. [82, 83] For each measurement, the trough was carefully cleaned with Milli-Q water and a fresh decane-water interface was created. Both troughs were temperature controlled by an external water bath. The measurements were conducted at $(20.0 \pm 0.5) \text{ °C}$. All samples were in aqueous solutions and mixed with 20 vol-% of propan-2-ol to facilitate spreading and minimizing partial loss of the interfacial active species. The samples were applied with a glass syringe forming droplets above the air-decane interface and then gently touching the interface. The syringe was weighed before and after application to obtain the mass of added solution.

The surface pressure, Π , was probed with a highly porous platinum Wilhelmy plate (perimeter = 39.24 mm, KSV NIMA, Biolin Scientific Oy, Finland) to ensure optimal wetting with the aqueous sub-phase and thus a contact angle of 0° . The probe was attached to an electronic film balance (KSV NIMA, Biolin Scientific Oy, Finland) and placed parallel to the barriers. For all measurements, the barriers were closed with a velocity of 10 mm min^{-1} .

7.3. Results and Discussion

The linear and star-shaped pNIPAM-based polymer samples (pNIPAM-lin and pNIPAM-star) were characterized by $^1\text{H-NMR}$ and GPC; the parameters for M_w and n_M are summarized in Table 7.1. Microgel samples (ULC, pNIPAM, HS60, and HS105 microgels) were analyzed by multi-angle dynamic light scattering, DLS (for details see Chapter 4). Additionally, the molecular weight of ULC and pNIPAM microgels were computed by the combination of the viscosity of microgel suspensions and DLS. For this, the time of fall, t , of a fixed volume of differently concentrated suspensions through a thin capillary of an Ubbelohde viscosimeter was measured and the kinematic viscosity, η_k , calculated. With a known sample density that can be approximated with the one from water ($\rho_{\text{H}_2\text{O}}$), due to the low microgel concentrations, η_k can be converted into the viscosity, $\eta = \eta_k \rho_{\text{H}_2\text{O}}$. The relative viscosity ($\eta_r = \eta/\eta_{\text{solvent}}$) as a function of the suspension concentration is fitted with the Einstein-Batchelor equation [223] to obtain the conversion constant k . This constant is related to the volume of the swollen microgels ($V_{sw} = 4/3\pi R_{h,20}^3$) and the mass of the particle. [165, 220] The values for the hydrodynamic radius in the swollen state, $R_{h,20}^{\circ\text{C}}$, the viscosity averaged molecular weight, M_{vis} , the number of monomer units, n_M , and the concentration of cross-linker in the synthesis, c_{cl} , are summarized in Table 7.1.

Table 7.1: List of used samples and summary of the parameters in solution and at the interface. M_w , is the weight averaged molecular weight, M_{vis} , is the viscosity averaged molecular weight, n_M is the number of monomer units, $R_{h,20}^{\circ\text{C}}$ is the hydrodynamic radius from dynamic light scattering, c_{cl} is the concentration of cross-linker in the synthesis, $area/mass_{cp}$ is the $area/mass$ at the contact point, and ζ_{mass} is the mass fraction of adsorbed polymer.

Sample	M_w/M_{vis}	n_M	$R_{h,20}^{\circ\text{C}}$	c_{cl}	$area/mass_{cp}$	ζ_{mass}
	(g mol $^{-1}$)	(-)	(nm)	(mol%)	(cm 2 mg $^{-1}$)	(-)
pNIPAM-lin	113000	≈ 1000	-	-	$\approx 1.6 \cdot 10^4$	(0.90 \pm 0.12)
pNIPAM-star	52650	≈ 500	-	-	$\approx 1.5 \cdot 10^4$	(0.83 \pm 0.07)
ULC microgel	$(1.36 \pm 0.1) \cdot 10^8^*$	$\approx 1.2 \cdot 10^6^*$	(134 ± 1)	0	$\approx 6.7 \cdot 10^3$	(0.43 \pm 0.04)
pNIPAM microgel	$(4.6 \pm 0.4) \cdot 10^8^*$	$\approx 4.3 \cdot 10^6^*$	(153 ± 3)	5	$\approx 2.0 \cdot 10^3$	(0.13 \pm 0.08)
HS60 microgel	-	-	(206 ± 3)	5	$\approx 4.7 \cdot 10^3$	(0.34 \pm 0.09)
HS105 microgel	-	-	(230 ± 5)	5	$\approx 4.7 \cdot 10^3$	(0.34 \pm 0.07)

* values were determined by combination of dynamic light scattering and viscosimetry

The interfacial phase behavior of the different pNIPAM-based systems was investigated with compression isotherms at the oil-water interface at 20 °C. The Π -area isotherms were normalized to the amount of species added to the interface, $area/mass$, and are presented in Figure 7.1. The errors and uncertainties associated with the repetition of the measurements and the amount of added spreading solution are indicated as shaded areas in the appropriate color.

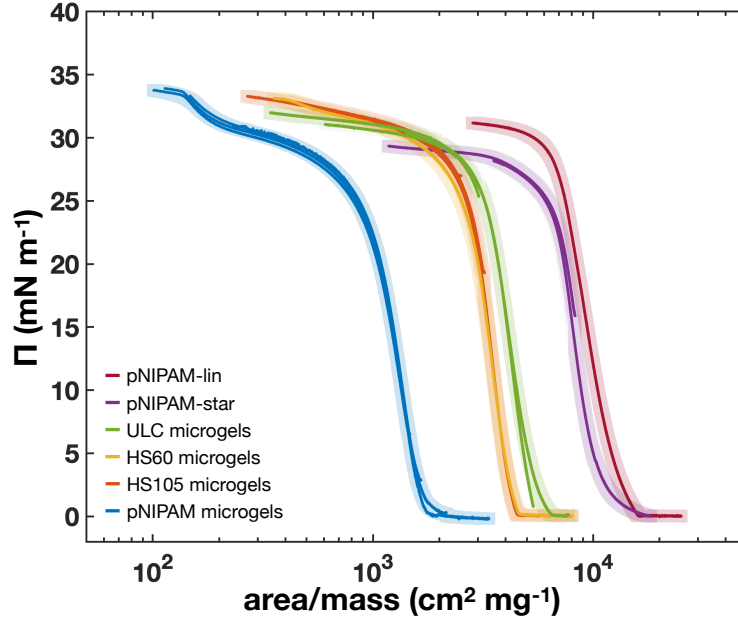


Figure 7.1: Π - $area/mass$ compression isotherms of all samples at $T = 20$ °C..

Most generally, the compression isotherms of the different samples display two trends: for the pNIPAM polymers, pNIPAM-lin and pNIPAM-star, and for the ULC and HS105 microgels a single increase is observed (Fig. 7.1, red, purple, green, and orange curves, respectively), which then passes over into a plateau at higher surface pressures. This course agrees with isotherms of linear pNIPAM homopolymers with different molecular weights and at different compression ratios found in the literature. [186, 187, 224] The pNIPAM (blue) and HS60 (golden) microgel isotherms in Figure 7.1 display two increases separated by a pseudo-plateau, representing the typical 2D phase behavior of microgel monolayers below the volume phase transition temperature (VPTT). [23, 76, 78, 84, 88] Besides this classification, all isotherms have similar slopes in the first increase.

For systems with more constraints, *e.g.*, grafting points or cross-links, the isotherms start to increase at lower $area/mass$. Starting from the pNIPAM polymers, pNIPAM-lin and pNIPAM-star, at the highest $area/mass$ values (Fig. 7.1, red and purple curves), a monotonic decrease towards lower $area/mass$ is observed for the ULC (green curves) to the pNIPAM microgels (blue curves). The introduction of a cavity into the polymeric network (HS60 and HS105 microgels) has the opposite effect; the onset point of the first increase is at larger $area/mass$ values (Figure 7.1 golden and orange curves) compared to the regular pNIPAM microgels with the same cross-linker amount and similar hydrodynamic radius.

The distinct onset points can be related to the architecture of the different species by calculating the mass fraction of adsorbed polymer, ζ_{mass} . Therefor, ζ_{mass} is de-

defined as the ratio of the amount of the polymer which contributes to the compression isotherms plotted in Π versus $area/mass$, $m_{adsorbed}$, and the initial amount of sample added to the interface, m_{added} , ($\zeta_{mass} = m_{adsorbed}/m_{added}$). Because $m_{adsorbed}$ is unknown, ζ_{mass} is calculated by collapsing the compression isotherms (Π versus $area/mass$) onto the isotherm of a reference sample, the linear pNIPAM, using $\zeta_{mass} = \sum (area/mass)_{sample} / \sum (area/mass)_{reference}$. Here, the isotherms display a similar slope in the first increase and all $area/mass$ values in the range of $\Pi = 5$ to 20 mN m^{-1} were used to compute ζ_{mass} .

Clearly, this calculation is dependent on the amount of pNIPAM segments of the linear polymer adsorbed to the interface. However, ζ_{mass} gives a measure of the strength of the samples' deformation in comparison to the most flexible state, the linear polymer. In other words, ζ_{mass} defines the amount of polymer in proximity to the interface, contributing to the compression isotherm in the Π versus $area/mass$ plot, and how much polymer is inaccessible, for example, because the network constrains further spreading. Besides making the polymer network more rigid, it has to be considered that ζ_{mass} decreases strongly with the size of the object because the volume is proportional to r^3 and the area to r^2 .

The isotherms collapsed onto the isotherm of pNIPAM-lin are shown in Figure 7.2A and the values of ζ_{mass} for the samples are presented in Figure 7.2B and summarized in the last column of Table 7.1. First, the influence of conformational constraints by the addition of grafting point or cross-links, pNIPAM-lin, pNIPAM-star, ULC, and pNIPAM microgels, are discussed. The conformation of polymers at liquid interfaces is related to the flexibility of the polymer and the interaction strength with the interface. [226] pNIPAM is a highly flexible polymer with a strong adsorption to the (decane-water) interface (gain of surface free energy $> k_b T$). [2, 227, 228] Typically, flexible polymers adsorb to an interface having trains (adsorbed segments), loops (segments in proximity to the interface between two trains) and tails (dangling chains into the aqueous phase). For non-linear polymers, such as star-shaped, brush-like, or branched polymers, the grafting points, *i.e.*, the center of the star, result in a decrease of conformational freedom at the interface. Adsorption of the same amount of polymer to the (same) interface would result in a significant decrease of entropy, consequently, less polymer is adsorbed. [229, 230] Here, for the used homopolymer stars with four arms, a slight decrease is visible to $\zeta_{mass} = 0.88$ compared to pNIPAM-lin (Fig. 7.2B, purple circle).

The introduction of cross-links, *i.e.*, the formation of a polymer network, leads to a further constraint of the stretching. Additionally to the decrease of conformational freedom, now due to the interconnected network, straitening or deformation of parts of the polymer are passed onto regions outside the interfacial plane. Indeed, one can see in Figure 7.2B that the ULC polymer displays a significantly smaller ζ_{mass} value of 0.43. Although the ULC microgels display the softest pNIPAM microgels which can be synthesized with precipitation polymerization [1, 199, 220] and thus one can assume that their polymer network has the lowest amount of cross-links, a large reduction of ζ_{mass} is observed.

Increasing the cross-linker content to 5 mol%, which is the pNIPAM microgel, leads to a reduction of the polymer adsorbed to the interface in relation to pNIPAM-lin to ≈ 0.13 . As already discussed in Chapters 4 - 5, these microgels, in fact, display a large fraction of polymer that is situated in the aqueous phase. In agreement with the literature [30, 86], ζ_{mass} shows that an increase of cross-linker in the synthesis

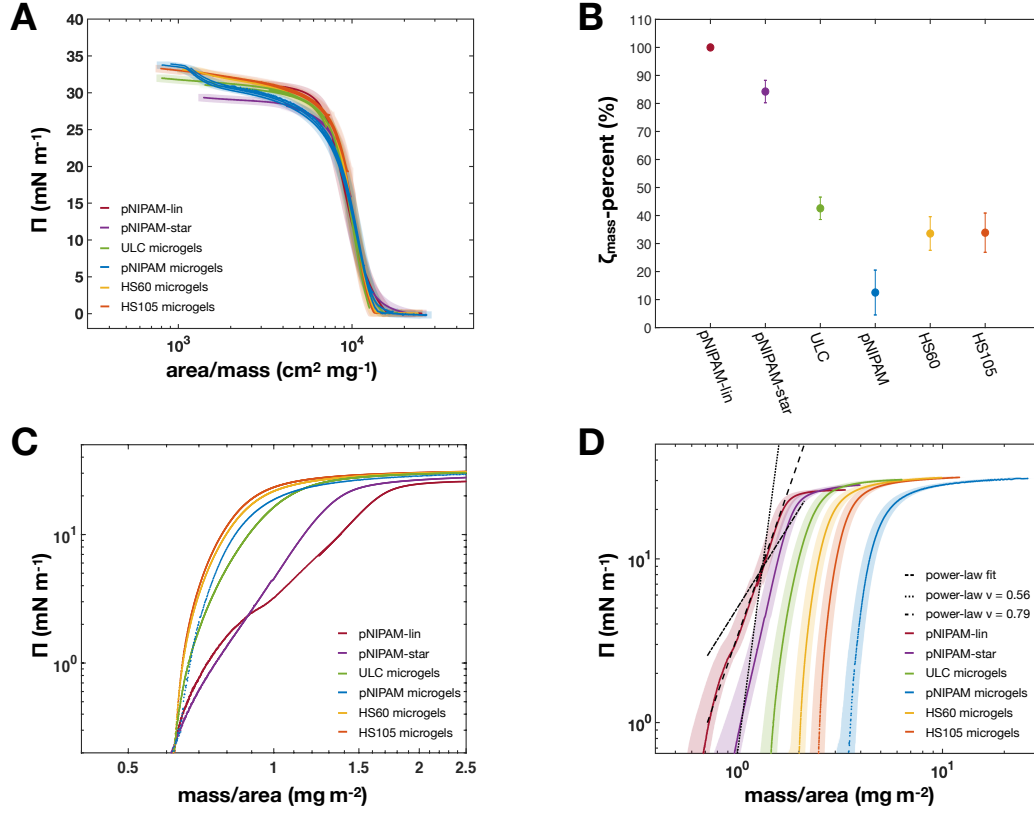


Figure 7.2: (A) Π -area/mass compression isotherms of all samples at $T = 20^\circ\text{C}$ shifted to the isotherm of pNIPAM-lin. (B) Calculated mass fraction of adsorbed polymer, ζ_{mass} , of the different species. (C) Π -mass/area (Γ) compression isotherms in log-log representation for all samples at $T = 20^\circ\text{C}$. The isotherms of pNIPAM-star, ULC, HS60, HS105, and pNIPAM microgels were shifted to the one of pNIPAM-lin using the ζ_{mass} values. No errors were plotted to make the curves more distinguishable. (D) Π -mass/area (Γ) compression isotherms in log-log representation for all samples at $T = 20^\circ\text{C}$. Isotherms of ULC, HS60, HS105, and pNIPAM microgels were shifted for better visibility. The black dashed line is a fit with a power-law dependence to the semidilute regime. The straight line in the log-log plot has a slope of $m_{2D} = 3.5960$ and $\nu = 0.65$. The black dotted and dash-dotted lines display experimental values of $\nu = 0.56$ and 0.79 . [225] For theta conditions, the straight is parallel to the y-axis.

leads to more rigid, less deformable (or soft) objects. The very same trend has already been reported for a series of differently cross-link pNIPAM microgels (from 1 to 10 mol%) at the air-water interface. [86] Furthermore, we can compare the results of our pNIPAM microgels to larger microgels with 5 mol% cross-linker ($R_h = 330$ nm). [89] These microgels display a area/mass value of ≈ 900 cm² mg⁻¹ at the contact point and thus a ζ_{mass} of roughly 0.06.

Interestingly, as aforementioned, the isotherms of ULC microgels do not show a second increase confined in 2D, although ULC microgels form stable polymer networks and display crystallization in three-dimensions [30]. The two-dimensional phase behavior and the influence of the extreme softness of the ULC microgels in solution and at the interface are discussed in more detail in Chapter 8.

The hollow microgels (HS60 and HS105) were synthesized by polymerization of a pNIPAM shell (with 5 mol% of BIS) around differently sized silica cores ($R_h \approx 60$ and 105 nm). In a second step, the silica core was removed by the means of sodium hydroxide (NaOH) solution. The dissolution of the cores leads to the formation of a solvent filled cavity. [165, 231] Figure 7.2B shows that this cavity leads to an increase of ζ_{mass} compared to the pNIPAM microgels, although the polymer network contains the same amount of cross-linker and the HS microgels have slightly larger hydrodynamic radii (Tab. 7.1). Thus, we can conclude that the substitution of a densely cross-linked core with the cavity increases the softness or deformability of microgels at interfaces. In fact, a similar correlation was observed for silica core-shell and hollow microgels, where the equivalent HS microgels display larger *area/particle*-value than the core-shell microgels. [88] On top of that, a recent study of the very same hollow-microgels (HS60) in overcrowded environment reports that the HS microgels display an even larger deswelling with an increase of the bulk concentration compared to ULC microgels. [165]

The behavior of the different samples within the first increase, sometimes referred to as the semidilute regime for linear polymers at interfaces, can be compared in more detail when plotted in a log-log representation (Figures 7.2C and D). In Figure 7.2C, the isotherms are shown as surface pressure versus the *mass/area* or surface coverage, Γ . The isotherms of the pNIPAM-star, ULC, HS60, HS105, and pNIPAM microgels were shifted to the one of pNIPAM-lin using the ζ_{mass} values depicted in Figure 7.2B. The curves are in agreement at low compressions ($\Pi < 0.7 \text{ mN m}^{-1}$), implying that the first interaction of all samples is the same. In Figure 4.3D of Chapter 4, it is even shown that even isotherms of microgels above their VPTT coincidence in this surface pressure range with the one of linear pNIPAM. At higher compressions ($\Pi > 1 \text{ mN m}^{-1}$), the isotherms deviate, but strikingly, all microgels samples show similar behavior. Furthermore, the isotherms of pNIPAM-lin, Figure 7.2C, red curves, display a linear course in the semidilute regime, typical for linear polymers.

In three dimensions, the scaling theories express that all physical properties of polymer solutions have power-law dependencies. [232, 233] For example, the radius of gyration, R_g , of an isolated chain can be written as $R_g \propto N^\nu$, where N is the number of bond segments and ν the critical exponent describing the solvent quality. This theory can be expended into the two-dimensional case of polymers in the semidiluted state. [225, 234] As a result, a power-law dependence, relating Γ and the surface pressure ($\Pi \propto \Gamma^{m_{2D}}$), is obtained. Here, the exponent m_{2D} gives the critical exponent, ν , by $m_{2D} = 2\nu/(2\nu-1)$. [225] The value of the critical exponent displays the quality of the interface as a solvent for the polymer. For theta conditions, ν is predicted to be 1/2, and for a good solvent $\nu \approx 3/4$. [225, 233, 235]

The linear increase in the log-log representation of pNIPAM-lin was fitted with the power-law, Figure 7.2D, red curve and black dashed line, respectively. From the slope in the narrow region between 2.5 to 17 mN m^{-1} and 1 to 1.6 mg m^{-2} , it was determined that ν has a value of 0.65 ± 0.04 , taking the error of the isotherms into account. This estimate of the 2D Flory exponent is in between the value for polymers in good and theta solvent conditions at interfaces. [225, 234] The literature reports experimental data of poly(butyl acrylate) [225], poly(methyl methacrylate) [234], and poly(vinyl acetate) [225] with ν values of 0.56, 0.57, and 0.79, respectively. For comparison, straights with the corresponding slopes for $\nu = 0.56$ and 0.79 are

plotted in Figure 7.2D, dotted and dash-dotted black lines. Although the liquid interface is a solvent with distinct different quality for these polymers, they are all insoluble in water. However, this could also be an explanation for the 2D Flory exponent of pNIPAM in between the theta and good solvent: Upon compression in the semidilute regime polymer segments of the linear pNIPAM might be easily pushed into the aqueous sub-phase. [187] As a consequence, the slope, *i.e.*, ν , is underestimated. [225]

In Fig. 7.2D, one can see that all other Π -*mass/area* isotherms are different and do not follow this power-law dependence in the semidilute regime. While for the pNIPAM-stars a linear increase can still be conjectured, none of the microgel samples' isotherms follow the scaling law. Please note again that the curves of ULC, HS60, HS105, and pNIPAM microgels (Fig. 7.2D, green, golden, orange, and blue curves) had to be shifted along the x-axis to a lower surface coverage for better visibility. Consequently, we learn from Figures 7.2C and D that although the isotherms of ULC and HS105 microgels (Fig. 7.1, green and orange curves) display only a single increase and that although the initial slope of all isotherms (Fig. 7.2A) looks very similar, when observed in more detail, their compressibility is different from linear pNIPAM. This difference has to be related to the stronger constraints of the network and the resulting larger amount of polymer within the aqueous side of the interface.

Lastly, we explore the difference in the compression isotherms for the HS60 and HS105 microgels more. The golden and orange curves in Figure 7.1 show that hollow microgels with a small cavity (and thicker polymer shell) have two increases and hollow microgels with a larger cavity (and thinner polymer shell) have a single increase. Thus, gradient Langmuir-Blodgett trough depositions were conducted (for details regarding the procedure see Chapter 4). In Figure 7.3A, C, and D, atomic force microscopy images of the deposited microgels in the dried state are shown. The HS60 microgels exhibit a circular shape with a flat center of constant height. Height profiles through the apices of the microgels in Figure 7.3A were extracted and averaged. The averaged profile, presented in Figure 7.3B, reveals that the HS60 microgels have a dent in their center, in contrast to regular microgels which display a bell-like shape (Chapter 5). Logically, this dent has to be related to the structure of the hollow microgels with a solvent filled cavity in the center: upon drying the solvent is removed and the polymer collapses. As there is no polymer in the center, it displays a lower height. Still, these microgels describe a core-corona structure.

In contrast, depositions of HS105 microgels at low compression (Fig. 7.3C, $\Pi = 5 \text{ mN m}^{-1}$) display irregularly shaped structures and (polymer) fragments of different heights. Upon close inspection, one can see that some of these fragments are connected forming larger regions that resemble popped balloons. The orange edging in the Figure 7.3C enframes a single connected region. At $\Pi = 30 \text{ mN m}^{-1}$ (Fig. 7.3D), nearly circular objects are observed. Therefore, it appears that the region in the AFM image at lower Π (Fig. 7.3C) are indeed the HS105 microgels, which under compression regain their shape. Whether this peculiar structure is a result of the strong adsorption of the network to the interface (chain scission [236]), a consequence of the deposition and drying, or if the structural integrity of the sample was lost before the Langmuir trough experiment is beyond the scope of this study. Nevertheless, their monolayer resembles much more a polymer layer, explaining the absence of the second increase in the compression isotherm.

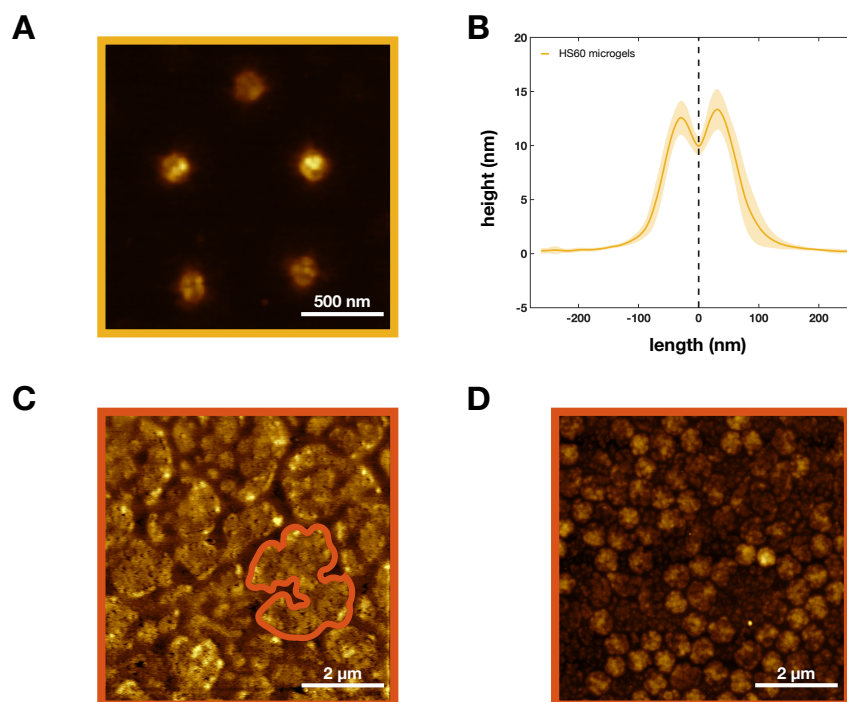


Figure 7.3: Atomic force micrographs and height profile of hollow microgels at $T = 20\text{ }^{\circ}\text{C}$. (A) AFM image of HS60 at approximately 20 mN m^{-1} . (B) Corresponding height profiles of the AFM image in A of HS60 microgels. The profile is averaged from 17 profiles through the apices of the microgels and at different angles with respect to the fast scan direction. (C) AFM image of HS105 at approximately 5 mN m^{-1} . A single connected fragment is enframed by an orange edging. (D) AFM image of HS105 at approximately 30 mN m^{-1} .

7.4. Conclusion

In this chapter, the effect of softness and deformability of different pNIPAM-based samples at decane-water interfaces was investigated using Langmuir trough experiments. Π -area compression isotherms normalized to the added amount of surface-active species display two general trends: for the pNIPAM polymers the isotherms display the expected course of polymers [186, 187, 224] at interfaces with a single increase. Surprisingly, the curves of ultra-low cross-linked and hollow microgels with a large cavity also have this trend. In contrast, the isotherms of regular microgel and hollow microgel with a small cavity in Figure 7.1 display two increases separated by a pseudo-plateau, representing the typical 2D phase behavior of microgel monolayers below the VPTT. [23, 76, 78, 84, 88]

Additionally, we introduced the mass fraction of adsorbed polymer, ζ_{mass} , which gives a measure of the polymer contributing to the Π -area/mass isotherm in relation to the most flexible architecture, a linear polymer. This parameter allows a comparison of samples with different numbers of grafting or cross-linking points and architectures.

Measurements of star-shaped polymers, ultra-low cross-linked, and regular cross-linked microgels display that increasing the number of cross-links leads to a significantly lower amount of polymer in the proximity of the interface (lower ζ_{mass}). As

already reported in the literature [86], we conclude that the increase of cross-linker leads to a reduction of deformability or softness not only in solutions but also at oil-water interfaces. Accompanied by the reduction of their deformability, the course of their compression isotherms changes from a single to two increases. The case of ultra-low cross-linked microgels, which show an eminent polymer-to-particle duality, is elucidated in more detail in Chapter 8. In solution, it has been shown that the architecture, *e.g.*, the introduction of a solvent filled cavity has an enormous effect on the deswelling behavior due to temperature and overcrowding. [165, 231] Here it is shown that this architectural change plays also an important role in their softness and deformability at oil-water interfaces. We investigated regular and hollow (HS) microgels and observed a strong increase of ζ_{mass} for the latter. This means that due to the presence of a solvent filled cavity, the HS microgels become softer and can deform stronger upon adsorption.

We observed that the compression isotherms of hollow microgels have two increases for the smaller cavity size (radius ≈ 60 nm) and a single increase for the larger cavity size (radius ≈ 105 nm). To elucidate this difference more, deposition experiments were conducted. For HS microgels with a small cavity, the averaged height profiles describe a “w” shape with lower heights in the center of the microgel. Interestingly, we observed that hollow microgels with large cavities do not keep their structural integrity and they resemble popped balloons. It is not clear whether this happens due to the strong adsorption to the interface, the deposition, or if the structure was already compromised before the interfacial experiments.

8. Exploring the Colloid-to-Polymer Transition for Ultra-Low Crosslinked Microgels from Three and Two Dimensions¹

8.1. Introduction

Aqueous solutions of flexible polymers and suspensions of colloids are two of the most important classes of materials in soft matter. Flexible polymers, which bend at length scales longer than their Kuhn length, have high degrees of entanglement and interpenetration, typical for linear polymers. [237] In contrast, colloids maintain their individuality as particles and show phase transitions between disordered and crystalline arrangements both in two and three dimensions. [238]

Microgels have properties of both flexible polymers and solid colloids particles. As a polymer, their swelling is affected by the solvent quality, and microgels can present volume phase transitions, *i.e.*, a microgel-to-colloid transition, depending on external stimuli. [68, 239] Furthermore, in the swollen state, they are soft and can be compressed or interpenetrate once in concentrated suspensions. [164, 165, 240] Nevertheless, their flow properties and phase behavior are the same as those of colloids interacting *via* soft potentials. This is due to the less cross-linked fuzzy periphery of microgels, which is composed of dangling polymeric chains. In addition, microgels are highly interfacially active and can be employed, similarly to solid particles, as emulsifiers. [60–64]

Due to the predominant colloidal-behavior, poly(*N*-isopropylacrylamide)-based (pNIPAM) microgels have been widely used as a model system for soft spheres to investigate fundamental questions related to strong and fragile glass formers [3, 4], to melting-freezing [9, 10, 195] and to solid-solid phase transitions, both in two- (“2D”) [76, 241, 242] and three dimensions (“3D”) [7, 8].

In this chapter, the polymer-to-particle transition is addressed and the question of whether microgels can be prepared with a predominant flexible-polymer-nature is studied. Obviously, the amount of cross-linker within the polymer network is responsible for the individual shape and swelling of the microgels. Higher incorporation of cross-linker produces stiffer microgels that behave more similar to hard incompressible colloids. [9] In contrast, therefore, decreasing the amount of cross-linker as much as possible will lead to microgels where the colloidal-nature should be minimized. Here, we use ultra-low cross-linked pNIPAM microgels. They represent the softest microgels that can be obtained by precipitation polymerization. Although no cross-linking agents are present during the synthesis, the formation of a polymeric network is still promoted *via* transfer reactions, leading to extremely soft micro- and nanogels. [197, 199, 243]

We investigate ultra-low cross-linked (ULC) microgels both in bulk aqueous solution as well as at fluid interfaces. Our results show that while the ULC microgels present a colloidal-like behavior in three dimensions, their nature changes once they are confined at interfaces. In two dimensions, the interplay between the extreme

¹This chapter has been adapted and reprinted in part with permission from Scotti, A., Bochenek, S., *et al.*, *Nature Communications*, **2019**, 10, 1418. Copyright 2019 Nature Research.

softness of the polymer network and the action of surface tension leads the ULC microgels to show properties typical of flexible polymers within a certain concentration range, as it can be seen in their compression isotherms or by the observed microstructure of deposited monolayers.

8.2. Experimental

8.2.1. Materials

N-isopropylacrylamide (NIPAM) (Acros Organics, Belgium), *N,N'*-methylenebisacrylamide (BIS) (Alfa Aesar, USA), sodium dodecyl sulfate (SDS) (Merck KGaA, Germany), and potassium peroxydisulfate (KPS) (Acros Organics, Belgium) were used as received.

For all interface experiments, ultrapure water (Astacus², membraPure GmbH, Germany) with a resistivity of 18,2 MΩ·cm was used as sub-phase. Decane (Merck KGaA, Germany) was used as oil-phase. The decane was filtered three times over basic aluminium oxide (90 standardized, Merck KGaA, Germany). The last filtration step was done just before the experiment. To facilitate spreading, propan-2-ol (Merck KGaA, Germany) was used.

8.2.2. Synthesis

Ultra-low cross-linked microgels (ULC microgels) were synthesized by precipitation polymerization according to Ref. [199]. Briefly, 3.9606 g NIPAM and 0.1802 g SDS were dissolved in 495 mL filtered (0.2 μm regenerate cellulose, RC, membrane filter) double-distilled water. In contrast to Ref. [199], SDS was used to have better control over the size polydispersity of the particles [244]. The monomer solution was purged with nitrogen under stirring at 100 rpm and heated to 70 °C. Separately, 0.2108 g of KPS in 5 mL filtered double-distilled water was degassed for one hour. The polymerization was initiated by transferring the KPS solution using a nitrogen-washed syringe and needle into the monomer solution. The reaction was left to proceed for 4 hours under constant nitrogen flow at 70 °C and 100 rpm. The resulting microgels were purified by threefold ultra-centrifugation at 50000 rpm and subsequent redispersion in freshwater. During the synthesis, many polymeric chains are trapped within the collapsed precursor particles but they are not linked to the polymeric network. These chains are then washed out of the particles during the purification process. Lyophilization was applied for storage.

The yield of the precipitation polymerization for ULC microgel formation is only ≈ 10 % while for regular cross-linked microgels is ≈ 90 %. This means that many chains containing initiator fragments carrying charges are not incorporated into the ULC microgels. In other words, only a few of the formed chains become part of the polymeric network of the ULC microgels. Therefore, those microgels are expected to incorporate a negligible amount of charges that will not produce significant effects on the interaction potential between the ULC microgels.

Ultra-low cross-linked were synthesized by M. Brugnoli. Linear pNIPAM polymer was synthesized by A. P. H. Gelissen and Dr. A. A. Steinschulte. [30] Regular 5 mol% cross-linked pNIPAM microgels, labeled pNIPAM microgels, are the same microgels used in Chapters 4, 5, 6 and 7. Details about the synthesis can be found in Chapter 4.

8.2.3. Capillary Viscosimetry

To obtain the viscosity, the average time of fall, t , of a constant volume of microgel suspension through a thin capillary of an Ubbelohde tube viscometer immersed in a water bath at a fixed temperature of $(20.0 \pm 0.1)^\circ\text{C}$ was measured. The average fall times of the suspensions at different concentrations are linked to the kinematic viscosities, η_k , by a constant, C , that only depends on the geometry of the capillary: $\eta_k = Ct$; in our experiments, $C = 3.156 \cdot 10^{-9} \text{ m}^2 \text{ s}^{-2}$. By knowing the sample density, that can be approximated with that of water ($\rho_{\text{H}_2\text{O}}$) due to the low concentration of microgels in all the measured suspensions, the viscosity of the microgel suspensions as a function of microgel concentration can be computed, $\eta = \eta_k \rho_{\text{H}_2\text{O}}$.

8.2.4. Rheology

Oscillatory rheology has been used to probe the flow properties of the suspensions. A Kinexus Pro Rheometer (Malvern Panalytical Ltd) with a cone-plate geometry (40 mm, 1.0°) was used. Before each frequency sweep, amplitude sweeps were performed to verify that the suspensions were in the linear viscoelastic regime at the frequencies $\omega = 0.1, 1$, and 10 rad s^{-1} and in the range of $\gamma_{\text{strain}\%} = 0.5\text{-}30\%$. At the end of the oscillatory experiments, a final amplitude sweep at $\omega = 1 \text{ rad s}^{-1}$ was repeated to check that the system was still in the linear viscoelastic regime.

8.2.5. Langmuir-Blodgett Trough

The mechanical properties of two-dimensional monolayers of microgels and linear pNIPAM at the decane-water interface were probed using a Langmuir-Blodgett trough with customized dipping well (KSV NIMA, Biolin Scientific Oy). The same strategy to synchronize the continuous compression of the monolayer and the deposition of the microgel arrangements to a solid substrate, reported in Chapter 4, was used. In short, two parallel-moving barriers were closed ($v = 6 \text{ mm/min}$) to increase the concentration of microgels at the interface by decreasing the available area. To probe the surface pressure a platinum Wilhelmy plate parallel to the barriers attached to an electronic film balance was used. At the same time, a cleaned piece of a silicon wafer was lifted up in between the barriers at an angle of $\approx 20^\circ$ with respect to the interface. Thus, the monolayers were immobilized in a Langmuir-Blodgett-type deposition on silicon wafers and subsequently investigated *ex situ* by atomic force microscopy. Compression isotherms and depositions were conducted at $(20.0 \pm 0.5)^\circ\text{C}$. More details can be found in Chapter 4

8.2.6. Atomic Force Microscopy

AFM measurements were performed using a Dimension Icon with a closed-loop (Veeco Instruments Inc., software: Nanoscope 8.15, Bruker Corporation). The measurements of the microgels in the dried state, at the solid-air interface, were recorded in tapping mode with TESPA tips with a resonance frequency of 320 kHz , a nominal spring constant of 42 N m^{-1} of the cantilever and a nominal tip radius of $\approx 8 \text{ nm}$ (Bruker Corporation). Images of $7.5 \times 7.5 \mu\text{m}$ (512×512 pixels) in a straight line along the gradient direction on the substrate every $250, 500$ or $1000 \mu\text{m}$ were

captured. For each line, an image at the position of highest compression was taken to obtain the position of the fixed point.

8.2.7. Image Analysis

Obtained AFM images were processed with the analysis software *Gwyddion* 2.48. The images were leveled to remove the tilt, the mean values were fixed to zero height and converted to grayscale. The AFM micrographs of ULC and pNIPAM microgels were analyzed with the custom-written Matlab explained in Chapter 4. An averaged height profile of the ULC microgels were determined, in contrast to Chapter 5 profiles, from a single microgel through the apex and at different angles with respect to the fast scan direction (every 10 °). This was done because ULC microgels show large size polydispersity ($\leq 20\%$). The analysis of the ULC microgel monolayers was extended by determining the roughness of the interface, γ_{RMS} . γ_{RMS} was computed as the second moment of the height distribution, μ_2 , over one AFM image using the free software *Gwyddion* according to the following equation [245]: $\gamma_{RMS} = \mu_2^{\frac{1}{2}}$. Given errors are the root-mean-square deviation.

8.3. Results

8.3.1. Characterization of Microgels in Solution

For regular microgels, the addition of cross-linker, e.g. *N,N'*methylenebisacrylamide (BIS), has two important consequences: first, it enforces the stiffness of the network; second, it leads to a characteristic fuzzy sphere architecture. This is due to the fact that the cross-linker has a faster reaction rate than the monomer leading to the formation of a more cross-linked core with higher polymer density, surrounded by a fuzzy corona with fewer cross-links and a lower polymer density [49, 158]. As a consequence of this architecture, the scattered intensity measured in a small-angle neutron (or X-ray) scattering (SANS) experiment of diluted suspensions of microgels, presents typical oscillations. This profile can be fitted using a model that accounts for a denser core with radius R_c , surrounded by a fuzzy shell of length $2\sigma_s$, with decreasing polymer content [49, 240]. The smaller is the core, the more inhomogeneous is the polymer distribution within the microgel. This form factor is similar to that of hard colloids, except for the less defined periphery. In contrast, it is significantly different with respect to the form factor of flexible polymers [246, 247] that does not show any oscillation, but after a plateau for low scattering vector, q , has a monotonic decrease.

Figure 8.1A shows the SANS intensity plotted versus q obtained by measuring a diluted suspension of ULC microgels in heavy water below and above their volume phase transition temperature (VPTT), at $T = (20.0 \pm 0.5)$ and (40.0 ± 0.5) °C, respectively. The total size of the microgel is $R = R_c + 2\sigma_s$. The structure parameters are obtained from the fits, and the radial distributions are shown in Figure 8.1B.

The microgels have a total radius in the swollen state (Figure 8.1A, blue circles) of (126 ± 1) nm with $R_c = (96.1 \pm 0.5)$ nm and $2\sigma_s = (29.8 \pm 0.3)$ nm. The fuzziness of the shell of the ULC microgels is less pronounced as compared to regular cross-linked microgels (Chapter 4). Still, the ULC microgels have the typical fuzzy sphere architecture. Thus, the polymer distribution within ULC microgels is more

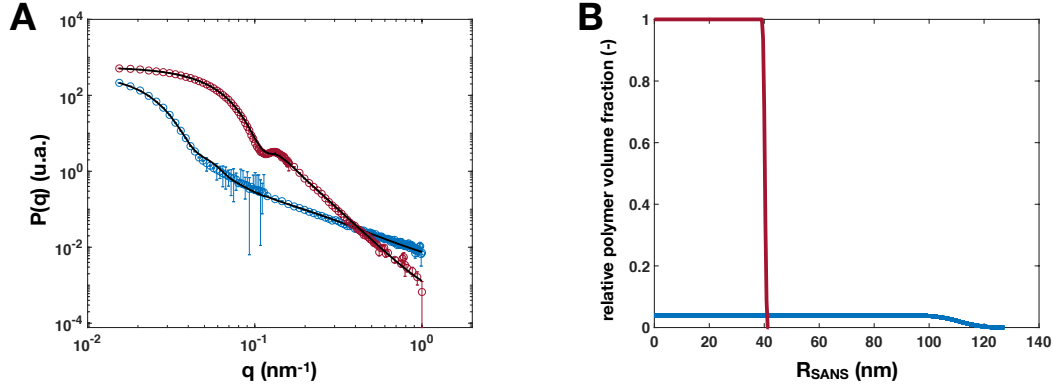


Figure 8.1: (A) Small-angle neutron scattering form factor, $P(q)$, versus scattering vector, q , for ultra-low cross-linked microgels in dilute suspensions of D_2O at $(20.0 \pm 0.5)^\circ\text{C}$, blue circles, and $(40.0 \pm 0.5)^\circ\text{C}$, red circles. The solid black lines are fits with the fuzzy sphere model [49]. (B) Relative polymer volume fraction versus radius obtained from the data fit for ultra-low cross-linked microgels at $(20.0 \pm 0.5)^\circ\text{C}$, blue solid line, and $(40.0 \pm 0.5)^\circ\text{C}$, red solid line.

homogeneous than for microgels synthesized with additional cross-linker. The polydispersity is $(11.3 \pm 0.7)\%$. The ULC microgels collapse to $(41 \pm 1) \text{ nm}$ and the fit shows that the external fuzziness disappears $((2 \pm 1) \text{ nm})$ once the temperature is above the VPTT of pNIPAM. Independent of the temperature, the fuzzy sphere model was used to fit the form factor above the VPTT to not impose any *a priori* knowledge to the data.

Temperature-dependent size measurements of the ULC microgels were performed with dynamic light scattering, DLS. From the intensity autocorrelation functions, the average decay rate, Γ , was obtained with second cumulant analysis. [248] The decay rates depend on the scattering vector *via* the average diffusion coefficient D_0 : $\Gamma = D_0 q^2$. The average diffusion coefficient was obtained by plotting Γ versus q^2 and fitting the data with linear regression. [249] Finally, the Stokes-Einstein relation was used to obtain the hydrodynamic radius, R_h . R_h as a function of the temperature is shown Figure 8.2, green squares, in comparison with the pNIPAM microgel (blue squares).

Microgels with different sizes can be compared by their swelling ratio between the hydrodynamic radius, R_h , and the radius at 20°C , R_{swollen} . This ratio is plotted in Figure 8.2B for the ULC and the pNIPAM microgels, green and blue squares, respectively. For both microgels, the volume phase transition temperature (VPTT) is at $\approx 32^\circ\text{C}$. The collapsed size of the pNIPAM microgels is about 55 % of the swollen radius $(153.2 \pm 0.6) \text{ nm}$. In contrast, the ULC microgels deswell to $(44.8 \pm 0.2) \text{ nm}$; $\approx 34\%$ of their initial size, $(134 \pm 1) \text{ nm}$.

Estimating the number of cross-links within the polymeric network is difficult and distinguishing between cross-links due to self-cross-linking of pNIPAM promoted by KPS and cross-links induced by BIS is impossible. However, the ratio of the hydrodynamic radii below and above the VPTT ($R_h(20^\circ\text{C})/R_h(40^\circ\text{C})$) can be a measure of the softness of the polymeric network. Recently, Lopez and Richtering have collected literature data and found a strong correlation between the effective amount of cross-linker incorporated within a microgel, f , and the hydro-

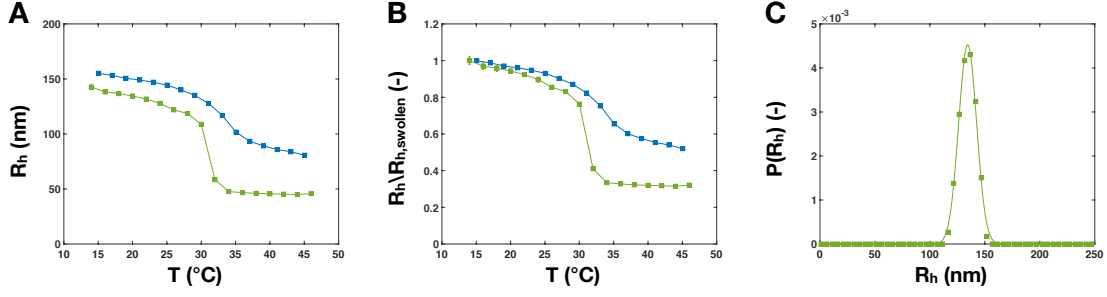


Figure 8.2: (A) DLS data of ULC and pNIPAM microgels. R_h versus temperature showing the volume phase transition temperature expected for pNIPAM polymers. (B) Swelling ratio, defined as the ratio between the hydrodynamic radius R_h and the hydrodynamic radius at (20.0 ± 0.1) °C, $R_{Swollen}$, versus the temperature for ultra-low cross-linked and pNIPAM microgels, green and blue squares, respectively. (C) Contin analysis (green solid line) of the DLS data (green solid squares) of ULC microgels at 20 °C.

dynamic radii below and above the VPTT [163]. They obtained the relationship $R_h(20^\circ\text{C})/R_h(40^\circ\text{C}) = 0.966 \cdot f^{-0.2}$ [163] for f . From the DLS data, we obtained for the ULC microgels $f = 0.35$ %. The literature data reported in Ref. [163] have always values larger than $f = 0.35$ %. This confirms that the ULC microgels have the polymeric network that contains the lowest amount of cross-linker.

Contin analysis [250, 251] implemented with L-curve criteria [252] has been performed to directly obtain the size distribution of the suspensions and evaluate the size polydispersity, p . Figure 8.2C displays an example of the Contin analysis for the ULC microgels at 20 °C. Sizes and size polydispersities obtained by SANS agree with the results of the analysis of the DLS data. The values for diluted samples at $T = (20.0 \pm 0.1)$ °C are shown in Table 8.1.

Table 8.1: Radii (R_h or R_{SANS}) and size polydispersities (p or σ_p) for the samples as obtained from DLS (second and third column) and SANS data (fourth and fifth column). Also, the conversion constants, k , from viscosimetry are shown. All the values refer to dilute samples at (20.0 ± 0.1) °C.

Sample	DLS		SANS		Viscosimetry
	R_h (nm)	p (%)	R_{SANS} (nm)	σ_p (%)	k (-)
ULC microgels	(134 ± 1)	(10 ± 1)	(126 ± 1)	(11.3 ± 0.7)	(44.7 ± 0.1)
pNIPAM microgels	(153 ± 3)	(9 ± 3)	(150 ± 2)	(7 ± 1)	(18 ± 1)

8.3.2. Bulk Phase Behavior

A marked difference between flexible polymers and colloidal suspensions is that the former shows a pronounced entanglement and interpenetration with increasing concentrations. In contrast, colloids reveal a liquid-to-solid transition depending on the concentration, which is connected to a transition from a disordered fluid to a

colloidal crystal with a coexistence region in between liquid and fully crystalline samples. Similarly, microgels can form crystals but at higher concentrations with respect to rigid colloids due to their soft interparticle potential. [9, 195] A shift of the transition boundaries is observed for other colloids interacting with soft potentials, e.g. slightly charged hard spheres. [253]

Bulk suspensions of the ULC microgels were investigated to understand if their extreme softness makes their phase behavior different with respect to that of the colloids. The phase behavior of microgels is a function of the generalized volume fraction, $\zeta = (NV_{\text{Swollen}})/V_{\text{tot}}$ where N is the number of microgels in the sample and V_{Swollen} and V_{tot} are the volume of the microgel in the swollen state and the total volume of the sample, respectively. In case of rigid colloids, ζ equals the volume fraction ϕ ; however, for soft microgels ζ can reach values well above 0.74 reflecting deformation [173], deswelling [195, 240] or interpenetration [164]. The generalized volume fraction, ζ , is proportional to the mass concentration of polymer within the suspension, $c_{\text{wt}\%}$, via a conversion constant, k : $\zeta = kc_{\text{wt}\%}$. k is obtained using viscosimetry [9], by measuring the average time of fall of a constant volume of microgel suspension through a thin capillary of an Ubbelohde tube viscometer at a fixed temperature. The relative viscosity ($\eta_r = \eta/\eta_{\text{solvent}}$) as a function of the sample concentration is fitted with the Einstein-Batchelor equation [223] to obtain the conversion constant k . The experimental data with solid lines representing $\eta_r = 1 + 2.5\zeta + 5.9\zeta^2 = 1 + 2.5kc_{\text{wt}\%} + 5.9(kc_{\text{wt}\%})^2$ for the ULC and pNIPAM microgels are presented in Figure 8.3A and B, respectively. The conversion constants are given in Table 8.1.

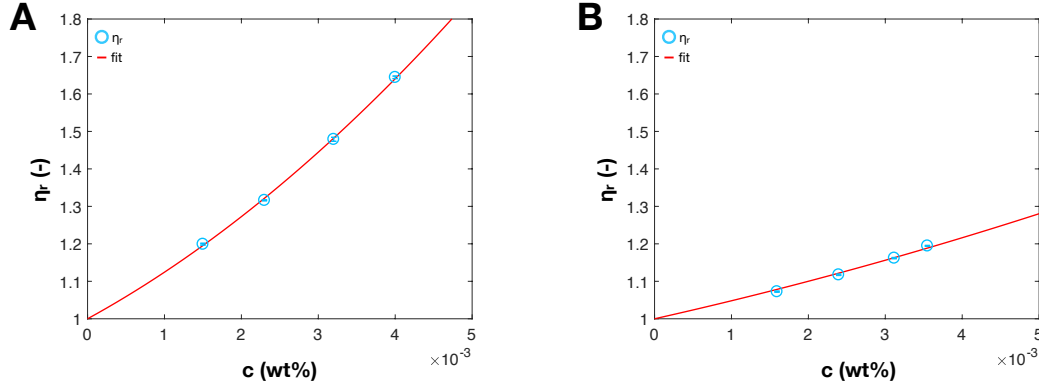


Figure 8.3: Relative viscosity, η_r , versus sample concentration, $c_{\text{wt}\%}$, (cyan circles) with fit of the Einstein-Batchelor equation (red solid lines). (A) ultra-low cross-linked microgels. (B) regular 5 mol% cross-linked microgels (pNIPAM microgels).

With the obtained conversion constant a series of ULC microgel samples, covering a ζ -range between 0.50 ± 0.01 and 3.02 ± 0.07 , was made and stored at $T = 20.0 \pm 0.5$ °C. The freezing point, *i.e.*, the onset of the coexistence of liquid and crystals, was found at $\zeta_f = 0.80 \pm 0.02$. With increasing ζ , fully crystalline samples were observed above $\zeta_m = 0.83 \pm 0.02$; this value is called the melting point. Before the samples became a glass, at $\zeta = 0.89 \pm 0.02$, crystalline samples are reported in Fig. 8.4A, demonstrating that ULC microgels behave like other colloids interacting with soft potentials [9, 195, 253, 254].

The softness is solely shifting the boundaries of the phase transitions to higher

ζ with respect to regular cross-linked microgels [9, 195]. This is a consequence of concomitant effects from deswelling [195], interpenetrating [164] and the interparticle potential [255]. Indeed, the potential between microgels can be modelled as $\Phi(r) \propto r^{-n}$, where r is the microgel-microgel distance and n contains information on the softness; smaller values of n correspond to softer potentials. The form of $\Phi(r)$ leads to a power-law dependence of the plateau modulus of G' on the volume fraction: $G_p \propto \zeta^m$. [256] The green line in Fig. 8.4B represents a fit of the data to ζ^m that leads to $m = 2.88 \pm 0.02$. This exponent is linked to the exponent n by the equation: $m = 1 + n/3$. $n = (5.6 \pm 0.1)$ is estimated from rheology measurements as a function of ζ . This value is significantly lower than for regular cross-linked microgels (golden and orange lines) and soft PMMA particles (light blue line) where it lies between 9 and 20 [9, 256, 257]. Nevertheless, ULC microgels still behave as colloids; for flexible macromolecules a linear behavior with a slope $n = 2.3$ is expected (purple line in Fig. 8.4B). [237]

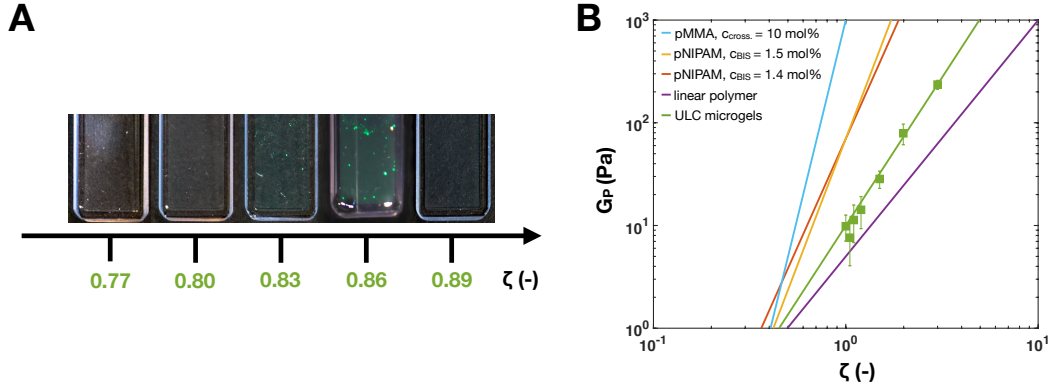


Figure 8.4: (A) Image of a series of samples of ultra-low cross-linked microgels of increasing volume fraction in water. (B) Plateau value of G' , G_p (green squares), versus the generalized volume fraction, ζ . Green line: data fit with $G_p \propto \zeta^m$. light blue, golden, orange and purple lines are taken from Refs. [9, 237, 256, 257], see text for details.

8.3.3. Mechanical Response of Monolayers

Next, we present the behavior of ULC microgels under two-dimensional confinement. For this purpose, the microgels are placed at the oil-water interface in a Langmuir-Blodgett trough. This allows us to determine the surface pressure as a function of concentration and simultaneously deposit the microgel monolayers onto a solid substrate (for details see Chapter 4). The structure of the deposited films of microgels is then probed *via* atomic force microscopy (AFM) in the dried state on the solid substrate.

In Fig. 8.5 the compression isotherms of ULC microgels (green lines) are presented. The surface pressure, Π , is plotted against the area normalized by the added amount of microgel ($area/mass$). For comparison, the isotherms of regular cross-linked microgels (pNIPAM microgels) and linear pNIPAM (PNL) are also reported, with the same colors as in Chapter 7, blue and red, respectively.

The blue curves in Fig. 8.5 exhibit two distinct increases after the contact. The

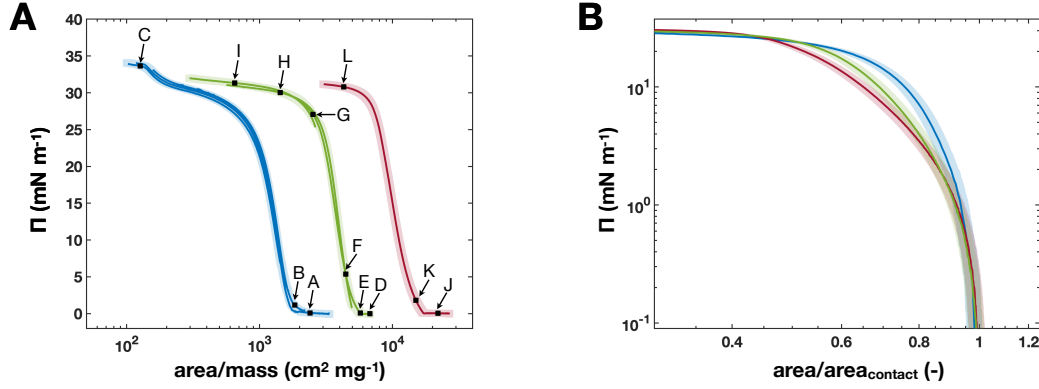


Figure 8.5: (A) Compression isotherms for linear pNIPAM, ULC, and regular pNIPAM microgels. Surface pressure, Π , versus the area normalized by added mass of microgels (area/mass) for 5 mol% cross-linked microgels (blue lines), ULC microgels (green lines) and linear pNIPAM (red lines) at $T = (20.0 \pm 0.5)^\circ\text{C}$. The black squares with letters A-L indicate the Π values of the atomic force micrographs in Fig. 8.6A-L. (B) Plot of Π versus the trough area normalized by the trough area at the contact point, $\text{Area}/\text{Area}_{\text{contact}}$, of 5 mol% cross-linked microgels (blue lines), ULC microgels (green lines) and linear pNIPAM (red lines) at $T = (20.0 \pm 0.5)^\circ\text{C}$ in log-log scale.

first, between $\text{area}/\text{mass} \approx 6 \cdot 10^2 \text{ cm}^2 \text{mg}^{-1}$ and $\approx 2 \cdot 10^3 \text{ cm}^2 \text{mg}^{-1}$. The second between $\approx 1.4 \cdot 10^2 \text{ cm}^2 \text{mg}^{-1}$ and $\approx 2.5 \cdot 10^2 \text{ cm}^2 \text{mg}^{-1}$. This two-stepped course is typical for microgels synthesized with the addition of cross-linker [29, 76, 84, 86, 89] and is due to their well-defined core-shell structure. Upon adsorption, microgels are deformed, but their well-defined cross-linking density profile produces heterogeneities in polymer fraction laterally [78] and vertically [155] to the interface. The different stiffness of the core and the shell under compression is the reason for the presence of the two distinct plateaus.

The linear homopolymers, Fig. 8.5 red curve, have a single-stepped course, in agreement with literature. [186, 187, 224] The reason for this is that flexible polymers can fully spread and cover the interface uniformly. [258] The compression isotherms of ultra-low cross-linked microgels (Fig. 8.5 green lines) exhibit a single-step increase, virtually identical to the linear pNIPAM. This also indicates that the ULC microgels cover the interface homogeneously due to the absence of a well-defined cross-linking density profile as highlighted by SANS. In other words, they behave as flexible polymers once confined at the interface. In contrast, for an ideal gas of hard spheres, Π is expected to be determined by the excluded area effects and the collision rate before diverging at the maximum packing fraction in 2D ($\pi/(2\sqrt{3})$). [259]

Figure 8.5B gives a closer look at the course of the compression isotherms at low Π . Here it is clear that the differences between the linear polymer and the ULC microgels (red and green lines) are less pronounced than the differences between ULC microgels and regular cross-linked microgels (black and blue lines). Nevertheless, deviations between the ULC microgels and the linear pNIPAM are visible for $2 \text{ mN m}^{-1} \lesssim \Pi \lesssim 25 \text{ mN m}^{-1}$. Those differences are larger than the experimental errors associated with the repetition of the measurements given by the shaded areas.

This suggests that the monolayer of the ULC microgels presents characteristic features. We further investigate this by determining the structure of the monolayers of all three systems. We have previously demonstrated that a Langmuir-Blodgett-type deposition of the microgels from the oil-water interface onto a solid substrate does not affect the structural order of the microgels in the monolayer. [108] Consequently, the phase behavior of microgels at interfaces can be investigated after deposition on a solid substrate by means of AFM in the dried state (Chapter 4).

8.3.4. Two Dimensional Phase Behavior

AFM micrographs are reported in Figure 8.6 for regular 5 mol% cross-linked microgels (blue box), ULC microgels (green box), and linear polymers (red box). pNIPAM microgels present a pronounced core-shell structure at the interface, Fig. 8.6A. In literature, it is shown that this fried-egg structure is observed even when a very low amount of cross-linker is added during the synthesis. [194] This indicates that microgels synthesized with little addition of cross-linker always present a more cross-linked core, harder to deform, surrounded by a soft fuzzy shell.

In contrast to regular microgels, before contact ULC microgels are strongly spread and flattened at the substrate into disks, surrounded by a very thin, less dense fuzzy shell (Fig. 8.6D). The phase contrast image in Fig. 8.6M shows the same structure. Height profiles in Figure 8.6A give a direct comparison of the dried pNIPAM (blue solid lines) and ULC microgels (green solid lines). The ULC microgel has a uniform height of ≈ 1.5 nm and lateral extension of roughly 650 nm, while the more cross-linked cores of the pNIPAM microgels protrude to approximately 20 nm. This difference emphasizes the lower volume fraction of polymer within the ULC microgel. Although both microgels have comparable sizes, the ULC microgels have less than one-tenth of the height.

Furthermore, the ratio between the radii in two- and three-dimensions for ULC microgels is 2.3 while for the regular cross-linked microgels in Fig. 8.6A is ≈ 1.8 (Chapter 4). This ratio is a measure of the microgel stretching. The larger ratio of the ULC microgels suggests that their polymeric network is more stretched at the interface with respect to regular cross-linked microgels. This observation and the fact that ULC microgels have a larger mesh size in bulk suggest that even at the interface the mesh size of ULC microgels is larger. [30]

It is important to notice that ULC microgels maintain an individual and almost circular shape while linear polymers are not distinguishable from the substrate, Fig. 8.6J. The higher capability of a flexible polymer to spread, produces an extremely flat profile. [187, 258] The individual polymers are indistinguishable from the substrate due to a height that is comparable to the substrate roughness and the finite dimensions of the tip. [260]

When the monolayers are compressed, the pNIPAM microgels remain distinguishable and arrange in a hexagonally packed lattice (Fig. 8.6B) as expected for colloids. Fig. 8.6E, however, shows that ULC microgels form a uniform polymer film where the single microgels are indistinguishable in both the phase and the height images, Figure 8.6E and N. This behavior is typical for both flexible polymers where, under compression, interpenetration and entanglement are not restricted by cross-links and soft macromolecules, e.g. arborescent microgels at liquid interfaces [261], where strong deformations produce a uniform coverage of the interface. Thus, at low compressions, ULC microgels cover uniformly the interface in contrast to col-

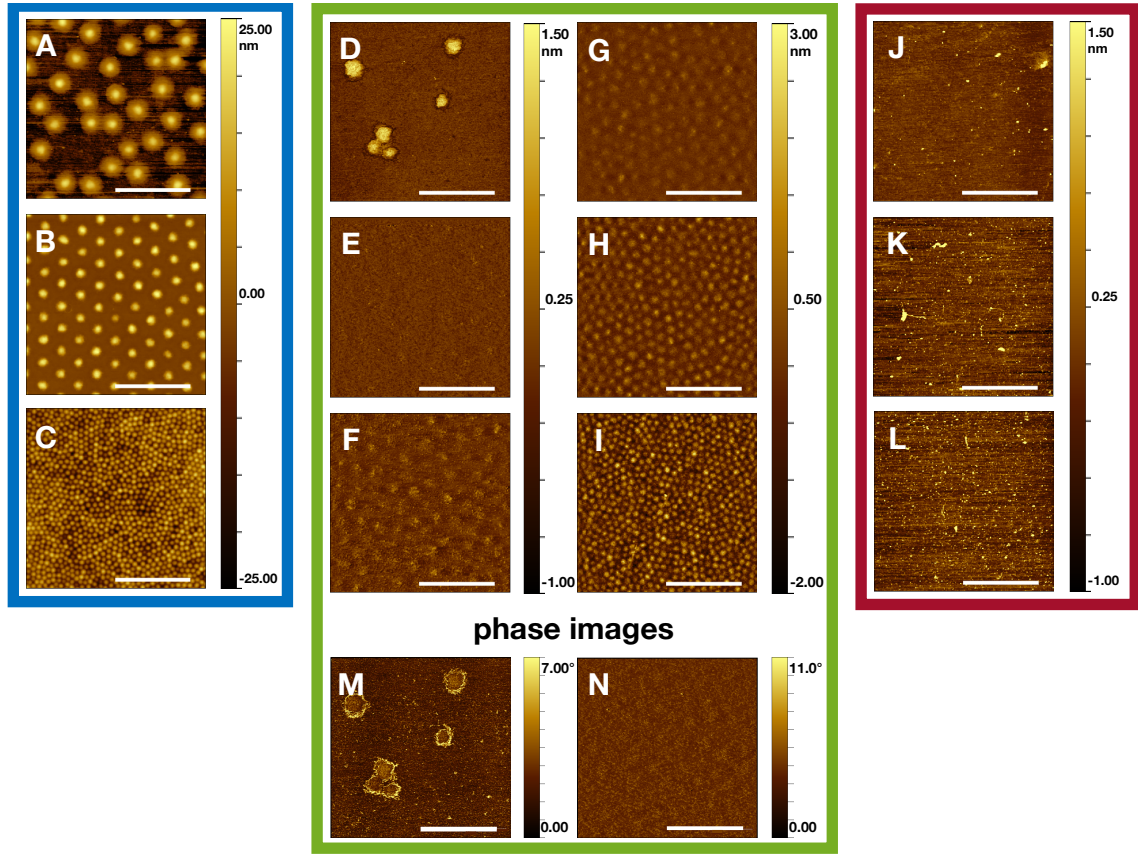


Figure 8.6: AFM Micrographs of deposited monolayers on solid substrates. Series of AFM images in the dried state corresponding to the positions A-L in Fig. 8.5 for pNIPAM microgels (blue box), ULC microgels (green box) and linear pNIPAM (red box) after deposition of the monolayer to a solid substrate at $T = (20.0 \pm 0.5)^\circ\text{C}$. (M) and (N) Phase images of (D) and (E). Scale bars correspond to $2\ \mu\text{m}$.

loids that always maintain their individual shape. Whether this is due to strong interpenetration, large deformation or both, cannot be deduced from Fig. 8.6E.

Upon further compression the ULC microgels become distinguishable again. The evolution shown in Fig. 8.6F-I makes ULC microgels different to flexible polymers confined at the interface where individual polymers remain indistinguishable independent of the compression Figs. 8.6K and 8.6L. In Figure 8.7B the root-mean-square roughness, γ_{RMS} , of the ultra-low cross-linked microgel monolayers is plotted as a function of the Π . In the graph the positions of the AFM images in Figure 8.6F-I are highlighted and four regimes (i-iv) are observed. For regime i the ULC microgels are separated and the roughness of the image is not computed. In regime ii, the microgels are virtually indistinguishable and we obtain $\gamma_{RMS} < 300\ \text{pm}$, the same as the substrate. With increasing Π , the roughness slowly increases (Fig. 8.7B iii) as the microgels are laterally compressed. In regime iv, γ_{RMS} increases steeply from $\approx 500\ \text{pm}$ to $1.3\ \text{nm}$ at the highest investigated Π (Fig. 8.6I). This observation can be understood considering that lateral compression increases the polymer fraction within a ULC microgel. At the transition from regime iii to iv ($\Pi = 28\ \text{mN m}^{-1}$), in-plane compression of polymer network becomes energetically unfavorable and more and more sub-chains are pushed out-of-plane. These segments become hydrated, but are still part of the network and connected by the polymer confined at the interface.

Consequently, the ULC microgels regain their colloidal shape.

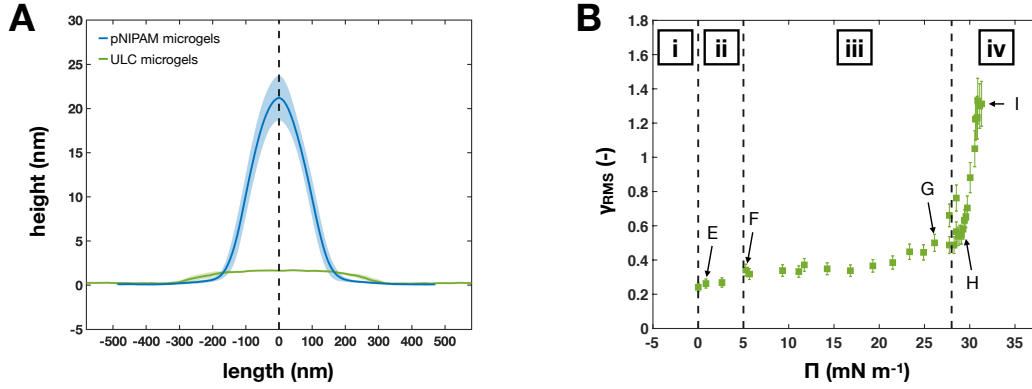


Figure 8.7: Averaged height profiles of dried ULC and pNIPAM microgels and γ_{RMS} of ULC monolayers at $T = 20^\circ\text{C}$. (A) Averaged height profiles of the pNIPAM microgels, blue solid lines, and ULC microgels, green solid lines. Standard deviations are plotted as error areas in the corresponding color. (B) The roughness, γ_{RMS} , of the deposited ultra-low cross-linked microgel monolayers in the dried state as a function of surface pressure Π . The positions of the images in Fig. 8.6E-I are highlighted. Black dashed lines delimit the different visible regimes: (i-iv).

Similarly to the three-dimensional case, a significant difference between spherical colloids and flexible polymers at interfaces is that the former can have three different phases liquid, hexatic and crystalline. Those phases are characterized by two second-order transitions, meaning that no fluid-crystal or hexatic-crystal regimes can coexist. [238] The pNIPAM microgels in Figure 8.6B show a hexagonal lattice that under compression evolves into another hexagonal lattice with a smaller lattice constant (Fig. 8.6C). The evolution from a crystal where microgels are in shell-shell contact, to a new lattice characterized by a core-core contact, is well illustrated in the literature. [29, 76, 89] For the pNIPAM microgels this is extensively investigated at both air- and oil-water interfaces in Chapter 5.

Figure 8.6F-I highlight that no crystallization of the ULC microgels at the interface is observed. The reason for the suppression of crystallization is the increase of size polydispersity of the ULC microgels once confined in 2D. The radius probability functions of ULC and pNIPAM microgels at low and high compression are presented in Figure 8.8A-D. For the ULC microgels the size polydispersity passes from $(11.3 \pm 0.7)\%$ in bulk to $(23 \pm 5)\%$ at the interface. In contrast, pNIPAM microgels display in both two- and three-dimensions a polydispersity of $\approx 7\%$. This can either significantly slow down the crystallization kinetic as observed in polydisperse suspensions of microgels in 3D [195], or suppresses the crystallization since polydispersity has a value higher than the theoretical limit that hinders crystallization for hard disks in two dimensions [262]. At higher compressions the polydispersity of the ULC microgels decreases, but is still too broad to allow crystallization. Even assuming that the distribution can become narrow enough, the ULC microgels within the monolayer are in too close contact, *i.e.*, jammed, to allow reorganization into ordered lattices.

This significant change between the size distribution in bulk and at the interface, can be understood by considering that microgels radially stretch and deform upon

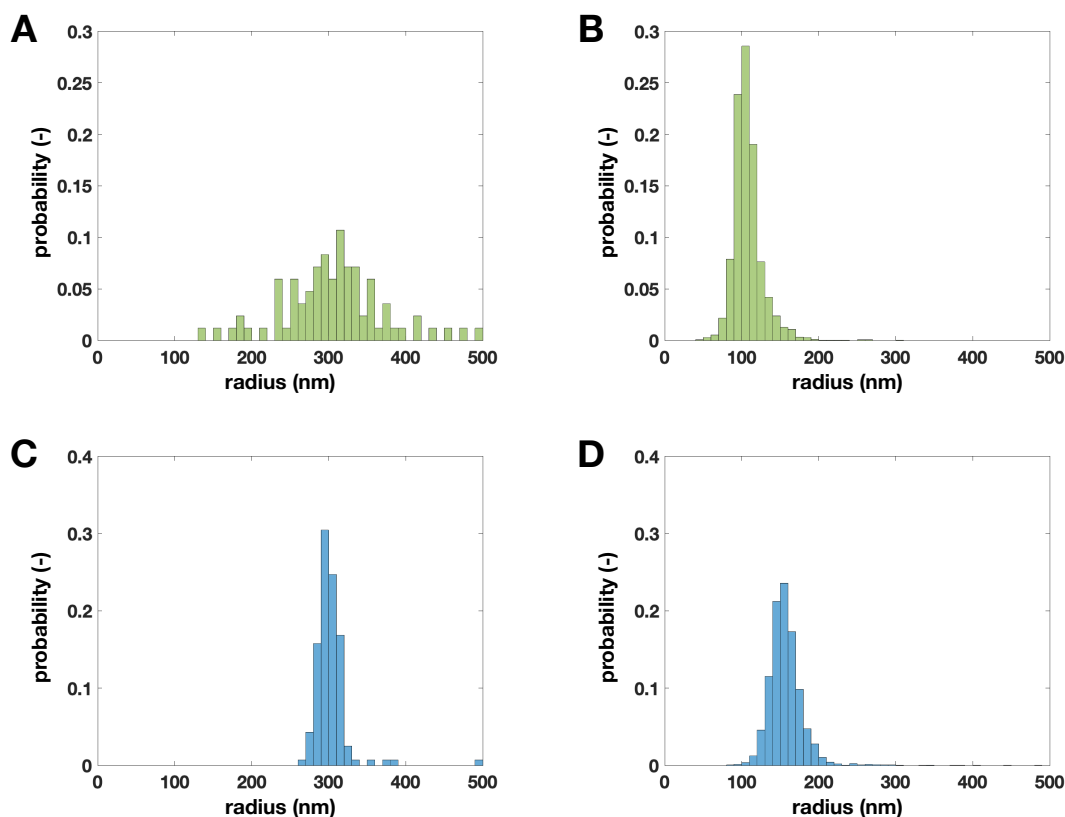


Figure 8.8: Radius probability distributions of ULC (A and B) and pNIPAM microgels (C and D). In A $r(nm)$ represents the interfacial radius measured from 64 ULC microgels. In B-D $r(nm)$ represents the half of the nearest neighbor distances, NND .

adsorption [70, 89] due to the interfacial free energy reduction as far as the internal elasticity of the network allows it. SANS and DLS both show that ULC microgels have a softer network and a less-defined cross-linking density profile, *i.e.*, they are more homogeneous, compared to regular cross-linked microgels. Larger variations in the topology of the networks of different ULC microgels can be expected, causing significant size variations upon interfacial adsorption.

8.4. Conclusion

To summarize, in this study we have shown that ultra-low cross-linked microgels behave as colloids in three dimensions but not in two. At interfaces, within a certain range of concentrations, their properties are very similar to those of flexible polymers. Therefore, a key parameter for the predominance of the colloidal-behavior is represented by the interplay between the softness of the network and the dimensionality.

In three dimensions, SANS highlights that ULC microgels are spherically shaped with a fuzzy shell architecture typical of microgels. [49]. However, they present a large homogeneous core surrounded by a thin fuzzy shell. Furthermore, their phase behavior is the same as that of colloids with liquid, crystalline, and glassy phases. [68, 253, 254] Rheology measurements show that their interaction potential is softer

than for usual microgels but still different from the scaling law of flexible polymers. [9, 237, 255] The sole consequence of the soft interaction potential is to shift the onset of the liquid-to-crystal transitions to higher concentrations as expected for soft microgels. [9, 195]

The confinement of ULC microgels at oil-water interfaces makes their polymeric nature dominant over their colloidal behavior. The compression isotherms of ULC microgels show a single-step increase as expected for flexible homopolymers. [186, 187, 224] Their weakly cross-linked network spreads more than regular cross-linked microgels creating a homogeneous coverage similar to linear pNIPAM. Nevertheless, a unique feature of ultra-low cross-linked microgels with respect to other soft objects is that with increasing concentration the topography at the interface changes.

This can be explained considering that the structure of regular cross-linked microgel is controlled by a competition between the elasticity of the network, which causes a spherical shape, and the gain in the interfacial energy due to adsorption of polymer sub-chains. The maximum gain would be achieved if all sub-chains are adsorbed (pancake shape), but this would be accompanied by a high penalty in elasticity. As a result, regular microgels at the solid interface show the typical fried-egg structure. [29, 86, 194]

In the case of ULC microgel, the amount of cross-links is low and adsorption of polymer segments to the interface is not accompanied by a high penalty in elasticity. Therefore, ULC microgels form a pancake structure, with a homogeneous core and thin fuzzy shell. In other words, strong adsorption overcomes elasticity. Compression and interpenetration lead to a higher polymer fraction inside the microgel making it stiffer since the elasticity of networks depends on the polymer fraction within a microgel. [4, 173] Therefore, starting from $\Pi = 28 \text{ mN m}^{-1}$, for further compression of the monolayer, an increase of the concentration of polymer at the interface becomes energetically unfavorable with respect to desorption and folding some of the polymer sub-chains of the microgels out-of-plane. As a consequence the ULC microgels tend to restore their individual shape: the stronger the compression, the higher the protrusion.

ULC microgels also present differences with respect to other soft colloidal objects like block copolymer micelles, which irreversibly change their internal conformation upon adsorption at an interface, exposing hydrophilic and hydrophobic blocks to the polar and non-polar phases, respectively. [263, 264] In contrast, the transition of ULC microgels from a homogeneous coverage to a disordered microgel-like layer is fully reversible. Furthermore, the interfacial phase behavior of ULC microgels, that only show disordered arrangements, differs from colloids that can crystallize. [265, 266]

This can be explained since the confinement of the ULC microgels in two dimensions produces a heterogeneous stretching of their loosely cross-linked polymeric networks. This is a consequence of both the few cross-links they have and the absence of a well-defined cross-linking profile: a more cross-linked core will preserve more the shape and limits the increase in size polydispersity as for regular cross-linked microgels. The consequent increase in the size polydispersity of the ULC microgels suppresses the crystallization of the system. With increasing the compression of the monolayer of ULC microgels their size distribution becomes narrower, but still too broad to allow crystals to form (Fig. 8.8B). [262] Even assuming that as in 3D [195] a higher compression further decreases the polydispersity, microgels are jammed

together making any rearrangements impossible and the materials fail to crystallize.

The capability of ULC microgels to behave either like flexible, linear polymers or like colloids depending on dimensionality and compression, makes them the perfect model system to explore common properties and differences between them and regular microgels and other polymer architectures, such as star-, hyperbranched-, and linear macromolecules. Consequently, these materials may also be of great interest for applications as biomaterials. For example, since ULC microgels are more deformable than the regular cross-linked microgels [199] they are particularly suitable for the development of nanomaterials for selective adsorption in physiological solution [197], or as bio-sensors [267], as recent findings show that the softness of microgels improves their adsorption onto a solid substrate [268]. Furthermore, it has been proven that ultra-low cross-linked microgels are a perfect system to generate porous fibrin networks facilitating cell migration and growth [269]. The capability of this system to have a topography under adsorption that depends on the compression and the suppression of crystallization in two dimensions would be of interest in these fields. Here we have also shown that while ULC microgels have a behavior similar to linear polymers at the interface, their flow properties are more comparable with colloids. This might be of interest to realize polymer coatings with surface morphologies ranging from flat, uniform films, e.g. linear or star polymers [270], to randomly close-packed monolayers of microgels [271].

8.5. Data Availability

Research data for this chapter may be accessed at <https://hdl.handle.net/21.11102/0f3e60d7-9576-11e8-9b95-e41f1366df48>.

9. Conclusion and Outlook

The main objectives of this thesis were the investigation of the influence of temperature on microgel monolayers (Chapters 4, 5, and 6) and the polymer-to-particle transition (Chapter 8). Additionally, the effect of the top-phase, which is decane or air, and the influence of the microgels' architecture were studied in Chapters 5 and 7, respectively. In section 9.1 the main findings are shortly summarized and concluded. In section 9.2 future prospects for microgel at interfaces are given.

9.1. Summary and Conclusion

We studied the influence of temperature on the two-dimensional phase diagram of microgels confined at interfaces. Therefore, the compressibility, the in-plane dimensions, and the out-of-plane thickness were investigated below and above their volume phase transition temperature (VPTT). It was found that adsorbed microgels possess thermo-sensitive (core) and non-thermo-sensitive (corona) regions and, consequently, their phase behavior differs only at high compressions.

Compression isotherms at the decane- and air-water interfaces of microgel monolayers at elevated temperatures do not display the typical behavior with two increases [70, 76, 78], but only show a single increase. However, the core-corona structure of the adsorbed microgels is preserved. The total diameter of individual microgels at the interfaces, D_{2D} , is nearly constant. In contrast, fractions of the microgels that are not in close proximity to the interface, *i.e.*, the core, can still deswell upon an increase of temperature; both the in-plane diameter of the core, D_{core} , and the total thickness of the monolayer significantly decreases (Chapters 4 and 6). This emphasizes that fractions of the microgels in direct contact with the interface lose their temperature-sensitivity due to the gain in surface free energy.

Accordingly, the first two stages of the compression isotherms and the microstructure of the microgel monolayers are identical below and above the VPTT (for area fractions below 2). Once the microgel cores get into contact, *i.e.*, the microgels' center-to-center distance $\approx D_{core}$, their 2D phase behavior differs. Below the VPTT, the fractions of the microgels that are located in the aqueous phase remain swollen during and after the isostructural transition, explaining the occurrence of a second increase. In contrast, at temperatures larger than the VPTT, these fractions are deswollen and the averaged polymer density of the core is increased. Thus, an intermediate phase, where the microgels can be further laterally compressed, is absent and no further increase of the surface pressure is registered.

The direct comparison of microgels monolayers at decane- and air-water interfaces at temperatures below and above the VPTT in Chapter 5 shows that D_{2D} changes significantly, but D_{core} is constant between the two interfaces; Giving a further proof that parts of the microgels' polymeric network in close proximity to the interface are dominated by the surface free energy. In contrast, the cores keep their thermo-sensitivity leading to the same temperature-dependent 2D phase behavior independently of the top-phase. Nevertheless, the higher surface free energy of the air-water interface in contrast to the decane-water interface leads to the adsorption of more polymer. This becomes clearly visible when the monolayers are fully compressed. Close to the monolayer failure, the microgels at the air-water interface have

larger center-to-center distances.

In conclusion, it is shown that microgels have a core-corona structure independent of temperature and top-phase. As the polymer segments within the interface lose their temperature-sensitivity, due to the surface free energy, the interactions between adsorbed microgels at low compression are governed by their highly stretched corona. At high compression, however, the portions of the microgels that are situated in the aqueous phase become relevant and prevail in the microgel interactions. These fractions can deswell, altering the isostructural phase transition. It is shown that the temperature-dependent swelling perpendicular to the interface (“3D”) affects the compressibility parallel to the interface (“2D”). Most generally, a microgel at interfaces has to be considered a quasi-2D object, since its perpendicular, out-of-plane structure is a crucial factor to always take into account.

Compression isotherms of different pNIPAM-based systems at the decane-water interface were studied to elucidate the influence of deformability or softness, respectively. Thereby, the number of grafting or cross-linking points was increased from linear polymer through star-shaped polymers to regularly cross-linked microgels. Furthermore, hollow microgels, which possess a solvent filled cavity in the center of their polymeric network, were investigated. The compression isotherms were normalized to the amount of material added to the interface. The fraction of adsorbed polymer relative to linear pNIPAM was calculated to compare the stretching or deformability of the different systems. Unsurprisingly, a decrease of deformability with increasing constraints, *i.e.*, an increasing number of grafting or cross-linking points, was observed. However, not only the number of constraints but also the architecture is an important aspect to take into account to predict the softness of adsorbed microgel systems. Similar to the 3D case, hollow microgels are distinctively more deformable than their regular counterparts (with similar sizes and cross-linker amount). Interestingly, hollow microgels with a thin polymer shell do not keep their structural integrity.

A closer look at the polymer-to-particle transition is taken in the last chapter (Chapter 8). The phase behavior of linear polymer, ultra-low cross-linked (ULC), and regularly cross-linked microgels at the decane-water interfaces is directly compared. It is found that for ULC microgels the dimensionality has a profound influence on their phase diagram with a polymer-like behavior at the interface (“2D”) and a colloidal particle-like behavior in bulk (“3D”).

In bulk, ULC microgels have a spherical shape with a fuzzy shell, typical for microgels. [49]. However, they present a large homogeneous core surrounded by a thin fuzzy shell. Their phase behavior is the same as that of colloids with liquid, crystalline, glassy, and jammed phases. [68, 253, 254] Although, rheology measurements show that their interaction potential is softer than for usual microgels it is still different from the scaling law of flexible polymers. [9, 237, 255] The sole consequence of the soft interaction potential is to shift the onset of the liquid-to-crystal transitions to much higher volume fractions.

Once confined at interfaces, ULC microgels display a dominant polymeric nature. The compression isotherms of ULC microgels show a single-step increase, virtually the same as linear pNIPAM polymer. [186, 187, 224] Gradient Langmuir-Blodgett type depositions reveal that their weakly cross-linked network spreads more homogeneously than regular cross-linked microgels, creating pancake structures. Furthermore, ULC microgel monolayers have a concentration-dependent topography: at

low concentrations, they form a homogeneous film, similar to linear polymers; upon increasing the compression this topography changes into a monolayer of distinguishable microgels.

In conclusion, ULC microgels have a distinctly different phase behavior than regular microgels. Their extremely soft polymer network leads to large variations in their topology, causing significant size variations upon interfacial adsorption, preventing crystallization. Furthermore, at interfaces, they show a concentration-dependent topography ranging from flat, homogeneous films to monolayers of distinguishable microgels. Therefore, ULC microgels are on the verge of the polymer-to-particle transition and are an interesting model system for fundamental studies and applications.

9.2. Outlook

Understanding of the demulsification (and defoaming) mechanism of microgels stabilized emulsions (and foams) is the key point in application-driven research of microgel monolayers. Already in 2008, Brugger *et al.* [60] suggested that the main property leading to the demulsification is the viscoelasticity of the microgel monolayer. Since then, some studies regarding these proprieties were conducted, noteworthy, the works of Rey *et al.* [76] and Maestro *et al.* [93] in which it is shown that the viscoelasticity of the interfaces is a function of compression and temperature. Maestro *et al.* explained the transition from a solid-liquid behavior (and the change in surface pressure) with increasing temperature due to the decrease in the in-plan diameter (and thus, to the formation of a free interface). Our two-dimensional phase diagrams (Chapters 4 and 5) and measurements as a function of temperature by Harrer *et al.* [79] show that the total diameter of the microgels is not significantly affected. However, the size of the core is reduced, and therefore, we suggest that the change of viscosity with temperature is in fact due to the collapse of the microgels core. At high coverage and low temperatures, the “thick” and solvent swollen interfacial film dominates the rheological properties. When the temperature is increased, the cores deswell and only a “thin” layer of directly adsorbed polymer contributes; as a consequence, the monolayer becomes more liquid-like.

We emphasize the need for further interfacial rheology measurements to clarify the above contradictory findings. In the Appendix A.2, we present a setup based on the design of Vermant *et al.* [272, 273] using a double wall-ring (DWR) geometry. The DWR can be used to perform shear rheology at air- and oil-water interfaces and its operation window is well suited for microgel monolayers. [274] In contrast to other methods [76, 93, 275], the Langmuir-trough-DWR setup allows for precise surface pressure control, does not need tracer particles, and has a large torque range. Furthermore, the custom made Langmuir trough can be tempered and used to measure the rheological properties as a function of temperature. Thus, one can expect that this setup will be ideal to study the viscoelasticity of regular cross-linked microgel monolayers at different compressions and temperatures but also as a function of other environmental changes, such as ionic strength or pH. Additionally, it will be interesting to look at different systems, such as ultra-low cross-linked microgels. In Chapter 8 it has been shown that their extreme softness and large variations in network topology give a distinctly different behavior compared to regular cross-linked microgels. A recent study reveals that ULC microgels combine the flow properties of

polymers and colloidal particles even in solution. [31] A comprehensive evaluation of their interfacial rheological properties might help to further understand the impact of softness on the polymer-to-particle transition.

Another important aspect is the out-of-plane structure of adsorbed microgels to fully understand the demulsification. We showed that the fractions situated in the aqueous phase play a dominant role, especially at higher area fractions. While the here presented reflectometry techniques (ellipsometry in Chapter 4 and neutron reflectometry in Chapter 6) are a powerful tool, a combination with imaging procedures would yield a more in-depth description of the microgels' conformations. State of the art super-resolution fluorescence microscopy (SRFM) has been used to determine their structure in an overcrowded environment in bulk. [276] Similarly, the structure and interaction of interface-bound microgels could be investigated. Such results will not only increase our understanding but also can be used as references for computer simulations and theoretical studies. Well tuned simulations can generate high output and allow time-efficient screening of the effects of different parameters, such as polydispersity, architecture, or solubility.

Besides further techniques, also the recent developments in the synthesis of hybrid and anisotropic microgels give novel opportunities for applications and fundamental studies. In Chapter 7 we already presented the compression isotherms of hollow microgels. From these measurements, it is shown that another parameter controlling the deformability of microgels is their architecture, *i.e.*, the incorporation of a solvent filled cavity. Therefore, the architecture is another property to tune the phase behavior of microgels in both 2D and 3D [165].

Furthermore, it has been proposed that hollow microgels are excellent drug delivery systems. [277, 278] An important factor to consider for this purpose is the adsorption and deformation of the microgels onto cell tissue. We present first AFM images of deposited hollow microgels in Chapter 7. Remarkably, the micrographs show that a thin shell leads to the disintegration of the microgels at the interface; while a hollow microgel with a thick polymer shell keeps its structural integrity. This effect can be both an advantage and a disadvantage, for example, whether a rapid or slow release is desired.

Lastly, an exciting system to investigate at interfaces are the anisotropic, thermo-responsive microgels with and without an inorganic core that have been realized recently. [201] Anisotropic building blocks are an essential tool to study ordering phenomena, not only in 3D but also at the interface. Their rod-like shape, coupled with their responsiveness and their soft interaction potential, is an ideal playground to explore liquid crystals and isotropic-to-nematic phase transitions. Additionally, their core is made from a magnetic material (hematite, or after reduction magnetite) which can be used to further explore their phase ordering in two dimensions as a function of the magnetic field, temperature, and compression.

List of Figures

2.1	Structure of a pNIPAM microgel synthesized <i>via</i> precipitation polymerization below and above the volume phase transition temperature.	17
2.2	Conformation of a pNIPAM microgel at the oil-water interface.	19
2.3	Schematic of the microstructures of microgel monolayers as a function of compression.	20
3.1	Schematic figure of a Langmuir trough used for gradient Langmuir-Blodgett type depositions.	24
3.2	Schematic structure and functionality of an atomic force microscope.	26
3.3	Connection of image positions and surface pressure.	29
3.4	Flow chart of the image analysis routine.	30
3.5	Working principle of a reflectometer.	32
3.6	Schematic reflectivity curve of a flat air-heavy water interface.	34
3.7	Working principle of an ellipsometer.	36
4.1	Characterization of pNIPAM microgels in solution.	44
4.2	Compression isotherms at $T = 20$ and $40\text{ }^{\circ}\text{C}$	45
4.3	In-plane diameter of microgels at $T = 20$ and $40\text{ }^{\circ}\text{C}$	46
4.4	Atomic force micrographs of the microgel monolayers at $T = 20$ and $40\text{ }^{\circ}\text{C}$	48
4.5	Results of the quantitative image analysis of all AFM images.	49
4.6	Pair correlation functions and 2D- <i>fast Fourier transform</i> patterns of microgel monolayers at $T = 20$ and $40\text{ }^{\circ}\text{C}$	51
4.7	Spectroscopic ellipsometry of microgel monolayers at the air-water interface as a function of temperature.	52
4.8	Sketch of the microgel monolayers under compression at $T = 20$ and $40\text{ }^{\circ}\text{C}$	55
5.1	Π - <i>area/mass</i> compression isotherms of pNIPAM microgels at the air-water and decane-water interface and at $T = 20$ and $40\text{ }^{\circ}\text{C}$	61
5.2	Π - N_{area} compression isotherms of pNIPAM microgels at the air-water and decane-water interface and at $T = 20$ and $40\text{ }^{\circ}\text{C}$	62
5.3	Atomic force micrographs of pNIPAM microgel monolayers at $T = 20$ and $40\text{ }^{\circ}\text{C}$	63
5.4	In-plane diameter of microgels at $T = 20$ and $40\text{ }^{\circ}\text{C}$ and air-water and decane-water interfaces	64
5.5	Results of the quantitative image analysis of all AFM images at $T = 20$ and $40\text{ }^{\circ}\text{C}$ and air-water and decane-water interfaces.	66
5.6	Averaged height profiles of dried microgels deposited at $T = 20$ and $40\text{ }^{\circ}\text{C}$ and from air-water and decane-water interfaces.	68
5.7	Conformation of a pNIPAM microgel at the oil-water interface with cross-section	69
5.8	Hexagonal order parameter of microgel monolayers at the air-water and decane-water interface and at $T = 20$ and $40\text{ }^{\circ}\text{C}$	72

6.1	Reflectivity curves of pNIPAM microgels at $T = 10, 20, 30$, and $40\text{ }^{\circ}\text{C}$ at the air- D_2O and air-ACMW interface.	80
6.2	Reflectivity curves of pNIPAM and ULC microgels at different surface pressures at the air- D_2O interface.	84
7.1	Π -area/mass compression isotherms of all samples at $T = 20\text{ }^{\circ}\text{C}$	92
7.2	Π -area/mass compression isotherms of all samples at $T = 20\text{ }^{\circ}\text{C}$ shifted to the isotherm of pNIPAM-lin.	94
7.3	Atomic force micrographs and height profile of hollow microgels at $T = 20\text{ }^{\circ}\text{C}$	97
8.1	Characterization of ULC microgels in solution with small-angle neutron scattering.	103
8.2	Characterization of ULC and pNIPAM microgels in solution with dynamic light scattering.	104
8.3	Relative viscosity of ULC and pNIPAM microgels.	105
8.4	3D phase behavior and rheology of ULC microgels at $T = 20\text{ }^{\circ}\text{C}$	106
8.5	Π -area/mass compression isotherms of linear pNIPAM, ULC, and regular pNIPAM microgels at $T = 20\text{ }^{\circ}\text{C}$	107
8.6	Atomic force microscopy micrographs of deposited monolayers on solid substrates.	109
8.7	Averaged height profiles of dried ULC and pNIPAM microgels and root-mean-square roughness of ULC monolayers.	110
8.8	Radius probability distributions of ULC and pNIPAM microgels. . . .	111
A.1	Characterization the microgels in solution with dynamic light scattering.	144
A.2	SANS data and analysis of pNIPAM-co-DEAAM and pDEAAM microgels.	145
A.3	Comparison of relative polymer volume fractions for the different microgel systems.	146
A.4	Relative viscosity of microgel samples.	147
A.5	Three-dimensional model of the Langmuir trough for interfacial shear rheology.	148
A.6	Three-dimensional model and image of the double wall cups for interfacial shear rheology.	149
A.7	Three-dimensional model and image of the ring geometries for interfacial shear rheology.	150
A.8	Interfacial shear rheology setup with Langmuir trough and double wall-ring.	150
A.9	Compression isotherm and interfacial amplitude sweeps of pNIPAM microgel monolayers.	152

List of Tables

4.1	In-plane physical dimensions of microgels monolayers at different compressions deposited from decane-water interfaces at $T = 20$ and 40 °C.	50
5.1	In-plane physical dimensions of microgels monolayers at different compressions deposited from air- and decane-water interfaces at $T = 20$ and 40 °C.	67
5.2	Physical dimensions of microgels monolayers at different compressions deposited from air- and decane-water interfaces at $T = 20$ and 40 °C.	71
6.1	Results of the three-layer model fit of the reflectivity curves for the pNIPAM microgels at different temperatures.	83
6.2	Results of the three-layer model fit of the reflectivity curves for the pNIPAM microgels at different compressions.	85
6.3	Results of the two-layer model fit of the reflectivity curves for the ULC microgels at different compressions.	87
7.1	List of used samples and summary of the parameters in solution and at the interface.	91
8.1	Physical dimensions of ULC and pNIPAM microgels in solution. . . .	104
A.1	Synthesis parameters for pNIPAM, pDEAAM, pNIPAM-co-DEAAM, and pNIPAM-co-DEAAM _{small} microgel systems.	143
A.2	Characterization parameters for pNIPAM, pDEAAM, pNIPAM-co-DEAAM, and pNIPAM-co-DEAAM _{small} microgel systems.	146

Bibliography

- (1) Pelton, R. Temperature-sensitive aqueous microgels. *Advances in colloid and interface science* **2000**, *85*, 1–33.
- (2) Fernandez-Nieves, A.; Wyss, H.; Mattsson, J.; Weitz, D. A., *Microgel suspensions: fundamentals and applications*; John Wiley & Sons: 2011.
- (3) Mattsson, J.; Wyss, H. M.; Fernandez-Nieves, A.; Miyazaki, K.; Hu, Z.; Reichman, D. R.; Weitz, D. A. Soft colloids make strong glasses. *Nature* **2009**, *462*, 83.
- (4) Van Der Scheer, P.; Van De Laar, T.; Van Der Gucht, J.; Vlassopoulos, D.; Sprakel, J. Fragility and strength in nanoparticle glasses. *ACS nano* **2017**, *11*, 6755–6763.
- (5) Pellet, C.; Cloitre, M. The glass and jamming transitions of soft polyelectrolyte microgel suspensions. *Soft matter* **2016**, *12*, 3710–3720.
- (6) Bhattacharjee, T.; Kabb, C. P.; O'Bryan, C. S.; Urueña, J. M.; Sumerlin, B. S.; Sawyer, W. G.; Angelini, T. E. Polyelectrolyte scaling laws for microgel yielding near jamming. *Soft matter* **2018**, *14*, 1559–1570.
- (7) Zhang, Z.; Xu, N.; Chen, D. T.; Yunker, P.; Alsayed, A. M.; Aptowicz, K. B.; Habdas, P.; Liu, A. J.; Nagel, S. R.; Yodh, A. G. Thermal vestige of the zero-temperature jamming transition. *Nature* **2009**, *459*, 230–233.
- (8) Paloli, D.; Mohanty, P. S.; Crassous, J. J.; Zaccarelli, E.; Schurtenberger, P. Fluid–solid transitions in soft-repulsive colloids. *Soft Matter* **2013**, *9*, 3000–3004.
- (9) Senff, H.; Richtering, W. Temperature sensitive microgel suspensions: Colloidal phase behavior and rheology of soft spheres. *J. Chem. Phys.* **1999**, *111*, 1705–1711.
- (10) Alsayed, A. M.; Islam, M. F.; Zhang, J.; Collings, P. J.; Yodh, A. G. Premelting at defects within bulk colloidal crystals. *Science* **2005**, *309*, 1207–1210.
- (11) Scotti, A.; Bochenek, S.; Brugnoli, M.; Fernandez-Rodriguez, M.; Schulte, M.; Houston, J.; Gelissen, A.; Potemkin, I.; Isa, L.; Richtering, W. Exploring the colloid-to-polymer transition for ultra-low crosslinked microgels from three to two dimensions. *Nature Communications* **2019**, *10*, 1418.
- (12) Lopez, V. C.; Hadgraft, J.; Snowden, M. The use of colloidal microgels as a (trans) dermal drug delivery system. *International journal of pharmaceutics* **2005**, *292*, 137–147.
- (13) Agrawal, G.; Agrawal, R.; Pich, A. Dual Responsive Poly (N-vinylcaprolactam) Based Degradable Microgels for Drug Delivery. *Particle & Particle Systems Characterization* **2017**, *34*, 1700132.
- (14) Dan, A.; Agnihotri, P.; Brugnoli, M.; Siemes, E.; Wöll, D.; Crassous, J. J.; Richtering, W. Microgel-stabilized liquid crystal emulsions enable an analyte-induced ordering transition. *Chemical Communications* **2019**, *55*, 7255–7258.

- (15) Álvarez-Puebla, R. A.; Contreras-Cáceres, R.; Pastoriza-Santos, I.; Pérez-Juste, J.; Liz-Marzán, L. M. Au@ pNIPAM colloids as molecular traps for surface-enhanced, spectroscopic, ultra-sensitive analysis. *Angewandte Chemie International Edition* **2009**, *48*, 138–143.
- (16) Sigolaeva, L.; Pergushov, D.; Oelmann, M.; Schwarz, S.; Brugnioni, M.; Kurochkin, I.; Plamper, F.; Fery, A.; Richtering, W. Surface functionalization by stimuli-sensitive microgels for effective enzyme uptake and rational design of biosensor setups. *Polymers* **2018**, *10*, 791.
- (17) Wiese, S.; Spiess, A. C.; Richtering, W. Microgel-stabilized smart emulsions for biocatalysis. *Angewandte Chemie International Edition* **2013**, *52*, 576–579.
- (18) Zhang, Y.; Zhang, H.; Liu, P.; Sun, H.; Li, B.-G.; Wang, W.-J. Programming Hydrogen Production via Controllable Emulsification/Demulsification in a Switchable Oil–Water System. *ACS Sustainable Chemistry & Engineering* **2019**, *7*, 7768–7776.
- (19) Barth, M.; Wiese, M.; Ogieglo, W.; Go, D.; Kuehne, A.; Wessling, M. Monolayer microgel composite membranes with tunable permeability. *Journal of membrane science* **2018**, *555*, 473–482.
- (20) Kajiwar, K.; Ross-Murphy, S. B. Synthetic gels on the move. *Nature* **1992**, *355*, 208–209.
- (21) Islam, M. R.; Li, X.; Smyth, K.; Serpe, M. J. Polymer-based muscle expansion and contraction. *Angewandte Chemie International Edition* **2013**, *52*, 10330–10333.
- (22) Rey, B. M.; Elnathan, R.; Ditzovski, R.; Geisel, K.; Zanini, M.; Fernandez-Rodriguez, M.-A.; Naik, V. V.; Frutiger, A.; Richtering, W.; Ellenbogen, T., et al. Fully tunable silicon nanowire arrays fabricated by soft nanoparticle templating. *Nano letters* **2015**, *16*, 157–163.
- (23) Scheidegger, L.; Fernández-Rodríguez, M. Á.; Geisel, K.; Zanini, M.; Elnathan, R.; Richtering, W.; Isa, L. Compression and deposition of microgel monolayers from fluid interfaces: particle size effects on interface microstructure and nanolithography. *Physical Chemistry Chemical Physics* **2017**, *19*, 8671–8680.
- (24) Xu, S.; Zhang, J.; Paquet, C.; Lin, Y.; Kumacheva, E. From hybrid microgels to photonic crystals. *Advanced Functional Materials* **2003**, *13*, 468–472.
- (25) Schmidt, S.; Zeiser, M.; Hellweg, T.; Duschl, C.; Fery, A.; Möhwald, H. Adhesion and mechanical properties of PNIPAM microgel films and their potential use as switchable cell culture substrates. *Advanced Functional Materials* **2010**, *20*, 3235–3243.
- (26) Xia, Y.; He, X.; Cao, M.; Chen, C.; Xu, H.; Pan, F.; Lu, J. R. Thermoresponsive microgel films for harvesting cells and cell sheets. *Biomacromolecules* **2013**, *14*, 3615–3625.
- (27) Schramm, L. L., *Emulsions, foams, and suspensions: fundamentals and applications*; John Wiley & Sons: 2006.

-
- (28) Raya, S. A.; Saaïd, I. M.; Ahmed, A. A.; Umar, A. A. A critical review of development and demulsification mechanisms of crude oil emulsion in the petroleum industry. *Journal of Petroleum Exploration and Production Technology* **2020**, 1–18.
- (29) Bochenek, S.; Scotti, A.; Ogieglo, W.; Fernández-Rodríguez, M. Á.; Schulte, M. F.; Gumerov, R. A.; Bushuev, N. V.; Potemkin, I. I.; Wessling, M.; Isa, L.; Richtering, W. Effect of the 3D Swelling of Microgels on Their 2D Phase Behavior at the Liquid–Liquid Interface. *Langmuir* **2019**, *35*, 16780–16792.
- (30) Scotti, A.; Bochenek, S.; Brugnoli, M.; Fernandez-Rodriguez, M.-A.; Schulte, M. F.; Houston, J.; Gelissen, A. P.; Potemkin, I. I.; Isa, L.; Richtering, W. Exploring the colloid-to-polymer transition for ultra-low crosslinked microgels from three to two dimensions. *Nature Communications* **2019**, *10*, 1418.
- (31) Scotti, A.; Brugnoli, M.; Lopez, C. G.; Bochenek, S.; Crassous, J. J.; Richtering, W. Flow properties reveal the particle-to-polymer transition of ultra-low crosslinked microgels. *Soft Matter* **2020**.
- (32) Pelton, R.; Chibante, P. Preparation of aqueous latices with N-isopropylacrylamide. *Colloids and Surfaces* **1986**, *20*, 247–256.
- (33) Heskins, M.; Guillet, J. E. Solution properties of poly (N-isopropylacrylamide). *Journal of Macromolecular Science—Chemistry* **1968**, *2*, 1441–1455.
- (34) Eliassaf, J. Aqueous solutions of poly (N-isopropylacrylamide). *Journal of applied polymer science* **1978**, *22*, 873–874.
- (35) Schild, H. G.; Tirrell, D. A. Microcalorimetric detection of lower critical solution temperatures in aqueous polymer solutions. *Journal of Physical Chemistry* **1990**, *94*, 4352–4356.
- (36) Winnik, F. M.; Ringsdorf, H.; Venzmer, J. Methanol-water as a co-nonsolvent system for poly (N-isopropylacrylamide). *Macromolecules* **1990**, *23*, 2415–2416.
- (37) Sawai, T.; Yamazaki, S.; Ikariyama, Y.; Aizawa, M. pH-Responsive swelling of the ultrafine microsphere. *Macromolecules* **1991**, *24*, 2117–2118.
- (38) Rodriguez, B.; Wolfe, M.; Fryd, M. Nonuniform swelling of alkali swellable microgels. *Macromolecules* **1994**, *27*, 6642–6647.
- (39) Snowden, M. J.; Chowdhry, B. Z.; Vincent, B.; Morris, G. E. Colloidal copolymer microgels of N-isopropylacrylamide and acrylic acid: pH, ionic strength and temperature effects. *Journal of the Chemical Society, Faraday Transactions* **1996**, *92*, 5013–5016.
- (40) Ohmine, I.; Tanaka, T. Salt effects on the phase transition of ionic gels. *The Journal of Chemical Physics* **1982**, *77*, 5725–5729.
- (41) Saunders, B. R.; Crowther, H. M.; Vincent, B. Poly [(methyl methacrylate)-co-(methacrylic acid)] microgel particles: swelling control using pH, conon-solvency, and osmotic deswelling. *Macromolecules* **1997**, *30*, 482–487.
- (42) Osada, Y.; Okuzaki, H.; Hori, H. A polymer gel with electrically driven motility. *Nature* **1992**, *355*, 242–244.

- (43) Nöjd, S.; Mohanty, P. S.; Bagheri, P.; Yethiraj, A.; Schurtenberger, P. Electric field driven self-assembly of ionic microgels. *Soft Matter* **2013**, *9*, 9199–9207.
- (44) Cook, J. P.; Riley, D. J. Electrical switching of microgel swelling and collapse for display applications. *Journal of Polymer Science Part B: Polymer Physics* **2012**, *50*, 516–522.
- (45) Mergel, O.; Wuennemann, P.; Simon, U.; Boeker, A.; Plamper, F. A. Microgel size modulation by electrochemical switching. *Chemistry of Materials* **2015**, *27*, 7306–7312.
- (46) Suzuki, A.; Tanaka, T. Phase transition in polymer gels induced by visible light. *Nature* **1990**, *346*, 345–347.
- (47) Garcia, A.; Marquez, M.; Cai, T.; Rosario, R.; Hu, Z.; Gust, D.; Hayes, M.; Vail, S. A.; Park, C.-D. Photo-, thermally, and pH-responsive microgels. *Langmuir* **2007**, *23*, 224–229.
- (48) Zakrevskyy, Y.; Richter, M.; Zakrevska, S.; Lomadze, N.; von Klitzing, R.; Santer, S. Light-Controlled Reversible Manipulation of Microgel Particle Size Using Azobenzene-Containing Surfactant. *Advanced Functional Materials* **2012**, *22*, 5000–5009.
- (49) Stieger, M.; Richtering, W.; Pedersen, J. S.; Lindner, P. Small-angle neutron scattering study of structural changes in temperature sensitive microgel colloids. *The Journal of chemical physics* **2004**, *120*, 6197–6206.
- (50) Wu, X.; Pelton, R.; Hamielec, A.; Woods, D.; McPhee, W. The kinetics of poly (N-isopropylacrylamide) microgel latex formation. *Colloid and polymer science* **1994**, *272*, 467–477.
- (51) Kröger, L. C.; Kopp, W. A.; Leonhard, K. Prediction of chain propagation rate constants of polymerization reactions in aqueous NIPAM/BIS and VCL/BIS systems. *The Journal of Physical Chemistry B* **2017**, *121*, 2887–2895.
- (52) Eckert, T.; Richtering, W. Thermodynamic and hydrodynamic interaction in concentrated microgel suspensions: Hard or soft sphere behavior? *The Journal of chemical physics* **2008**, *129*, 124902.
- (53) Pyett, S.; Richtering, W. Structures and dynamics of thermosensitive microgel suspensions studied with three-dimensional cross-correlated light scattering. *The Journal of chemical physics* **2005**, *122*, 034709.
- (54) Karg, M.; Pich, A.; Hellweg, T.; Hoare, T.; Lyon, L. A.; Crassous, J. J.; Suzuki, D.; Gumerov, R. A.; Schneider, S.; Potemkin, I. I.; Richtering, W. Nanogels and Microgels: From Model Colloids to Applications, Recent Developments, and Future Trends. *Langmuir* **2019**, *35*, 6231–6255.
- (55) Duracher, D.; Elaïssari, A.; Pichot, C. Preparation of poly (N-isopropylmethacrylamide) latexes kinetic studies and characterization. *Journal of Polymer Science Part A: Polymer Chemistry* **1999**, *37*, 1823–1837.
- (56) Duracher, D.; Elaïssari, A.; Pichot, C. Characterization of cross-linked poly (N-isopropylmethacrylamide) microgel latexes. *Colloid and Polymer Science* **1999**, *277*, 905–913.

-
- (57) Panayiotou, M.; Freitag, R. Synthesis and characterisation of stimuli-responsive poly (N,N'-diethylacrylamide) hydrogels. *Polymer* **2005**, *46*, 615–621.
- (58) Keerl, M.; Richtering, W. Synergistic depression of volume phase transition temperature in copolymer microgels. *Colloid and Polymer Science* **2007**, *285*, 471–474.
- (59) Keerl, M.; Smirnovas, V.; Winter, R.; Richtering, W. Interplay between hydrogen bonding and macromolecular architecture leading to unusual phase behavior in thermosensitive microgels. *Angewandte Chemie International Edition* **2008**, *47*, 338–341.
- (60) Brugger, B.; Rosen, B. A.; Richtering, W. Microgels as Stimuli-Responsive Stabilizers for Emulsions. *Langmuir* **2008**, *24*, 12202–12208.
- (61) Brugger, B.; Rütten, S.; Phan, K.-H.; Möller, M.; Richtering, W. The colloidal suprastructure of smart microgels at oil–water interfaces. *Angewandte Chemie International Edition* **2009**, *48*, 3978–3981.
- (62) Ngai, T.; Behrens, S. H.; Auweter, H. Novel emulsions stabilized by pH and temperature sensitive microgels. *Chemical communications* **2005**, 331–333.
- (63) Ngai, T.; Auweter, H.; Behrens, S. H. Environmental responsiveness of microgel particles and particle-stabilized emulsions. *Macromolecules* **2006**, *39*, 8171–8177.
- (64) Fujii, S.; Read, E. S.; Binks, B. P.; Armes, S. P. Stimulus-Responsive Emulsifiers Based on Nanocomposite Microgel Particles. *Advanced Materials* **2005**, *17*, 1014–1018.
- (65) Dupin, D.; Howse, J. R.; Armes, S. P.; Randall, D. P. Preparation of stable foams using sterically stabilized pH-responsive latexes synthesized by emulsion polymerization. *Journal of Materials Chemistry* **2008**, *18*, 545–552.
- (66) Horiguchi, Y.; Kawakita, H.; Ohto, K.; Morisada, S. Temperature-responsive Pickering foams stabilized by poly (N-isopropylacrylamide) nanogels. *Advanced Powder Technology* **2018**, *29*, 266–272.
- (67) Wu, D.; Mihali, V.; Honciuc, A. pH-responsive pickering foams generated by surfactant-free soft hydrogel particles. *Langmuir* **2018**, *35*, 212–221.
- (68) Lyon, L. A.; Fernandez-Nieves, A. The polymer/colloid duality of microgel suspensions. *Annual review of physical chemistry* **2012**, *63*, 25–43.
- (69) Monteillet, H.; Workamp, M.; Appel, J.; Kleijn, J. M.; Leermakers, F. A.; Sprakel, J. Ultrastrong anchoring yet barrier-free adsorption of composite microgels at liquid interfaces. *Advanced Materials Interfaces* **2014**, *1*, 1300121.
- (70) Geisel, K.; Isa, L.; Richtering, W. Unraveling the 3D localization and deformation of responsive microgels at oil/water interfaces: a step forward in understanding soft emulsion stabilizers. *Langmuir* **2012**, *28*, 15770–15776.
- (71) Destribats, M.; Lapeyre, V.; Wolfs, M.; Sellier, E.; Leal-Calderon, F.; Ravaine, V.; Schmitt, V. Soft microgels as Pickering emulsion stabilisers: role of particle deformability. *Soft Matter* **2011**, *7*, 7689–7698.

- (72) Camerin, F.; Fernández-Rodríguez, M. Á.; Rovigatti, L.; Antonopoulou, M.; Gnan, N.; Ninarello, A.; Isa, L.; Zaccarelli, E. Microgels Adsorbed at Liquid-Liquid Interfaces: A Joint Numerical and Experimental Study. *ACS Nano* **2019**, *13*, 4548–4559.
- (73) Fleer, G.; Stuart, M. C.; Scheutjens, J. M.; Cosgrove, T.; Vincent, B., *Polymers at interfaces*; Springer Science & Business Media: 1993.
- (74) Li, Z.; Ming, T.; Wang, J.; Ngai, T. High internal phase emulsions stabilized solely by microgel particles. *Angewandte Chemie International Edition* **2009**, *48*, 8490–8493.
- (75) Faulde, M.; Tonn, J.; Jupke, A. Microgels for the Intensification of Liquid-Liquid Extraction Processes—Feasibility and Advantages. *Chemical Engineering & Technology* **2020**, *43*, 137–142.
- (76) Rey, M.; Fernandez-Rodriguez, M. A.; Steinacher, M.; Scheidegger, L.; Geisel, K.; Richtering, W.; Squires, T. M.; Isa, L. Isostructural solid-solid phase transition in monolayers of soft core-shell particles at fluid interfaces: structure and mechanics. *Soft Matter* **2016**, *12*, 3545–3557.
- (77) Rauh, A.; Rey, M.; Barbera, L.; Zanini, M.; Karg, M.; Isa, L. Compression of hard core–soft shell nanoparticles at liquid–liquid interfaces: influence of the shell thickness. *Soft Matter* **2017**, *13*, 158–169.
- (78) Pinaud, F.; Geisel, K.; Massé, P.; Catargi, B.; Isa, L.; Richtering, W.; Ravaine, V.; Schmitt, V. Adsorption of microgels at an oil–water interface: correlation between packing and 2D elasticity. *Soft Matter* **2014**, *10*, 6963–6974.
- (79) Harrer, J.; Rey, M.; Ciarella, S.; Löwen, H.; Janssen, L. M. C.; Vogel, N. Stimuli-Responsive Behavior of PNIPAM Microgels under Interfacial Confinement. *Langmuir* **2019**, *35*, PMID: 31304759, 10512–10521.
- (80) Romeo, G.; Imperiali, L.; Kim, J.-W.; Fernandez-Nieves, A.; Weitz, D. A. Origin of de-swelling and dynamics of dense ionic microgel suspensions. *The Journal of chemical physics* **2012**, *136*, 124905.
- (81) Minato, H.; Murai, M.; Watanabe, T.; Matsui, S.; Takizawa, M.; Kureha, T.; Suzuki, D. The deformation of hydrogel microspheres at the air/water interface. *Chemical Communications* **2018**, *54*, 932–935.
- (82) Geisel, K.; Henzler, K.; Guttman, P.; Richtering, W. New insight into microgel-stabilized emulsions using transmission x-ray microscopy: nonuniform deformation and arrangement of microgels at liquid interfaces. *Langmuir* **2014**, *31*, 83–89.
- (83) Schmidt, S.; Liu, T.; Rütten, S.; Phan, K.-H.; Moeller, M.; Richtering, W. Influence of microgel architecture and oil polarity on stabilization of emulsions by stimuli-sensitive core-shell poly (N-isopropylacrylamide-co-methacrylic acid) microgels: Mickering versus Pickering behavior? *Langmuir* **2011**, *27*, 9801–9806.
- (84) Geisel, K.; Isa, L.; Richtering, W. The Compressibility of pH-Sensitive Microgels at the Oil-Water Interface: Higher Charge Leads to Less Repulsion. *Angewandte Chemie International Edition* **2014**, *53*, 4905–4909.

- (85) Maldonado-Valderrama, J.; del Castillo-Santaella, T.; Adroher-Benítez, I.; Moncho-Jordá, A.; Martín-Molina, A. Thermoresponsive microgels at the air–water interface: the impact of the swelling state on interfacial conformation. *Soft Matter* **2017**, *13*, 230–238.
- (86) Rey, M.; Hou, X.; Tang, J. S. J.; Vogel, N. Interfacial arrangement and phase transitions of PNiPAm microgels with different crosslinking densities. *Soft Matter* **2017**, *13*, 8717–8727.
- (87) Gong, Y.; Zhang, Z.; He, J. Deformation and stability of core–shell microgels at oil/water interface. *Industrial & Engineering Chemistry Research* **2017**, *56*, 14793–14798.
- (88) Geisel, K.; Rudov, A. A.; Potemkin, I. I.; Richtering, W. Hollow and core–shell microgels at oil–water interfaces: Spreading of soft particles reduces the compressibility of the monolayer. *Langmuir* **2015**, *31*, 13145–13154.
- (89) Picard, C.; Garrigue, P.; Tatry, M.-C.; Lapeyre, V.; Ravaine, S.; Schmitt, V.; Ravaine, V. Organization of microgels at the air–water interface under compression: Role of electrostatics and cross-linking density. *Langmuir* **2017**, *33*, 7968–7981.
- (90) Tatry, M.-C.; Qiu, Y.; Lapeyre, V.; Garrigue, P.; Schmitt, V.; Ravaine, V. Sugar-responsive Pickering emulsions mediated by switching hydrophobicity in microgels. *Journal of colloid and interface science* **2020**, *561*, 481–493.
- (91) Binks, B. P.; Murakami, R.; Armes, S. P.; Fujii, S. Effects of pH and salt concentration on oil-in-water emulsions stabilized solely by nanocomposite microgel particles. *Langmuir* **2006**, *22*, 2050–2057.
- (92) Tsuji, S.; Kawaguchi, H. Thermosensitive Pickering emulsion stabilized by poly (N-isopropylacrylamide)-carrying particles. *Langmuir* **2008**, *24*, 3300–3305.
- (93) Maestro, A.; Jones, D.; SÁnchez de Rojas Candela, C.; Guzman, E.; Duits, M. H. G.; Cicuta, P. Tuning Interfacial Properties and Processes by Controlling the Rheology and Structure of Poly(N-isopropylacrylamide) Particles at Air/Water Interfaces. *Langmuir* **2018**, *34*, 7067–7076.
- (94) Li, Z.; Richtering, W.; Ngai, T. Poly (N-isopropylacrylamide) microgels at the oil–water interface: temperature effect. *Soft Matter* **2014**, *10*, 6182–6191.
- (95) Deen, G. R.; Alsted, T.; Richtering, W.; Pedersen, J. S. Synthesis and characterization of nanogels of poly (N-isopropylacrylamide) by a combination of light and small-angle X-ray scattering. *Physical Chemistry Chemical Physics* **2011**, *13*, 3108–3114.
- (96) Brugger, B.; Vermant, J.; Richtering, W. Interfacial layers of stimuli-responsive poly-(N-isopropylacrylamide-co-methacrylicacid)(PNIPAM-co-MAA) microgels characterized by interfacial rheology and compression isotherms. *Physical Chemistry Chemical Physics* **2010**, *12*, 14573–14578.
- (97) Liu, T.; Seiffert, S.; Thiele, J.; Abate, A. R.; Weitz, D. A.; Richtering, W. Non-coalescence of oppositely charged droplets in pH-sensitive emulsions. *Proceedings of the National Academy of Sciences* **2012**, *109*, 384–389.
- (98) Israelachvili, J. N., *Intermolecular and surface forces*; Academic press: 2015.

- (99) Butt, H.-J.; Graf, K.; Kappl, M., *Physics and chemistry of interfaces*; John Wiley & Sons: 2013.
- (100) Lyklema, J., *Fundamentals of interface and colloid science: soft colloids*; Elsevier: 2005; Vol. 5.
- (101) Roberts, G., *Langmuir-blodgett films*; Springer Science & Business Media: 2013.
- (102) KSV NIMA, *Software Manual, Langmuir and Langmuir Blodgett Devices*, 1.4; Biolin Scientific Oy: 2013.
- (103) Blodgett, K. B. Monomolecular Films of Fatty Acids on Glass. *Journal of the American Chemical Society* **1934**, *56*, 495–495.
- (104) Blodgett, K. B. Films Built by Depositing Successive Monomolecular Layers on a Solid Surface. *Journal of the American Chemical Society* **1935**, *57*, 1007–1022.
- (105) Schulman, J.; Waterhouse, B.; Spink, J. Adhesion of amphipathic molecules to solid surfaces. *Kolloid-Zeitschrift* **1956**, *146*, 77–95.
- (106) Langmuir, I.; Schaefer, V. J. Activities of Urease and Pepsin Monolayers. *Journal of the American Chemical Society* **1938**, *60*, 1351–1360.
- (107) Gaines, G., *Insoluble Monolayers at Liquid-gas Interfaces*; Interscience Publisher: 1991.
- (108) Geisel, K.; Richtering, W.; Isa, L. Highly ordered 2D microgel arrays: compression versus self-assembly. *Soft Matter* **2014**, *10*, 7968–7976.
- (109) AFM and combined optical techniques. *Materials Today* **2009**, *12*, 40–45.
- (110) Reifengerger, R., *Fundamentals of Atomic Force Microscopy: Part I: Foundations*; World Scientific Publishing Company Pte. Limited: 2016.
- (111) Akamine, S.; Barrett, R.; Quate, C. Improved atomic force microscope images using microcantilevers with sharp tips. *Applied Physics Letters* **1990**, *57*, 316–318.
- (112) Lee, J. S.; Song, J.; Kim, S. O.; Kim, S.; Lee, W.; Jackman, J. A.; Kim, D.; Cho, N.-J.; Lee, J. Multifunctional hydrogel nano-probes for atomic force microscopy. *Nature communications* **2016**, *7*, 1–14.
- (113) Meyer, E.; Hug, H. J.; Bennewitz, R., *Scanning probe microscopy: the lab on a tip*; Springer Science & Business Media: 2003.
- (114) Wilson, N. R.; Macpherson, J. V. Carbon nanotube tips for atomic force microscopy. *Nature nanotechnology* **2009**, *4*, 483.
- (115) Butt, H.-J. Measuring electrostatic, van der Waals, and hydration forces in electrolyte solutions with an atomic force microscope. *Biophysical journal* **1991**, *60*, 1438–1444.
- (116) Ducker, W. A.; Senden, T. J.; Pashley, R. M. Direct measurement of colloidal forces using an atomic force microscope. *Nature* **1991**, *353*, 239–241.
- (117) Meyer, G.; Amer, N. M. Novel optical approach to atomic force microscopy. *Applied physics letters* **1988**, *53*, 2400–2402.

- (118) Marti, O.; Elings, V.; Haugan, M.; Bracker, C.; Schneir, J.; Drake, B.; Gould, S.; Gurley, J.; Hellemans, L.; Shaw, K., et al. Scanning probe microscopy of biological samples and other surfaces. *Journal of microscopy* **1988**, *152*, 803–809.
- (119) Zhong, Q.; Inniss, D.; Kjoller, K.; Elings, V. Fractured polymer/silica fiber surface studied by tapping mode atomic force microscopy. *Surface Science Letters* **1993**, *290*, L688–L692.
- (120) Schmitz, I.; Schreiner, M.; Friedbacher, G.; Grasserbauer, M. Phase imaging as an extension to tapping mode AFM for the identification of material properties on humidity-sensitive surfaces. *Applied surface science* **1997**, *115*, 190–198.
- (121) Magonov, S.; Elings, V.; Whangbo, M.-H. Phase imaging and stiffness in tapping-mode atomic force microscopy. *Surface science* **1997**, *375*, L385–L391.
- (122) Mendoza, F.; Lu, R., *Basics of image analysis*; Springer: 2015, pp 9–56.
- (123) Pavlidis, T. Image analysis. *Annual review of computer science* **1988**, *3*, 121–146.
- (124) Somerville, P. J. Method and apparatus for barcode recognition in a digital image., US Patent 4,992,650, 1991.
- (125) Bauer, S.; Wiest, R.; Nolte, L.-P.; Reyes, M. A survey of MRI-based medical image analysis for brain tumor studies. *Physics in Medicine & Biology* **2013**, *58*, R97.
- (126) Socolinsky, D. A.; Selinger, A., *A comparative analysis of face recognition performance with visible and thermal infrared imagery*, 2002; Vol. 4, pp 217–222.
- (127) Häne, C.; Sattler, T.; Pollefeys, M., *Obstacle detection for self-driving cars using only monocular cameras and wheel odometry*, 2015, pp 5101–5108.
- (128) Crocker, J. C.; Grier, D. G. Methods of Digital Video Microscopy for Colloidal Studies. *Journal of Colloid and Interface Science* **1996**, *179*, 298–310.
- (129) Blair, D.; Dufresne, E. The Matlab Particle Tracking Code Repository. <http://site.physics.georgetown.edu/matlab/> (accessed 03/01/2010).
- (130) Canny, J. A computational approach to edge detection. *IEEE Transactions on pattern analysis and machine intelligence* **1986**, 679–698.
- (131) Prewitt, J. M. Object enhancement and extraction. *Picture processing and Psychopictorics* **1970**, *10*, 15–19.
- (132) Henderson, D. J.; Parmeter, C. F.; Russell, R. R. Modes, weighted modes, and calibrated modes: evidence of clustering using modality tests. *Journal of Applied Econometrics* **2008**, *23*, 607–638.
- (133) Tompkins, H.; Irene, E. A., *Handbook of ellipsometry*; William Andrew: 2005.
- (134) Fujiwara, H., *Spectroscopic ellipsometry: principles and applications*; John Wiley & Sons: 2007.
- (135) Cubitt, R.; Fragneto, G., *Neutron Reflection: Principles and Examples of Applications*; Elsevier: 2002, pp 1198–1208.

- (136) Daillant, J.; Gibaud, A., *X-ray and neutron reflectivity: principles and applications*; Springer: 2008; Vol. 770.
- (137) Penfold, J.; Thomas, R. K. Neutron reflectivity and small angle neutron scattering: An introduction and perspective on recent progress. *Current opinion in colloid & interface science* **2014**, *19*, 198–206.
- (138) Fragneto, G.; Delhom, R.; Joly, L.; Scoppola, E. Neutrons and model membranes: Moving towards complexity. *Current opinion in colloid & interface science* **2018**, *38*, 108–121.
- (139) Braun, L.; Uhlig, M.; von Klitzing, R.; Campbell, R. A. Polymers and surfactants at fluid interfaces studied with specular neutron reflectometry. *Advances in colloid and interface science* **2017**, *247*, 130–148.
- (140) Römer, H. Theoretical optics. *Weinheim: Wiley-VCH* **2005**.
- (141) Gross, H. Handbook of Optical Systems, Volume 1, Fundamentals of Technical Optics. **2005**, 848.
- (142) Hentschel, K. Das Brechungsgesetz in der Fassung von Snellius. *Archive for history of exact sciences* **2001**, *55*, 297–344.
- (143) Born, M.; Wolf, E., *Principles of optics: electromagnetic theory of propagation, interference and diffraction of light*; Elsevier: 2013.
- (144) Sears, V. F. An Introduction to the Theory of Neutron Optical Phenomena and Their Applications., 1989.
- (145) Sears, V. F. Neutron scattering lengths and cross sections. *Neutron news* **1992**, *3*, 26–37.
- (146) Heavens, O. S., *Optical properties of thin solid films*; Courier Corporation: 1991.
- (147) Glaisher, J. On a class of definite integrals. *Philosophical Magazine and Journal of Science* **1871**, *42*, 294–302.
- (148) Hauptman, H. The direct methods of X-ray crystallography. *Science* **1986**, *233*, 178–183.
- (149) Bosch, S. Double layer ellipsometry: an efficient numerical method for data analysis. *Surface science* **1993**, *289*, 411–417.
- (150) Charlot, D.; Maruani, A. Ellipsometric data processing: an efficient method and an analysis of the relative errors. *Applied optics* **1985**, *24*, 3368–3373.
- (151) Schmitt, V.; Ravaine, V. Surface compaction versus stretching in Pickering emulsions stabilised by microgels. *Current Opinion in Colloid & Interface Science* **2013**, *18*, 532–541.
- (152) Destribats, M.; Lapeyre, V.; Sellier, E.; Leal-Calderon, F.; Schmitt, V.; Ravaine, V. Water-in-oil emulsions stabilized by water-dispersible poly (N-isopropylacrylamide) microgels: Understanding anti-Finkle behavior. *Langmuir* **2011**, *27*, 14096–14107.
- (153) Style, R. W.; Isa, L.; Dufresne, E. R. Adsorption of soft particles at fluid interfaces. *Soft Matter* **2015**, *11*, 7412–7419.
- (154) Mehrabian, H.; Harting, J.; Snoeijer, J. H. Soft particles at a fluid interface. *Soft Matter* **2016**, *12*, 1062–1073.

-
- (155) Schulte, M. F.; Scotti, A.; Gelissen, A. P.; Richtering, W.; Mourran, A. Probing the Internal Heterogeneity of Responsive Microgels Adsorbed to an Interface by a Sharp SFM Tip: Comparing Core–Shell and Hollow Microgels. *Langmuir* **2018**, *34*, 4150–4158.
- (156) Destribats, M.; Eyharts, M.; Lapeyre, V.; Sellier, E.; Varga, I.; Ravaine, V.; Schmitt, V. Impact of pNIPAM microgel size on its ability to stabilize Pickering emulsions. *Langmuir* **2014**, *30*, 1768–1777.
- (157) Deshmukh, O. S.; Maestro, A.; Duits, M. H.; van den Ende, D.; Stuart, M. C.; Mugele, F. Equation of state and adsorption dynamics of soft microgel particles at an air–water interface. *Soft Matter* **2014**, *10*, 7045–7050.
- (158) Siemes, E.; Nevskiy, O.; Sysoiev, D.; Turnhoff, S. K.; Oppermann, A.; Huhn, T.; Richtering, W.; Wöll, D. Nanoscopic visualization of cross-linking density in polymer networks with diarylethene photoswitches. *Angewandte Chemie International Edition* **2018**, *57*, 12280–12284.
- (159) Li, Z.; Geisel, K.; Richtering, W.; Ngai, T. Poly(N-isopropylacrylamide) microgels at the oil-water interface: adsorption kinetics. *Soft Matter* **2013**, *9*, 9939–9946.
- (160) Hu, X.; Tong, Z.; Lyon, L. A. Synthesis and physicochemical properties of cationic microgels based on poly (N-isopropylmethacrylamide). *Colloid and polymer science* **2011**, *289*, 333–339.
- (161) Gelissen, A. P.; Oppermann, A.; Caumanns, T.; Hebbeker, P.; Turnhoff, S. K.; Tiwari, R.; Eisold, S.; Simon, U.; Lu, Y.; Mayer, J.; Richtering, W.; Walther, A.; Woell, D. 3D structures of responsive nanocompartmentalized microgels. *Nano letters* **2016**, *16*, 7295–7301.
- (162) Lopez-Leon, T.; Ortega-Vinuesa, J. L.; Bastos-Gonzalez, D.; Ellassari, A. Cationic and Anionic Poly(N-isopropylacrylamide) Based Submicron Gel Particles: Electrokinetic Properties and Colloidal Stability. *The Journal of Physical Chemistry B* **2006**, *110*, 4629–4636.
- (163) Lopez, C. G.; Richtering, W. Does Flory-Rehner theory quantitatively describe the swelling of thermoresponsive microgels? *Soft Matter* **2017**, *13*, 8271–8280.
- (164) Mohanty, P. S.; Nöjd, S.; Van Gruijthuijsen, K.; Crassous, J. J.; Obiols-Rabasa, M.; Schweins, R.; Stradner, A.; Schurtenberger, P. Interpenetration of polymeric microgels at ultrahigh densities. *Scientific reports* **2017**, *7*, 1487.
- (165) Scotti, A.; Denton, A. R.; Brugnoli, M.; Houston, J. E.; Schweins, R.; Potemkin, I. I.; Richtering, W. Deswelling of Microgels in Crowded Suspensions Depends on Cross-Link Density and Architecture. *Macromolecules* **2019**, *52*, 3995–4007.
- (166) Cors, M.; Wiehemeier, L.; Hertle, Y.; Feoktystov, A.; Cousin, F.; Hellweg, T.; Oberdisse, J. Determination of Internal Density Profiles of Smart Acrylamide-Based Microgels by Small-Angle Neutron Scattering: A Multishell Reverse Monte Carlo Approach. *Langmuir* **2018**, *34*, 15403–15415.
- (167) Hasegawa, Y., *Compendium of Surface and Interface Analysis*; Springer Singapore: 2018.

- (168) Ricardo, G. In *Amplitude Modulation Atomic Force Microscopy*; John Wiley and Sons, Ltd: 2010; Chapter 7, pp 91–101.
- (169) Zeppieri, S.; Rodríguez, J.; López de Ramos, A. Interfacial tension of alkane+water systems. *Journal of Chemical & Engineering Data* **2001**, *46*, 1086–1088.
- (170) Zielińska, K.; Sun, H.; Campbell, R. A.; Zarbakhsh, A.; Resmini, M. Smart nanogels at the air/water interface: structural studies by neutron reflectivity. *Nanoscale* **2016**, *8*, 4951–4960.
- (171) Authier, A. International Tables for Crystallography: Physical properties of crystals. *Elastic* **2003**, *70*, 6.
- (172) Bolhuis, P.; Hagen, M.; Frenkel, D. Isostructural solid-solid transition in crystalline systems with short-ranged interaction. *Physical Review E* **1994**, *50*, 4880.
- (173) De Aguiar, I. B.; Van de Laar, T.; Meireles, M.; Bouchoux, A.; Sprakel, J.; Schroën, K. Deswelling and deformation of microgels in concentrated packings. *Scientific reports* **2017**, *7*, 10223.
- (174) Möhwald, H. Surfactant layers at water surfaces. *Reports on Progress in Physics* **1993**, *56*, 653.
- (175) Wu, J.; Zhou, B.; Hu, Z. Phase behavior of thermally responsive microgel colloids. *Physical Review Letters* **2003**, *90*, 048304.
- (176) Friedman, J. H.; Bentley, J. L.; Finkel, R. A. An algorithm for finding best matches in logarithmic expected time. *ACM Transactions on Mathematical Software (TOMS)* **1977**, *3*, 209–226.
- (177) Rumyantsev, A. M.; Gumerov, R. A.; Potemkin, I. I. A polymer microgel at a liquid–liquid interface: theory vs. computer simulations. *Soft Matter* **2016**, *12*, 6799–6811.
- (178) Vargaftik, N.; Volkov, B.; Voljak, L. International tables of the surface tension of water. *Journal of Physical and Chemical Reference Data* **1983**, *12*, 817–820.
- (179) Behroozi, F. Theory of elasticity in two dimensions and its application to Langmuir-Blodgett films. *Langmuir* **1996**, *12*, 2289–2291.
- (180) Thorpe, M.; JaSIUK, I. New results in the theory of elasticity for two-dimensional composites. *Proceedings of the Royal Society of London. Series A: Mathematical and Physical Sciences* **1992**, *438*, 531–544.
- (181) Camerin, F.; Gnan, N.; Ruiz-Franco, J.; Ninarello, A.; Rovigatti, L.; Zaccarelli, E. Microgels at interfaces behave as 2D elastic particles featuring reentrant melting. *arXiv preprint arXiv:2001.06237* **2020**.
- (182) Burmistrova, A.; Richter, M.; Uzum, C.; Klitzing, R. v. Effect of cross-linker density of P (NIPAM-co-AAc) microgels at solid surfaces on the swelling/shrinking behaviour and the Young's modulus. *Colloid and Polymer Science* **2011**, *289*, 613–624.
- (183) Hashmi, S. M.; Dufresne, E. R. Mechanical properties of individual microgel particles through the deswelling transition. *Soft Matter* **2009**, *5*, 3682–3688.

-
- (184) Voudouris, P.; Florea, D.; van der Schoot, P.; Wyss, H. M. Micromechanics of temperature sensitive microgels: dip in the Poisson ratio near the LCST. *Soft Matter* **2013**, *9*, 7158–7166.
 - (185) Boon, N.; Schurtenberger, P. Swelling of micro-hydrogels with a crosslinker gradient. *Physical Chemistry Chemical Physics* **2017**, *19*, 23740–23746.
 - (186) Okumura, Y.; Kawaguchi, M. Surface pressure–area isotherms and surface dilational moduli of poly (N-isopropyl acrylamide) monolayers spread at air–water interface. *Colloids and Surfaces A: Physicochemical and Engineering Aspects* **2014**, *441*, 275–280.
 - (187) Saito, W.; Mori, O.; Ikeo, Y.; Kawaguchi, M.; Imae, T.; Kato, T. Surface pressure, ellipsometric, and atomic force microscopic study of poly (N-isopropylacrylamide) film at the air-water interface. *Macromolecules* **1995**, *28*, 7945–7946.
 - (188) Richardson, R. M.; Pelton, R.; Cosgrove, T.; Zhang, J. A Neutron Reflectivity Study of Poly (N-isopropylacrylamide) at the Air- Water Interface with and without Sodium Dodecyl Sulfate. *Macromolecules* **2000**, *33*, 6269–6274.
 - (189) Backes, S.; Von Klitzing, R. Nanomechanics and nanorheology of microgels at interfaces. *Polymers* **2018**, *10*, 978.
 - (190) Tagit, O.; Tomczak, N.; Vancso, G. J. Probing the Morphology and Nanoscale Mechanics of Single Poly (N-isopropylacrylamide) Microgels Across the Lower-Critical-Solution Temperature by Atomic Force Microscopy. *Small* **2008**, *4*, 119–126.
 - (191) Vasudevan, S. A.; Rauh, A.; Kröger, M.; Karg, M.; Isa, L. Dynamics and Wetting Behavior of Core–Shell Soft Particles at a Fluid–Fluid Interface. *Langmuir* **2018**, *34*, 15370–15382.
 - (192) Treloar, L. R. G., *The physics of rubber elasticity*; Oxford University Press, USA: 1975.
 - (193) Demond, A. H.; Lindner, A. S. Estimation of interfacial tension between organic liquids and water. *Environmental science & technology* **1993**, *27*, 2318–2331.
 - (194) Mourran, A.; Wu, Y.; Gumerov, R. A.; Rudov, A. A.; Potemkin, I. I.; Pich, A.; Moeller, M. When colloidal particles become polymer coils. *Langmuir* **2016**, *32*, 723–730.
 - (195) Scotti, A.; Gasser, U.; Herman, E.; Han, J.; Menzel, A.; Lyon, L. A.; Fernandez-Nieves, A. Phase behavior of binary and polydisperse suspensions of compressible microgels controlled by selective particle deswelling. *Physical Review E* **2017**, *96*, 032609.
 - (196) Yunker, P. J.; Chen, K.; Gratale, M. D.; Lohr, M. A.; Still, T.; Yodh, A. Physics in ordered and disordered colloidal matter composed of poly (N-isopropylacrylamide) microgel particles. *Reports on Progress in Physics* **2014**, *77*, 056601.
 - (197) Brown, A. C.; Stabenfeldt, S. E.; Ahn, B.; Hannan, R. T.; Dhada, K. S.; Herman, E. S.; Stefanelli, V.; Guzzetta, N.; Alexeev, A.; Lam, W. A., et al. Ultrasoft microgels displaying emergent platelet-like behaviours. *Nature materials* **2014**, *13*, 1108–1114.

- (198) Karg, M.; Pastoriza-Santos, I.; Liz-Marzán, L. M.; Hellweg, T. A versatile approach for the preparation of thermosensitive PNIPAM core-shell microgels with nanoparticle cores. *ChemPhysChem* **2006**, *7*, 2298–2301.
- (199) Virtanen, O. L. J.; Mourran, A.; Pinard, P. T.; Richtering, W. Persulfate initiated ultra-low cross-linked poly(N-isopropylacrylamide) microgels possess an unusual inverted cross-linking structure. *Soft Matter* **2016**, *12*, 3919–3928.
- (200) Wypysek, S. K.; Scotti, A.; Alziyadi, M. O.; Potemkin, I. I.; Denton, A. R.; Richtering, W. Tailoring the Cavity of Hollow Polyelectrolyte Microgels. *Macromolecular rapid communications* **2020**, *41*, 1900422.
- (201) Nickel, A. C.; Scotti, A.; Houston, J. E.; Ito, T.; Crassous, J.; Pedersen, J. S.; Richtering, W. Anisotropic Hollow Microgels That Can Adapt Their Size, Shape, and Softness. *Nano letters* **2019**, *19*, 8161–8170.
- (202) Gavrilov, A. A.; Richtering, W.; Potemkin, I. I. Polyelectrolyte Microgels at a Liquid-Liquid Interface: Swelling and Long-Range Ordering. *The Journal of Physical Chemistry B* **2019**, *123*, 8590–8598.
- (203) Pynn, R., *Neutron scattering—a non-destructive microscope for seeing inside matter*; Springer: 2009, pp 15–36.
- (204) Zielińska, K.; Campbell, R. A.; Zarbakhsh, A.; Resmini, M. Adsorption versus aggregation of NIPAM nanogels: new insight into their behaviour at the air/water interface as a function of concentration. *Physical Chemistry Chemical Physics* **2017**, *19*, 17173–17179.
- (205) Gutfreund, P.; Saerbeck, T.; Gonzalez, M. A.; Pellegrini, E.; Laver, M.; Dewhurst, C.; Cubitt, R. Towards generalized data reduction on a chopper-based time-of-flight neutron reflectometer. *Journal of Applied Crystallography* **2018**, *51*, 606–615.
- (206) Richard, D.; Ferrand, M.; Kearley, G. Lamp, the large array manipulation program. *J. Neutron Res* **1996**, *4*, 33–39.
- (207) Parratt, L. G. Surface studies of solids by total reflection of X-rays. *Physical review* **1954**, *95*, 359.
- (208) Nelson, A. Co-refinement of multiple-contrast neutron/X-ray reflectivity data using MOTOFIT. *Journal of applied crystallography* **2006**, *39*, 273–276.
- (209) Nevot, L.; Croce, P. Characterization of surfaces by grazing X-ray reflection: Application to the study of the polishing of various silicate glasses. *Rev. Phys. Appl.* **1991**, *15*, 761–779.
- (210) Andrews, L. C., *Special functions of mathematics for engineers*; Spie Press: 1998; Vol. 49.
- (211) NCNR Neutron Activation and Scattering Calculator. <https://www.ncnr.nist.gov/resources/activation/> (accessed 02/03/2019).
- (212) Kiessig, H. Interferenz von Röntgenstrahlen an dünnen Schichten. *Annalen der Physik* **1931**, *402*, 769–788.
- (213) Bragg, W. H.; Bragg, W. L. The reflection of X-rays by crystals. *Proceedings of the Royal Society of London. Series A, Containing Papers of a Mathematical and Physical Character* **1913**, *88*, 428–438.

-
- (214) Fritzsche, H.; Huot, J.; Fruchart, D., *Neutron scattering and other nuclear techniques for hydrogen in materials*; Springer: 2016.
- (215) Korosi, G.; Kovats, E. S. Density and surface tension of 83 organic liquids. *Journal of Chemical and Engineering Data* **1981**, *26*, 323–332.
- (216) Gumerov, R. A.; Rumyantsev, A. M.; Rudov, A. A.; Pich, A.; Richtering, W.; Möller, M.; Potemkin, I. I. Mixing of two immiscible liquids within the polymer microgel adsorbed at their interface. *ACS Macro Letters* **2016**, *5*, 612–616.
- (217) Brugnioni, M.; Nickel, A. C.; Kröger, L. C.; Scotti, A.; Pich, A.; Leonhard, K.; Richtering, W. Synthesis and structure of deuterated ultra-low cross-linked poly (N-isopropylacrylamide) microgels. *Polymer Chemistry* **2019**, *10*, 2397–2405.
- (218) Schulte, M. F.; Scotti, A.; Brugnioni, M.; Bochenek, S.; Mourran, A.; Richtering, W. Tuning the Structure and Properties of Ultra-Low Cross-Linked Temperature-Sensitive Microgels at Interfaces via the Adsorption Pathway. *Langmuir* **2019**, *35*, 14769–14781.
- (219) Rennie, A.; Crawford, R.; Lee, E.; Thomas, R.; Crowley, T.; Roberts, S.; Qureshi, M.; Richards, R. Adsorption of poly (ethylene oxide) at the air-solution interface studied by neutron reflection. *Macromolecules* **1989**, *22*, 3466–3475.
- (220) Scotti, A.; Brugnioni, M.; Lopez, C. G.; Bochenek, S.; Crassous, J. J.; Richtering, W. Flow properties reveal the particle-to-polymer transition of ultra-low crosslinked microgels. *Soft Matter* **2020**.
- (221) Wang, J.-S.; Matyjaszewski, K. Controlled/" living" radical polymerization. atom transfer radical polymerization in the presence of transition-metal complexes. *Journal of the American Chemical Society* **1995**, *117*, 5614–5615.
- (222) Kato, M.; Kamigaito, M.; Sawamoto, M.; Higashimura, T. Polymerization of methyl methacrylate with the carbon tetrachloride/dichlorotris-(triphenylphosphine) ruthenium (II)/methylaluminum bis (2, 6-di-tert-butylphenoxide) initiating system: possibility of living radical polymerization. *Macromolecules* **1995**, *28*, 1721–1723.
- (223) Batchelor, G. K. The effect of Brownian motion on the bulk stress in a suspension of spherical particles. *J. Fluid Mech.* **1977**, *83*, 97–117.
- (224) Liu, R. C.; Cantin, S.; Perrot, F.; Winnik, F. M. Effects of polymer architecture and composition on the interfacial properties of temperature-responsive hydrophobically-modified poly (N-isopropylacrylamides). *Polymers for advanced technologies* **2006**, *17*, 798–803.
- (225) Vilanove, R.; Rondelez, F. Scaling description of two-dimensional chain conformations in polymer monolayers. *Physical Review Letters* **1980**, *45*, 1502.
- (226) Netz, R. R.; Andelman, D. Neutral and charged polymers at interfaces. *Physics reports* **2003**, *380*, 1–95.
- (227) Zhang, J.; Pelton, R. The surface tension of aqueous poly (N-isopropylacrylamide-co-acrylamide). *Journal of Polymer Science Part A: Polymer Chemistry* **1999**, *37*, 2137–2143.

- (228) De Gennes, P. Polymers at an interface; a simplified view. *Advances in colloid and interface science* **1987**, *27*, 189–209.
- (229) Zhao, L.; Lin, Z. Self-assembly of non-linear polymers at the air/water interface: the effect of molecular architecture. *Soft Matter* **2011**, *7*, 10520–10535.
- (230) Halperin, A.; Joanny, J. Adsorption of star polymers. *Journal de Physique II* **1991**, *1*, 623–636.
- (231) Dubbert, J.; Nothdurft, K.; Karg, M.; Richtering, W. Core–Shell–Shell and Hollow Double-Shell Microgels with Advanced Temperature Responsiveness. *Macromolecular rapid communications* **2015**, *36*, 159–164.
- (232) Flory, P. J., *Principles of polymer chemistry*; Cornell University Press: 1953.
- (233) Daoud, M.; Cotton, J.; Farnoux, B.; Jannink, G.; Sarma, G.; Benoit, H.; Duplessix, C.; Picot, C.; De Gennes, P. Solutions of flexible polymers. Neutron experiments and interpretation. *Macromolecules* **1975**, *8*, 804–818.
- (234) Witte, K. N.; Kewalramani, S.; Kuzmenko, I.; Sun, W.; Fukuto, M.; Won, Y.-Y. Formation and collapse of single-monomer-thick monolayers of poly (n-butyl acrylate) at the air- water interface. *Macromolecules* **2010**, *43*, 2990–3003.
- (235) Kawaguchi, M.; Yoshida, A.; Takahashi, A. Experimental determination of the temperature-concentration diagram of Daoud and Jannink in two-dimensional space by surface pressure measurements. *Macromolecules* **1983**, *16*, 956–961.
- (236) Lebedeva, N. V.; Sun, F. C.; Lee, H.-i.; Matyjaszewski, K.; Sheiko, S. S. “Fatal Adsorption” of Brushlike Macromolecules: High Sensitivity of C–C Bond Cleavage Rates to Substrate Surface Energy. *Journal of the American Chemical Society* **2008**, *130*, 4228–4229.
- (237) Rubinstein, M.; Colby, R. H., et al., *Polymer physics*; Oxford university press New York: 2003; Vol. 23.
- (238) Gasser, U. Crystallization in three-and two-dimensional colloidal suspensions. *Journal of Physics: Condensed Matter* **2009**, *21*, 203101.
- (239) Keidel, R.; Ghavami, A.; Lugo, D. M.; Lotze, G.; Virtanen, O.; Beumers, P.; Pedersen, J. S.; Bardow, A.; Winkler, R. G.; Richtering, W. Time-resolved structural evolution during the collapse of responsive hydrogels: The microgel-to-particle transition. *Science advances* **2018**, *4*, eaao7086.
- (240) Scotti, A.; Gasser, U.; Herman, E. S.; Pelaez-Fernandez, M.; Lyon, L. A.; Fernandez-Nieves, A. The role of ions in the self-healing behavior of soft particle suspensions. *Proc. Natl. Acad. Sci. USA* **2016**, *113*, 5576–5581.
- (241) Han, Y.; Ha, N.; Alsayed, A.; Yodh, A. Melting of two-dimensional tunable-diameter colloidal crystals. *Physical Review E* **2008**, *77*, 041406.
- (242) Peng, Y.; Li, W.; Wang, F.; Still, T.; Yodh, A. G.; Han, Y. Diffusive and martensitic nucleation kinetics in solid-solid transitions of colloidal crystals. *Nature communications* **2017**, *8*, 1–12.
- (243) Gao, J.; Frisken, B. J. Cross-linker-free N-isopropylacrylamide gel nanospheres. *Langmuir* **2003**, *19*, 5212–5216.

-
- (244) Andersson, M.; Maunu, S. L. Structural studies of poly (N-isopropylacrylamide) microgels: Effect of SDS surfactant concentration in the microgel synthesis. *Journal of Polymer Science Part B: Polymer Physics* **2006**, *44*, 3305–3314.
- (245) Klapetek, P.; Necas, D.; Anderson, C. Gwyddion user guide., 2018.
- (246) Le Coeur, C.; Demé, B.; Longeville, S. Compression of random coils due to macromolecular crowding. *Physical Review E* **2009**, *79*, 031910.
- (247) Watkins, H. M.; Simon, A. J.; Sosnick, T. R.; Lipman, E. A.; Hjelm, R. P.; Plaxco, K. W. Random coil negative control reproduces the discrepancy between scattering and FRET measurements of denatured protein dimensions. *Proceedings of the National Academy of Sciences* **2015**, *112*, 6631–6636.
- (248) Koppel, D. E. Analysis of macromolecular polydispersity in intensity correlation spectroscopy: the method of cumulants. *The Journal of Chemical Physics* **1972**, *57*, 4814–4820.
- (249) Burchard, W.; Richtering, W. In *Relaxation in Polymers*, Pietralla, M., Pechhold, W., Eds.; Steinkopff: Darmstadt, 1989, pp 151–163.
- (250) Provencher, S. W. Inverse problems in polymer characterization: direct analysis of polydispersity with photon correlation spectroscopy. *Die Makromolekulare Chemie: Macromolecular Chemistry and Physics* **1979**, *180*, 201–209.
- (251) Provencher, S. W. A constrained regularization method for inverting data represented by linear algebraic or integral equations. *Computer Physics Communications* **1982**, *27*, 213–227.
- (252) Scotti, A.; Liu, W.; Hyatt, J. S.; Herman, E. S.; Choi, H. S.; Kim, J.; Lyon, L. A.; Gasser, U.; Fernandez-Nieves, A. The CONTIN algorithm and its application to determine the size distribution of microgel suspensions. *J. Chem. Phys.* **2015**, *142*, 234905.
- (253) Royall, C. P.; Poon, W. C.; Weeks, E. R. In search of colloidal hard spheres. *Soft Matter* **2013**, *9*, 17–27.
- (254) Pusey, P. N.; Van Megen, W. Phase behaviour of concentrated suspensions of nearly hard colloidal spheres. *Nature* **1986**, *320*, 340–342.
- (255) Agrawal, R.; Kofke, D. A. Thermodynamic and structural properties of model systems at solid-fluid coexistence: I. fcc and bcc soft spheres. *Molecular physics* **1995**, *85*, 23–42.
- (256) Paulin, S.; Ackerson, B.; Wolfe, M. Equilibrium and Shear Induced Nonequilibrium Phase Behavior of PMMA Microgels Spheres. *J. Colloid and Inter. Sci.* **1996**, *178*, 251–262.
- (257) Stieger M. Lindner, P.; Richtering, W. Structure formation in thermoresponsive microgel suspensions under shear flow. *J. of Phys.: Cond. Matt.* **2004**, *16*, S3861.
- (258) Roiter, Y.; Minko, S. AFM single molecule experiments at the solid- liquid interface: in situ conformation of adsorbed flexible polyelectrolyte chains. *Journal of the American Chemical Society* **2005**, *127*, 15688–15689.
- (259) Luding, S. Global equation of state of two-dimensional hard sphere systems. *Physical Review E* **2001**, *63*, 042201.

- (260) Samorí, P.; Ecker, C.; Gössl, I.; de Witte, P. A.; Cornelissen, J. J.; Metselaar, G. A.; Otten, M. B.; Rowan, A. E.; Nolte, R. J.; Rabe, J. P. High shape persistence in single polymer chains rigidified with lateral hydrogen bonded networks. *Macromolecules* **2002**, *35*, 5290–5294.
- (261) Gumerov, R. A.; Rudov, A. A.; Richtering, W.; Moeller, M.; Potemkin, I. I. Amphiphilic Arborescent Copolymers and Microgels: From Unimolecular Micelles in a Selective Solvent to the Stable Monolayers of Variable Density and Nanostructure at a Liquid Interface. *ACS Appl. Mater. Interfaces* **2017**, *9*, 31302–31316.
- (262) Pronk, S.; Frenkel, D. Melting of polydisperse hard disks. *Physical Review E* **2004**, *69*, 066123.
- (263) Cox, J. K.; Yu, K.; Constantine, B.; Eisenberg, A.; Lennox, R. B. Polystyrene-Poly (ethylene oxide) Diblock Copolymers Form Well-Defined Surface Aggregates at the Air/Water Interface. *Langmuir* **1999**, *15*, 7714–7718.
- (264) Cox, J.; áBruce Lennox, R., et al. Compression of polystyrene–poly (ethylene oxide) surface aggregates at the air/water interface. *Physical Chemistry Chemical Physics* **1999**, *1*, 4417–4421.
- (265) Szekeres, M.; Kamalin, O.; Grobet, P.; Schoonheydt, R.; Wostyn, K.; Clays, K.; Persoons, A.; Dékány, I. Two-dimensional ordering of Stoeber silica particles at the air/water interface. *Colloids and Surfaces A: Physicochemical and Engineering Aspects* **2003**, *227*, 77–83.
- (266) Meijer, J.-M.; Pal, A.; Ouahjji, S.; Lekkerkerker, H. N.; Philipse, A. P.; Petukhov, A. V. Observation of solid–solid transitions in 3D crystals of colloidal superballs. *Nature communications* **2017**, *8*, 1–8.
- (267) Sigolaeva, L. V.; Gladyr, S. Y.; Mergel, O.; Gelissen, A. P.; Noyong, M.; Simon, U.; Pergushov, D. V.; Kurochkin, I. N.; Plamper, F. A.; Richtering, W. Easy-preparable butyrylcholinesterase/microgel construct for facilitated organophosphate biosensing. *Analytical chemistry* **2017**, *89*, 6091–6098.
- (268) Matsui, S.; Kureha, T.; Hiroshige, S.; Shibata, M.; Uchihashi, T.; Suzuki, D. Fast adsorption of soft hydrogel microspheres on solid surfaces in aqueous solution. *Angewandte Chemie* **2017**, *129*, 12314–12317.
- (269) Douglas, A. M.; Fragkopoulos, A. A.; Gaines, M. K.; Lyon, L. A.; Fernandez-Nieves, A.; Barker, T. H. Dynamic assembly of ultrasoft colloidal networks enables cell invasion within restrictive fibrillar polymers. *Proceedings of the National Academy of Sciences* **2017**, *114*, 885–890.
- (270) Eibel, A.; Fast, D. E.; Sattelkow, J.; Zalibera, M.; Wang, J.; Huber, A.; Müller, G.; Neshchadin, D.; Dietliker, K.; Plank, H., et al. Star-shaped Polymers through Simple Wavelength-Selective Free-Radical Photopolymerization. *Angewandte Chemie International Edition* **2017**, *56*, 14306–14309.
- (271) Uhlig, K.; Wegener, T.; He, J.; Zeiser, M.; Bookhold, J.; Dewald, I.; Godino, N.; Jaeger, M.; Hellweg, T.; Fery, A.; Duschl, C. Patterned thermoresponsive microgel coatings for noninvasive processing of adherent cells. *Biomacromolecules* **2016**, *17*, 1110–1116.
- (272) Franck, A.; Vandebril, S.; Vermant, J.; Fuller, G. Double wall ring geometry to measure interfacial rheological properties. *dimensions* **2008**, *22*, R32.

-
- (273) Hermans, E.; Vermant, J. Interfacial shear rheology of DPPC under physiologically relevant conditions. *Soft matter* **2014**, *10*, 175–186.
- (274) Renggli, D.; Alicke, A.; Ewoldt, R. H.; Vermant, J. Operating windows for oscillatory interfacial shear rheology. *Journal of Rheology* **2020**, *64*, 141–160.
- (275) Huang, S.; Gawlitza, K.; von Klitzing, R.; Steffen, W.; Auernhammer, G. K. Structure and rheology of microgel monolayers at the water/oil interface. *Macromolecules* **2017**, *50*, 3680–3689.
- (276) Conley, G. M.; Aebischer, P.; Nöjd, S.; Schurtenberger, P.; Scheffold, F. Jamming and overpacking fuzzy microgels: Deformation, interpenetration, and compression. *Science advances* **2017**, *3*, e1700969.
- (277) Nayak, S.; Gan, D.; Serpe, M. J.; Lyon, L. A. Hollow thermoresponsive microgels. *Small* **2005**, *1*, 416–421.
- (278) Schmid, A. J.; Dubbert, J.; Rudov, A. A.; Pedersen, J. S.; Lindner, P.; Karg, M.; Potemkin, I. I.; Richtering, W. Multi-shell hollow nanogels with responsive shell permeability. *Scientific reports* **2016**, *6*, 22736.
- (279) Richtering, W. Responsive emulsions stabilized by stimuli-sensitive microgels: emulsions with special non-Pickering properties. *Langmuir* **2012**, *28*, 17218–17229.
- (280) Rey, M.; Fernandez-Rodriguez, M. A.; Karg, M.; Isa, L.; Vogel, N. Poly-N-isopropylacrylamide Nanogels and Microgels at Fluid Interfaces. *Accounts of Chemical Research* **2020**.
- (281) Derkach, S.; Krägel, J.; Miller, R. Methods of measuring rheological properties of interfacial layers (Experimental methods of 2D rheology). *Colloid journal* **2009**, *71*, 1–17.
- (282) Lee, M. H.; Reich, D. H.; Stebe, K. J.; Leheny, R. L. Combined passive and active microrheology study of protein-layer formation at an air- water interface. *Langmuir* **2010**, *26*, 2650–2658.

Appendix

A.1. Microgel Synthesis and Characterization

Four different microgel model systems with different VPTTs were synthesized for this thesis. All systems contained small amounts of the comonomer APMH (≈ 2 mol%) to allow for post modification of the microgels, such as covalent labeling with fluorescent dyes. [160, 161] This primary amine is positively charged at neutral pH. Therefore, a cationic initiator (V50) and surfactant (CTAB) were used to prevent aggregation during the synthesis. There are no indications that the small amount of APMH influences the interfacial behavior of the microgels. All microgels were synthesized with the same following procedure, the values (mass of monomers, volumes, and so forth) are given in Table A.1. pNIPAM, pDEAAM, pNIPAM-co-DEAAM, and pNIPAM-co-DEAAM_{small} correspond to the sample codes SB_104c, SB_105c, SB_103c, and SB_106c in the lab journal and the sample codes SFB985_B8_SB_M000585, SFB985_B8_SB_M000586, SFB985_B8_SB_M000587, and SFB985_B8_SB_M000588 on the SFB 985 sharepoint, respectively. Additional experimental data may be found on the SFB 985 sharepoint using the sample codes.

Table A.1: Synthesis parameters for different microgel systems. The first two rows contain the sample code in the lab journal and the used abbreviations in Chapter 4 to 8. The weighed mass of NIPAM, m_{NIPAM} , weighed mass of DEAAM, m_{DEAAM} , weighed mass of APMH, m_{APMH} , weighed mass of BIS, m_{BIS} , weighed mass of CTAB, m_{CTAB} , and weighed mass of initiator (V50), $m_{initiator}$, are given in grams (g). T_{vessel} is the temperature measured in the reaction vessel. V_{vessel} is the total volume of water used for the synthesis. c_{total} is the total monomer concentration. The molar composition of the initiator, $mol_{initiator}$, molar composition of the cross-linker, mol_{BIS} , molar composition of APMH, mol_{APMH} , is calculated from the weighed-in masses. The revolutions per minute, RPM , and the relative centrifugal force, RCF , of the rotor for purification are given.

Parameter	Unit	SB104c	SB105c	SB103c	SB106c
-	-	pNIPAM	pDEAAM	pNIPAM-co-DEAAM	pNIPAM-co-DEAAM _{small}
m_{NIPAM}	(g)	5.4546	0	2.0069	2.71019
m_{DEAAM}	(g)	0	5.5140	3.4854	4.7246
m_{APMH}	(g)	0.1474	0.1327	0.1384	0.1632
m_{BIS}	(g)	0.3398	0.3607	0.3748	0.4998
m_{CTAB}	(g)	0.0340	0.0221	0.0251	0.0574
$m_{initiator}$	(g)	0.2253	0.2165	0.2151	0.2822
T_{vessel}	(°C)	65	65	62	72
V_{vessel}	(mL)	370	333	346	808
c_{total}	(mM)	141.23	142.57	142.42	82.31
$mol_{initiator}$	(mol%)	1.59	1.68	1.61	1.56
mol_{BIS}	(mol%)	4.22	4.93	4.93	4.87
mol_{APMH}	(mol%)	1.98	1.97	1.97	1.73
RPM	(rpm)	30 000	30 000	30 000	33 000
RCF	(-)	70 000	70 000	70 000	84 000

Microgels were synthesized by precipitation polymerization. The monomers,

NIPAM, and/or DEAAM, BIS, and APMH were dissolved in double-distilled water. The monomer solution was heated and purged with nitrogen under constant stirring. Simultaneously, the initiator (V50) and CTAB were each dissolved in 20 mL water in two separate vessels and degassed for one hour. The surfactant was injected into the reaction vessel and stirred for 30 more minutes to equilibrate. The polymerization was initiated by adding the initiator solution. The reaction was carried out for 4 h at T_{vessel} under constant nitrogen flow and stirring. The obtained microgels were purified by threefold ultra-centrifugation at RPM and subsequent re-dispersion in fresh, double-distilled water. Lyophilization was applied for storage.

All microgel samples were characterized by multi-angle dynamic light scattering. The hydrodynamic radii, R_h , as a function of temperature are presented in Figure A.1. The results for R_h at different swelling-states and temperatures are highlighted in Table A.2.

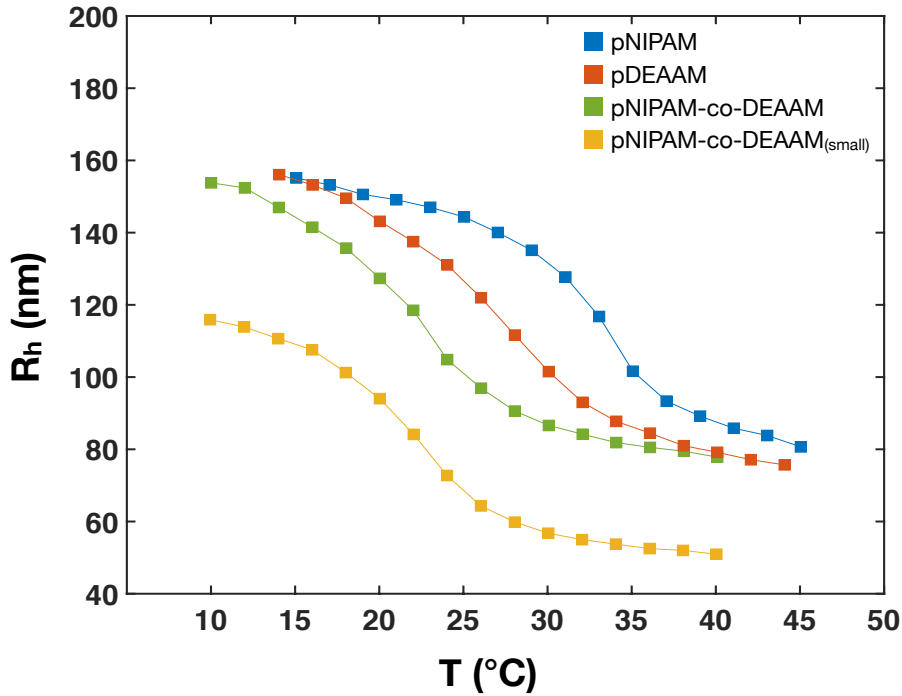


Figure A.1: Multi angle light scattering data of synthesized microgel samples. Plot of R_h versus Temperature, T , for different samples.

The internal structure of pNIPAM, pNIPAM-co-DEAAM and pDEAAM microgels was additionally characterized by small-angle neutron scattering (SANS). SANS form factors, $P(q)$, versus scattering vector, q , for pNIPAM-co-DEAAM and pDEAAM microgels in dilute suspensions of D₂O at $T = 20$, blue circles, and 40 °C, red circles, are presented in Figure A.2A and C, respectively. The SANS data of the pNIPAM microgels are given in Figure 4.1C of Chapter 4. For both temperatures and all microgels, the scattering curves were fitted with a fuzzy sphere model. The results of the fits are shown in Figure A.2B and D for pNIPAM-co-DEAAM and pDEAAM microgels. The results for pNIPAM microgels are shown in Figure 4.1D of Chapter 4. The radii, R_{SANS} , and size polydispersities, σ_p , are summarized in Table A.2.

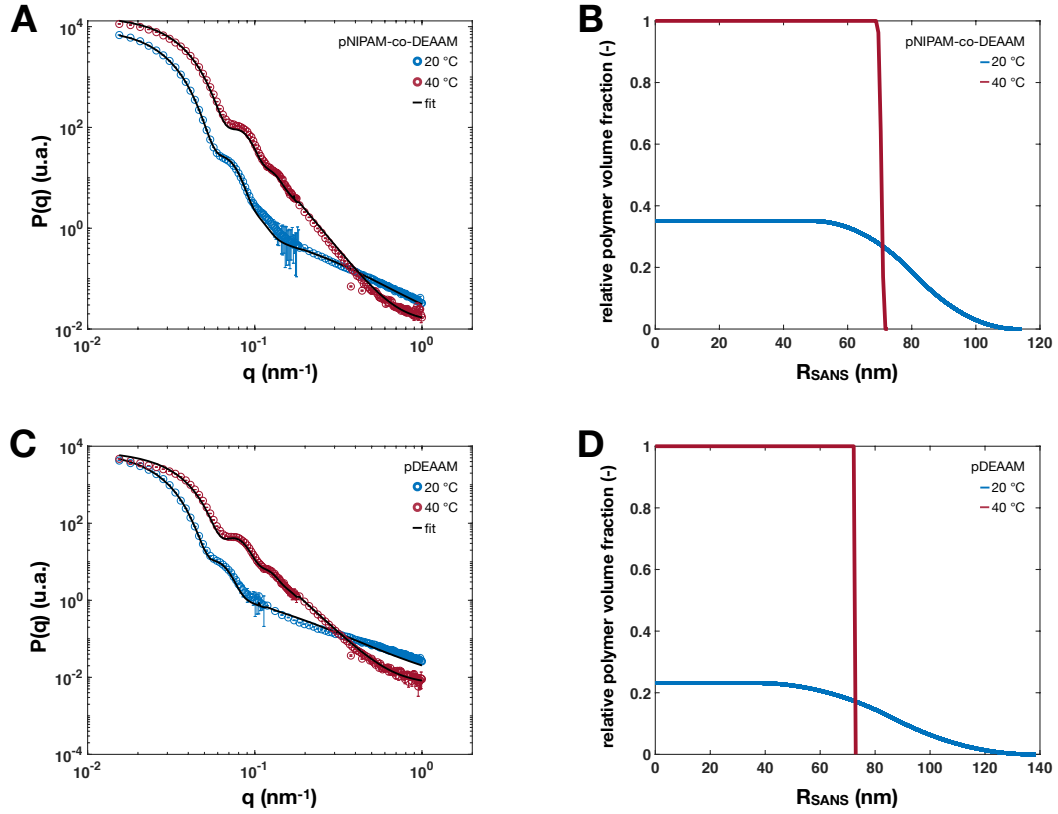


Figure A.2: SANS data and analysis of pNIPAM-co-DEAAM and pDEAAM microgels. (A and C) SANS form factor, $P(q)$, versus scattering vector, q , for pNIPAM-co-DEAAM and pDEAAM microgels in dilute suspensions of D₂O at $T = 20$, blue circles, and 40 °C, red circles. The solid black lines are fits with the fuzzy sphere model [49]. (B and D) Relative polymer volume fraction versus radius obtained from the data fits at $T = 20$, blue solid line, and 40 °C, red solid line.

In Figure A.3A-C, a direct comparison of the pNIPAM, pNIPAM-co-DEAAM and pDEAAM relative polymer volume fraction profiles at $T = 20$ and 40 °C is displayed.

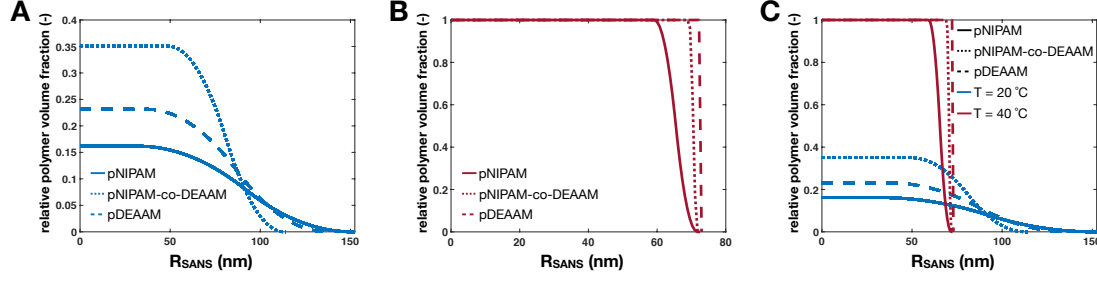


Figure A.3: Relative polymer volume fraction versus radius obtained from the data fits at $T = 20$ and 40 °C. (A-C) pNIPAM, solid lines, pNIPAM-co-DEAAM, dotted lines, pDEAAM, dashed lines. $T = 20$ and 40 °C are depicted in blue and red, respectively. (A) Comparison at $T = 20$ °C. (B) Comparison at $T = 40$ °C. (C) Comparison at $T = 20$ and 40 °C

The molecular weight, M_{vis} , of all synthesized microgels was computed by the combination of the viscosity of microgel suspensions and DLS. For this, the time of fall, t , of a fixed volume of differently concentrated suspensions through a thin capillary of an Ubbelohde viscosimeter ($C = 3.156 \cdot 10^9 \text{ mm}^2 \text{ s}^{-2}$) was measured and the kinematic viscosity, $\eta_k = Ct$, calculated. With a know sample density that can be approximated with the one from water ($\rho_{\text{H}_2\text{O}}$) due to the low microgel concentrations, η_k can be converted into the viscosity $\eta = \eta_k \rho_{\text{H}_2\text{O}}$. The relative viscosity ($\eta_r = \eta/\eta_{\text{solvent}}$) as a function of the suspension concentration is fitted with the Einstein-Batchelor equation ($\eta_r = 1 + 2.5kc_{wt\%} + 5.9(kc_{wt\%})^2$) [223] to obtain the conversion constant k . The graphs of η_r versus the mass fraction are given in Figure A.4A-D. All measurements shown were conducted at $T = 20$ °C. The conversion constant is related to the volume of the swollen microgels ($V_{sw} = 4/3\pi R_{h,20}^3$) and the mass of the particle. [165, 220] The values for the viscosity averaged molecular weight, M_{vis} , the number of monomer units, n_M , and the conversion constant, k , are summarized in Table A.2.

Table A.2: Characterization of different microgel systems. The hydrodynamic radii are given in swollen state, $R_{h,swollen}$, at $T = 20$ °C, $R_{h,20^\circ\text{C}}$, and in deswollen state $R_{h,deswollen}$. The SANS radii were measured at $T = 20$ °C, $R_{SANS,20^\circ\text{C}}$, and $T = 40$ °C, $R_{SANS,40^\circ\text{C}}$. Size polydispersities, σ_p , are the averaged values of both temperatures. Conversion constants were computed in swollen state, $k_{swollen}$, and at $T = 20$ °C, $k_{20^\circ\text{C}}$. The viscosity averaged molecular weight, M_{vis} , was averaged from both temperatures if available.

Parameter	Units	SB104c	SB105c	SB103c	SB106c
-	-	pNIPAM	pDEAAM	pNIPAM-co-DEAAM	pNIPAM-co-DEAAM _{small}
$R_{h,swollen}$	(nm)	(155 ± 3)	(156 ± 2)	(162 ± 1)	(116 ± 1)
$R_{h,20^\circ\text{C}}$	(nm)	(153 ± 3)	(143 ± 2)	(127 ± 1)	(94 ± 1)
$R_{h,deswollen}$	(nm)	(76 ± 2)	(74 ± 1)	(78 ± 1)	(50 ± 1)
$R_{SANS,20^\circ\text{C}}$	(nm)	(150 ± 2)	(137 ± 3)	(113 ± 3)	-
$R_{SANS,40^\circ\text{C}}$	(nm)	(72 ± 1)	(73 ± 1)	(73 ± 2)	-
σ_p	(%)	(7 ± 1)	(9 ± 1)	(8 ± 1)	-
$k_{swollen}$	(-)	(18.5 ± 0.1)	(17.1 ± 1)	(16.6 ± 0.9)	-
$k_{20^\circ\text{C}}$	(-)	(18.5 ± 0.1)	(12.7 ± 0.2)	(7.8 ± 0.6)	(13.0 ± 0.1)
M_{vis}	(10 ⁸ · g mol ⁻¹)	(4.3 ± 0.3)	(5.7 ± 0.2)	(6.4 ± 0.2)	(1.3 ± 0.5)

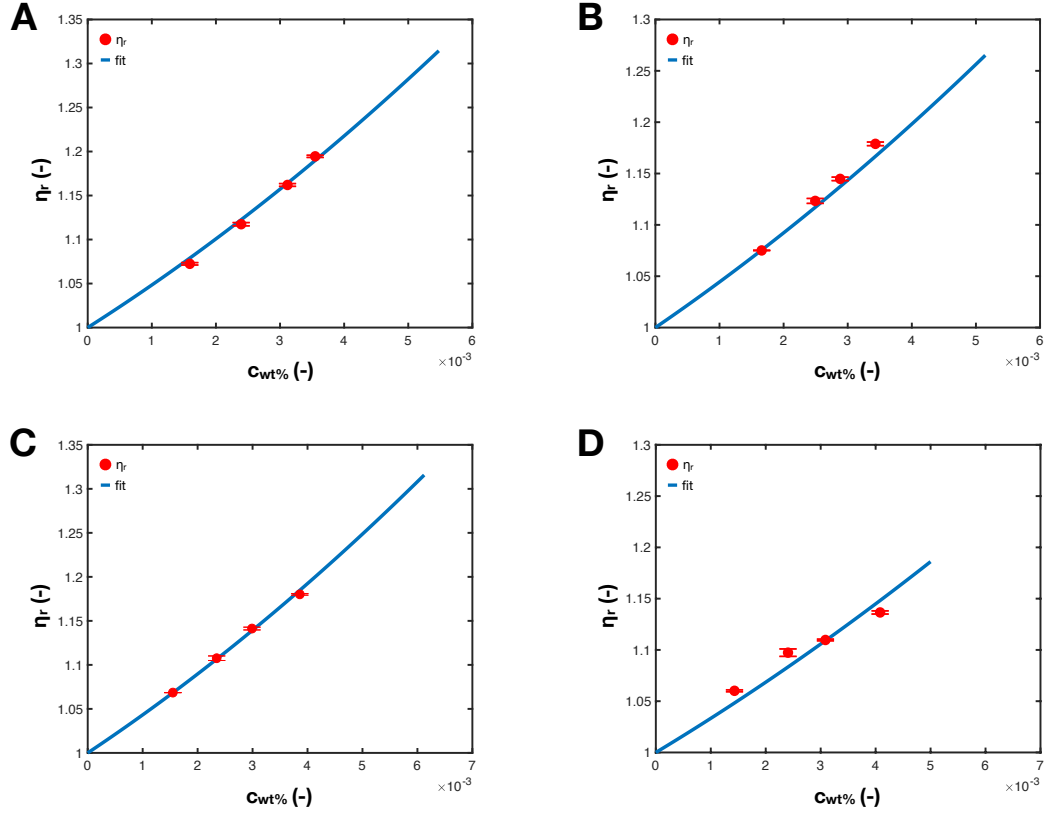


Figure A.4: Relative viscosity of microgel samples. (A) pNIPAM microgels, (B) pDEAAM microgels, (C) pNIPAM-co-DEAAM microgels and (D) pNIPAM-co-DEAAM_{small} microgels. Red circles are measurement data with error bars and blue lines are the fits with the Einstein-Batchelor equation [223]. All measurements were conducted at $T = 20$ °C.

A.2. Interfacial Rheology

The rheological properties of microgel monolayers are of great interest to elucidate the mechanisms of emulsion stabilization. [61, 279, 280] The measurement of these properties is experimentally feasible with different methods. For dilational rheology, a pendant drop or Langmuir trough setup can be used in oscillating drop or barrier mode, respectively. Interfacial shear rheology can be conducted with special geometries, such as bicone or double wall-ring (DWR), attached to a standard shear rheometer or with a magnetic interfacial stress rheometer. Indeed, there are other possible methods and techniques which can be used for interfacial rheology. [76, 274, 275, 281, 282]

In the scope of this thesis, it was planned to measure the rheological properties of microgel monolayers with the commercial available double wall-ring (DWR) setup, but this setup has an eminent disadvantage: measurement of the surface pressure or interfacial tension and *in situ* control of the particle density at the interface is not possible. Therefore, a device that combines a Langmuir trough with an interfacial shear rheometer using a DWR geometry following Ref. [272] and [273] was built.

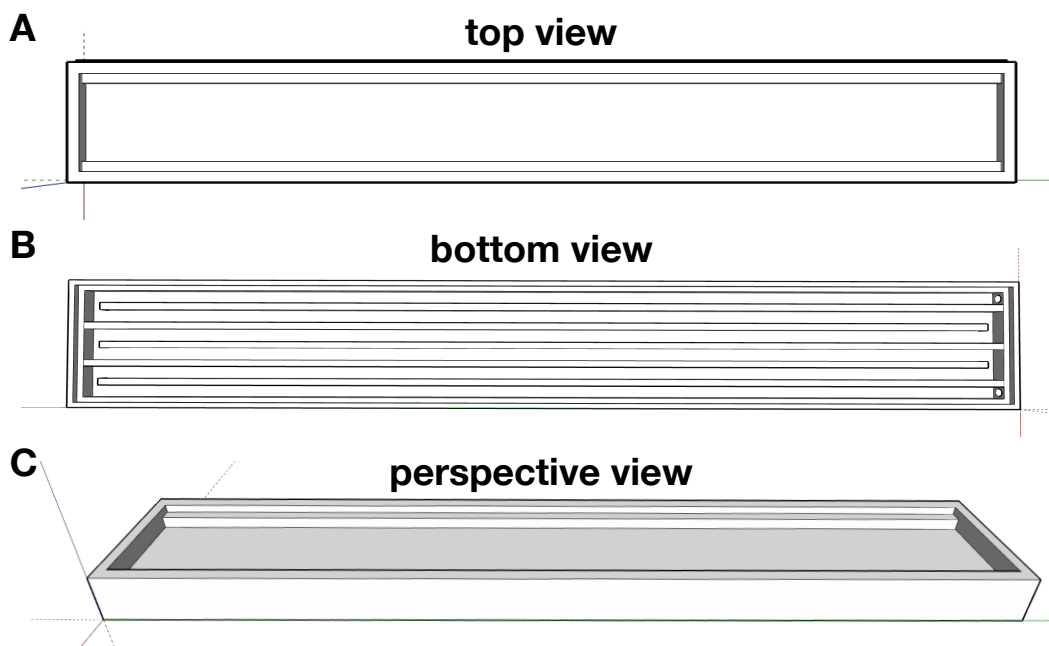


Figure A.5: Three-dimensional model of the Langmuir trough for interfacial shear rheology. (A) Top view of the inner and outer compartment, (B) bottom view of the thermal labyrinth, and (C) perspective view. Lines in red, green, and blue are the y-axis, x-axis, and z-axis, respectively.

A liquid-liquid Langmuir trough was custom made in cooperation with the shared mechanical workshop of the institute of inorganic and physical chemistry. The commercially available liquid-liquid troughs could not be used, because their size (width = 54 mm) is not sufficient to fit reasonably sized DWR geometries. The trough was cut directly from a single piece of poly(oxymethylene) glycol (POM). The inner compartment, for the sub-phase, has the dimensions of 790 mm \times 85 mm \times 10mm and the outer compartment, for the top-phase, the dimensions of 790 mm \times 105 mm \times

7mm (Length \times Width \times Height). Excluding the barriers, the trough has a maximum interfacial area of roughly 630 cm² and a minimum area of 60 cm². Equipped with the DWR extension the minimum area is \approx 120 cm². A thermal labyrinth with a large surface area that can be connected to a water bath was milled on the other side of the POM block. The labyrinth is sealed watertight using a thin plate of POM (\approx 3 mm). Top, bottom, and perspective views of the 3D model of the trough are shown in Figure A.5. The finished rheo-Langmuir trough is shown in Figure A.8.

The double wall cup for the DWR geometry was grooved from POM. Two cups were manufactured with two different diameters ($\varnothing_{total} = 55$ and 72 mm) for two sizes of ring geometries. The inner, \varnothing_{in} , outer, \varnothing_{out} , and total diameter, \varnothing_{total} , of the cups are given in Figure A.6. Both walls have a 1 mm sharp edge step (Figure A.6C, notch) at 10 mm distance from the bottom to pin and create planar interfaces. In contrast to the commercially available setup, the double wall cup has inlets (Figure A.6C, opening) for the interface which are placed in direction of the long axis of the trough. These opening allowing the surface-active material to enter or leave the cup, for example, when the monolayer is compressed.

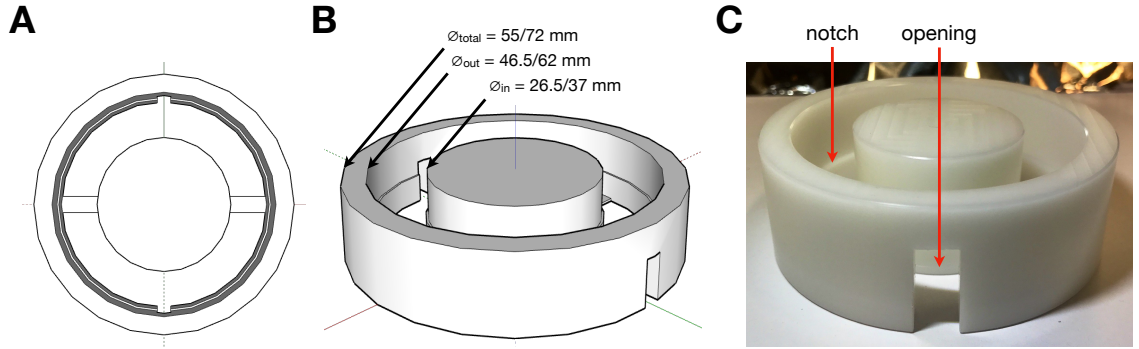


Figure A.6: Three-dimensional model and image of the double wall cups for interfacial shear rheology. (A) Top view, (B) perspective view with inner, \varnothing_{in} , outer, \varnothing_{out} , and total diameter, \varnothing_{total} , and (C) digital image of the double wall cup with $\varnothing_{total} = 72$ mm. The notch and openings are highlighted. Lines in red, green and blue are the y-axis, x-axis and z-axis, respectively.

The ring geometries were custom made by direct metal printing (3D Systems public, LayerWise NV, Belgium) from medical-grade titanium (Ti6Al4V Grade 23). In Figure A.7A-B a 3D model of the geometries and in Figure A.7C the finished product after 3D printing is shown. The ring itself has a diamond-shaped cross-section with an edge length of $\sqrt{0.5}$ mm to pin the interface. Furthermore, it has three openings to enable the exchange of the inner and outer area while compression of the monolayer and ensure homogeneous Π . The diameters of the geometries, inner, \varnothing_{in} , outer, \varnothing_{out} and averaged diameter, \varnothing_{mid} , for both sizes are given in Figure A.7. The two sizes can be used to extend the accessible strain or/and stress of the DWR setup. [274]

Construction drawings of the double wall cups and ring geometries were provided by the Vermant Group, ETH Zurich.

In Figure A.8 the “ready-to-measure” interfacial shear rheology devices is shown. The whole setup is placed inside a poly(methyl methacrylate) box to reduce airflow

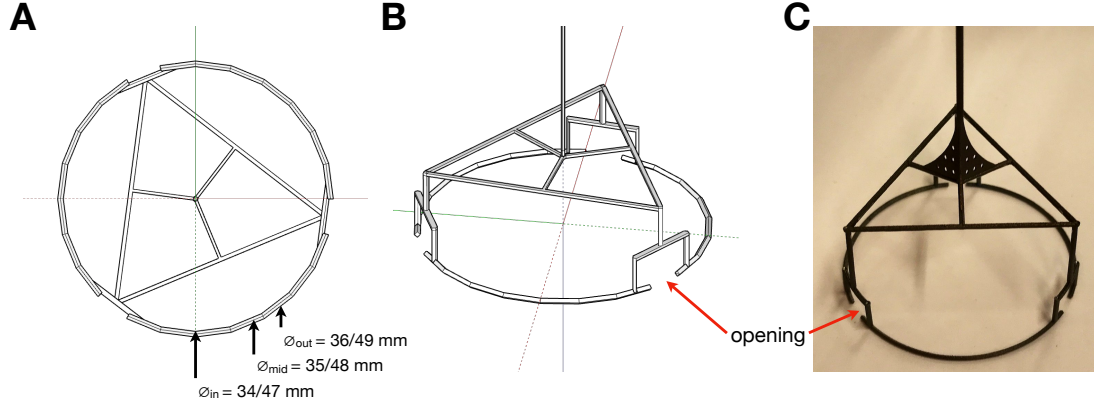


Figure A.7: Three-dimensional model and image of the ring geometries for interfacial shear rheology. (A) Top view with inner, \varnothing_{in} , outer, \varnothing_{out} and averaged diameter, \varnothing_{mid} , (B) perspective view, and (C) digital image of the ring geometry with $\varnothing_{mid} = 48$ mm. The openings are highlighted in (B) and (C). Lines in red, green, and blue are the y-axis, x-axis, and z-axis, respectively.

and the adsorption of dirt to the interface. A passive damped optical table (air-cushions) to reduce vibrations is used.

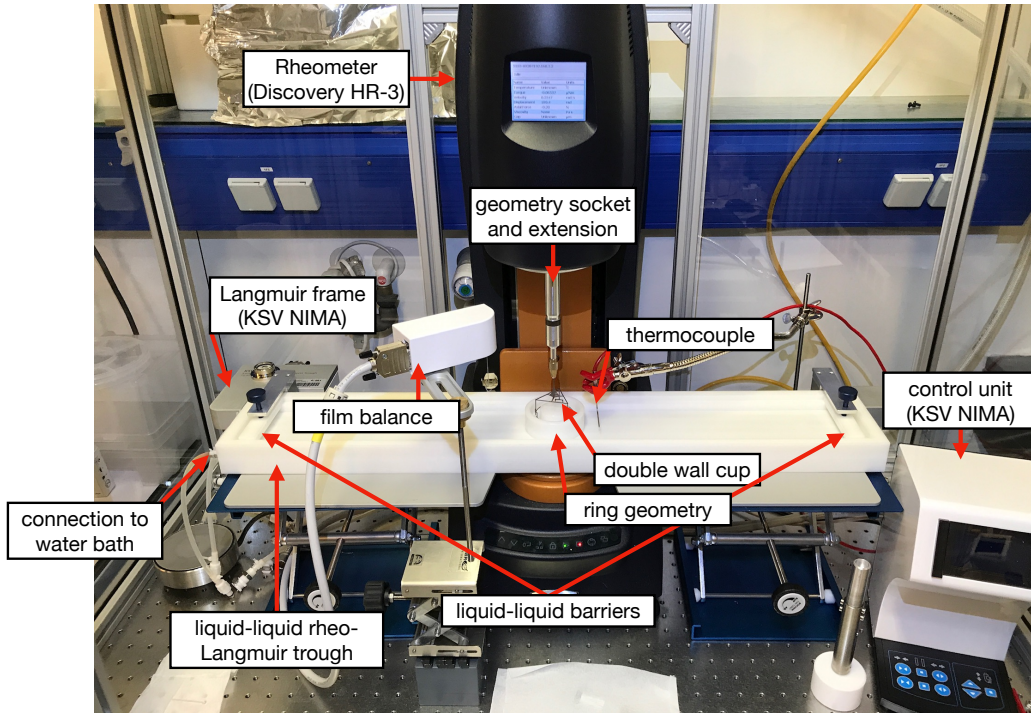


Figure A.8: Interfacial shear rheology setup with Langmuir trough and double wall-ring.

The new interfacial shear rheology setup was tested by measuring compression isotherms and amplitude sweeps of monolayers of the pNIPAM microgel discussed

in Chapters 4, 6, 7 and 8 at $T = 20\text{ }^{\circ}\text{C}$. Therefore, all components were carefully cleaned. The ring geometry with a 48 mm diameter was attached to the rheometer and calibrated. The double wall cup was inserted into the trough and roughly 720 ml of ultrapure water (18,2 MOhm-cm) were filled in. A highly porous platinum Wilhelmy plate (perimeter = 39.24 mm) was mounted to the electronic film balance and contacted with the interface. The Wilhelmy plate was aligned parallel to the barriers. The air-water interface was cleaned by carefully removing dust and surface-active impurities with a suction pump. Subsequently, the geometry was placed at the interface while monitoring the axial force. A strong change in axial force was used to identify whether the geometry was attached to the interface. Additionally, the position of the ring was checked with the bare eye and a flashlight. After performing a compression-expansion cycle to verify that the interface was clean, three times filtered decane ($\approx 280\text{ mL}$) were added as top-phase. The decane was carefully and slowly poured into the trough over the edge step to minimize irritation and prevent detachment the geometry from the interface. The cleanness of the decane-water interface was checked again by a compression and expansion cycle. The microgel monolayer was created by the addition of an aqueous solution of pNIPAM microgels with a Hamilton syringe.

Measurements of the compression isotherms and amplitude sweeps were performed at the same time. The interface was compressed at 5 mm min^{-1} and when a desired Π was reached all barrier movements were stopped. After equilibration (roughly 20 min) amplitude sweeps at $1\text{ rad s}^{-1} = 0.16\text{ s}^{-1}$ and $3\text{ rad s}^{-1} = 0.48\text{ s}^{-1}$ were performed. The amplitude, γ_{Rheo} , was varied between 0.1 and 10 % ($1.16\text{ }10^{-4}$ to $2.32\text{ }10^{-2}$ rad) in 25 steps. After the amplitude sweeps, the next surface pressure was approached. The full compression isotherm was measured (Figure A.9A) starting from different initial microgel amounts spread to the interface. Interfacial shear rheology measurements were performed between 1 and 32 mN m^{-1} . In Figure A.9B-C examples at 1, 10, 20, 25, 30 mN m^{-1} are shown by full circles, diamonds, squares, hexagonal stars, and triangles, respectively. The measurement points are highlighted with the same symbols in Figure A.9A.

Compression isotherms measured in the new trough show qualitatively the same trend as in the commercial available Langmuir troughs (Chapter 5, Figure 5.1). Differences in the *area/mass*-values can be seen at higher compression, which can be explained by the reduced available area of the trough due to the double wall cup. In this compression isotherm the area of the trough was not yet reduced by the area the cup takes up, especially at high compression (low trough areas) this bias the *area/mass*-values.

The amplitude sweeps for 1 and 3 rad s^{-1} (Figure A.9B and C) show the same trend. At low compression, 1 mN m^{-1} , values of G' and G'' are within or close to the machine limits. Increasing Π stepwise to 25 mN m^{-1} , close to the onset point of the isostructural phase transition, increases the storage modulus significantly and the loss modulus slightly (Figure A.9B and C, blue and green diamonds, squares and hexagonal stars). Compression the monolayer to values above 25 mN m^{-1} leads to a decrease of G' (Fig. A.9B and C, blue triangles), while G'' stays nearly constant (Fig. A.9B and C, green triangles). The decrease of the elasticity of microgel monolayers was already observed in Ref. [76] using a different interfacial rheology setup (interfacial microdisk rheology) for similar microgels. Furthermore, the absolute values for G' and G'' measured with the microdisk and DWR method have

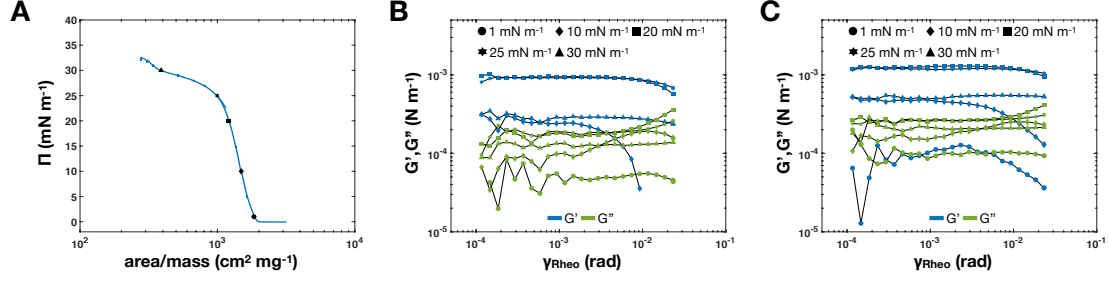


Figure A.9: Compression isotherm and interfacial amplitude sweeps of pNIPAM microgel monolayers. (A) Π - $area/mass$ isotherm of pNIPAM microgel monolayers measured with the new Langmuir trough at $T = 20\text{ }^{\circ}\text{C}$. For more details see text. (B-C) Storage (blue symbols), G' , and loss modulus (green symbols), G'' , versus the oscillatory displacement, γ_{Rheo} , of pNIPAM microgel monolayers at 1, 10, 20, 25, 30 mN m^{-1} and $T = 20\text{ }^{\circ}\text{C}$. (B) Amplitude sweeps at $1\text{ rad s}^{-1} = 0.16\text{ s}^{-1}$. For 1 mN m^{-1} G' is always below the machine limits and not shown. (C) Amplitude sweeps at $3\text{ rad s}^{-1} = 0.48\text{ s}^{-1}$.

the same order of magnitude. These measurements show that the Langmuir trough interfacial shear rheology setup works within the expected parameters and is ready for further measurements.

Acknowledgments

Here, I would like to thank the many people who have helped me during this thesis.

First of all, I would like to thank Walter for the opportunity to do my thesis in his group, the supervision, and the discussions. I would also like to thank him for the opportunity to attend many conferences and courses. Most of all, I would like to thank him for being patient when I (and Andrea) once again had an idea to build a new device or get beam-time somewhere.

I want to thank Prof. Isa for agreeing to be the second referee of my thesis. Furthermore, I would also like to thank him for allowing me to stay in his group at ETH Zurich (twice), interesting discussions, and improvements to the manuscripts. His works together with K. Geisel, M. Rey, and W. Richtering were the starting point of my thesis.

I would like to thank all my colleagues and former colleagues from the IPC, the SFB 985, and other facilities, not only for the good working atmosphere but also great Friday afternoon (and night) beers, scientific retreats, group excursions, and a lot of cakes. I like to thank my students for their hard work. A big thank you to my former office mates from the “Bärchenbüro”, Pascal and Cornelius, who showed me how computational chemistry scientists work (I guess you have to buy Birkenstock sandals for that). I would also like to thank the “Witches of 2-1-2”, Monia “McTony” Brugnoli, Andrea “Melle” Melle, and Frieda “Oh come on guys” Schulte; It was amazing to share a room with you in Nawlins.

A tremendous thank you goes to my office mates from room 211, Andrea P. D. Scotti, who’s calmness, organization talent, and superb handwriting should be an inspiration for the whole scientific community, and Maximilian C. Schmiddy, who was “immer stets bemüht” to follow my Matlab comments: “Andiamo, fratelli. Non Mastroianni tutti i Funions. Andiamo,... fratelli. Non Mastroianni... tutti ... i Funions!”.

I want to thank Frieda, Andrea, and Max for critically reviewing my thesis and improving my thesis. I finally know the difference between “I like cooking my family and my pets” and “I like cooking, my family, and my pets”.

I want to thank all collaborators who directly or indirectly contributed to my thesis: the members of the Isa group for making the stay(s) very pleasant, especially Miguel Angel, Michele, and Siddarth. Prof. Vermant and Damian Renggli for letting me copy the interfacial rheology setup. The members of the mechanical workshop of the IPC/IAC, foremost Thorsten Marioneck, and the electronical workshop of the IPC, for making my ideas into real devices. I want to thank Armando Maestro, Philipp Gutfreund, and Thomas Geue for the help with the neutron reflectometry experiments. I also would like to thank Wojciech Ogieglo for introducing and greatly helping with the ellipsometry measurements.

In the case I forgot to name you personally, please feel thanked deeply anyway and follow the link: “<https://www.youtube.com/watch?v=dQw4w9WgXcQ>”.

Finally, I want to thank my parents, my brother and his wife, my whole family, and my girlfriend for the continuous support and the prerequisites to conduct and accomplish my work.

Thank you! That’s all folks!

Courses

September 2019 Good Scientific Practice Workshop

July 2018 2nd Joint Summer School SFB 985 & Georgia Institute of
Technology in Monschau, Germany

2016-2017 Introductory course to Matlab, Einführung in MATLAB (fit
in IT)

Conference Contributions

Oral Contributions

- September 2019** 33rd Conference of the European Colloid and Interface Society (ECIS) in Leuven, Belgium
- March 2019** APS March Meeting 2019 in Boston, USA
- April 2017** 13th Zsigmondy Colloquium in Saarbrücken, Germany

Poster Contributions

- September 2018** 32nd Conference of the European Colloid and Interface Society (ECIS) Ljubljana, Slovenia
- March 2018** 255th ACS National Meeting 2018 in New Orleans, USA
- October 2017** Kolloidtagung 2017 in Munich, Germany
- July 2017** 10th Liquid Matter Conference in Ljubljana, Slovenia

Supervised Students

Dominik Braunmiller	Research assistant, Characterization of Microgels with Small-Angle Scattering Techniques and Rheology (2018)
Sarah Michael	Research student, Microgels at Interfaces: Influence of Cononsolvency on the Interfacial Properties of Microgels (2017)
Tim Kurtschildgen	Research student, Synthese von NIPAM-Sternpolymeren und deren Oberflächeneigenschaften (2017)
Lisa Brück	Research student, Microgels at Interfaces: Synthesis and Characterization of Double Thermo-Responsive Core-Shell Microgels (2017)

Curriculum Vitae

Personal Information

Name	Steffen Bochenek
Date of Birth	08.08.1989
Nationality	German

Education

2016-Present	PhD candidate, RWTH Aachen University, Germany
2013-2016	Master of Science Chemistry, RWTH Aachen University, Germany
2010-2013	Bachelor of Science Chemistry, RWTH Aachen University, Germany
2009	General Qualification for University Entrance (Abitur), Werner-Jäger-Gymnasium, Nettetal